The Properties of Semileptonic Decays of Charmed D Mesons

Thesis by
Daniel Mark Coffman

In Partial Fulfillment of the Requirements
for the Degree of
Doctor of Philosophy

California Institute of Technology
Pasadena, California

1987

(Submitted December 8, 1986)

Abstract

The MARK III collaboration has collected a large sample of D mesons produced at the $\psi(3770)$ resonance. The reconstruction of several thousand hadronic D decays makes possible for the first time the reconstruction of exclusive semileptonic D decays. Absolute branching ratios are measured for the nine decays $D^0 \to K^- e^+ \nu_e$, $D^0 \to K^- \pi^0 e^+ \nu_e$, $D^0 \to \overline{K}^0 \pi^- e^+ \nu_e$, $D^+ \to \overline{K}^0 e^+ \nu_e$, $D^+ \to K^- \pi^+ e^+ \nu_e$, $D^0 \to \pi^- e^+ \nu_e$, $D^0 \to K^- \mu^+ \nu_\mu$, $D^0 \to \overline{K}^0 \pi^- \mu^+ \nu_\mu$, and $D^+ \to \overline{K}^0 \mu^+ \nu_\mu$. The sums of the exclusive branching ratios are in good agreement with the inclusive semileptonic branching ratios measured by the MARK III. The rate of the Cabibbo-suppressed decays is consistent with the predicted rate. The contribution of the $K^*(892)$ to the K–π invariant mass spectrum for decays of the type $D \to K \pi e^+ \nu_e$ is found to be about 55%. The vector form factor in the decays $D^0 \to K^- e^+ \nu_e$ and $D^0 \to K^- \mu^+ \nu_\mu$ is measured and found to be consistent with a simple pole form.

Acknowledgements

I could never have completed this thesis had I not received support and encouragement from many people. First among them are my parents who provided an inexhaustible source of understanding and solace, humor and council. My younger brother proved to me time and again that there is much more to life than science, a lesson I have always tended to forget; if I understood people only half as well as he, I would be a very wise man. My older brother and sister-in-law have provided the newest addition to the Coffman family; I marvel at this constantly.

To my thesis advisor David Hitlin I owe an extraordinary debt of gratitude. He has used his great physical insights on many occasions to lend direction and focus to my efforts. I have benefited greatly from many conversations with him during which the topic might wander from physics to literature to music. The aspect of our relationship I have most appreciated is Dave's unfailing faith in me, a faith that often has far exceeded my own.

It has been a great pleasure to carry out my research as a member of the MARK III collaboration. I have gotten to know many remarkable people and I wish to acknowledge not only the assistance but also the friendship of several past and present members of the MARK III: Al Odian, Terry Schalk, Norbert Wermes, Walter Toki, Jay Hauser, and Günter Wolf. My 'mentor in residence' has been Rafe Schindler to whom I owe a great deal, not the least being several good bottles of wine. Finally, I must thank some of my fellow graduate students for the pleasant, collegial atmosphere I have so enjoyed: Bijan Nemati, Tim Bolton, Steve Wasserbaech, Basil Tripsas, Tim Freese, Constantin Simopolous, and my fellow Floridian Gregory Dubois.

Table of Contents

List of Tables

List of Figures

Chapter 1: Introduction

The greatest triumph of high energy physics over the last forty years has been the development of the *Standard Model* — the gauge theory of the electromagnetic, weak, and strong interactions. This theory describes successfully so seemingly different processes as the production of muon pairs in electron-positron collisions and the decay of vector bosons in proton-antiproton collisions. So successful in fact is this theory that one is tempted to assume that its content should somehow have been obvious to earlier investigators, but this, of course, was not the case. Physicists found themselves confronted with a baffling array of phenomena and it is remarkable that they were able to impose order on this apparent chaos. Credit for this is due largely to a few bold theoretical conjectures and a number of sophisticated experiments designed to test them.

By the end of the 1950's, the gauge theory of electromagnetism — Quantum Electrodynamics or QED — was well established. In particular, the *renormalizability* of the theory had been demonstrated. The divergences, which had so perplexed many physicists, could be cancelled order-by-order in a perturbation expansion to yield finite results. Calculations carried out even to quite high order were consistently in agreement with experiment. The predicted and measured value of the Lamb shift for the hydrogen atom were in excellent agreement. Perhaps most impressive of all was the value predicted for the gyromagnetic ratio of the electron.[1] Experiments have shown this to be one of the most accurately predicted values in the history of science.

If all appeared well for the interactions of photons with the two leptons then known — the electron and muon — the weak and strong interactions were far from being understood. By 1953, twelve hadrons had been identified: the baryons $p, n, \Lambda^0, \Sigma^-, \Sigma^+$, and Ξ^-, and the mesons $\pi^-, \pi^0, \pi^+, K^-, K^0$, and K^+. Although, some similarities and regularities among these particles had been recognized, it was impossible to predict many of their production and decay properties.

The most troublesome of the known particles were the hyperons. For example, it was difficult to understand the copious production but long lifetime of the Λ^0. In 1953, Gell-Mann[2] and Nishijima[3] introduced a new additive quantum number — strangeness — which would be conserved in strong and electromagnetic interactions. They predicted the existence of three new particles — Σ^0, Ξ^0, and $\overline{K}^0$. The Σ^0 was subsequently discovered in the decay $\Sigma^0 \rightarrow \Lambda^0\ \gamma$, and the Ξ^0 in the decay $\Xi^0 \rightarrow \Lambda^0\ \pi^0$.

An internal symmetry known as isospin, with mathematical properties identical to those of angular momentum, had been identified as a symmetry of the strong interactions.[4] Under isospin, protons and neutrons transform jointly as an eight-component isospinor. With the introduction of strangeness, isospin was no longer sufficient to explain the properties of the known hadrons since strangeness is also conserved in strong interactions. In 1956, Sakata[5] put forward a model in which the Λ^0 was joined with the proton and neutron in a triplet of fundamental particles. The strong interactions would then be invariant under the group SU(3), a larger group that the SU(2) of isospin.

Mesons have baryon number zero, so they would consist of a bound state of a baryon and an antibaryon. An octet and a singlet of mesons may be formed from a triplet of baryons and a triplet of antibaryons, as evidenced in the formula $3 \otimes \bar{3} = 8 \oplus 1$. The octet contains four isospin multiplets: I(isospin)$= \frac{1}{2}$, s(strangeness)$=$ 1; $I = 1,\ s = 0$; $I = \frac{1}{2},\ s = -1$; and $I = 0,\ s = 0$. The seven pseudoscalars then known filled the first three of these multiplets. In 1961,[6] an eighth pseudoscalar — the η^0 — was discovered and determined to be the $I = 0,\ s = 0$ singlet.

The Sakata model was highly successful in describing mesons but less so in describing baryons. Gell-Mann[7] and Ne'eman[8] proposed that baryons should also belong to an octet representation of SU(3). This model is known as the *eightfold way.* As well as accounting for the known baryons, it was able to predict the mass splitting within the octet. The Gell-Mann–Okubo mass formula,[9] in which electromagnetic mass splittings within isospin multiplets are ignored, may

be written as

$$M = M_1 + M_2 Y + M_3 (I(I+1) - \frac{1}{4}Y^2)$$

where M is the expectation value of the mass operator; Y the hypercharge; and M_1, M_2, and M_3 constants depending only on the group representation. In this parameterization, $M_N = M_1 + M_2 + \frac{1}{2}M_3$, $M_\Sigma = M_1 + 2M_3$, $M_\Lambda = M_1$, and $M_\Xi = M_1 - M_2 + \frac{1}{2}M_3$. Further, $\frac{1}{2}(M_N + M_\Xi) = \frac{1}{4}(3M_\Lambda + M_\Xi)$, a prediction borne out by experiment. Indeed, $\frac{1}{2}(M_N + M_\Xi) = 1129$ MeV/c^2, and $\frac{1}{4}(3M_\Lambda + M_\Sigma) = 1135$ MeV/c^2, where average values have been used for masses within isospin multiplets.

The eightfold way model was able to predict the existence and properties of the Ω^- baryon.[10] A number of baryon resonances had been observed in K^-N reactions. When two octets — for example, the pseudoscalar and baryon octets — are combined, a number of irreducible representations result: $8 \otimes 8 = 1 \oplus 8 \oplus 8 \oplus 10 \oplus \overline{10} \oplus 27$. The $\Delta(1232)$, observed in K^-N reactions, has $I = \frac{3}{2}$ and $Y = +1$; a multiplet with these quantum numbers occurs in the 10 and 27 representations. The 27 representation also contains many resonances not observed, so baryon resonances observed in K^-N scattering belong to a 10 representation of SU(3). This representation includes a state with $I = 0$ and $Y = -2$, termed the Ω^- by Gell-Mann. The mass formula given above predicts equal spacing within the decuplet and a mass of 1685 MeV/c^2 for the Ω^-. This state is stable against decay by the strong and electromagnetic interaction as there are no lighter $s = -3$ states. It would decay weakly into $K^-\Lambda^0, \pi^-\Xi^0$, or $\pi^0\Xi^-$. A particle with mass 1686 ± 12 MeV/c^2 and the other predicted properties was discovered in 1964 at Brookhaven.[11] This discovery helped catalyze support for the eightfold way.

The "vector minus axial-vector", or V–A, structure of weak currents had been inferred from the decay of muons and the β decay of nuclei. In 1963,[12] Cabibbo proposed an extension to this model which was able to incorporate both $\Delta s = 0$ and $\Delta s = \Delta Q = 1$ decays. The weak current would transform as an SU(3) octet and consist of not only vector and axial-vector parts, but also $\Delta s = 0$ and

$\Delta s = 1$ parts. In the notation of Cabibbo, $J_\mu = a(j_\mu^{(0)} + g_\mu^{(0)}) + b(j_\mu^{(1)} + g_\mu^{(1)})$ where j_μ and g_μ are vector and axial-vector currents, respectively; the superscript refers to the change in strangeness. In order to preserve a form of universality, Cabibbo required that $a^2 + b^2 = 1$. The weak current could then be written $J_\mu = \cos\vartheta_C(j_\mu^{(0)} + g_\mu^{(0)}) + \sin\vartheta_C(j_\mu^{(1)} + g_\mu^{(1)})$. [The notation "$\vartheta_C$" is *not* Cabibbo's, but the relation $\tan\vartheta_C = b/a$ is.] With this *Ansatz*, it is possible to compare $\Delta s = 0$ and $\Delta s = 1$ decay rates. For example,

$$\frac{\Gamma(K^- \to \mu^- \bar{\nu}_\mu)}{\Gamma(\pi^- \to \mu^- \bar{\nu}_\mu)} = \tan^2\vartheta_C \left|\frac{f_K}{f_\pi}\right|^2 \frac{m_K(1 - m_\mu^2/m_K^2)^2}{m_\pi(1 - m_\mu^2/m_\pi^2)^2}$$

It is also possible to predict the relative rates of all allowed transitions among members of the same SU(3) multiplet.

With the failure of the Sakata model to describe the structure of the baryon multiplets, there was no adequate theoretical explanation for why the known mesons and baryons populate octet representations of SU(3). Gell-Mann,[13] and independently Zweig,[14] developed a model in 1964 in which there would again be a triplet of fundamental fermion fields as in the Sakata model. These fields, or quarks[15] would, however, have baryon number 1/3 and would therefore not be identified with any known particles. As before, mesons would consist of a quark-antiquark pair, but baryons would now consist of three quarks. This would be possible as $3 \otimes 3 \otimes 3 = 1 \oplus 8 \oplus 8 \oplus 10$. Thus, the new quark model would retain the important features of the eightfold way.

Cabibbo's hypothesis was easily incorporated into the quark model. The weak currents would now be written: $j_\mu^{(0)} + g_\mu^{(0)} = \bar{d}\gamma_\mu(1-\gamma_5)u$, $j_\mu^{(1)} + g_\mu^{(1)} = \bar{s}\gamma_\mu(1-\gamma_5)u$, and $J_\mu = \cos\vartheta_C\bar{d}\gamma_\mu(1-\gamma_5)u + \sin\vartheta_C\bar{s}\gamma_\mu(1-\gamma_5)u$.

A major shortcoming of any theory containing only charged weak currents, like the currents above, is that it is not renormalizable. Consider the scattering process $\nu_\mu\bar{\nu}_\mu \to W^+W^-$ for which the lowest order Feynman diagram is shown

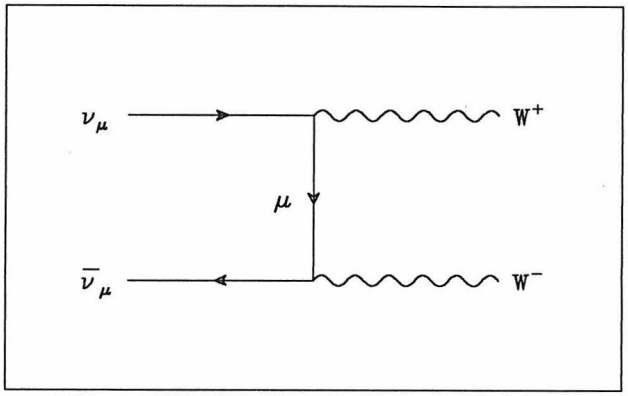

Figure 1.1: Tree level diagram for $\nu_\mu \overline{\nu}_\mu \rightarrow W^+ W^-$

in Fig. 1.1. At very high energies, the cross section increases with energy:

$$\frac{d\sigma}{d\Omega} = G_F^2 \frac{E^2 \sin^2 \vartheta}{8\pi^2}$$

where ϑ is the polar scattering angle. This violates *unitarity* in that all partial waves must decrease in their contribution to the cross section as $1/E^2$. The behavior of this cross section is dominated by the *longitudinal* component of the W polarization. This situation does not occur in QED; the gauge invariance of the electromagnetic interaction allows the longitudinal polarization states to be removed from calculations. Further, in QED, all "loop integrals" are at worst logarithmically divergent. Such divergences may be tamed with the introduction of a finite number of parameters. In this simple model of the weak interaction, many loop integrals diverge as a power of the loop momentum. This necessitates the introduction of an *infinite* number of parameters.

It is the gauge invariance of QED which insures that calculations at any order will yield finite results. Glashow[16] proposed in 1961 that SU(2) be considered a symmetry of the weak interaction. This was added to the U(1) symmetry of the electromagnetic interactions, so the total symmetry group was then SU(2)×U(1). Under this symmetry, *left-handed* spinors would transform as

follows:

$$\begin{pmatrix} e \\ \nu_e \end{pmatrix}_L \longrightarrow \exp\left[i\vec{\alpha}(x)\cdot\vec{\tau}/2 + i\beta(x)\right]\begin{pmatrix} e \\ \nu_e \end{pmatrix}_L$$

Here, $\vec{\alpha}(x)$, and $\beta(x)$ are continuous functions, and $\vec{\tau}$ are the generators of SU(2). The covariant derivative for such a transformation is $D^\mu = \partial^\mu + i\frac{1}{2}g\vec{\tau}\cdot\vec{W}^\mu - i\frac{1}{2}g'B^\mu$. $\vec{W}^\mu$ are the three SU(2) gauge fields and B^μ the one U(1) gauge field. The important point here is that there are now *two* neutral fields B^μ, and $W^{0\mu}$. The combination of fields $A^\mu = \sin\vartheta_W W^{0\mu} + \cos\vartheta_W B^\mu$ is massless and may be identified with the photon. The orthogonal combination $Z^\mu = \cos\vartheta_W W^{0\mu} - \sin\vartheta_W B^\mu$ has mass $M_Z = M_W/\cos\vartheta_W$. This weak mixing angle is determined by the relative magnitude of the couplings g and g': $\tan\vartheta_W = g'/g$. This Z^0 boson is the neutral partner of the charged weak bosons, W^+, and W^-, so it will be responsible for neutral weak decays. Neutral currents were observed for the first time in 1973, by the Gargamelle bubble chamber group[17] at CERN, in neutrino-nucleon interactions.

By 1971, 't Hooft[18] had succeeded in proving that a theory based on SU(2)× U(1) is renormalizable. There still remained several serious problems, two of them associated with the decays of neutral kaons. The Cabibbo hypothesis may be thought of as implying mixing between the d and s quarks, that the weak and strong interaction eigenstates are not the same. This mixing may be written as $d' = d\cos\vartheta_C + s\sin\vartheta_C$, and the charged current becomes $J_\mu = \overline{d}'\gamma_\mu(1-\gamma_5)u$. It was then expected that the neutral current would have a similar form: $N_\mu = \overline{u}\gamma_\mu(1-\gamma_5)u + \overline{d}'\gamma_\mu(1-\gamma_5)d'$. It is interesting to display the mixing angle explicitly. $N_\mu = \overline{u}\gamma_\mu(1-\gamma_5)u + \cos^2\vartheta_C\overline{d}\gamma_\mu(1-\gamma_5)d + \sin^2\vartheta_C\overline{s}\gamma_\mu(1-\gamma_5)s + \sin\vartheta_C\cos\vartheta_C(\overline{d}\gamma_\mu(1-\gamma_5)s + \overline{s}\gamma_\mu(1-\gamma_5)d)$. The first three terms conserve strangeness but the last two have a change of strangeness of ± 1.

Such strangeness changing neutral currents should be observed in the decays of the K_L^0. The decay $K^- \to \mu^-\overline{\nu}_\mu$ has a large branching ratio. Since the

SU(2)×U(1) model predicts nearly equal couplings for charged and neutral currents, it was expected that the decay $K_L^0 \to \mu^+\mu^-$ should also occur with a large rate. That such strangeness changing neutral currents were not observed was striking. The prediction of a large rate was a severe failure of the SU(2)×U(1) model.

Another failure was the prediction of a K_L^0–K_S^0 mass difference — Δm — which was much larger than that which had already been measured. It is instructive to examine this prediction in some detail. The mass difference comes about through the mixing of the K^0 and $\overline{K}^0$ states. The lowest order processes are shown in Fig. 1.2a and 1.2b. The mass of the K_L^0 will be raised to $(m_{K^0}^2 + < \overline{K}^0|H_W|K^0 >)^{1/2}$ and that of the K_S^0 will similarly be lowered to $(m_{K^0}^2 - < \overline{K}^0|H_W|K^0 >)^{1/2}$. The difference in these values is approximately $m_{K^0}^{-1} < \overline{K}^0|H_W|K^0 >$.

If all external momenta are neglected — the mass scale here is set by M_W so ignoring external momenta results in only a small error — the matrix element corresponding to Fig. 1.2a may be written, in the Feynman–'t Hooft gauge, as:

$$\begin{aligned} M_a = i\left(-i\frac{g}{2\sqrt{2}}\sin\vartheta_C\right)^2 i\left(-i\frac{g}{2\sqrt{2}}\cos\vartheta_C\right)^2 \int \frac{d^4k}{(2\pi)^4} \\ \cdot \bar{s}_1\gamma_\lambda(1-\gamma_5)\left(\frac{\not{k}+m_u}{k^2-m_u^2}\right)\gamma_\rho(1-\gamma_5)d_2 \\ \cdot \bar{s}_2\gamma_\alpha(1-\gamma_5)\left(\frac{\not{k}+m_u}{k^2-m_u^2}\right)\gamma_\sigma(1-\gamma_5)d_1 \\ \cdot \left(-i\frac{g^{\lambda\sigma}}{k^2-M_W^2}\right)\left(-i\frac{g^{\alpha\rho}}{k^2-M_W^2}\right) \end{aligned}$$

Note that $(1-\gamma_5)m_u\gamma_\rho(1-\gamma_5) = m_u\gamma_\rho(1+\gamma_5)(1-\gamma_5) = 0$. Now:

$$\begin{aligned} M_a = -i\frac{g^2}{2}\sin^2\vartheta_C\cos^2\vartheta_C\,\bar{s}_1\gamma_\lambda\gamma^\alpha\gamma_\sigma(1-\gamma_5)d_2\bar{s}_2\gamma^\sigma\gamma^\beta\gamma^\lambda(1-\gamma_5)d_1 \\ \cdot \int \frac{d^4k}{(2\pi)^4}\frac{k_\alpha k_\beta}{(k^2-M_W^2)^2(k^2-m_u^2)^2} \end{aligned}$$

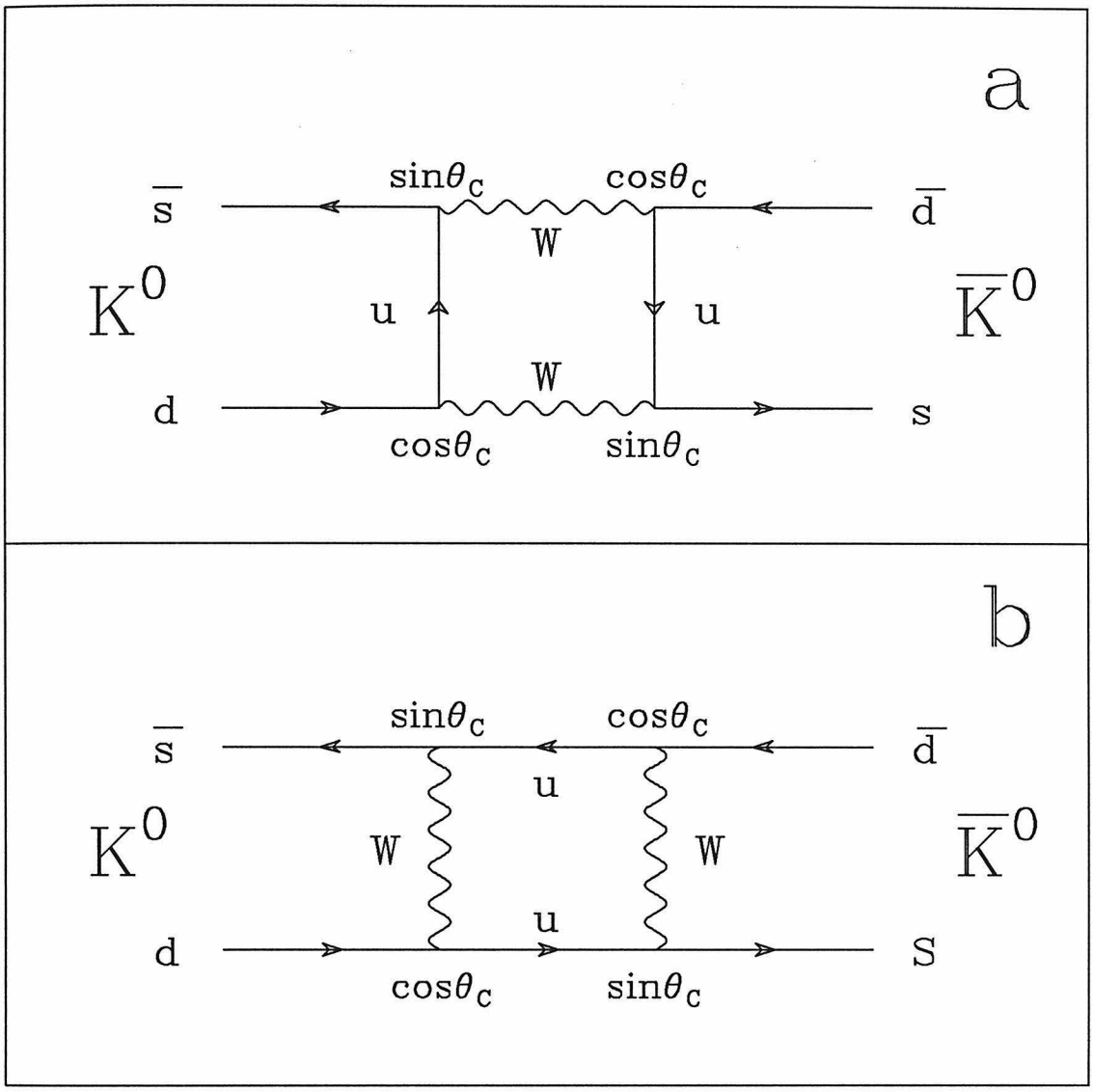

Figure 1.2: Lowest order processes contributing to $K_L - K_S$ mass difference.

The integration is easily performed to lowest order in m_u/M_W:

$$\int \frac{d^4k}{(2\pi)^4} \frac{k_\alpha k_\beta}{(k^2 - M_W^2)^2 (k^2 - m_u^2)^2} = -i \frac{g_{\alpha\beta}}{64\pi^2 M_W^2} (1 + \frac{m_u^2}{M_W^2} + \cdots)$$

As $m_u^2/M_W^2 \ll 1$, only the first term need be retained. It is useful to apply the

identity:

$$\cdots\gamma_\lambda\gamma_\alpha\gamma_\sigma(1-\gamma_5)\cdots\gamma^\sigma\gamma^\alpha\gamma^\lambda(1-\gamma_5)\cdots = 4\cdots\gamma_\lambda(1-\gamma_5)\cdots\gamma^\lambda(1-\gamma_5)\cdots$$

After collecting terms and substituting $g = 2^{5/4}G_F^{1/2}M_W$

$$M_a = -\frac{G_F^2 M_W^2}{8\pi^2}\sin^2\vartheta_C\cos^2\vartheta_C\bar{s}_1\gamma_\lambda(1-\gamma_5)d_2\bar{s}_2\gamma^\lambda(1-\gamma_5)d_1$$

The matrix element corresponding to Fig. 1.2b is precisely the same so

$$M = M_a + M_b = -\frac{G_F^2 M_W^2}{4\pi^2}\sin^2\vartheta_C\cos^2\vartheta_C\bar{s}_1\gamma_\lambda(1-\gamma_5)d_2\bar{s}_2\gamma^\lambda(1-\gamma_5)d_1$$

In order to calculate the mass difference, it is necessary to carry out a Fierz transformation on the field operators in M to group s_1 and d_1, and s_2 and d_2, together. Then it is possible to make the vacuum insertion: $|0><0| \approx 1$.

$$\Delta m = \frac{G_F^2 M_W^2}{4\pi^2 m_K}\sin^2\vartheta_C\cos^2\vartheta_C < \overline{K}^0|\bar{s}\gamma_\lambda\gamma_5 d|0><0|\bar{s}\gamma^\lambda\gamma_5 d|K^0>$$

The partially conserved axial-vector current hypothesis — PCAC — relates $<0|\bar{s}\gamma_\lambda\gamma_5 d|K^0>$ to $<0|\bar{s}\gamma_\lambda\gamma_5 u|K^+> = if_K P_K^\lambda$. With this *Ansatz*,

$$\frac{\Delta m}{m_K} = \frac{G_F^2}{4\pi^2}M_W^2\sin^2\vartheta_C\cos^2\vartheta_C f_K^2$$

If the measured values of $f_K\sin\vartheta_C = 33$ MeV and $M_W = 80.8$ GeV/c^2 are used, this formula predicts $\Delta m/m_K \approx 2\times10^{-11}$. This quantity has been measured to be 7.1×10^{-15}, in terrible disagreement with the prediction.

In 1970, Glashow, Illiopolous, and Maiani[19] proposed a mechanism — now known as the GIM mechanism — to insure that perturbative expansions in the weak coupling constant would converge. This mechanism had the fortuitous

result that strangeness-changing neutral currents would disappear and that the $K_L^0 - K_S^0$ mass difference calculation would be rendered sensible. They proposed the existence of a fourth quark field associated with a new quantum number, charm. With the introduction of this new quark, there would be the same number of quarks and leptons.

The leptonic weak current may be written $J_L^\mu = \bar{l} C_L \gamma^\mu (1 - \gamma_5) l$ where l is a column vector $(\nu_e, \nu_\mu, e^-, \mu^-)$ and C_L is a 4×4 matrix:

$$C_L = \begin{pmatrix} 0 & 0 & 1 & 0 \\ 0 & 0 & 0 & 1 \\ 0 & 0 & 0 & 0 \\ 0 & 0 & 0 & 0 \end{pmatrix}$$

By analogy with this, the hadronic weak current may be written as $J_H^\mu = \overline{q} C_H \gamma^\mu (1 - \gamma_5) q$ where $q = (c, u, s, d)$. C_H is given by

$$C_H = \begin{pmatrix} 0 & 0 & -\sin\vartheta_C & \cos\vartheta_C \\ 0 & 0 & \cos\vartheta_C & \sin\vartheta_C \\ 0 & 0 & 0 & 0 \\ 0 & 0 & 0 & 0 \end{pmatrix}$$

Here, ϑ_C is the Cabibbo angle. Thus, the GIM mechanism may be seen as an extension of Cabibbo's hypothesis. Most significant, though, is the symmetry between the leptonic and hadronic currents in this four-quark model; C_L and C_H are equivalent under an SU(4) rotation.

It was noted above that Cabibbo's hypothesis could be understood as a type of mixing among the mass eigenstates. This idea may be extended to the four-quark model. The weak eigenstates — those appearing above — are linear combinations of the mass eigenstates. The form of the mixing is given by C_H: $d' = d\cos\vartheta_C + s\sin\vartheta_C$ and $s' = -d\sin\vartheta_C + s\cos\vartheta_C$. Now the hadronic current may be written $J_H^\mu = \overline{d}' \gamma^\mu (1 - \gamma_5) u + \overline{s}' \gamma^\mu (1 - \gamma_5) c$. In this parameterization,

the form of the weak neutral current is $N^\mu = \overline{u}\gamma^\mu(1-\gamma_5)u + \overline{d}'\gamma^\mu(1-\gamma_5)d'$ $+\overline{c}\gamma^\mu(1-\gamma_5)c + \overline{s}'\gamma^\mu(1-\gamma_5)s'$. In terms of the mass eigenstates: $N^\mu = \overline{u}\gamma^\mu(1-\gamma_5)u$ $+\overline{d}\gamma^\mu(1-\gamma_5)d + \overline{c}\gamma^\mu(1-\gamma_5)c + \overline{s}\gamma^\mu(1-\gamma_5)s$. The mixing angle has disappeared from the neutral current as has any strangeness-changing part.

Even though, through the introduction of the GIM mechanism, strangeness-changing neutral currents have been removed, the decay $K_L^0 \to \mu^+\mu^-$ could still receive a substantial contribution from the second order weak process shown in Fig. 1.3a. This, however, will be substantially cancelled by the processes in Fig. 1.3b – 1.3d. The resulting matrix element[20] for the sum of the processes illustrated in Fig. 1.3a – 1.3d is:

$$M(\overline{s}d \to \mu^+\mu^-) = \frac{G_F^2}{4\pi^2}\cos\vartheta_C \sin\vartheta_C m_c^2 \overline{v}(\mu^+)\gamma_\alpha\gamma_5 u(\mu^-)\overline{s}\gamma^\alpha(1-\gamma_5)d$$

The decay rate, in the PCAC limit — $\overline{s}\gamma^\alpha\gamma_5 d \Rightarrow i f_K P_{K^0}^\alpha$ — is:

$$\begin{aligned}\Gamma(K^0 \to \mu^+\mu^-) &= \frac{G_F^4}{32\pi^5}\cos^2\vartheta_C \sin^2\vartheta_C m_c^4 f_K^2 m_\mu^2 \sqrt{m_{K^0}^2 - 4m_\mu^2} \\ &= 5.0 \times 10^{-29}\ \text{GeV}\end{aligned}$$

The corresponding branching ratio is $B(K_L^0 \to \mu^+\mu^-) = 3.9 \times 10^{-12}$. This result is much smaller than the measured branching ratio of $9.1 \pm 1.9 \times 10^{-9}$. The GIM mechanism thus removes the large second order weak contribution. This decay probably proceeds through an intermediate state consisting of two photons.

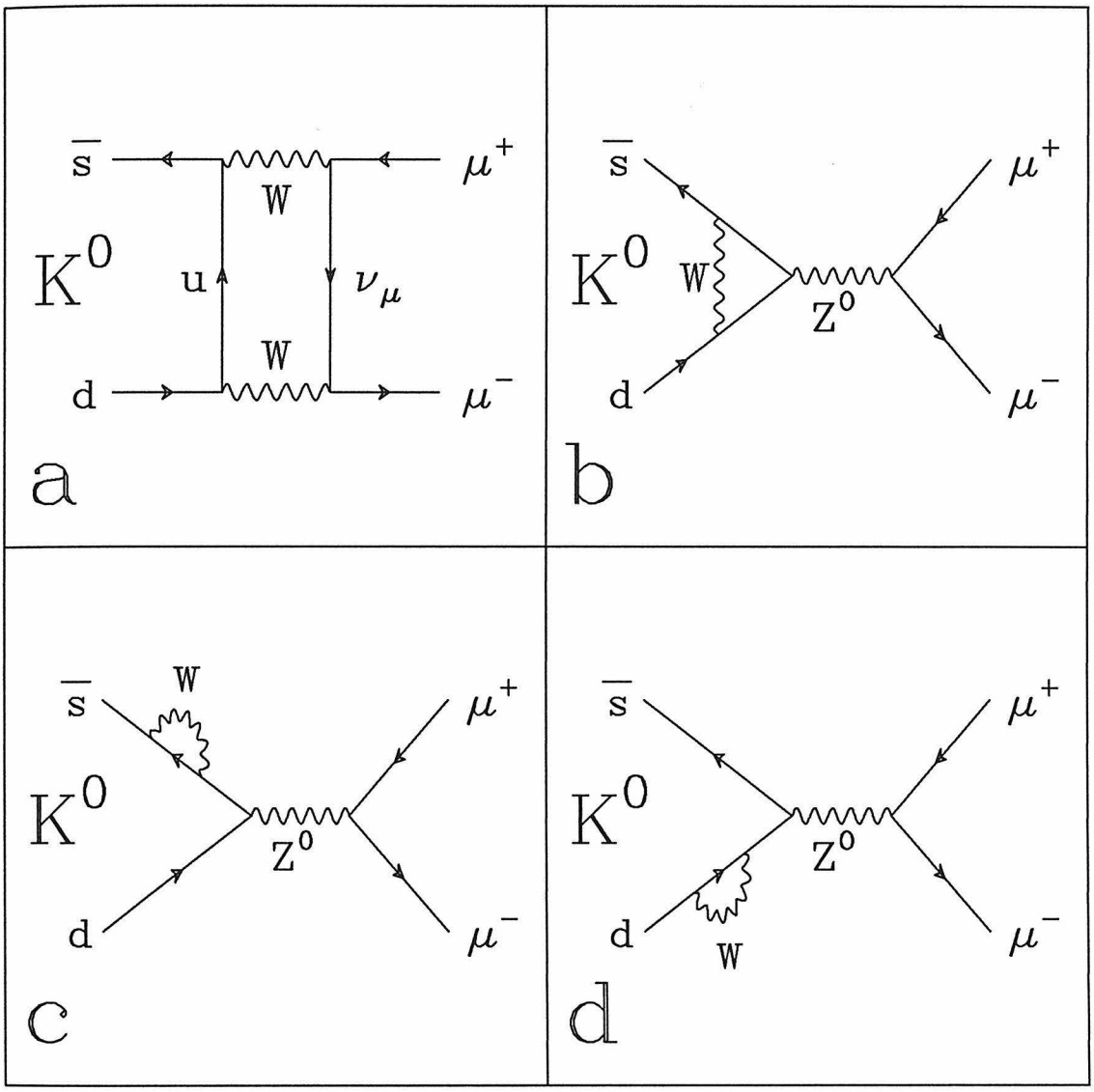

Figure 1.3: Second order diagrams for $K_L \to \mu^+ \mu^-$

The Δm calculation given above must be modified to incorporate the charm quark. Now the matrix element will be given by

$$M_a = -i\frac{g^2}{2}\sin^2\vartheta_C\cos^2\vartheta_C\,\bar{s}_1\gamma_\lambda\gamma^\alpha\gamma_\sigma(1-\gamma_5)d_2\bar{s}_2\gamma^\sigma\gamma^\beta\gamma^\lambda(1-\gamma_5)d_1$$
$$\cdot\int\frac{d^4k}{(2\pi)^4}k_\alpha k_\beta\left[\frac{1}{(k^2-M_W^2)^2(k^2-m_u^2)^2}+\frac{1}{(k^2-M_W^2)^2(k^2-m_c^2)^2}\right.$$
$$\left.-2\frac{1}{(k^2-M_W^2)^2(k^2-m_u^2)(k^2-m_c^2)}\right]$$

The integral may be evaluated exactly, but it is more instructive to keep only those terms which are of lowest order in m_i/M_W.

$$\int\frac{d^4k}{(2\pi)^4}k_\alpha k_\beta\left[\frac{1}{(k^2-M_W^2)^2(k^2-m_u^2)^2}+\frac{1}{(k^2-M_W^2)^2(k^2-m_c^2)^2}\right.$$
$$\left.-2\frac{1}{(k^2-M_W^2)^2(k^2-m_u^2)(k^2-m_c^2)}\right]=-i\frac{g_{\alpha\beta}}{64\pi^2M_W^2}\frac{m_u^2+m_c^2}{M_W^2}+\cdots$$

With the assumption that $m_c \gg m_u$ the mass difference becomes

$$\frac{\Delta m}{m_K}=\frac{G_F^2}{4\pi^2}m_c^2\sin^2\vartheta_C\cos^2\vartheta_C f_K^2$$

Gaillard and Lee[21] used this formula to predict $m_c \approx 1.5$ GeV/c^2, certainly a remarkable prediction, especially since it made several months before the announcement of the discovery of the J/ψ!

Late in 1974, the extraordinary resonance known as the J/ψ was discovered. A group at the Brookhaven AGS[22] investigated the reaction $p + Be \rightarrow e^+ + e^- + X$. They observed a very prominent peak in the e^+ e^- invariant mass distribution at a mass of 3.1 GeV/c^2. The resonance was denoted J by this group.

Independently, and simultaneously, a group at SPEAR[23] observed a very large enhancement in the total hadronic cross section; the peak value of the cross

section was reported as 2300±200 nb. Similar enhancements were observed in the $\mu^+ \mu^-$ and $e^+ e^-$ cross sections. The hadronic cross section, in particular, exhibits the high mass radiative tail characteristic of initial state radiation in electron-positron storage rings. The resonance, denoted ψ, was determined to have mass $M_\psi = 3.105 \pm 0.003$ GeV/c^2 and width $\Gamma_\psi < 1.3$ MeV. After the announcement of this discovery, three groups at the ADONE facility[24] at Frascati confirmed both the existence of the resonance and its mass.

The J/ψ was determined to have the spin, spatial parity, and charge conjugation parity of the photon; at a center-of-mass energy of 3.1 GeV, electron-positron interactions occur predominantly through annihilation to a single photon. The J/ψ also has odd G-parity since it decays most often to final states containing an odd number of pions. Since $G = (-1)^{I+J}$, this implies that the J/ψ has even isospin. The final states $\rho^-\pi^+$, $\rho^0\pi^0$, and $\rho^+\pi^-$ occur with equal frequency, so the isospin of the J/ψ must be zero.

It is very difficult to imagine that the J/ψ could be formed from u, d, and s quarks. The J/ψ is much narrower than meson resonances of lower mass. If the J/ψ did consist just of the three light quarks, it should decay quickly to final states containing lower mass mesons. There would certainly be generous phase-space available for such decays.

An explanation for the extremely narrow width of the J/ψ is that it consists of a bound pair of charm quarks. Charm is conserved in strong and electromagnetic interactions, so the J/ψ should decay to a pair of mesons, each containing one charm quark, as shown in Fig. 1.4a. If, however, the charmed mesons have masses which are too large, the J/ψ would have to decay through the OZI suppressed process shown in Fig. 1.4b. This process should proceed only slowly, accounting for the narrow width. A similar effect is observed in the decays of the ϕ resonance. The ϕ is also quite narrow: there is very little phase-space available for the OZI allowed decay $\phi \rightarrow K\overline{K}$ but a great deal available for the OZI suppressed decay $\phi \rightarrow \pi^+\pi^-\pi^0$. Despite the difference in phase-space, the ϕ decays predominately

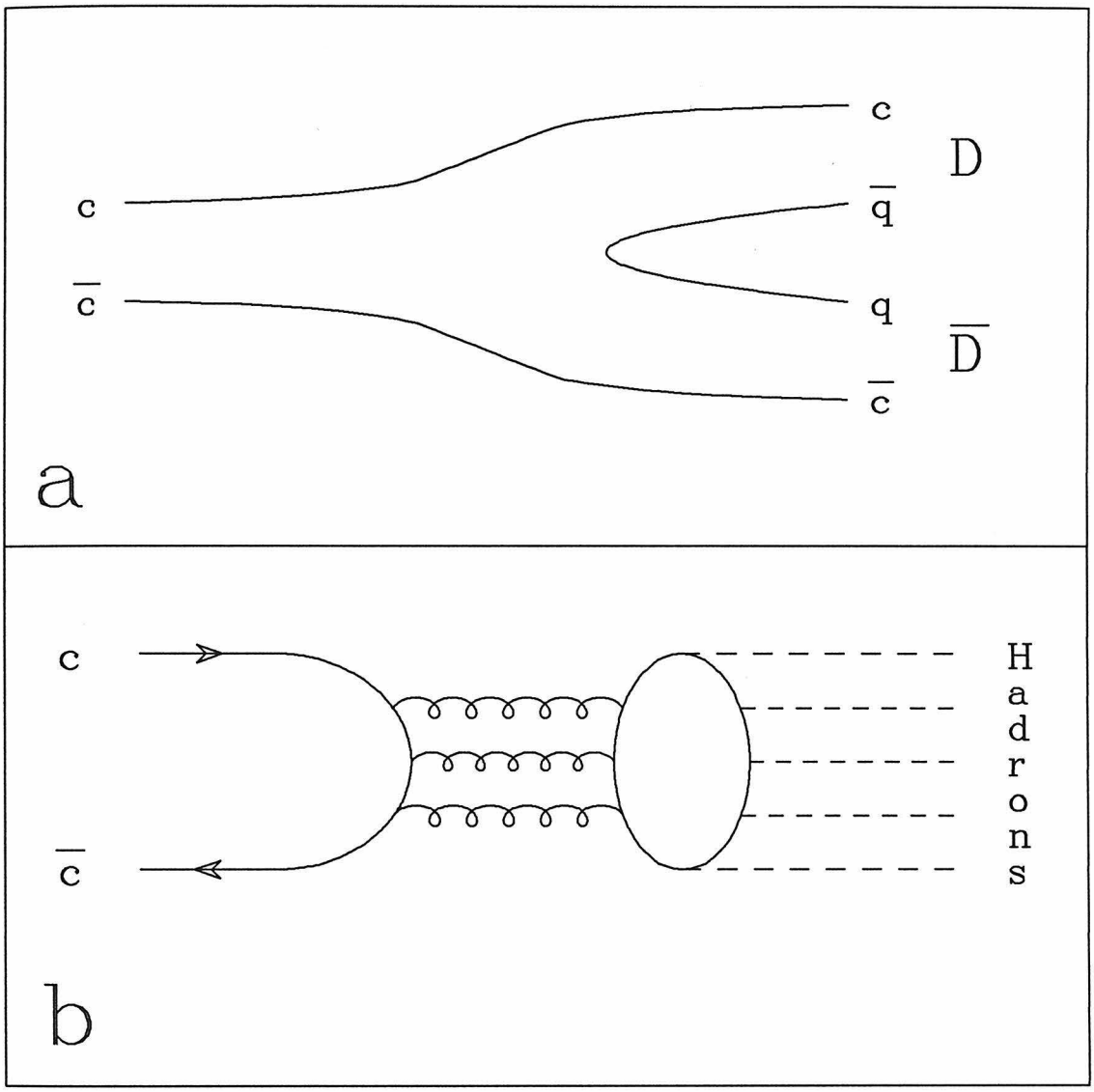

Figure 1.4: OZI allowed (a) and suppressed(b) decays of charmonia

to $K\overline{K}$.

Shortly after the discovery of the J/ψ, another narrow resonance — the ψ' — was discovered at SPEAR at a center-of-mass energy of 3.685 GeV. This resonance was also very narrow and was determined to have the same quantum numbers as the ψ.

If the J/ψ were a bound state of two charm quarks, the relative motion of these quarks should be largely nonrelativistic; the quark mass may be assumed to be of order $1/2M_{\psi}$. The spectrum of states should then be similar to that of positronium — a bound state of a positron and an electron. The major difference between these systems — positronium and *charmonium* — lies in the nature of the binding potential. The charmonium potential has not yet been computed from first principles, but it must become large when the quarks are separated by a large distance as they are *confined* to the interior of the meson. Thus, the charmonium potential cannot be a simple Coulomb potential.[25]

The energy levels of positronium are shown in Fig. 1.5a. The states are identified in spectroscopic notation. The observed states of charmonium are shown in Fig. 1.5b. The similarity is quite striking. The J/ψ and the ψ' are identified as the first and second $^3S_1$ states, respectively. The ^3P states — denoted χ_0, χ_1, and χ_2 — are not produced directly in $e^+ e^-$ collisions. Rather, they are observed in radiative transitions[26] of the type $\psi' \rightarrow \gamma \chi_J$. Thus they have positive $C-$ parity as do the corresponding positronium states. The lowest lying $^1S_0$ state — the η_C — has been studied extensively.[27] Finally, evidence for the next higher $^1S_0$ state, denoted η'_C has been reported;[28] the mass reported is 3590 MeV/c^2.

The $\psi(3770)$ resonance — hereafter referred to as the ψ'' — is identified as the lowest lying $^3D_1$ state, but it is probably not a pure state. The van Royen–Weisskopf formula predicts a leptonic width for the ψ'' of

$$\Gamma(\psi'' \rightarrow l\bar{l}) = \frac{16\pi(e_c)^2\alpha^2}{M^2_{\psi''}}\left|\psi(0)\right|^2$$

where e_c is the charm quark charge of $2/3$. The wavefunction for a pure D state has a node at the origin, so this formula predicts a leptonic width of zero. This is, however, not correct as the ψ'' is observed in $e^+ e^-$ collisions. The measured leptonic width of the ψ'' is 280 eV. The non-zero leptonic width[29] may come

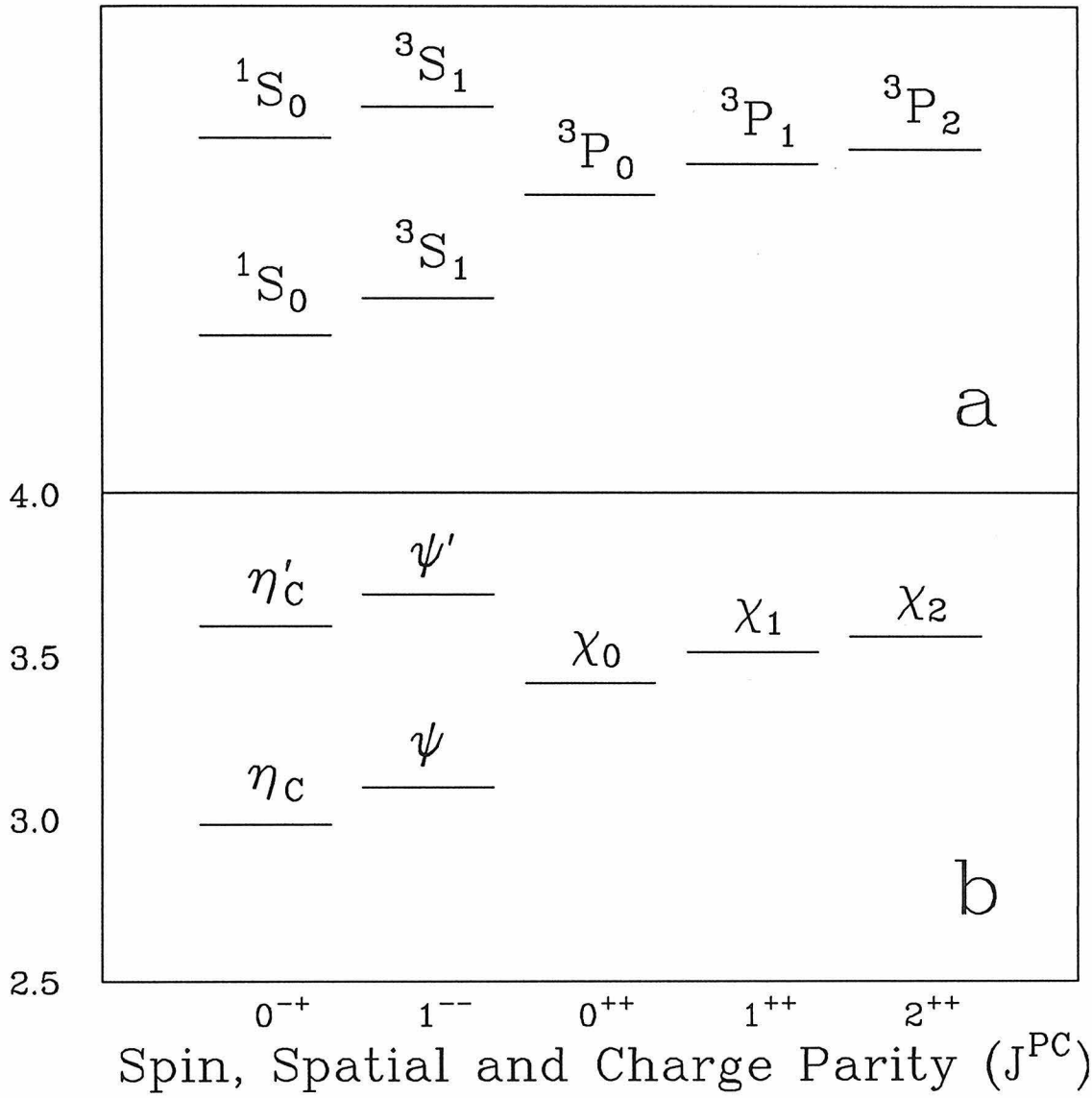

Figure 1.5: Energy levels of positronium (a) and mass spectrum of charmonium (b)

about through mixing of the $^3D_1$ state with the nearby $^3S_1$, the ψ' which has a leptonic width of 1.7 keV.

The ψ'' is much broader than the J/ψ or the ψ', with a total width of 25 MeV. This is usually attributed to the fact that the mass of the ψ'' lies above the threshold for producing the lightest explicitly charmed particles — the D mesons.

The decays of ψ'' to charmed particles is no longer suppressed by the OZI rule, so they proceed very rapidly. The mass, however, lies below the threshold for producing D's in combination with other, heavier charmed mesons. Since charm is conserved in strong and electromagnetic interactions, the ψ'' decays only to $D\overline{D}$ pairs when it decays to charmed particles.

The four quark model was highly successful, but it had to be extended due to two later discoveries. The first was the discovery of the τ lepton.[30] This extraordinary particle exhibits all of the properties of the e and μ, except that its mass is so large that it may decay to hadrons. The branching ratios[31] of the τ to many final states may be predicted unambiguously, and these predictions are consistently in good agreement with experiment. These calculations require that the τ be accompanied by a new neutrino, the ν_τ. Even though this particle has not been observed directly, its existence is not disputed.

The second major discovery was that of the Υ family of resonances;[32] the mass of the ground state $\Upsilon(1S)$ is 9.4600 GeV/c^2. These exhibited properties quite similar to those of the ψ family, and were interpreted as bound states of a new quark and antiquark — the bottom or b quark. The spectrum of *bottomonium* states is similar to that of charmonium. The level splitting of the $^3S_1$ states is nearly identical.

$$M_{\psi'} - M_{\psi} = 589.06 \pm 0.13 \text{ MeV/c}^2$$
$$M_{\Upsilon'} - M_{\Upsilon} = 563.3 \pm 0.4 \text{ MeV/c}^2$$
$$M_{\psi(4030)} - M'_{\psi} = 345 \pm 5 \text{ MeV/c}^2$$
$$M_{\Upsilon''} - M_{\Upsilon'} = 332.2 \pm 0.7 \text{ MeV/c}^2$$

The four quark model had to be revised to accommodate the new particles. If there were six leptons but five quarks, the lepton-quark symmetry so attractive in the four quark model would have to be abandoned. The existence of a sixth quark — the top or t quark — was postulated to recover this symmetry. The leptons have the same couplings, and the leptonic current the same structure, as before,

but the quark currents are slightly different. With four quarks, there was only one parameter — the Cabibbo angle — to describe the difference between the weak and mass eigenstates. In a model with six quarks, the mixing is described by a 3×3 unitary matrix. Such a matrix has nine independent elements, but five of these may be absorbed as phases in the definitions of the quark fields. Hence, a model with six quarks will have four mixing parameters. In the Kobayashi-Maskawa (KM) parameterization,[33] the mixing matrix is written

$$U = \begin{array}{c} \\ u \\ c \\ t \end{array} \begin{array}{c} \begin{array}{ccc} d & s & b \end{array} \\ \begin{pmatrix} c_1 & -s_1c_3 & -s_1s_3 \\ s_1c_2 & c_1c_2c_3 - s_2s_3e^{i\delta} & c_1c_2c_3 + s_2c_3e^{i\delta} \\ s_1s_2 & c_1s_2c_3 - c_2s_3e^{i\delta} & c_1s_2s_3 - c_2c_3e^{i\delta} \end{pmatrix} \end{array}$$

With this form for U, the charged current is written

$$J_H^\mu = (\overline{u}, \overline{c}, \overline{t})\gamma^\mu(1 - \gamma_5)U \begin{pmatrix} d \\ s \\ b \end{pmatrix}$$

A recent compilation[34] of the absolute values of the KM matrix elements reports

$$U = \begin{array}{c} \\ u \\ c \\ t \end{array} \begin{array}{c} \begin{array}{ccc} d & s & b \end{array} \\ \begin{pmatrix} 0.9742 - 0.9756 & 0.219 - 0.225 & 0.000 - 0.008 \\ 0.219 - 0.225 & 0.973 - 0.975 & 0.037 - 0.053 \\ 0.002 - 0.018 & 0.036 - 0.052 & 0.9986 - 0.9993 \end{pmatrix} \end{array}$$

The range given for these values corresponds to the 90% confidence level. The values were obtained from a global fit using the experimental values and the unitarity of the matrix as constraints. Unitarity is, of course, only insured if there are six quarks.

The experimental values come from a number of sources. U_{ud} is obtained by comparing the rates for muon decay and neutron beta decay. In this case, U_{ud} is equivalent to the Cabibbo angle. U_{us} is obtained from the semileptonic decays of hyperons — $\Sigma^- \rightarrow ne^-\overline{\nu}_e$, $\Sigma^- \rightarrow \Lambda^0 e^-\overline{\nu}_e$, $\Xi^- \rightarrow \Lambda^0 e^-\overline{\nu}_e$, $\Xi^- \rightarrow \Sigma^0 e^-\overline{\nu}_e$, and $\Lambda^0 \rightarrow pe^-\overline{\nu}_e$ — and of kaons — $K^+ \rightarrow \pi^0 l^+ \nu_l$ and $K^0 \rightarrow \pi^- l^+ \nu_l$. The element U_{cd} is obtained from neutrino induced charm production. The charmed-strange quark element U_{cs} is derived from the semileptonic decay of D mesons. The ratio $|U_{ub}|/|U_{cb}|$ is obtained by studying the endpoint of the lepton momentum spectrum in semileptonic decays of B mesons. The final element U_{cb} may be extracted by assuming that the measured semileptonic branching ratio of B mesons is determined by the semileptonic decay rate of the b quark. The experimental results may be summarized:

$$
\begin{aligned}
U_{ud} &= 0.9729 \pm 0.0012 \\
U_{us} &= 0.221 \pm 0.002 \\
U_{cd} &= 0.24 \pm 0.03 \\
U_{cs} &> 0.66 \ @ \ 90\% \ \mathrm{CL} \\
\frac{|U_{ub}|}{|U_{cb}|} &\leq 0.14 \ @ \ 90\% \mathrm{CL} \\
0.037 < U_{cb} &< 0.053
\end{aligned}
$$

Wolfenstein[35] has pointed out that the KM matrix exhibits a well-developed structure, that this matrix deviates only slightly from the unit matrix. Setting $\lambda = U_{us}$ and $A = U_{cb}/\lambda^2$, the KM matrix, to second order in λ, may be written:

$$
U = \begin{pmatrix} 1 - 1/2\lambda^2 & \lambda & 0 \\ -\lambda & 1 - 1/2\lambda^2 & A\lambda^2 \\ 0 & -A\lambda^2 & 1 \end{pmatrix}
$$

So far, no widely accepted model has been able to explain the structure of the KM matrix, as displayed above. This structure suggests strongly that some additional symmetry must be at work to determine the pattern of quark mixing.

Chapter 2: Decays of D mesons

2.1: Phenomenology of D Meson Decay

Two new particles[36] — the D^0 and the D^+ — were discovered in 1976 at SPEAR. They were determined to be charmed mesons on the basis of a few key observations. That they had spin zero made it unlikely that they could be hadronic resonances of some sort. They decayed most often into final states containing strange particles, as would be expected from the structure of the charm-changing weak current. Finally, the masses were quite large, greater than one-half that of the J/ψ, which was already believed to be a $c\bar{c}$ resonance.

The D^0, D^+, and F^+ are the lightest charmed particles. They are all pseudoscalar mesons, and together they transform as a $\bar{3}$-representation of SU(3). The masses of the D^0, D^+, and F^+ are 1864.7 MeV/c^2, 1869.2 MeV/c^2, and 1971 MeV/c^2, respectively. Each is believed to be a bound state of a charm quark and light antiquark: $D^0 \Rightarrow c\bar{u}$, $D^+ \Rightarrow c\bar{d}$, and $F^+ \Rightarrow c\bar{s}$. Their antiparticles are the $\overline{D}^0$, D^-, and F^-. D mesons have isospin 1/2 while the F^+ has isospin zero.

When the existence of charmed particles was reported, it was expected that the D^0, D^+, and F^+ would have nearly identical lifetimes. It was surely a surprise when the D^0 and D^+ lifetimes were determined to be significantly different. The first measurements of the ratio of lifetimes relied on the fact that the weak Hamiltonian for a $c \rightarrow s l^+ \nu_l$ transition is an isoscalar, so $\Gamma(D^0 \rightarrow l^+ X) = \Gamma(D^+ \rightarrow l^+ X)$. With this equality, and neglecting Cabibbo suppressed contributions, the ratio of inclusive semileptonic branching ratios for the D^0 and D^+ may be related to the ratio of their lifetimes.[37]

$$\frac{B(D^+ \rightarrow l^+ X)}{B(D^0 \rightarrow l^+ X)} = \frac{\Gamma(D^+ \rightarrow l^+ X)}{\Gamma(D^0 \rightarrow l^+ X)} \cdot \frac{\Gamma_{tot}(D^0)}{\Gamma_{tot}(D^+)} = \frac{\Gamma_{tot}(D^0)}{\Gamma_{tot}(D^+)} = \frac{\tau(D^+)}{\tau(D^0)}$$

Recently, the MARK III collaboration performed a high statistics measure-

ment of the inclusive semileptonic branching ratios with the following results:[38]

$$B(D^+ \to e^+ X) = 17.0 \pm 1.9 \pm 0.7\%$$
$$B(D^0 \to e^+ X) = 7.5 \pm 1.1 \pm 0.4\%$$
$$\frac{\tau(D^+)}{\tau(D^0)} = 2.3^{+0.5+0.1}_{-0.4-0.1}$$

The lifetimes of the D^0 and D^+ have also been obtained directly by several collaborations by measuring the decay distance in bubble chambers, silicon strip vertex detectors, and proportional tube vertex chambers. The results of the experiments are summarized in Table 2.1.I. The world average values of the D^0 and D^+ lifetimes from these experiments are:[39]

$$\tau_{D^+} = (10.29^{+0.54}_{-0.43}) \times 10^{-13} \text{ sec}$$
$$\tau_{D^0} = (4.43^{+0.19}_{-0.17}) \times 10^{-13} \text{ sec}$$
$$\frac{\tau_{D^+}}{\tau_{D^0}} = 2.39^{+0.16}_{-0.14}$$

This is in very good agreement with the ratio given above based on the inclusive semileptonic branching ratios.

A great number of different decay modes of D mesons have been observed. Recent measurements of the MARK III collaboration are collected in Table 2.1.II. If the inclusive semileptonic branching ratios for muons are assumed to be the same as those for electrons, then most of the decay modes have been accounted for; the sum of the listed branching ratios for the D^0 is 85% and for the D^+ it is 82%. It is possible to examine the three-body decays for signs of any resonant substructure. Such an analysis has been carried out by the MARK III for the decays $D^0 \to K^-\pi^+\pi^0$, $D^0 \to \overline{K}^0\pi^+\pi^-$, and $D^+ \to \overline{K}^0\pi^+\pi^0$. The preliminary results are summarized in Table 2.1.III. It is interesting to note that in each case these three-body final states are dominated by two-body decays of the vector-pseudoscalar type.

Table 2.1.I: Measurements of Lifetime of Charmed Particles

	D^+		D^0	
Experiment	Decays	$\tau(10^{-13}s)$	Decays	$\tau(10^{-13}s)$
E-531	23	$11.1^{+4.4}_{-2.9}$	58	$4.3^{+0.7+0.1}_{-0.5-0.2}$
WA-58	27	$5.0^{+1.5}_{-1.0} \pm 1.9$	44	$3.6^{+1.2}_{-0.8} \pm 0.7$
SHF	48	$8.6 \pm 1.3^{+0.7}_{-0.3}$	50	$6.1 \pm 0.9 \pm 0.3$
NA-16	15	$8.4^{+3.5}_{-2.2}$	16	$4.1^{+1.3}_{-1.0}$
NA-18	7	$6.3^{+4.9}_{-2.3} \pm 1.5$	9	$4.1^{+2.6}_{-1.3} \pm 0.5$
NA-27	147	$10.6^{+1.3}_{-0.9}$	129	$4.2^{+0.5}_{-0.4}$
NA-1	98	$9.5^{+3.1}_{-1.9}$	51	$4.3^{+1.4}_{-0.9}$
NA-11	28	$10.6^{+3.6}_{-2.4} \pm 1.6$	26	$3.7^{+1.0}_{-0.7} \pm 0.5$
NA-32	42	$9.8^{+1.9}_{-1.5}$	42	$3.9^{+0.6}_{-0.5}$
E-691	480	$10.9^{+0.8}_{-0.7} \pm 0.6$	672	$4.4 \pm 0.2 \pm 0.2$
DELCO				$4.6 \pm 1.5^{+0.7}_{-0.6}$
MKII	16	$8.9^{+3.8}_{-2.7} \pm 1.3$	66	$4.7^{+0.9}_{-0.8} \pm 0.5$
HRS	114	$8.1 \pm 1.2 \pm 1.6$	53	$4.2 \pm 0.9 \pm 0.6$
TASSO			13	$4.3^{+2.0}_{-1.4} \pm 0.8$
CLEO	247	$11.4 \pm 1.6 \pm 1.0$	317	$5.0 \pm 0.7 \pm 0.4$
Total	1361	$10.29^{+0.54}_{-0.43}$	1546	$4.43^{+0.19}_{-0.17}$

2.2: Transformation Properties of the Weak Hamiltonian

Many of the features of the Hamiltonian responsible for weak decay may be inferred from its properties under SU(2) and SU(3) transformations. The weak Hamiltonian is composed of the contraction of two weak currents: $H_w = J_\mu J^{\dagger\mu}$. The current has the form: $J_\mu U_{ij} \overline{q}_i \gamma_\mu (1 - \gamma_5) q_j$; U_{ij} is the element of the mixing matrix corresponding to quarks q_i, and q_j. In a model with three quarks invariant

Table 2.1.II: D Branching Ratios as Measured by MARK III

D^0		D^+	
Decay Mode	Branching Ratio	Decay Mode	Branching Ratio
Cabibbo Allowed Decays			
$K^-\pi^+$	$5.6 \pm 0.4 \pm 0.3\%$	$\overline{K}^0\pi^+$	$4.1 \pm 0.6 \pm 0.3$
$\overline{K}^0\pi^0$	$2.4 \pm 0.5 \pm 0.2\%$	$K^-\pi^+\pi^+$	$11.6 \pm 1.4 \pm 0.7$
$\overline{K}^0\eta$	$2.0 \pm 0.9 \pm 0.3\%$	$\overline{K}^0\pi^+\pi^0$	$12.9^{+2.7}_{-2.6} \pm 2.1\%$
$\overline{K}^0\omega$	$4.2 \pm 1.7 \pm 1.1\%$	$\overline{K}^0\pi^+\pi^+\pi^-$	$9.1^{+1.4}_{-1.5} \pm 0.9\%$
$K^-\pi^+\pi^0$	$17.5 \pm 1.3 \pm 1.3\%$	$K^-\pi^+\pi^+\pi^0$	$6.3^{+1.4}_{-1.3} \pm 1.2\%$
$\overline{K}^0\pi^+\pi^-$	$8.3 \pm 0.9 \pm 0.8\%$		
$K^-\pi^+\pi^+\pi^-$	$11.8 \pm 0.9 \pm 1.1\%$		
$\overline{K}^0\pi^+\pi^-\pi^0$	$14.9^{+2.7}_{-2.8} \pm 3.5\%$		
Cabibbo Suppressed Decays			
$\pi^-\pi^+$	$0.18 \pm 0.06 \pm 0.04\%$	$\pi^+\pi^0$	$< 0.53\%$ (90% CL)
K^-K^+	$0.68 \pm 0.11 \pm 0.08\%$	$\overline{K}^0K^+$	$1.30 \pm 0.40 \pm 0.22\%$
$K^{*-}K^+$	$1.1 \pm 0.5 \pm 0.2$	$\pi^-\pi^+\pi^+$	$0.49 \pm 0.19 \pm 0.12\%$
$\overline{K}^{*0}K^0$	$< 0.80\%$ (90% CL)	$\phi\pi^+$	$0.97 \pm 0.27 \pm 0.14\%$
$\overline{K}^0K^+\pi^-_{\text{non-res}}$	$< 1.8\%$ (90% CL)	$\overline{K}^{*0}K^+$	$0.56 \pm 0.25 \pm 0.13\%$
$\pi^+\pi^-\pi^0$	$1.1 \pm 0.4 \pm 0.2\%$	$K^-K^+\pi^+_{\text{non-res}}$	$0.68 \pm 0.31 \pm 0.11\%$
$\pi^-\pi^+\pi^+\pi^-$	$1.5 \pm 0.6 \pm 0.2\%$		
Semileptonic Decays			
e^+X	$7.5 \pm 1.1 \pm 0.4\%$	e^+X	$17.0 \pm 1.9 \pm 0.7\%$

under SU(3), the quark fields transform as the fundamental representation. The weak current then transforms as:[40]

$$J_\mu \Rightarrow \overline{3} \otimes 3 = 1 \oplus 8$$

Table 2.1.III: Resonant Structure of Three-body Decays

Mode	Fraction of total	Branching Ratio
$D^0 \to K^- \pi^+ \pi^0$		
$\overline{K}^{*0}\pi^0$	$7.6 \pm 3.3 \pm 2.0\%$	$2.0 \pm 0.9 \pm 0.5\%$
$K^{*-}\pi^+$	$12.9 \pm 2.7 \pm 2.0\%$	$6.8 \pm 1.5 \pm 1.2\%$
$K^-\rho^+$	$74.0 \pm 4.7 \pm 5.0\%$	$13.0 \pm 1.3 \pm 1.3\%$
non-resonant	$5.5 \pm 4.4 \pm 3.0\%$	$1.0 \pm 0.8 \pm 0.5\%$
$D^0 \to \overline{K}^0 \pi^+ \pi^-$		
$\overline{K}^0\rho^0$	$16.8 \pm 5.3 \pm 2.5\%$	$1.4 \pm 0.5 \pm 0.2\%$
$K^{*-}\pi^+$	$63.9 \pm 7.6 \pm 4.5\%$	$8.0 \pm 1.3 \pm 0.9\%$
non-resonant	$19.3 \pm 8.6 \pm 3.5\%$	$1.6 \pm 0.7 \pm 0.3\%$
$D^+ \to \overline{K}^0 \pi^+ \pi^0$		
$\overline{K}^0\rho^+$	$86.5 \pm 9.1 \pm 5.0\%$	$11.2 \pm 2.6 \pm 1.9\%$
$K^{*0}\pi^+$	$7.0 \pm 4.3 \pm 4.0\%$	$2.7 \pm 1.8 \pm 1.6\%$
non-resonant	$6.5 \pm 5.5 \pm 4.0\%$	$0.8 \pm 0.7 \pm 0.5\%$

The singlet will henceforth be neglected from further consideration. Now the weak Hamiltonian transforms as:

$$H_w = J_\mu J^{\dagger\mu} \Rightarrow 8 \otimes 8 = 1 \oplus 8_s \oplus 8_a \oplus 10_a \oplus \overline{10}_a \oplus 27_s$$

The Hamiltonian must be symmetric, so only the symmetric irreducible representations — 1, 8, and 27 — may contribute. These may be decomposed to reveal the irreducible representations of SU(2) they contain:

$$8 \supset 2_{\Delta s=-1} \oplus (1 \oplus 3)_{\Delta s=0} \oplus 2_{\Delta s=+1}$$

$$27 \supset 3_{\Delta s=-2} \oplus (2 \oplus 4)_{\Delta s=-1} \oplus (1 \oplus 3 \oplus 5)_{\Delta s=0} \oplus (2 \oplus 4)_{\Delta s=+1} \oplus 3_{\Delta s=+2}$$

It is well known that kaon decays are almost always accompanied by a change in isospin of $1/2$, even though both $\Delta I = 1/2$, and $\Delta I = 3/2$ amplitudes exist in

principle. The dimensionality of an SU(2) multiplet is $2I+1$, so the $\Delta I = 1/2$ and $\Delta I = 3/2$ terms in the Hamiltonian correspond to the 2 and 4-representations of SU(2), respectively. For $\Delta s = -1$, as in kaon decay, both the 2 and 4 of SU(2) are contained in the 27 of SU(3), whereas the 8 of SU(3) contains only the 2 of SU(2). In order to retain the $\Delta I = 1/2$ rule, it seems natural to assume that the octet part of the weak Hamiltonian should dominate over the 27-plet part; this is known as *octet dominance.*

For charm decays, the appropriate symmetry group is SU(4). Now $J_\mu \Rightarrow \overline{4} \otimes 4 = 1 \oplus 15$. The weak Hamiltonian will transform as

$$H_w \Rightarrow 15 \otimes 15 = 1 \oplus 15_s \oplus 15_a \oplus 20'_s \oplus 45_a \oplus \overline{45}_a \oplus 84_s$$

Of these irreducible representations of SU(4), only the $20'$ and the 80-representations have charm changing parts. Their SU(3) decompositions are:

$$20' \supset \overline{6}_{\Delta c=-1} \oplus 8_{\Delta c=0} \oplus 6_{\Delta c=+1}$$
$$84 \supset \overline{6}_{\Delta c=-2} \oplus (3 \oplus 15_m)_{\Delta c=-1} \oplus (1 \oplus 8 \oplus 27)_{\Delta c=0} \oplus (\overline{3} \oplus \overline{15}_m)_{\Delta c=+1} \oplus 6_{\Delta c=+2}$$

Here, the 84 of SU(4) contains both the charm-conserving 8 and 27-representations of SU(3), but the $20'$ of SU(4) contains only the 8 of SU(3) assumed to be dominant in strangeness-changing decays. Hence, it might be tempting to assume that the 20-plet should dominate over the 84-plet in charm-changing decays. The consequences of this assumption will be discussed later.

The decays of charmed mesons are accompanied by a change of charm of -1, so the relevant part of the weak Hamiltonian has the following properties: $H_{w,\Delta c=-1} \Rightarrow 3 \oplus \overline{6} \oplus 15$. Suppose that a charmed meson decays to a pair of non-charmed pseudoscalars. The transition amplitude for such a decay may be written: $A = < c|H_{w,\Delta c=-1}|pp >$. The notation $|c>$ represents the wavefunction of the charmed meson and $|pp>$ the wavefunction of the system of the two pseudoscalars. $|c> \Rightarrow \overline{3}$, and $|pp> \Rightarrow 8 \otimes 8 = 1 \oplus 8_s \oplus 8_a \oplus 10_a \oplus \overline{10}_a \oplus 27_a$.

Since the two scalars are in an $l = 0$ state, Bose statistics require that $|pp>$ be symmetric. Thus $|pp> \Rightarrow 1 \oplus 8 \oplus 27$, and $A \Rightarrow \overline{3} \otimes (3 \otimes \overline{6} \oplus 15) \otimes (1 \oplus 8 \oplus 27)$.

The amplitude A must be an SU(3) singlet, so only some of the nine terms implied above may contribute. Specifically, only five of the terms in the product $(3 \otimes \overline{6} \oplus 15) \otimes (1 \oplus 8 \oplus 27)$ contain a 3, which when combined with the $\overline{3}$ will yield a singlet.

$$
\begin{aligned}
3 \otimes 1 &= 3 \\
3 \otimes 8 &= 3 \oplus \overline{6} \oplus 15 \\
3 \otimes 27 &= 15 \oplus 24 \oplus 42 \\
\overline{6} \otimes 1 &= \overline{6} \\
\overline{6} \otimes 8 &= 3 \oplus \overline{6} \oplus 15 \oplus 24 \\
\overline{6} \otimes 27 &= \overline{6} \oplus 15 \oplus 15' \oplus 24 \oplus 42 \oplus 60 \\
15 \otimes 1 &= 15 \\
15 \otimes 8 &= 3 \oplus \overline{6} \oplus 15 \oplus 15 \oplus 15' \oplus 24 \oplus 42 \\
15 \otimes 27 &= 3 \oplus \overline{6} \oplus 15 \oplus 15 \oplus 15' \oplus 21 \oplus 24 \oplus 24 \oplus 42 \oplus 42 \oplus 48 \oplus 60 \oplus 90
\end{aligned}
$$

The five independent transition amplitudes are then, in the notation of Quigg,[41] given by:

$$
\begin{aligned}
S &= < c|\overline{6}|8 > \\
T &= < c|15|27 > \\
E &= < c|15|8 > \\
F &= < c|3|8 > \\
G &= < c|3|1 >
\end{aligned}
$$

Quigg calculated the amplitude for several decays into two pseudoscalars in terms of the five amplitudes introduced above. His results are given in Tables 2.2.I – 2.2.II.

Table 2.2.I: D^0 decays into two pseudoscalar mesons

Final State	Amplitude
$K^-\pi^+$	$(2T + E - S)\, U_{ud}\, U_{cs}$
$\overline{K}^0\pi^0$	$\frac{1}{\sqrt{2}}(3T - E + S)\, U_{ud}\, U_{cs}$
$\overline{K}^0\eta_8$	$\frac{1}{\sqrt{6}}(3T - E + S)\, U_{ud}\, U_{cs}$
$\overline{K}^0\eta_0$	$\frac{2}{\sqrt{3}}(E - S)\, U_{ud}\, U_{cs}$
K^+K^-	$(2T + E - S)\Sigma + \frac{1}{2}(3T + 2G + F - E)\Delta$
$\pi^+\pi^-$	$-(2T + E - S)\Sigma + \frac{1}{2}(3T + 2G + F - E)\Delta$
$\pi^0\pi^0$	$\frac{1}{2}(3T - E + S)\Sigma + \frac{1}{4}(-7T + 2G + F - E)\Delta$
$K^0\overline{K}^0$	$\frac{1}{2}(-T + 2G - 2F + 2E)\Delta$
$\eta_8\eta_8$	$-\frac{1}{2}(3T - E + S)\Sigma + \frac{1}{4}(-3T + 2G - F + E)\Delta$
$\eta_0\eta_0$	$\frac{1}{2}G\Delta$
$\pi^0\eta_8$	$-\frac{1}{\sqrt{3}}(3T - E + S)\Sigma + \frac{1}{2\sqrt{3}}(-6T + 3F - 3E)\Delta$
$\eta_8\eta_0$	$\sqrt{2}(S - E)\Sigma + \frac{1}{\sqrt{2}}(F - E)\Delta$
$\pi^0\eta_0$	$\sqrt{\frac{2}{3}}(E - S)\Sigma - \frac{1}{2}\sqrt{\frac{2}{3}}(3F - 3E)\Delta$
$K^+\pi^-$	$(2T + E - S)\, U_{us}\, U_{cd}$
$K^0\pi^0$	$\frac{1}{\sqrt{2}}(3T - E + S)\, U_{us}\, U_{cd}$
$K^0\eta_8$	$\frac{1}{\sqrt{6}}(3T - E + S)\, U_{us}\, U_{cd}$
$K^0\eta_0$	$\frac{2}{\sqrt{3}}(E - S)\, U_{us}\, U_{cd}$
$\Sigma = \frac{1}{2}(U_{us}U_{cs} - U_{ud}U_{cd})$	
$\Delta = \frac{1}{2}(U_{us}U_{cs} + U_{ud}U_{cd})$	

2.3: Construction of the Effective Weak Hamiltonian

To lowest order in α_s, a charmed meson decays when its valence charm quark decays. If this quark decays through the emission of a W boson, which subsequently materializes as a quark or lepton pair, the light valence quark in the

Table 2.2.II: D^+ decays into two pseudoscalar mesons

Final State	Amplitude
$\overline{K}^0\pi^+$	$5T\,U_{ud}\,U_{cs}$
$\pi^+\pi^0$	$\frac{5}{\sqrt{2}}T\Sigma - \frac{5}{\sqrt{2}}T\Delta$
$\pi^+\eta_8$	$-\frac{1}{\sqrt{6}}(9T+2E+2S)\Sigma + \frac{1}{\sqrt{6}}(-3T+E+3F)\Delta$
$K^+\overline{K}^0$	$(3T-E-S)\Sigma + \frac{1}{2}(2T+E+3F)\Delta$
$\pi^+\eta_0$	$-\frac{2}{\sqrt{3}}(E+S)\Sigma + \frac{1}{\sqrt{3}}(E+3F)\Delta$
$K^0\pi^+$	$(2T+E+S)\,U_{us}\,U_{cd}$
$K^+\pi^0$	$\frac{1}{\sqrt{2}}(-3T+E+S)\,U_{us}\,U_{cd}$
$K^+\eta_8$	$\frac{1}{\sqrt{6}}(3T-E-S)\,U_{us}\,U_{cd}$
$K^+\eta_0$	$\frac{2}{\sqrt{3}}(E+S)\,U_{us}\,U_{cd}$
$\Sigma = \frac{1}{2}(U_{us}U_{cs} - U_{ud}U_{cd})$	
$\Delta = \frac{1}{2}(U_{us}U_{cs} + U_{ud}U_{cd})$	

meson plays no important role in the dynamics of the decay; it is said just to be a *spectator.*

The simplest spectator decays are processes like the one shown in Fig. 2.3.1. The weak Hamiltonian governing this decay is given in the Standard Model by:*

$$H_w = i\left(i\frac{g}{2\sqrt{2}}\right)^2 U_{cs}\,U_{ud}\,\bar{s}\gamma_\mu(1-\gamma_5)c\,\bar{u}\gamma_\nu(1-\gamma_5)d \left[-i\frac{g^{\mu\nu}}{q^2-M_W^2}\right]$$

Since $m_c \ll M_W$, $q^2 \ll M_W^2$ and the Hamiltonian may be reduced to the point

* This derivation follows that of Rückl.[42]

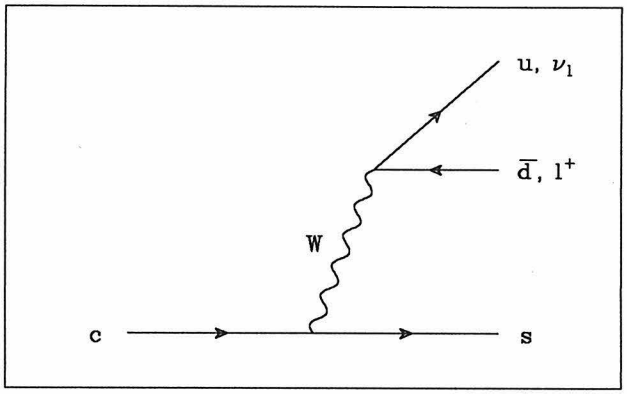

Figure 2.3.1: Simple spectator process

interaction:

$$H_W = \frac{G_F}{\sqrt{2}} U_{cs} U_{ud} \, \bar{s}\gamma_\mu(1-\gamma_5)c \, \bar{u}\gamma^\mu(1-\gamma_5)d$$

The presence of gluons will affect the form of this Hamiltonian. To lowest order in α_s, only four diagrams will be important; these are shown in Figs. 2.3.2a-2.3.2d. For clarity, they are shown, with the u quark moved to the initial state. If all external momenta are ignored, the matrix element corresponding to Fig. 2.3.2a is:

$$\begin{aligned} M_a = -i\left(i\frac{g}{2\sqrt{2}}\right)^2\left(i\frac{g_s}{2}\right)^2 U_{cs}\,U_{ud}\int \frac{d^4k}{(2\pi)^4}\bar{s}\gamma_\mu(1-\gamma_5)\left[\frac{\not{k}+m_c}{k^2-M_W^2}\right]\gamma_\lambda\lambda_a c \\ \cdot\,\bar{u}\gamma_\rho(1-\gamma_5)\lambda_b\left[\frac{\not{k}+m_c}{k^2-M_W^2}\right]\gamma_\sigma(1-\gamma_5)d \\ \left(-i\frac{g^{\lambda\rho}g^{ab}}{k^2}\right)\left(-i\frac{g^{\mu\sigma}}{k^2-M_W^2}\right) \end{aligned}$$

This may be simplified by assuming that the quarks are massless but off mass-shell by an amount μ. Further, if M_W is used as the ultraviolet cutoff point, the weak interaction may again be reduced to a point.

$$\begin{aligned} M_a = -i\frac{G_F}{\sqrt{2}}\pi\alpha_s\,U_{cs}\,U_{ud}\,\bar{s}\gamma_\mu\gamma^\alpha\gamma_\lambda(1-\gamma_5)\lambda_a c\bar{u}\gamma^\lambda\gamma^\beta\gamma^\mu(1-\gamma_5)\lambda^a d \\ \cdot\int\frac{d^4k}{(2\pi)^4}\frac{k_\alpha k_\beta}{k^6} \end{aligned}$$

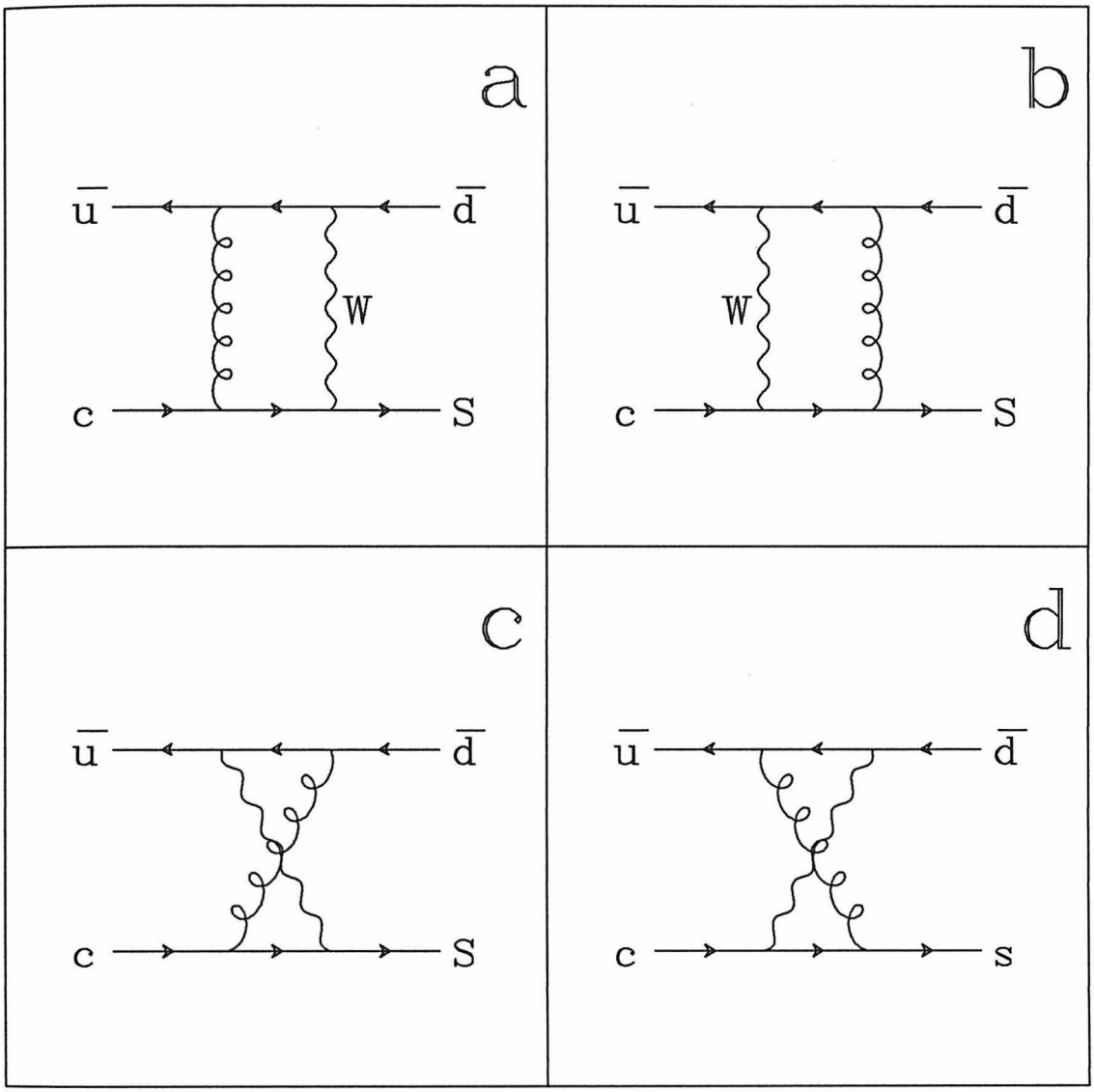

Figure 2.3.2: Order α_s corrections to spectator process

The integration is easily performed:

$$\int \frac{d^4k}{(2\pi)^4}\frac{k_\alpha k_\beta}{k^6} = \frac{i}{64\pi^2}\log(\frac{M_W^2}{\mu^2})\, g_{\alpha\beta}$$

Finally,

$$M_a = \frac{G_F}{\sqrt{2}}\frac{1}{16}\frac{\alpha_s}{\pi}\log\left(\frac{M_W^2}{\mu^2}\right) U_{cs}\, U_{ud}\, \bar{s}\gamma_\mu(1-\gamma_5)\lambda_a c\bar{u}\gamma^\mu(1-\gamma_5)\lambda^a d$$

Diagram b gives an equal contribution. Diagrams c and d also yield the same result with two changes. First, the crossing of the gauge bosons will introduce an overall change of sign. Second, use will be made of the identity

$$\cdots\gamma_\mu\gamma_\alpha\gamma_\lambda(1-\gamma_5)\cdots\gamma^\mu\gamma^\alpha\gamma^\lambda(1-\gamma_5)\cdots = 16\cdots\gamma_\mu(1-\gamma_5)\cdots\gamma^\mu(1-\gamma_5)\cdots$$

This introduces a factor of 4. Now, the total matrix element $M \equiv M_a + M_b + M_c + M_d$ is:

$$M = \frac{G_F}{\sqrt{2}}\left(\frac{1}{16}+\frac{1}{16}-\frac{1}{4}-\frac{1}{4}\right)\frac{\alpha_s}{\pi}\log\left(\frac{M_W^2}{\mu^2}\right) U_{cs}\, U_{ud}$$
$$\bar{s}\gamma_\mu(1-\gamma_5)\lambda_a c\bar{u}\gamma^\mu(1-\gamma_5)\lambda^a d$$

Thus, the first order change in the weak Hamiltonian is

$$H_w = -\frac{G_F}{\sqrt{2}}\frac{3}{8}\frac{\alpha_s}{\pi}\log\left(\frac{M_W^2}{\mu^2}\right) U_{cs}\, U_{ud}\, \bar{s}\gamma_\mu(1-\gamma_5)\lambda_a c\bar{u}\gamma^\mu(1-\gamma_5)\lambda^a d$$

The first order change has the same chiral and flavor structure as the lowest order Hamiltonian, but now it contains currents which are color octets. These

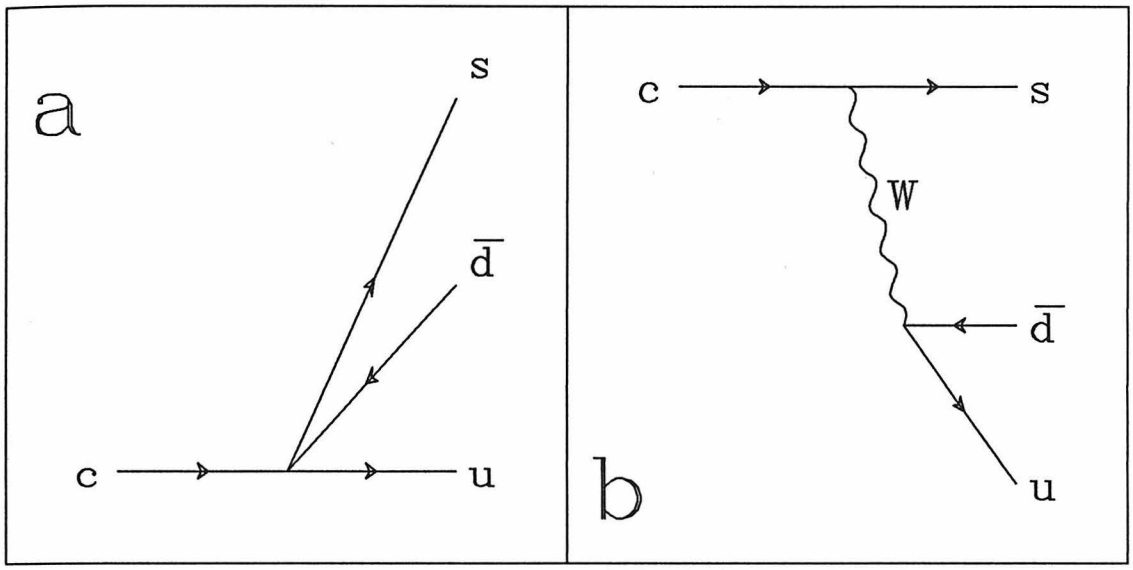

Figure 2.3.3: Induced neutral decay: reduced (a), unreduced (b)

may be expanded in terms of color singlets by making use of several identities:

$$\left[\gamma_\mu(1-\gamma_5)\right]_{\alpha\beta}\left[\gamma^\mu(1-\gamma_5)\right]_{\gamma\delta} = -\left[\gamma_\mu(1-\gamma_5)\right]_{\alpha\delta}\left[\gamma^\mu(1-\gamma_5)\right]_{\gamma\beta}$$

$$\left(\lambda_a\right)_{ij}\left(\lambda^a\right)_{kl} = -\frac{2}{3}\delta_{ij}\delta_{kl} + 2\delta_{il}\delta_{kj}$$

$$\{c,\,\overline{u}\} = 0 = \{c,\,\overline{d}\} = \{\overline{u}\,d\}$$

These may be combined to yield:

$$\begin{aligned}\overline{s}\gamma_\mu(1-\gamma_5)\lambda_a c\,\overline{u}\gamma^\mu(1-\gamma_5)\lambda^a d \\ = -\frac{2}{3}\,\overline{s}\gamma_\mu(1-\gamma_5)c\,\overline{u}\gamma^\mu(1-\gamma_5)d \\ +2\,\overline{s}\gamma_\mu(1-\gamma_5)d\,\overline{u}\gamma^\mu(1-\gamma_5)c\end{aligned}$$

This result is remarkable in that the hard gluon exchange has induced an effective *neutral* interaction. If the weak interaction had not been reduced to a point interaction, this effective neutral interaction, as shown in Fig. 2.3.3a, would be seen to correspond to the diagram in Fig. 2.3.3b.

It is useful to rewrite the corrected Hamiltonian in terms of operators with definite symmetry properties. As shown above, $H_{w,\Delta c=-1} \Rightarrow \overline{6} \oplus 3 \oplus 15$. The

$\overline{6}$-representation is antisymmetric but the 3 is symmetric under interchange of two quarks. Consider now the combinations

$$O_{\pm} = \frac{1}{2}\left[\bar{s}\gamma_{\mu}(1-\gamma_5)c\,\bar{u}\gamma^{\mu}(1-\gamma_5)d \right. \\ \left. \pm\, \bar{s}\gamma_{\mu}(1-\gamma_5)d\,\bar{u}\gamma^{\mu}(1-\gamma_5)c\right]$$

The operator O_+ is symmetric and so corresponds to the 3-representation. The operator O_- is antisymmetric and corresponds to the $\overline{6}$-representation. After substituting the definitions of O_+ and O_- into that for H_w:

$$H_{w,\Delta c=-1} = \frac{G_F}{\sqrt{2}}(C_+O_+ + C_-O_-)$$

$$C_+ = 1 - \frac{\alpha_s}{2\pi}\log\left(\frac{M_W^2}{\mu^2}\right)$$
$$C_- = 1 + \frac{\alpha_s}{\pi}\log\left(\frac{M_W^2}{\mu^2}\right)$$

This result may be extended to all orders of perturbation theory through the use of renormalization group techniques.

$$C_{\pm} \approx \left[\frac{\alpha_s(\mu^2)}{\alpha_s(M_W^2)}\right]^{\gamma_{\pm}}$$

This is known as the *leading-logarithm* result. The constants γ_+ and γ_- are given by

$$\gamma_+ = -\frac{6}{33-2N_f} \qquad\qquad \gamma_- = \frac{12}{33-2N_f}$$

For the decay of the charmed quark, there are three lighter quarks which may participate — $N_f = 3$ — so $\gamma_+ = -2/9$ and $\gamma_- = 4/9$. Using the charmed quark mass to set the scale, $\mu = m_c \approx 1.5$ GeV/c^2, $C_+ = 0.74$, and $C_- = 1.8$.

2.4: Shortcomings of the Spectator Model

Armed with an explicit form of the weak Hamiltonian, it is possible to make specific predictions for various decay processes. As a first example, consider the inclusive semileptonic branching ratios of D mesons. If only Cabibbo favored spectator amplitudes are included, the non-leptonic decay proceeds via $c \to s\,u\,\overline{d}$, and the semileptonic decay via $c \to s\,l^+\,\nu_l$. For the non-leptonic decay, it is useful the rewrite the Hamiltonian yet again as a sum of color singlet and color octet parts. To do this, use is made of the identity:

$$\begin{aligned}
&\overline{s}\gamma_\mu(1-\gamma_5)d\,\overline{u}\gamma^\mu(1-\gamma_5)c \\
&\qquad = \frac{1}{3}\,\overline{s}\gamma_\mu(1-\gamma_5)c\,\overline{u}\gamma^\mu(1-\gamma_5)d \\
&\qquad\quad +\frac{1}{2}\,\overline{s}\gamma_\mu(1-\gamma_5)\lambda_a c\,\overline{u}\gamma^\mu(1-\gamma_5)\lambda^a d
\end{aligned}$$

The weak Hamiltonian is now:

$$\begin{aligned}
H_{w,\Delta c=-1} = \frac{G_F}{\sqrt{2}}\Bigg[&\frac{1}{3}(2C_+ + C_-)\overline{s}\gamma_\mu(1-\gamma_5)c\,\overline{u}\gamma^\mu(1-\gamma_5)d \\
&+\frac{1}{4}(C_+ - C_-)\overline{s}\gamma_\mu(1-\gamma_5)\lambda_a c\,\overline{u}\gamma^\mu(1-\gamma_5)\lambda^a d\Bigg]
\end{aligned}$$

The two terms in this expression have different color structures and hence do not interfere. To simplify the notation, write $H^{(1)}$ for the singlet part of H_w and $H^{(8)}$ for the color octet part. In order to calculate the decay rate, it is necessary to square $H^{(1)}$ and $H^{(8)}$, sum the results over final state spins and colors, and average over the initial state spin and color. After performing the color calculations:

$$\begin{aligned}
\left|H^{(1)}\right|^2 &\propto \frac{1}{3}\left(\delta_{lb}\delta^{bl}\,\delta_{jd}\delta^{dj}\right) = \frac{1}{3}\cdot 3\cdot 3 = 3 \\
\left|H^{(8)}\right|^2 &\propto \frac{1}{3}(\lambda_b)_{lk}(\lambda_a)^{kl}\,(\lambda^b)_{ji}(\lambda^a)^{ij} \\
&= \frac{1}{3}(-\frac{2}{3}\delta_{ij}\delta_{kl} + 2\delta_{il}\delta_{jk})(-\frac{2}{3}\delta_{ji}\delta_{lk} + 2\delta_{jk}\delta_{il}) = \frac{32}{3}
\end{aligned}$$

$$\left|H_{w,\Delta c=-1}\right|^2 \propto 3\left(\frac{1}{3}(2C_+ + C_-)\right)^2 + \frac{32}{3}\left(\frac{1}{4}(C_+ - C_-)\right)^2 = 2C_+^2 + C_-^2$$

$$\left|H_{w,\Delta c=-1}\right|^2 = \frac{G_F}{\sqrt{2}}(2C_+^2 + C_-^2)\Big(\bar{d}\gamma^\sigma(1-\gamma_5)u\,\bar{c}\gamma_\sigma(1-\gamma_5)s \cdot\bar{s}\gamma_\mu(1-\gamma_5)c\,\bar{u}\gamma^\mu(1-\gamma_5)d \Big)$$

The spin calculations must now be performed, and the result integrated over the available phase-space. This task is greatly simplified by noting that, if the u and d quarks are considered massless, the spinor expression above is equivalent to that for the decay $\mu^- \rightarrow e^-\,\overline{\nu}_e\nu_\mu$. Borrowing the muon decay result, the non-leptonic decay rate is:

$$\Gamma(c \rightarrow s\,u\,\bar{d}) = (2C_+^2 + C_-^2)\frac{G_F^2 m_c^5}{192\pi^3}\,g\left(m_s^2/m_c^2\right)$$

The function g corrects the decay rate for the non-zero strange quark mass: $g(x) = 1 - 8x + 8x^3 - x^4 - 12x^2\log x$. For $m_s = 0.5$ GeV/c^2 and $m_c = 1.5$ GeV/c^2, $g(m_s^2/m_c^2) = 0.45$.

The semileptonic decay rates may be calculated in a similar manner.

$$\Gamma(c \rightarrow s\,l^+\,\nu_l) = \frac{G_F^2 m_c^5}{192\pi^3}\,g\left(m_s^2/m_c^2\right)$$

The total decay rate is given by the sum of the non-leptonic and semileptonic decay rates:

$$\begin{aligned}\Gamma_{tot} &= \Gamma(c \rightarrow s\,u\,\bar{d}) + \Gamma(c \rightarrow s\,e^+\,\nu_e) + \Gamma(c \rightarrow s\,\mu^+\,\nu_\mu) \\ &= (2C_+^2 + C_-^2 + 1 + 1)\frac{G_F^2 m_c^5}{192\pi^3}\,g\left(m_s^2/m_c^2\right)\end{aligned}$$

The semileptonic branching ratios are finally:

$$B(c \rightarrow s\,l^+\,\nu_l) = \frac{\Gamma(c \rightarrow s\,l^+\nu_l)}{\Gamma_{tot}} = \frac{1}{2C_+^2 + C_-^2 + 2}$$

If the values from the leading-logarithm calculation — $C_+ = 0.74$, and $C_- = 1.8$ — are used, the branching ratio is $B(c \rightarrow s\,l^+\,\nu_l) = 16\%$. This applies to all

charmed pseudoscalar mesons: the F^+ as well as the D^0 and D^+. This is the first major shortcoming of the spectator model. The semileptonic branching ratio obtained here is in reasonable agreement with that of the D^+ but very far from that of the D^0.

There are two conventional mechanisms for correcting this problem. The first is to notice that in some exclusive hadronic decays of the D^+, several amplitudes may interfere, thus reducing the overall non-leptonic decay rate. For example, consider the decay $D^+ \to \overline{K}^0 \pi^+$:

$$\begin{aligned} &< \overline{K}^0 \pi^+ | H_{w,\Delta c=-1} | D^+ > \\ &\qquad = \frac{G_F}{\sqrt{2}} \Big[< \pi^+ | \overline{u}\gamma^\mu\gamma_5 d|0 >< \overline{K}^0 | \overline{s}\gamma^\mu c | D^+ > (\frac{2}{3}C_+ + \frac{1}{3}C_-) \\ &\qquad\quad + < \overline{K}^0 | \overline{s}\gamma^\mu\gamma_5 d|0 >< \pi^+ | \overline{u}\gamma^\mu c | D^+ > (\frac{2}{3}C_+ - \frac{1}{3}C_-) \Big] \end{aligned}$$

In the limit that SU(3) is not broken

$$\begin{aligned} < \overline{K}^0 | \overline{s}\gamma^\mu c | D^+ > &= < \pi^+ | \overline{u}\gamma^\mu c | D^+ > \\ < \pi^+ | \overline{u}\gamma^\mu\gamma_5 d|0 > &= < \overline{K}^0 | \overline{s}\gamma^\mu\gamma_5 d|0 > \end{aligned}$$

In this limit, then, the terms proportional to C_- interfere destructively, and the matrix element is:

$$< \overline{K}^0 \pi^+ | H_{w,\Delta c=-1} | D^+ > = \frac{G_F}{\sqrt{2}} \frac{4C_+}{3} < \pi^+ | \overline{u}\gamma^\mu\gamma_5 d|0 >< \overline{K}^0 | \overline{s}\gamma^\mu c | D^+ >$$

A similar calculation yields the matrix element for $D^0 \to K^-\pi^+$.

$$\begin{aligned} &< K^-\pi^+ | H_{w,\Delta c=-1} | D^0 > \\ &\qquad = \frac{G_F}{3\sqrt{2}} \Big((2C_+ + C_-) < \pi^+ | \overline{u}\gamma_\mu\gamma_5 d|0 >< K^- | \overline{s}\gamma^\mu c | D^0 > \\ &\qquad\quad + (2C_+ - C_-) < K^-\pi^+ | \overline{s}\gamma_\mu d|0 >< 0 | \overline{u}\gamma^\mu\gamma_5 c | D^0 > \Big) \end{aligned}$$

Consider the second term for a moment. The matrix element between the D and

the vacuum is related to the pseudoscalar decay constant of the D:

$$< 0|\overline{u}\gamma^{\mu}\gamma_5 c|D^0 > \propto f_D P_D^{\mu} = f_D(P_s + P_{\overline{d}})^{\mu}$$

Now it is possible to use the Dirac equation to simplify the matrix element between the $K^-\pi^+$ system and the vacuum:

$$(P_s + P_{\overline{d}})_{\mu}\, \overline{s}\gamma^{\mu} d = (m_s - m_d)\overline{s}d$$

After combining these relations:

$$< K^-\pi^+|\overline{s}\gamma^{\mu} d|0 >< 0|\overline{u}\gamma^{\mu}\gamma_5 c|D^0 > \sim f_D(m_s - m_d) < K^-\pi^+|\overline{s}d|0 >$$

This vanishes in the limit of SU(3) symmetry and will be neglected for now.

By using the two matrix elements calculated above, it is now possible to compare the decay rates for $D^0 \to K^-\pi^+$ and $D^+ \to \overline{K}^0\pi^+$.

$$\frac{\Gamma(D^+ \to \overline{K}^0\pi^+)}{\Gamma(D^0 \to K^-\pi^+)} = \frac{(4C_+)^2}{(2C_+ + C_-)^2} \approx 0.8$$

The recent measurements of the MARK III, as given in Table 2.1.II, indicate that the ratio is actually much lower.

$$\frac{\Gamma(D^+ \to \overline{K}^0\pi^+)}{\Gamma(D^0 \to K^-\pi^+)} = \frac{B(D^+ \to \overline{K}^0\pi^+)}{B(D^0 \to K^-\pi^+)} \cdot \frac{\tau(D^0)}{\tau(D^+)} = 0.32^{+0.09}_{-0.08} \pm 0.03$$

Thus, if the values of C_+ and C_- obtained from perturbative QCD are used, interference alone is unable to account for the smallness of the decay rate for $D^+ \to \overline{K}^0\pi^+$.

The second mechanism for correcting the semileptonic decay rates is to assume that there is a large non-leptonic enhancement in decays of the D^0. Then the non-leptonic decays of the D^0 will be increased over those of the D^+, as there are no Cabibbo favored annihilation processes for the D^+.

Table 2.4.I: Branching ratios of possible annihilation processes

Experiment	Decay Mode	Branching Ratio
ARGUS	$D^0 \to \overline{K}^0\phi$	$0.99 \pm 0.32 \pm 0.17\%$
CLEO	$D^0 \to \overline{K}^0\phi$	$1.18 \pm 0.40 \pm 0.17\%$
MARK III	$D^0 \to \overline{K}^0\phi$	$1.1^{+0.7+0.4}_{-0.5-0.2}\%$
	$D^0 \to \overline{K}^0 K^+K^-_{\text{non}-\overline{K}^0\phi}$	$1.1^{+0.4+0.3}_{-0.3-0.2}\%$
	$D^0 \to \overline{K}^0 K^0$	$< 0.60\%$ (90% CL)

There are several experimentally tractable final states from D^0 decay which contain no u quarks, and thus must come about through flavor annihilation. Specifically, these are $\overline{K}^0\phi$, $\overline{K}^0K^0$, and $\overline{K}^{*0}K^0$. The latter two are Cabibbo suppressed, but the first is Cabibbo favored. This final state has been observed by a number of collaborations.[43] The measured branching ratios are given in Table 2.4.I.

An inspection of Table 2.1.II will make it clear that a branching ratio of 1.1% is not particularly small. Further, in the decay $D^0 \to \overline{K}^0\phi$, as $s\overline{s}$ pair must be produced from the vacuum. When a $u\overline{u}$ or $d\overline{d}$ pair is produced instead, it is expected that the corresponding amplitude will be substantially larger, maybe by as much as a factor of five.

There is further evidence that annihilation processes may be very important. The amplitude for $D^0 \to \overline{K}^0\pi^0$ has both spectator and annihilation components, as does that for $D^0 \to K^-\pi^+$.

$$
\begin{aligned}
&< \overline{K}^0\pi^0|H_{w,\Delta c=-1}|D^0 > \\
&\qquad = \frac{G_F}{3\sqrt{2}}\Big((2C_+ - C_-) < \overline{K}^0|\overline{s}\gamma_\mu\gamma_5 d|0 >< \pi^0|\overline{u}\gamma^\mu c|D^0 > \\
&\qquad\qquad +(2C_+ - C_-) < \overline{K}^0\pi^0|\overline{s}\gamma_\mu d|0 >< 0|\overline{u}\gamma^\mu\gamma_5 c|D^0 > \Big)
\end{aligned}
$$

If the annihilation term is neglected, the ratio of $\overline{K}^0\pi^0$ and $K^-\pi^+$ decay rates is:

$$\frac{\Gamma(D^0 \to \overline{K}^0\pi^0)}{\Gamma(D^0 \to K^-\pi^+)} = \frac{1}{2}\frac{(2C_+ - C_-)^2}{(2C_+ + C_-)^2} \approx 0.005$$

On the other hand, if the annihilation terms are much larger than the spectator terms, and if SU(3) invariance is valid,

$$\frac{\Gamma(D^0 \to \overline{K}^0\pi^0)}{\Gamma(D^0 \to K^-\pi^+)} \sim \frac{1}{2}$$

Experimentally, this ratio is quite large.

$$\frac{B(D^0 \to \overline{K}^0\pi^0)}{B(D^0 \to K^-\pi^+)} = 0.43 \pm 0.09 \pm 0.04$$

That this ratio is so much closer to the prediction based on annihilation dominance than to the prediction based on spectator dominance implies that annihilation processes may be very important in decays of the D^0

In summary, predictions for the non-leptonic decay rates of D mesons may be brought into line with experimental results if:

1. annihilation effects are important in D^0 decays.
2. SU(3) invariance leads to interference among the amplitudes for D^+ decay.
3. the operator coefficients obeys the inequality $C_- \gg C_+$. This the same as the assumption of 20-plet dominance mentioned earlier.

The last assumption is required to reduce the rate for $D^+ \to \overline{K}^0\pi^+$ relative to $D^0 \to K^-\pi^+$. Precisely this assumption, however, reduces the inclusive semileptonic branching ratio of the D^+. Thus it is very difficult to obtain a comprehensive picture of D decay including both non-leptonic and semileptonic processes.

Chapter 3: Semileptonic Decays of D Mesons

3.1: The Difficulties of Non-leptonic Decays

In chapter 2, it was shown that it is very difficult to develop a consistent procedure for calculating the decay rates of charmed particles. As pointed out by Rückl,[44] the problem does not lie with the weak Hamiltonian as derived in section 2.2. The form of the weak Hamiltonian is *exact.*

$$H_{w,\Delta c=-1} = \frac{G_F}{\sqrt{2}}\left(C_+ O_+ + C_- O_-\right)$$

$$O_\pm = \frac{1}{2}\left(\bar{u}\gamma_\mu(1-\gamma_5)d\,\bar{s}\gamma^\mu(1-\gamma_5)c \right.$$
$$\left. \pm \bar{s}\gamma_\mu(1-\gamma_5)d\,\bar{u}\gamma^\mu(1-\gamma_5)c\right)$$

The leading-logarithm values of C_+, and C_- — 0.74 and 1.8, respectively — may be modified by higher order process, but the operator structure will not change. Under SU(3) of color, $H_{w,\Delta c=-1} \Rightarrow 3 \otimes 3 = \bar{3} \oplus 6$. The $\bar{3}$-representation is antisymmetric whereas the 6-representation is symmetric. Thus, under $SU(3)_{color}$, $O_+ \Rightarrow 6$, and $O_- \Rightarrow \bar{3}$. Since the strong interactions are invariant under $SU(3)_{color}$, the addition of more gluons — the higher order processes mentioned above — will not affect the operator structure.

The difficulties lie rather with the calculation of the matrix elements of this Hamiltonian. Several assumptions were made in section 2.3. The most important are:

1. that charmed mesons consist only of valence quarks which are in a color singlet state.
2. that the vacuum insertion, $|0><0| \approx 1$, is applicable.
3. that final state interactions are negligible.

The second assumption has the consequence that currents transforming as color octets may be neglected; these cannot connect mesonic states with each other or with the vacuum. Such currents may in fact be important. A large, negative contribution would correct the predictions for both $D^0 \rightarrow \overline{K}^0\pi^0$, and $D^+ \rightarrow \overline{K}^0\pi^+$. The exact size of this contribution is, unfortunately, very difficult to calculate.

The assumption that charmed mesons consist only of two valence quarks is probably indefensible. As has been pointed out, a large annihilation amplitude is required phenomenonologically to produce the desired enhancement of non-leptonic decays of the D^0. The arguments given in section 2.3, by which the annihilation amplitudes vanish in the limit of $SU(3)_{\text{flavor}}$ symmetry, are invalidated if the meson also contains soft gluons.

Finally, it is probably not the case that final state interactions may be ignored. There are several large hadronic resonances in the 0.5-1.5 GeV/c^2 range, particularly the $\rho(770)$ and $K^*(892)$. These, of course, play only a small role in the decays of kaons, for which final state interactions are not very important. In the case of D mesons, however, these interactions may have a dominant effect. Donoghue[45] has pointed out that even the 'smoking gun' test of flavor annihilation — the observation of the decay $D^0 \rightarrow \overline{K}^0\phi$ — may not be unambiguous. He argues that this final state may be produced by a spectator process such as $D^0 \rightarrow \overline{K}^{*0}\eta$ which is subsequently modified by quark exchange between the $\overline{K}^{*0}$ and the η as shown in Fig. 3.1.1.

The conclusion one is forced to draw from the preceding discussion is that it is difficult, if not impossible, at the present time to make firm predictions for exclusive non-leptonic decay rates. Before this will become possible, it will be necessary to construct meson wavefunctions including all gluonic degrees of freedom. It will also be necessary to discover the appropriate machinery for calculating matrix elements of operators which are not color singlets. It should be noted, however, that of late some progress[46] has been made through the use

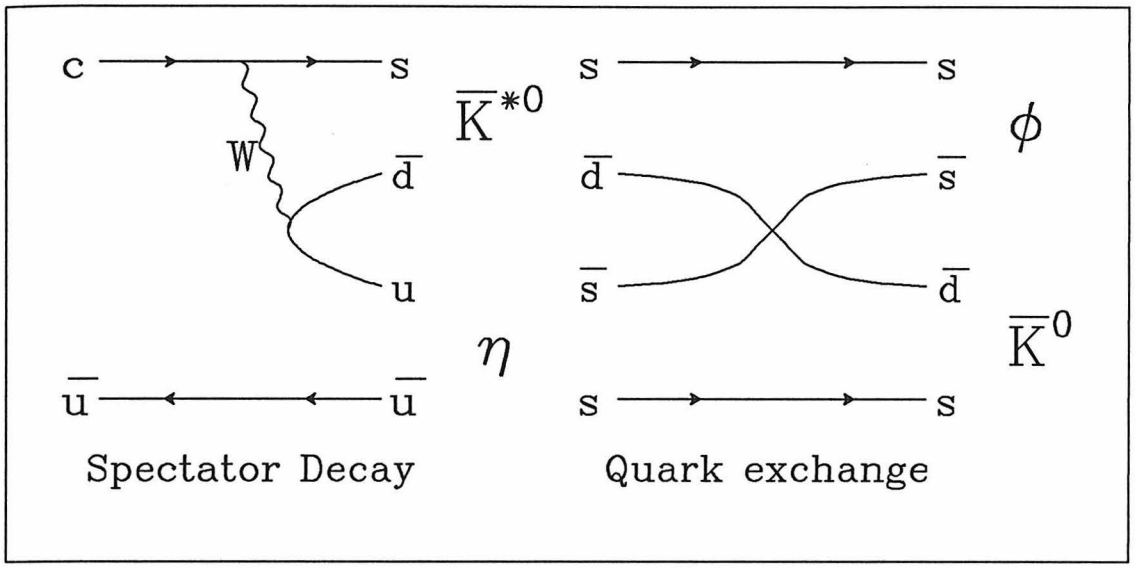

Figure 3.1.1: Alternative origin of $D^0 \to \overline{K}^0 \phi$ events

of a $1/N_c$ expansion, where N_c is the number of colors.

If it is difficult to make comprehensive predictions for non-leptonic decays, the semileptonic decays are much easier to understand. In particular, Cabibbo favored semileptonic decays proceed only through spectator processes. Further, only matrix elements of color singlet operators may contribute. The Feynman diagram for Cabibbo allowed semileptonic decay is shown in Fig. 3.1.2. Clearly there are no strong interaction effects to be considered between the leptons and quarks.

3.2: Parameterization of Hadronic Matrix Elements

Cabibbo allowed semileptonic decays proceed through processes like that shown in Fig. 3.2.1. The weak Hamiltonian for any such spectator process is given in the Standard Model by:

$$H_w = \frac{G_F}{\sqrt{2}} J^{\mu}_{hadron} J_{\mu,lepton}$$

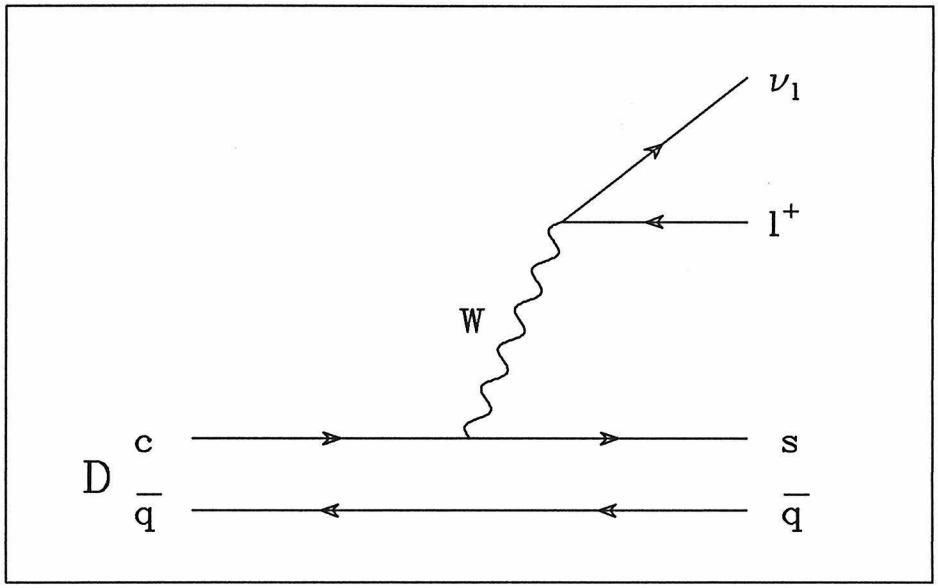

Figure 3.1.2: Feynman diagram for Cabibbo allowed semileptonic decay

$$J_{\mu,lepton} = \overline{\nu}_l \gamma_\mu (1 - \gamma_5) l$$
$$J^\mu_{hadron} = \overline{q} U_{qc} \gamma^\mu (1 - \gamma_5) c$$

The final state quark, q, may be either an s or d quark. The factor U_{qc} is the appropriate element of the quark mixing matrix. The transition amplitude is then $M =< h\, l^+\, \nu_l | H_w | D >$, where the notation h stands for the hadrons produced in the final state.

As noted at the end of section 3.1, semileptonic processes are free of strong interactions between the leptons and quarks. If electromagnetic radiative corrections are neglected, there can be no question of the validity of factorizing the amplitude M into leptonic and hadronic parts.

$$M =< \nu_l\, l^+ | J_{\mu,lepton} | 0 >< h | J^\mu_{hadron} | D >$$

The matrix element of the leptonic current is very simple. The leptons are free pointlike particles. The matrix element may be written using free particle

wavefunctions as:

$$< \nu_l\, l^+ | J_{\mu,lepton} | 0 >= \overline{u}(\nu_l)\gamma_\mu(1-\gamma_5)v(l)$$

It is precisely the fact that the matrix element of the leptonic current is well-understood which makes the study of the semileptonic decays of mesons interesting. The dynamics of the leptonic current may be exploited to probe the structure of the hadronic matrix elements.

The simplest prediction for the matrix element of the hadronic current obtains when the quarks are also treated as free pointlike particles. In this case, the hadronic matrix element is similar to the leptonic matrix element.

$$< h | J^\mu_{hadron} | D >= U_{qc}\overline{u}(q)\gamma^\mu(1-\gamma_5)u(c)$$

In this case, the transition amplitude is

$$M = \frac{G_F}{\sqrt{2}} U_{qc}\overline{u}(q)\gamma_\mu(1-\gamma_5)u(c)\,\overline{u}(\nu_l)\gamma^\mu(1-\gamma_5)v(l)$$

As was shown in section 2.3, this matrix element leads to a value for the semileptonic decay rate of:

$$\Gamma(c \rightarrow s\, l\, \nu_l) = \frac{G_F^2 m_c^5}{192\pi^3} g(m_s^2/m_c^2)$$

The lifetime of a charmed meson in this model is:

$$\tau_D = \frac{B(D \rightarrow l + X)}{\Gamma(c \rightarrow s\, l\, \nu_l)}$$

If the constituent masses of $m_c = 1.5$ GeV/c^2, and $m_s = 0.5$ GeV/c^2 and the measured branching ratios of $B(D^0 \rightarrow eX) = 7.5 \pm 1.1 \pm 0.4\%$ and $B(D^+ \rightarrow eX) = 17.0 \pm 1.9 \pm 0.7\%$ are used, this formula predicts lifetimes of $\tau_{D^0} = 6.4 \times 10^{-13}$ sec and $\tau_{D^+} = 1.4 \times 10^{-12}$ sec. These are larger than the measured values, but they

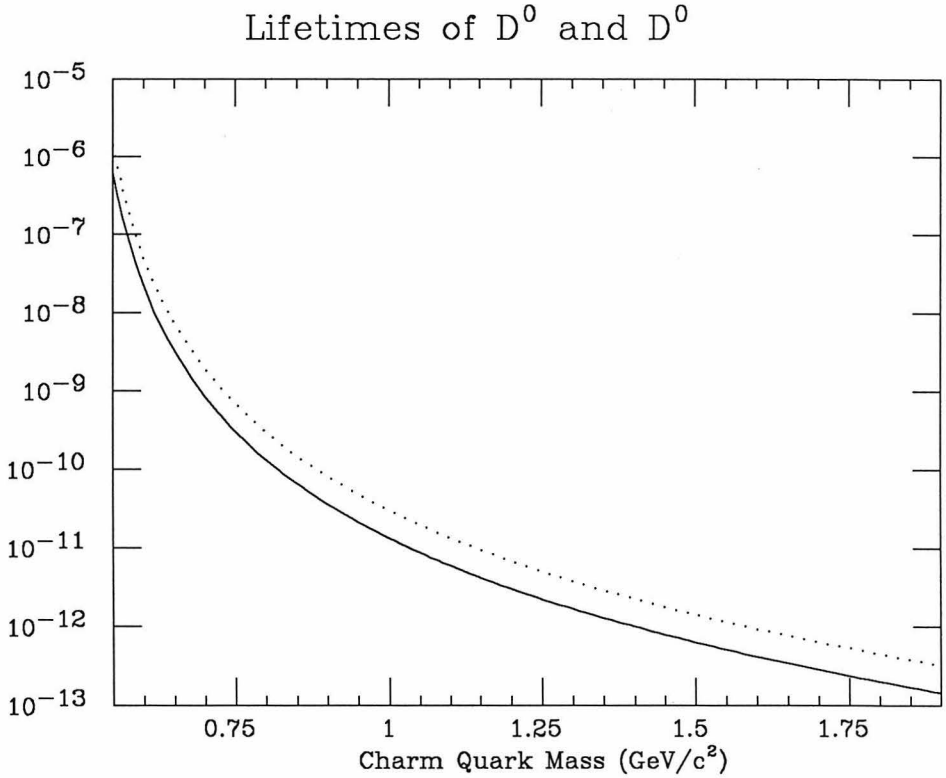

Figure 3.2.1: D^0 and D^+ lifetimes in the free fermion approximation

depend critically on the value chosen for the masses. The predicted lifetimes are shown in Fig. 3.2.1 as a function of m_c; a dependence on m_s enters only through g, a slowly varying function, whereas the lifetime is proportional to m_c^{-5}.

This free quark hadronic current may be corrected to first order in α_s by including the processes of Fig. 3.2.2. Similar processes enter into the calculation of radiative corrections to muon decay. It is possible to adapt these calculations to the present case through the substitution:

$$\alpha_{QED} \longrightarrow \alpha_s \cdot \frac{1}{3}\mathrm{Tr}\left[\left(\frac{1}{2}\lambda^a\right)\left(\frac{1}{2}\lambda_a\right)\right] = \frac{4}{3}\alpha_s$$

The result of this calculation may be written:[47]

$$\Gamma^{(1)}(c \to s\, l\, \nu_l) = \frac{G_F^2 m_c^5}{192\pi^3} g(m_s^2/m_c^2)\left[1 - \frac{2}{3}\frac{\alpha_s(m_c^2)}{\pi} f(m_s/m_c)\right]$$

The values of f and $\Gamma^{(1)}/\Gamma$ are given in Table 3.2.I for a number of values of

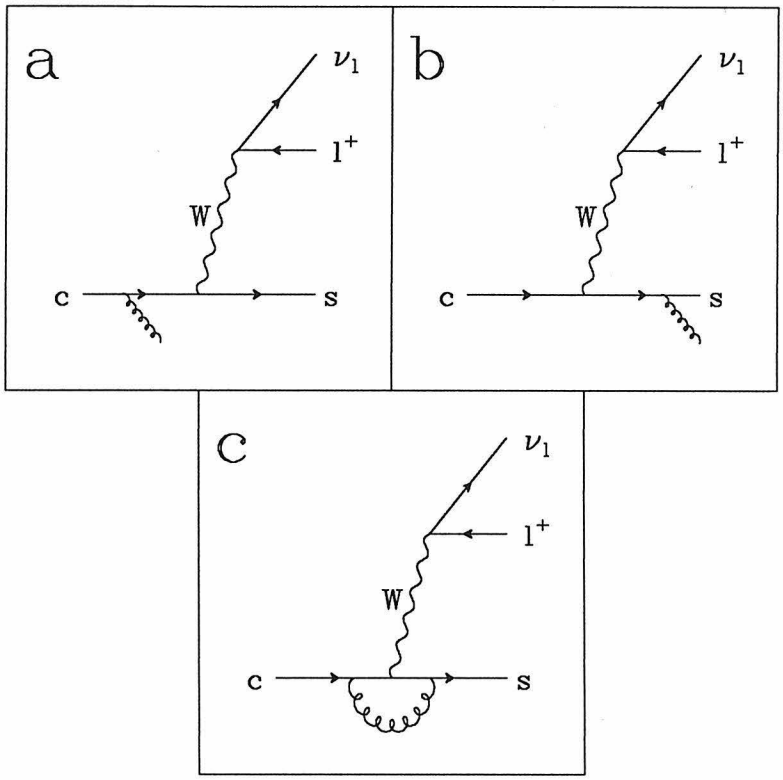

Figure 3.2.2: Lowest order corrections to free fermion approximation

$\lambda \equiv m_s/m_c$, with $\alpha_s(m_c^2)$ taken to be 0.7 It is important to note that the function f is positive, so that the first order corrections increase the predicted D lifetime. This makes it even more difficult to reconcile the measured lifetimes with reasonable estimates of m_c and m_s.

The failure of this calculation should in no way be a surprise. The quarks in the semileptonic process under consideration are not even approximately free; they are confined to the interior of the hadrons. Any successful calculation will have to take into account this non-perturbative aspect of the problem.

Having demonstrated that a realistic approach to charmed meson decays will have to be based on the properties of hadrons, and not merely on those of free quarks, it is useful to identify the types of hadrons which may be produced. It is easy to show that the masses of such hadrons should be tightly constrained.[48] If m_h is the hadron mass, $m_h^2 \sim (P_s + P_{\bar{q}})^2 = m_s^2 + m_{\bar{q}}^2 + 2P_s \cdot P_{\bar{q}}$. The c quark

Table 3.2.I: First order correction to $\Gamma(c \rightarrow s\, l\, \nu_l)$

$\lambda = m_s/m_c$	$f(\lambda)$	$\Gamma^{(1)}/\Gamma$
0.0	3.62	0.46
0.1	3.25	0.52
0.2	2.84	0.58
0.3	2.50	0.63
0.4	2.23	0.67
0.5	2.01	0.81
0.6	1.83	0.74
0.7	1.70	0.74
0.8	1.59	0.77
0.9	1.53	0.77

is so massive that its rest frame nearly coincides with that of the decaying D. If the Fermi motion of the $\overline{q}$ quark is ignored, it will be at rest within this meson. Thus, in the rest frame of the c quark, $P_s \cdot P_{\overline{q}} \approx m_{\overline{q}} E_s$. In the three body decay $c \rightarrow s\, l\, \nu_l$, if the leptons are considered approximately massless, the energy of the s quark must obey the inequality $E_s \leq (1/2m_c)(m_c^2 + m_s^2)$. The mass range available is thus:

$$m_K^2 \leq m_h^2 \leq m_s^2 + m_{\overline{q}}^2 + \frac{m_{\overline{q}}}{m_c}(m_c^2 + m_s^2)$$

If the constituent quark masses of $m_u \approx m_d \approx 0.3$ GeV/c^2, $m_s \approx 0.5$ GeV/c^2, and $m_c \approx 1.5$ GeV/c^2 are used, the mass range is

$$0.49 \text{ GeV/c}^2 \leq m_h \leq 0.9 \text{ GeV/c}^2$$

The hadronic final state consists of an $s\overline{q}$ pair, and possibly additional $u\overline{u}$ or $d\overline{d}$ pairs, so it has isospin 1/2. It is probable that the semileptonic decay amplitude will be dominated by final states consisting of a single kaon, the $K^*(892)$

resonance, or non-resonant K–π pairs. No higher mass strange resonances are energetically accessible.

Consider the simplest hadronic final state, in which the final state quarks form a kaon. The matrix element of the hadronic current is in that case given by

$$J_\mu =< K|\bar{s}\gamma_\mu(1-\gamma_{5)}c|D >$$

The D and K mesons are both pseudoscalars so only a vector current — a vector of odd parity — may connect them.*

$$J_\mu =< K|\bar{s}\gamma_\mu c|D >$$

This matrix element must be a vector. The states of the D and K are determined by their 4-momenta, so J_μ may depend only on these 4-momenta. Only two linearly independent combinations may be constructed from two 4-vectors. If these are chosen to be the sum and difference of these vectors, the hadronic matrix element may be parameterized as:

$$J_\mu = f_+ (P_D + P_K)_\mu + f_- (P_D - P_K)_\mu$$

The coefficients are scalar functions or *form factors.* Since they are scalar functions, they may depend only on the four scalars P_D^2, P_K^2, $(P_D + P_K)^2$, and $(P_D - P_K)^2$. Of these, the first two are trivial as $P_D^2 = m_D^2$ and $P_K^2 = m_K^2$. The last two are not independent; consider the sum of these two terms.

$$(P_D + P_K)^2 + (P_D - P_K)^2 = 2m_D^2 + 2m_K^2$$

It is conventional to choose $t \equiv (P_D - P_K)^2$ as the independent variable. The

---

* J_μ is a vector and so has odd parity. If V_μ and A_μ are vector and axial-vector operators, the matrix elements $< K|V_\mu|D >$ and $< K|A_\mu|D >$ have odd and even parity, respectively. Thus, $J_\mu \propto < K|V_\mu|D >$.

hadronic matrix element is finally:

$$J_\mu = f_+(t)\,(P_D + P_K)_\mu + f_-(t)\,(P_D - P_K)_\mu$$

The case of the production of a vector meson — or of a pair of pseudoscalar mesons in a relative P wave — is somewhat more complicated. Such a state is characterized by both its momentum and polarization. The hadronic matrix element will then depend on three 4-vectors. Four combinations of these may be formed which are linear in the polarization: three axial-vector and one polar-vector combination. The matrix element in now

$$< K^*|\bar{s}\gamma_\mu c|D >= ig(t)\epsilon_{\mu\nu\rho\sigma}\epsilon^{*\nu}(P_D + P_{K^*})^\rho(P_D - P_{K^*})^\sigma$$

$$< K^*|\bar{s}\gamma_\mu\gamma_5 c|D >= f(t)\epsilon^*_\mu + a_+(t)(\epsilon^*\cdot P_D)(P_D+P_{K^*})_\mu + a_-(t)(\epsilon^*\cdot P_D)(P_D-P_{K^*})_\mu$$

Similar arguments may be used to parameterize the hadronic matrix elements for several other final states. Results are quoted below for four additional final states.[49]

$\underline{^3P_2}$

$$< X(^3P_2)|\bar{s}\gamma_\mu c|D >= ih(t)\epsilon_{\mu\nu\lambda\rho}\epsilon^{*\nu\alpha}P_{D\alpha}(P_D + P_X)^\lambda(P_D - P_X)^\rho$$

$$\begin{aligned}< X(^3P_2)|\bar{s}\gamma_\mu\gamma_5 c|D >= {} & k(t)\epsilon^*_{\mu\nu}P_D^\nu + b_+(t)(\epsilon^*_{\alpha\beta}P_D^\alpha P_D^\beta(P_D + P_X)_\mu \\ & + b_-(t)(\epsilon^*_{\alpha\beta}P_D^\alpha P_D^\beta(P_D - P_X)_\mu\end{aligned}$$

$\underline{^3P_1}$

$$< X(^3P_1)|\bar{s}\gamma_\mu c|D >= l(t)\epsilon^*_\mu + c_+(t)(\epsilon^*\cdot P_D)(P_D+P_X)_\mu + c_-(t)(\epsilon^*\cdot P_D)(P_D-P_X)_\mu$$

$$< X(^3P_1)|\bar{s}\gamma_\mu\gamma_5 c|D >= iq(t)\epsilon_{\mu\nu\rho\sigma}\epsilon^{*\nu}(P_D + P_X)^\rho(P_D - P_X)^\sigma$$

$\underline{^3P_0}$

$$< X(^3P_0)|\bar{s}\gamma_\mu\gamma_5 c|D >= u_+(t)\,(P_D + P_K)_\mu + u_-(t)\,(P_D - P_K)_\mu$$

$\underline{^1P_1}$

$$< X(^1P_1)|\bar{s}\gamma_\mu c|D >= r(t)\epsilon^*_\mu + s_+(t)(\epsilon^* \cdot P_D)(P_D + P_X)_\mu + s_-(t)(\epsilon^* \cdot P_D)(P_D - P_X)_\mu$$

$$< X(^1P_1)|\bar{s}\gamma_\mu\gamma_5 c|D >= iv(t)\epsilon_{\mu\nu\rho\sigma}\epsilon^{*\nu}(P_D + P_X)^\rho(P_D - P_X)^\sigma$$

3.3 Prediction of Form Factors

There are several procedures which yield predictions for the various form factors listed at the end of section 3.2. Perhaps the simplest predictions are based on current algebra techniques. As an illustration, consider the decay $D \to K\, e\, \nu_e$. The corresponding transition amplitude is $< K|V_\mu|D >$. The divergence of the vector current is not zero, but it is a scalar.[50] Thus the matrix element of this divergence must correspond to the exchange of a scalar quantum. The divergence of the part of the hadronic current corresponding to exchange of a vector quantum must be zero.

$$< K|\partial^\mu V_\mu|D >= (P_D - P_K)^\mu J_\mu^{(j=1)} = 0$$

Here, $J_\mu = f_+(t)(P_D + P_K)_\mu + f_-(t)(P_D - P_K)_\mu$ as shown in the previous section.

To find $J_\mu^{(j=1)}$ it is only necessary to project J_μ onto the surface orthogonal to $(P_D - P_K)^\mu$.

$$J_\mu^{(j=1)} = \left(g_{\mu\nu} - \frac{(P_D - P_K)_\mu (P_D - P_K)_\nu}{t}\right) J^\nu$$

$$J_\mu^{(j=1)} = f_+(t)\left((P_D + P_K)_\mu - \left(\frac{m_D^2 - m_K^2}{t}\right)(P_D - P_K)_\mu\right)$$

Since the vector part of the amplitude is proportional to $f_+(t)$, this is usually called the *vector* form factor.

The part of the amplitude corresponding to scalar exchange is just that part of J_μ parallel to $(P_D - P_K)_\mu$: $J_\mu^{(j=0)} = J_\mu - J_\mu^{(j=1)}$. If the *scalar* form factor, $f_0(t)$, is defined by the relation

$$(m_D^2 - m_K^2) f_0(t) \equiv (m_D^2 - m_K^2) f_+(t) + t f_-(t)$$

the scalar amplitude is

$$J_\mu^{(j=0)} = f_0(t)\left(\frac{m_D^2 - m_K^2}{t}\right)(P_D - P_K)_\mu$$

The form factors, $f_+(t)$ and $f_0(t)$, govern the exchange of quanta of different angular momenta, so they are independent functions. After making a few assumptions, it is possible to make simple predictions for f_+ and f_0.

1. Returning to the form of the transition amplitude, the two form factors, f_+ and f_-, must be relatively real in order to insure the time reversal invariance of this amplitude. The form factors may thus be chosen to be real over the kinematically allowed range $0 \leq t \leq (m_D - m_K)^2$.

2. It is reasonable to assume that f_+ and f_0 are analytic functions over the entire complex t plane.

3. For unitarity to be respected, it is necessary that $f(t) \to 0$ as $|t| \to \infty$.

4. The positions of any singularities will be given by the masses of resonances with the appropriate quantum numbers.

The exchanged quanta must have the quantum numbers of charm and strangeness as they couple to explicitly charmed and strange particles, the D and K. The F^* vector resonance has the correct quantum numbers so $f_+(t)$ will have a singularity at $t = m_{F^*}^2$. Since f_+ is an analytic function, it may be evaluated by making use of Cauchy's integral formula.

$$f_+(t) = \frac{1}{2\pi i} \int_C \frac{f_+(t')\, dt'}{t' - t}$$

The threshold at a mass of $M = m_D + m_K$ results in a square-root singularity in the complex t plane since $t \propto M^2$. The branch cut is chosen along the positive real axis from $t_0 = (m_D + m_K)^2$ to ∞. The mass of the F^* is not necessarily above this D-K threshold; the value of 2140 MeV/c^2, as reported in the *Review of Particle Properties*, lies well below this threshold. If $m_{F^*} \geq m_D + m_K$ an appropriate integration contour is given in Fig. 3.3.1a. If $m_{F^*} < m_D + m_K$, the singularity at $t = m_{F^*}^2$ will be to the left of the branch cut and the contour in Fig. 3.3.1b must be used.

In either case, the contribution from the large circle may be neglected since $f(t) \to 0$ as $|t| \to \infty$. The integrations above and below the branch cut may be combined. Since $f_+(t)$ is real for $0 \leq t \leq (m_D - m_K)^2$, the Schwarz reflection principle guarantees that $f_+(t^*) = f_+^*(t)$ for all t. With this relation,

$$f_+(t' + i\epsilon) - f_+(t' - i\epsilon) = 2i\, \mathrm{Im} f_+(t' + i\epsilon)$$

$$\frac{1}{2\pi i}\left(\lim_{\epsilon \to 0} \int_{t_0}^{\infty} \frac{f_+(t' + i\epsilon)\, dt'}{t' + i\epsilon - t} - \lim_{\epsilon \to 0} \int_{t_0}^{\infty} \frac{f_+(t' - i\epsilon)\, dt'}{t' - i\epsilon - t} \right) = \frac{1}{\pi} \int_{t_0}^{\infty} \frac{\mathrm{Im} f_+(t')\, dt'}{t' - t}$$

Finally, two dispersion relations result, corresponding to the two integration

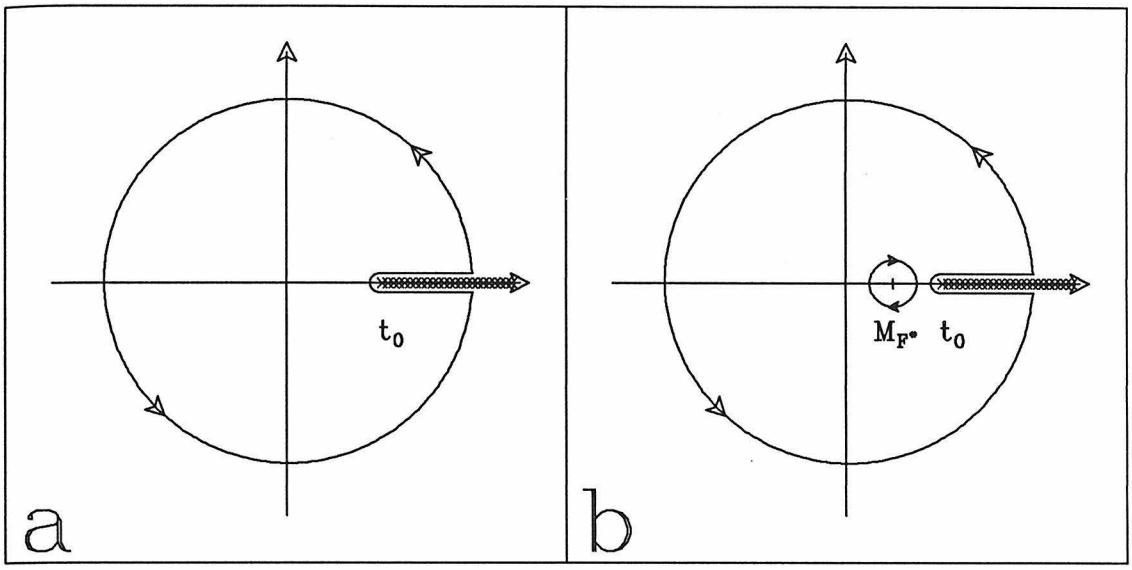

Figure 3.3.1: Integration contours for form factor evaluation

contours.

$$f_+(t) = \frac{1}{\pi}\int_{t_0}^{\infty} \frac{\mathrm{Im} f_+(t')\,dt'}{t'-t} \qquad m_{F^*} \geq \sqrt{t_0}$$

$$f_+(t) = \frac{1}{\pi}\int_{t_0}^{\infty} \frac{\mathrm{Im} f_+(t')\,dt'}{t'-t} - \frac{1}{2\pi i}\oint \frac{f_+(t')\,dt'}{t'-t} \qquad m_{F^*} < \sqrt{t_0}$$

For $t > t_0$, f_+ will simply be a Breit-Wigner amplitude.

$$f_+(t') = \frac{C_+}{t' - m_{F^*}^2 + i\Gamma m_{F^*}}$$

where Γ is the resonance width. For $(m_D - m_K)^2 < t < (m_D + m_K)^2$, f_+ will be given by the analytic continuation of the Breit-Wigner amplitude above.

$$f_+(t') = \frac{C_+}{t' - m_{F^*}^2 - \Gamma m_{F^*}}$$

For $t > t_0$, the imaginary part of f_+ is

$$\mathrm{Im} f_+(t') = \frac{-C_+\Gamma m_{F^*}}{(t' - m_{F^*}^2)^2 + \Gamma^2 m_{F^*}^2}$$

In the range $0 \leq t \leq (m_D - m_K)^2$, f_+ is given by the dispersion relations above. The two relations may be combined into one by making use of the Heaviside function $H(\sqrt{t_0} - m_{F^*})$:

$$H(\sqrt{t_0} - m_{F^*}) = \begin{cases} 0 & \text{if } \sqrt{t_0} \leq m_{F^*} \\ 1 & \text{if } \sqrt{t_0} > m_{F^*} \end{cases}$$

The dispersion relation is now:

$$f_+(t) = -\frac{C_+ \Gamma m_{F^*}}{\pi} \int_{t_0}^{\infty} \frac{dt'}{(t'-t)\left((t'-m_{F^*}^2)^2 + \Gamma^2 m_{F^*}^2\right)} - \frac{1}{2\pi i} H(\sqrt{t_0} - m_{F^*}) \oint \frac{f_+(t')\,dt'}{t'-t}$$

Performing the indicated integrations:

$$f_+(t) = -\frac{C_+}{\pi}(m_{F^*}^4 + m_{F^*}^2\Gamma^2 - 2m_{F^*}^2 t + t^2)^{-1} \cdot \left\{ (m_{F^*}^2 - t)\left[\frac{\pi}{2} - \arctan\left(\frac{1}{\Gamma m_{F^*}}(t_0 - m_{F^*}^2)\right)\right] + \frac{\Gamma m_{F^*}}{2} \log\left(\frac{\Gamma^2 m_{F^*}^2 + (t_0 - m_{F^*}^2)^2}{(t_0 - t)^2}\right)\right\} - C_+ \frac{H(\sqrt{t_0} - m_{F^*})}{m_{F^*}^2 + \Gamma m_{F^*} - t}$$

In the limit that Γm_{F^*} is small, the above prediction for f_+ becomes quite simple

$$f_+(t) = -\frac{C_+}{m_{F^*}^2 - t}$$

Such an expression is usually normalized so that the unknown constant is $f_+(0)$.

$$f_+(t) = f_+(0)\frac{m_{F^*}^2}{m_{F^*}^2 - t}$$

This is the conventional prediction for $f_+(t)$. As has been shown, however, it is only valid in the limit in which the width of the F^* may be ignored.

The behavior of the vector form factor f_+ is dominated by the existence of the charmed, strange vector resonance, the $F^*(2140)$. In a similar manner, the behavior of the scalar form factor f_0 will dominated by a charmed, strange scalar resonance. Unfortunately, no such state has been observed. Nevertheless, the four quark model with SU(4) symmetry predicts the existence of a 15-plet of scalar mesons. This 15-plet contains the SU(3) scalar non-charmed nonet and two SU(3) triplets of charmed mesons. These mesons will hereafter be referred to as D_0^0, D_0^+, and F_0^+ with quark content $c\bar{u}$, $c\bar{d}$, and $c\bar{s}$, respectively.

An approximate mass formula may be used to estimate the masses of the charmed scalar meson masses. The Gell-Mann – Okubo mass formula may be extended to encompass the SU(4) symmetry group.[51] As is well known, the mass splittings within meson multiplets are best described by a formula for the quadratic mass of these mesons.

$$M^2 = \mu_0^2 + \mu_1^2 C^2 + \mu_2^2 \left(I(I+1) - \frac{1}{4}Y^2\right)$$

Here, the hypercharge is given by $Y = B + S - C$, where B, S, and C are baryon number, strangeness, and charm, respectively. Making use of this formula, it is simple to derive the relations:

$$m_F^2 - m_D^2 = m_{\eta^8}^2 - m_K^2$$
$$m_{F_0}^2 - m_{D_0}^2 = m_{\eta_0^8}^2 - m_\kappa^2$$

The isoscalar components of the pseudoscalar and scalar octets are denoted η^8 and η_0^8. These are combinations of the observed states η and η', and of the $S^*(975)$ and $\epsilon(1300)$.

There is no formula which relates the masses of the charmed mesons separately to the masses of non-charmed mesons. It is, however, quite reasonable to assume that the difference in the D and K masses is caused primarily by the large difference between the c and s quark masses. The difference in masses between equivalent elements of different multiplets should thus be approximately

the same. This may be demonstrated in the case of the pseudoscalar and vector 15-plets:

$$m^2_{D^0} - m^2_{K^0} = \mu_1^2(0^-) = 3.229 \pm 0.002$$
$$m^2_{D^{0*}} - m^2_{K^{0*}} = \mu_1^2(1^-) = 3.233 \pm 0.008$$

It will be assumed from now on that μ_1^2 is a constant, denoted β, with a value of $\beta = 3.23$. Now the masses of the scalar charmed mesons may be predicted.

$$m^2_{D_0} = m^2_\kappa + \beta$$
$$m^2_{D_0} = 2.25 \mathrm{GeV/c^2}$$

$$m^2_{F_0} = m^2_{D_0} + m^2_{\eta_0^8} - m^2_\kappa = m^2_{\eta_0^8} + \beta$$

The mass of the isoscalar η_0^8 is not known, but it must lie in the range $m_{S^*} \leq m_{\eta_0^8} \leq m_\epsilon$. There is thus a corresponding range in the predicted mass of the F_0.

$$2.05 \text{ GeV/c}^2 \leq m_{F_0} \leq 2.22 \text{ GeV/c}^2$$

The mass given above for the F_0 should not be taken as a precise prediction, as the SU(4) symmetry is known to be badly broken, but rather as an indication of the general order of the mass to be expected. The results of this discussion are summarized in Table 3.3.I.

The scalar form factor will be estimated on the assumption that the mass of the F_0 lies above $D-K$ threshold. As in the case of the vector form factor, there will be constant which cannot be determined from the dispersion relation. From the definition of $f_0(t)$, it may be seen, however, that $f_0(0) = f_+(0)$.

Finally, the scalar form factor is given by:

$$f_0(t) = f_+(0)\frac{m^2_{F_0}}{m^2_{F_0} - t}$$

Table 3.3.I: Charmed Meson Masses

Scalar (predicted)	
D_0	2.25 GeV/c^2
F_0	2.05 – 2.22 GeV/c^2
Pseudoscalar (measured)	
D^0	1.8646 ± 0.0006 GeV/c^2
D^+	1.8693 ± 0.0006 GeV/c^2
F^+	1.9705 ± 0.0025 GeV/c^2
Vector (measured)	
D^{*0}	2.0072 ± 0.0021 GeV/c^2
D^{*+}	2.0101 ± 0.0007 GeV/c^2
F^{*+}	2.110 ± 0.0060 GeV/c^2
Axial-Vector (predicted)	
D_A	2.2 – 2.3 GeV/c^2
F_A	2.2 – 2.3 GeV/c^2

Alternatively, the form factor f_- is predicted to be:

$$f_-(t) = f_+(0)\left(\frac{m_D^2 - m_K^2}{t}\right)\left(\frac{m_{F_0}^2}{m_{F_0}^2 - t} - \frac{m_{F^*}^2}{m_{F^*}^2 - t}\right)$$

A similar approach may be used to predict the behavior of the form factors in the decay $D \to K^* e \nu_e$. As shown in section 3.2, the transition amplitude is:

$$< K^*|V_\mu - A_\mu|D > = ig(t)\epsilon_{\mu\nu\rho\sigma}\epsilon^{*\nu}(P_D + P_{K^*})^\rho(P_D - P_{K^*})^\sigma - f(t)\epsilon_\mu^* \\ - a_+(t)(\epsilon^* \cdot P_D)(P_D + P_{K^*})_\mu - a_-(t)(\epsilon^* \cdot P_D)(P_D - P_{K^*})_\mu$$

The vector part of this amplitude is:

$$\begin{aligned} J_\mu^{(j=1)} &= ig(t)\epsilon_{\mu\nu\rho\sigma}\epsilon^{*\nu}(P_D+P_{K^*})^\rho(P_D-P_{K^*})^\sigma \\ &- f(t)\Big(\epsilon^*_\mu - \Big(\frac{\epsilon^*\cdot P_D}{t}\Big)(P_D-P_{K^*})_\mu\Big) \\ &- a_+(t)(\epsilon^*\cdot P_D)\Big((P_D+P_{K^*})_\mu - \Big(\frac{m_D^2-m_K^2}{t}\Big)(P_D-P_{K^*})_\mu\Big) \end{aligned}$$

After collecting terms proportional to $P_D \pm P_{K^*}$, the vector part of the matrix element is:

$$\begin{aligned} J_\mu^{(j=1)} &= ig(t)\epsilon_{\mu\nu\rho\sigma}\epsilon^{*\nu}(P_D+P_{K^*})^\rho(P_D-P_{K^*})^\sigma - f(t)\epsilon^*_\mu \\ &- a_+(t)(\epsilon^*\cdot P_D)(P_D+P_{K^*})_\mu \\ &+ \Big(\frac{\epsilon^*\cdot P_D}{t}\Big)\big(f(t)+(m_D^2-m_K^2)a_+(t)\big)(P_D-P_{K^*})_\mu\Big) \end{aligned}$$

The scalar part is found by subtracting $J_\mu^{j=0}$ from J_μ:

$$J_\mu^{(j=0)} = -\Big(\frac{\epsilon^*\cdot P_D}{t}\Big)\big(f(t)+(m_D^2-m_K^2)a_+(t)+ta_-(t)\big)(P_D-P_{K^*})_\mu\Big)$$

It is useful to define two new functions:

$$(m_D^2-m_K^2)a_0(t) = f(t)+(m_D^2-m_K^2)a_+(t)+ta_-(t)$$

$$(m_D^2-m_K^2)a_3(t) = f(t)+(m_D^2-m_K^2)a_+(t)$$

With these new definitions:

$$\begin{aligned} J_\mu^{(j=1)} &= ig(t)\epsilon_{\mu\nu\rho\sigma}\epsilon^{*\nu}(P_D+P_{K^*})^\rho(P_D-P_{K^*})^\sigma - f(t)\epsilon^*_\mu \\ &- a_+(t)(\epsilon^*\cdot P_D)(P_D+P_{K^*})_\mu \\ &+ a_3(t)(\epsilon^*\cdot P_D)\Big(\frac{m_D^2-m_K^2}{t}\Big)(P_D-P_{K^*})_\mu\Big) \end{aligned}$$

Consider now the divergence of this amplitude:

$$\begin{aligned} &< K^*|\partial^\mu V_\mu|D> = 0 \\ &< K^*|\partial^\mu A_\mu|D> = -a_0(t)(\epsilon^*\cdot P_D)(m_D^2-m_K^2) \end{aligned}$$

The divergence of an axial-vector is a pseudoscalar, so $a_0(t)$ must be dominated

by the exchange of a pseudoscalar quantum. In this case, there is no ambiguity; the F meson is known to be a charmed, strange pseudoscalar.

The form factor $g(t)$ corresponds to exchange of a vector meson, the F^*. The remaining two form factors, $f(t)$ and $a_+(t)$, will both be dominated by the exchange of axial-vector quanta. These states have not yet been detected, but a prediction like that for the scalar mesons may be made. The only complication is that the mixing of the $Q(1280)$ and $Q(1400)$ introduces an additional uncertainty. The charmed axial-vector mesons will be denoted D_A^0, D_A^+, and F_A^+ with quark content $c\overline{u}$, $c\overline{d}$, and $c\overline{s}$, respectively.

$$m^2_{Q(1280)} + \beta \leq m^2_{D_A} \leq m^2_{Q(1400)} + \beta$$

$$2.2 \text{ GeV/c}^2 \leq m_{D_A} \leq 2.3 \text{ GeV/c}^2$$

$$m^2_{F_A} = m^2_{\eta^8_A} + \beta$$

$$m^2_{D(1285)} + \beta \leq m^2_{F_A} \leq m^2_{E(1420)} + \beta$$

$$2.2 \text{ GeV/c}^2 \leq m_{F_A} \leq 2.3 \text{ GeV/c}^2$$

The form factors for $D \rightarrow K^* \, e \, \nu_e$ are given by the formulae:

$$g(t) = g(0)\frac{m^2_{F^*}}{m^2_{F^*} - t}$$

$$f(t) = f(0)\frac{m^2_{F_A}}{m^2_{F_A} - t}$$

$$a_+(t) = a_+(0)\frac{m^2_{F_A}}{m^2_{F_A} - t}$$

$$a_0(t) = \left(a_+(0) + \frac{f(0)}{m^2_D - m^2_K}\right)\frac{m^2_F}{m^2_F - t}$$

$$a_3(t) = \left(a_+(0) + \frac{f(0)}{m^2_D - m^2_K}\right)\frac{m^2_{F_A}}{m^2_{F_A} - t}$$

Before the task at hand may be considered finished, it is necessary to calculate

the values of the four constants $f_+(0)$, $g(0)$, $f(0)$, and $a_+(0)$. Wirbel, Stech and Bauer[52] base their calculation of these constants on a relativistic harmonic oscillator potential. They describe the initial and final state mesons as relativistic bound states of a quark q_1 and an antiquark q_2. The wavefunctions of these mesons are given by:

$$|\vec{p}, m, j, j_z> = \sqrt{2}(2\pi)^{3/2} \sum_{s1,s2} \int d^3p_1 d^3p_2 \delta^3(\vec{p} - \vec{p}_1 - \vec{p}_2)$$
$$\varphi_m^{j,j_z}(\vec{p}_{1T}, x, s_1, s_2) a_1^{s_1}(\vec{p}_1) b_2^{s_2}(\vec{p}_2)|0>$$

The various notations used are: $\vec{p}$ is the momentum of the meson; x is the fraction of the longitudinal momentum carried by quark q_1, $x \equiv p_{1z}/p$; $\vec{p}_{1T}$ is the transverse momentum vector of quark q_1.

These authors then express the weak hadronic current in terms of creation and annihilation operators. They form the matrix element $< X|j_\mu|D >$ and compare the result with a parameterization for the transition amplitude. (Their parameterization differs slightly from that given above.) In this way they obtain the form factors in terms of the meson wavefunctions. They find, for a pseudoscalar final state, the unknown constant to be:

$$h_1 = h_0 = \int d^2p_T \int_0^1 dx \varphi^*_{m_K}(\vec{p}_T, x) \varphi_{m_D}(\vec{p}_T, x)$$

For the case of a vector meson in the final state:

$$h_{A_0} = h_{A_3} = \int d^2p_T \int_0^1 dx \varphi^{*1,0}_{m_{K^*}}(\vec{p}_T, x) \sigma_z^{(1)} \varphi_{m_D}(\vec{p}_T, x)$$

The operator $\sigma_z^{(1)}$ is a Pauli matrix acting on the spin of the decaying c quark.

$$h_V = \frac{m_c - m_s}{m_D - m_{K^*}} J$$
$$h_{A_1} = \frac{m_c + m_s}{m_D + m_{K^*}} J$$
$$J = \sqrt{2} \int d^2 p_T \int_0^1 \frac{dx}{x} \varphi^{*1,-1}_{m_{K^*}}(\vec{p}_T, x) i\sigma_y^{(1)} \varphi_{m_D}(\vec{p}_T, x)$$

As mentioned above these authors use an eigenstate of a relativistic harmonic oscillator potential for their meson wavefunction. The momentum part of this wavefunction is:

$$\varphi_m(\vec{p}_T, x) = N_m \sqrt{x(1-x)} e^{-p_T^2/2\omega^2} \exp\left(-\frac{m^2}{2\omega^2}\left(x - \frac{1}{2} - \frac{m_{q_1}^2 - m_{q_2}^2}{2m^2}\right)\right)$$

This form contains the parameter ω which determines the average transverse momentum of the quarks within the meson: $< p_T^2 >= \omega^2$. This parameter should be about the same for all mesons as the potential is flavor independent.

The results of Wirbel, Stech and Bauer's calculations* are listed in Table 3.3.II for two different values of the parameter ω.

---

* The parameterization used by Wirbel, Stech, and Bauer differs from that of section 3.2. The two parameterizations are related through the following equations:

$$f_+(t) = F_1(q^2)$$
$$f_0(t) = F_0(q^2)$$

$$f(t) = -i(m_D + m_{K^*}) A_1(q^2)$$
$$a_+(t) = \frac{i}{m_D + m_{K^*}} A_2(q^2)$$
$$a_3(t) = -i\left(\frac{2m_{K^*}}{m_D^2 - m_{K^*}^2}\right) A_3(q^2)$$
$$a_0(t) = -i\left(\frac{2m_{K^*}}{m_D^2 - m_{K^*}^2}\right) A_0(q^2)$$
$$g(t) = \frac{i}{m_D + m_{K^*}} V(q^2)$$

Table 3.3.II: Form Factor Constants à la Wirbel, Stech, and Bauer

Constant	Average p_T	
	$\omega = 0.4$ MeV	$\omega = 0.5$ MeV
$D \to K\, e\, \nu_e$		
$f_+(0)$	0.76	0.82
$D \to K^*\, e\, \nu_e$		
$g(0)$	$0.46i$	$0.56i$
$f(0)$	$-2.43i$	$-2.95i$
$a_+(0)$	$0.42i$	$0.55i$

The constituent quark model was used by Grinstein, Wise and Isgur[49] to calculate the hadronic matrix element directly. They chose non-relativistic wavefunctions which are solutions of Schrödinger's equation with a potential

$$V(r) = -\frac{4\alpha_s}{3r} + c + br$$

The parameters are given the values: $\alpha_s = 0.5$, $c = -0.84$, and $b = 0.18$ GeV^2. The form of the potential above is similar to that of the charmonium model detailed in chapter 1. The first term has the $1/r$ dependence characteristic of the Coulomb potential; it attempts to account for the short range behavior of the strong interaction. The term linear in r provides a potential increasing with distance, corresponding to the confining behavior of the strong interaction at large spatial separations.

The matrix element of the weak current with respect to the non-relativistic wavefunctions is expanded in terms of form factors $\tilde{f}$. It is possible to calculate these $\tilde{f}$ analytically if they multiply terms which are of sufficiently low order in the momenta. The form factors f, which appear in the expansion of the matrix element with respect to the physical states, are taken to equal the non-relativistic form factors at the zero recoil point.

The results of the these calculations are quoted below. A description of the notation is in order. The parameters β_D, β_K and β_{K^*} appear in the meson wavefunctions; they have the values $\beta_D = 0.39$, $\beta_K = 0.34$, and $\beta_{K^*} = 0.30$. The combinations $\beta_{DK}^2 \equiv 1/2(\beta_D^2 + \beta_K^2)$ and $\beta_{DK^*}^2 \equiv 1/2(\beta_D^2 + \beta_{K^*}^2)$ also appear in the formulae. The maximum momentum transfer for a state X is $t_m = (m_D - m_X)^2$. The quark masses appear in the combinations: $\mu_\pm \equiv (m_q^{-1} \pm m_c^{-1})^{-1}$ where q is a u or d quark. Finally, the t-dependence of the form factors is given by the function:

$$F = \left(\frac{\tilde{m}_X}{\tilde{m}_D}\right)^{1/2} \left(\frac{\beta_D \beta_X}{\beta_{DX}}\right)^{3/2} \exp\left[-\left(\frac{m_d^2}{4\tilde{m}_D \tilde{m}_X}\right)\frac{t_m - t}{\beta_{DX}^2}\right]$$

The state X denotes either K or K^*. The masses marked with a *tilde* are the constituent quark model masses: $\tilde{m}_D = m_c + m_q$, $\tilde{m}_K = m_{K^*} = m_s + m_q$.

$$\underline{D \to K\, e\, \nu_e}$$

$$f_+(t) = F(t)\left[1 + \frac{m_c}{2\mu_-} - \frac{m_c m_q}{4\mu_+\mu_-}\frac{m_d}{\tilde{m}_K}\frac{\beta_D^2}{\beta_{DK}^2}\right]$$

$$f_-(t) = F(t)\left[1 - (\tilde{m}_D + \tilde{m}_K)\frac{1}{2m_q} - \frac{1}{4\mu_+}\frac{m_d}{\tilde{m}_K}\frac{\beta_D^2}{\beta_{DK}^2}\right]$$

$$\underline{D \to K^*\, e\, \nu_e}$$

$$f(t) = 2\tilde{m}_D F(t)$$

$$g(t) = \frac{1}{2}F(t)\left[\frac{1}{m_q} - \frac{1}{2\mu_-}\frac{m_d}{\tilde{m}_{K^*}}\frac{\beta_D^2}{\beta_{DK^*}^2}\right]$$

It is not possible to calculate $a_+(t)$. The authors conclude, however, that

$$a_+(t) = O\left(\frac{f}{\tilde{m}_D \tilde{m}_{K^*}}\right)$$

Chapter 4: The MARK III Detector

4.1: An Overview

The MARK III is a general purpose magnetic spectrometer installed in the West interaction of the electron-positron storage ring SPEAR. Although the detector is essentially conventional in design, it differs from detectors used at higher energy facilities in two major ways. First, the amount of structural material was kept to an absolute minimum. At SPEAR, the average momentum of charged tracks is only about 400 - 500 MeV/c. Multiple Coulomb scattering will cause a serious deterioration of the momentum resolution for such low momentum particles unless the amount of material is small. Table 4.1.I summarizes the materials used in the construction of the drift chamber. Second, the MARK III is the first magnetic detector installed at SPEAR with its shower detectors mounted inside the magnet, allowing the reconstruction of many final states which contain a low energy photon or π^0.

Table 4.1.I: Materials in Drift Chamber

Component	Thickness(% of radiation length)
Beam pipe	0.40 %
Layer 1	0.68 %
Inner Wall of Drift chamber	0.16 %
Drift chamber gas	0.75 %
Drift chamber wires	0.15 %
Total	2.14 %

The innermost part of the MARK III is a trigger drift chamber which surrounds the beryllium beam pipe. Immediately outside of the trigger chamber is the main drift chamber. The scintillation counters of the time-of-flight (ToF) system are attached to the outside of the main drift chamber. The barrel shower

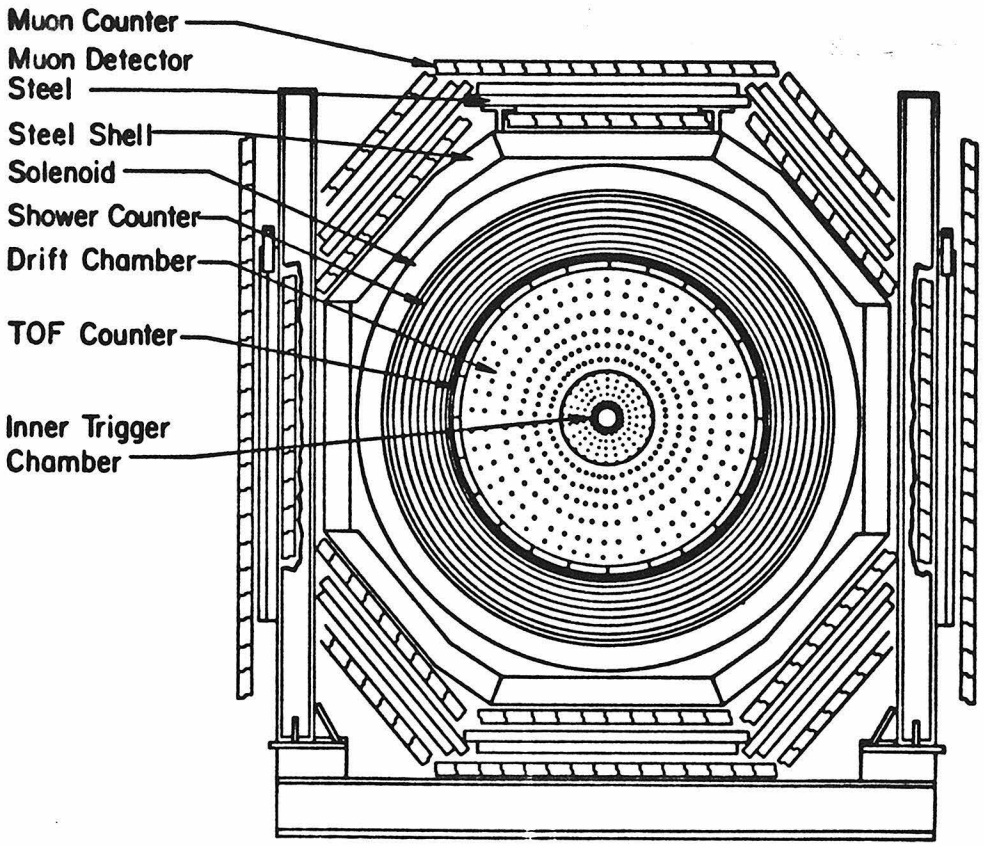

Figure 4.1.1: MARK III detector, front view

detector is installed between the ToF counters and the magnet which produces an axial field of about 0.4 T. The two endcap shower detectors are mounted within the iron flux return parallel to the face of the main drift chamber. Outside of the flux return are two banks of proportional tubes used for the detection of muons. Figs. 4.1.1 and 4.1.2 are drawings of the MARK III from the front and side.

4.2: Trigger Chamber

The MARK III is quite a large detector, so some method is necessary to limit the number of triggers caused by cosmic rays. In previous detectors at SPEAR,

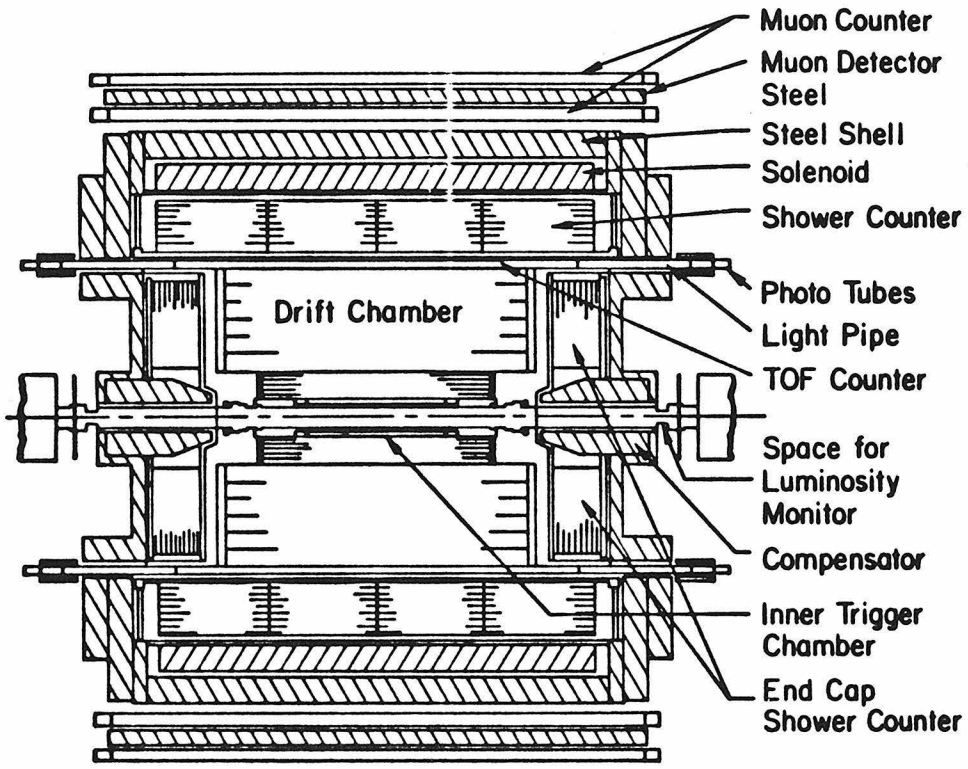

Figure 4.1.2: MARK III detector, side view

scintillation counters were placed around the beam pipe. A signal was required in one of these for the detector to be triggered. The cosmic ray rate was reduced because of the very small area and good time resolution of the counters.

A similar approach was used in the MARK III except that a set of four concentric low-mass cylindrical drift chambers replaced the scintillation counters. An axial view of these chambers is shown in Fig. 4.2.1a. Collectively, the four are called Layer 1. Each chamber is 1.1 m long. The inner radius of the innermost chamber is 9.2 cm and the outer radius of the outermost chamber is 13.7 cm so the thickness of each chamber is 1.1 cm. The cylindrical walls are made of Rohacell foam 2 mm thick, clad on both sides with 0.5 mm of aluminized mylar.

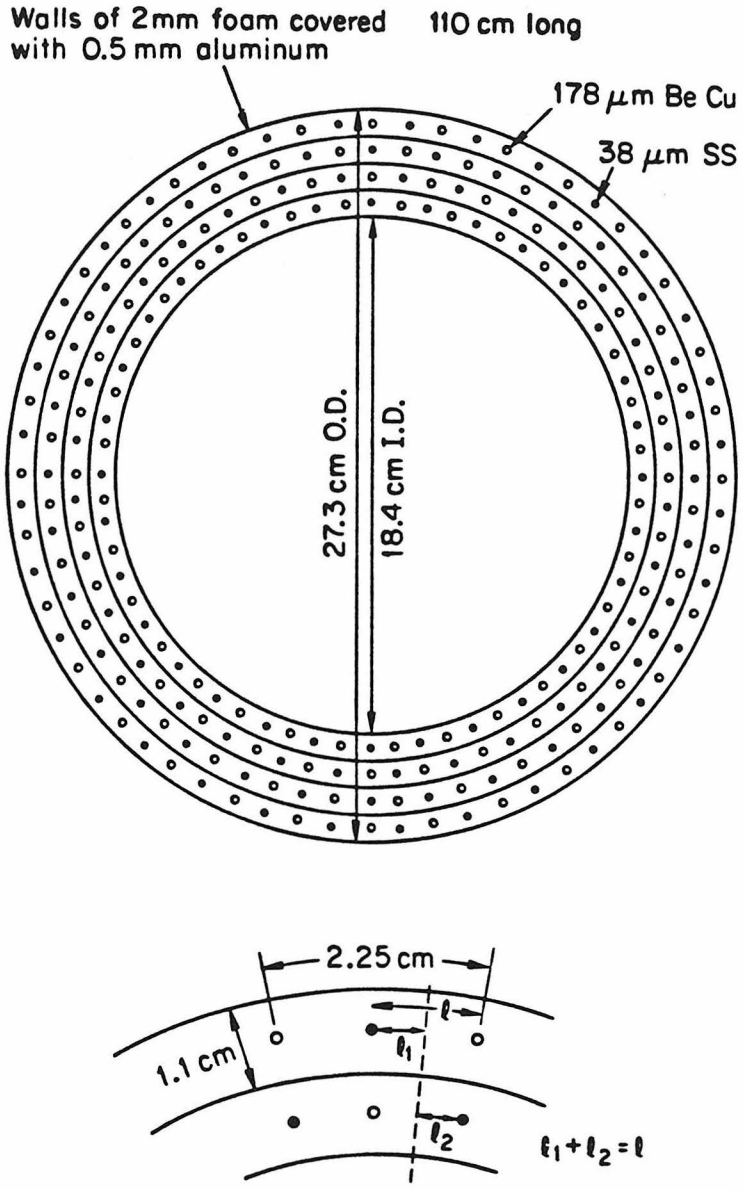

Figure 4.2.1: Layer 1 from front (a), Layer 1 cell structure (b)

Each chamber contains thirty-two cells, the boundaries of which are defined by thirty-two field shaping wires of 178 μm copper-beryllium (CuBe). Centered between each field shaping wire is a sense wire of 38 μm stainless steel (SS). The

sense wires are operated at a voltage of +2175 V, and the field wires at -200 V. The aluminized surfaces of the cylindrical walls are maintained at ground potential.

All four chambers are used for tracking, but only the innermost two are used in the trigger. If the only trigger requirement were a hit in one of these layers, the trigger 'window', during which a hit would have to appear, would have to be at least as wide as the maximum drift time. The spacing between a field wire and its neighboring sense wire is 1.125 cm in the second chamber; this is, of course, slightly different in the other chambers. The velocity at which ionization drifts in the gas — 70% argon and 30% ethane — is about 5 cm/μsec, so the maximum drift time is about 230 nsec. At SPEAR, the beam crossing frequency is 1.28 mHz, so the beams cross every 781 nsec. A gate width of 230 nsec would thus represent a reduction in cosmic ray trigger rate of only about 70%.

This situation may, however, be improved substantially. The chambers in Layer 1 are alternately offset by one-half cell; a sense wire aligns radially with field wires in the adjoining chambers. Tracks so close to the interaction point are all approximately radial, so the sum of the times in adjacent chambers is nearly equal to the maximum drift time. This is illustrated in Fig. 4.2.1b.

The sum of times is accomplished digitally by the use of a bidirectional tapped delay line or *chronotron.*[53] The pulse heights on the sense wires vary widely. To limit the resulting time slewing, the pulses from both ends of each wire are fed to discriminators and the discriminated pulses passed on to an *OR*-gate. The resulting pulses from the nearest sense wires in adjacent chambers are fed into opposite ends of one of the sixty-four Layer 1 chronotrons. The pulses are clocked in opposite directions through the chronotron. A coincidence of the pulses at any tap produces an output pulse. The distribution of chronotron times for hadronic and cosmic ray events is shown in Fig. 4.2.2. The times for hadronic events peak at about 250 nsec as expected while the distribution of times for cosmic ray events is approximately uniform. A window of 100 nsec is used in the trigger. A

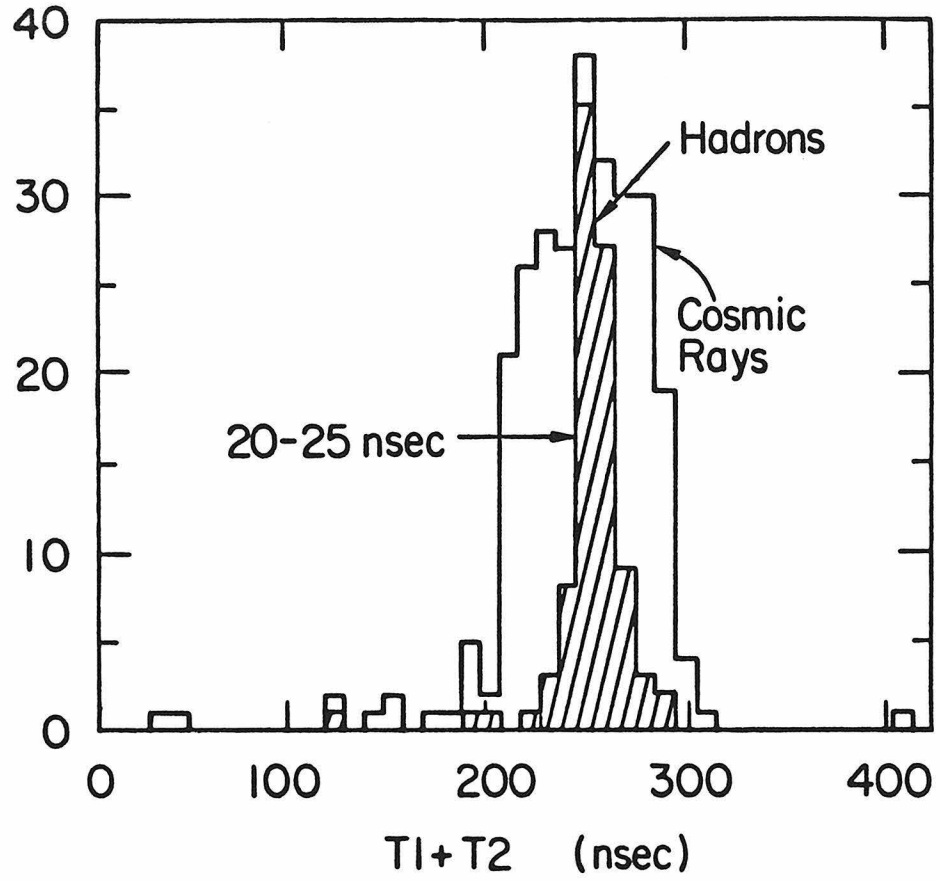

Figure 4.2.2: Layer 1 chronotron times

chronotron pulse must fall within this window to be considered valid. The total reduction in the cosmic ray trigger rate is thus about 87%.

The cells in Layer 1 are relatively large, given the small radius of the chambers, so the electric field is quite non-uniform within the cells. The spatial resolution of the cells is therefore modest, only about 350 μm. The addition of four spatial points close to the interaction point is, however, of considerable use in detecting steeply inclined tracks and in locating secondary vertices.

The stainless steel sense wires of Layer 1 have a resistance about 1.3 KΩ, making possible the use of charge division to determine the z position of hits. This technique is described fully in the following section.

4.3: Main Drift Chamber

The main drift chamber[54] is also cylindrical. The inner wall, of radius 14.47 cm and length 177.8 cm, is a tube of Hexcell, a *honeycomb* of shellacked paper formed into a tube and covered on the inside and outside with phenolic plastic. Such a structure exhibits extraordinary strength in spite of the fact that it is nearly massless. The Hexcell is clad on the inner and outer surfaces with aluminized mylar. The outer wall of the drift chamber consists of curved plates of 6.25 mm thick aluminum. The outer radius of this wall is 114.26 cm and the length is 233.7 cm. The front and back faces of the chamber are made of G-10 fiberglass on aluminum clad Hexcell.

The chamber has an inner and outer section. The inner section — Layer 2 — is as long as the inner Hexcell, making room for the compensating magnets; it extends in radius to 31.45 cm. The remainder of the chamber — Layers 3-8 — is as long as the outer aluminum wall. The difference in length of these two sections is bridged with an aluminum 'top hat'. A drawing of the main drift chamber is given in Fig. 4.3.1.

The thirty-two cells of Layer 2 align radially with the cells of Layer 1. The cells are bounded by two sets of fifteen field shaping wires of 175 μm CuBe. These are spaced 1 cm apart radially. Between these field wires are thirteen 20 μm tungsten sense wires with a guard wire of 57 μm SS at the top and bottom of the cell. The center sense wire is not used. Alternate sense wires are staggered +150 μm or -150 μm azimuthally from the center line of the cell. This aids in resolving the *left-right ambiguity*, as will be described below.

The pulse heights on the twelve instrumented sense wires give twelve measurements of the rate of ionization loss — dE/dx — by a particle passing through Layer 2. In order to accomplish this, this layer is operated at a low gain of about 2×10^4 to prevent saturation. The voltage applied to the field wires must be increased with radius to make up for the increasing cell size. The voltage ranges

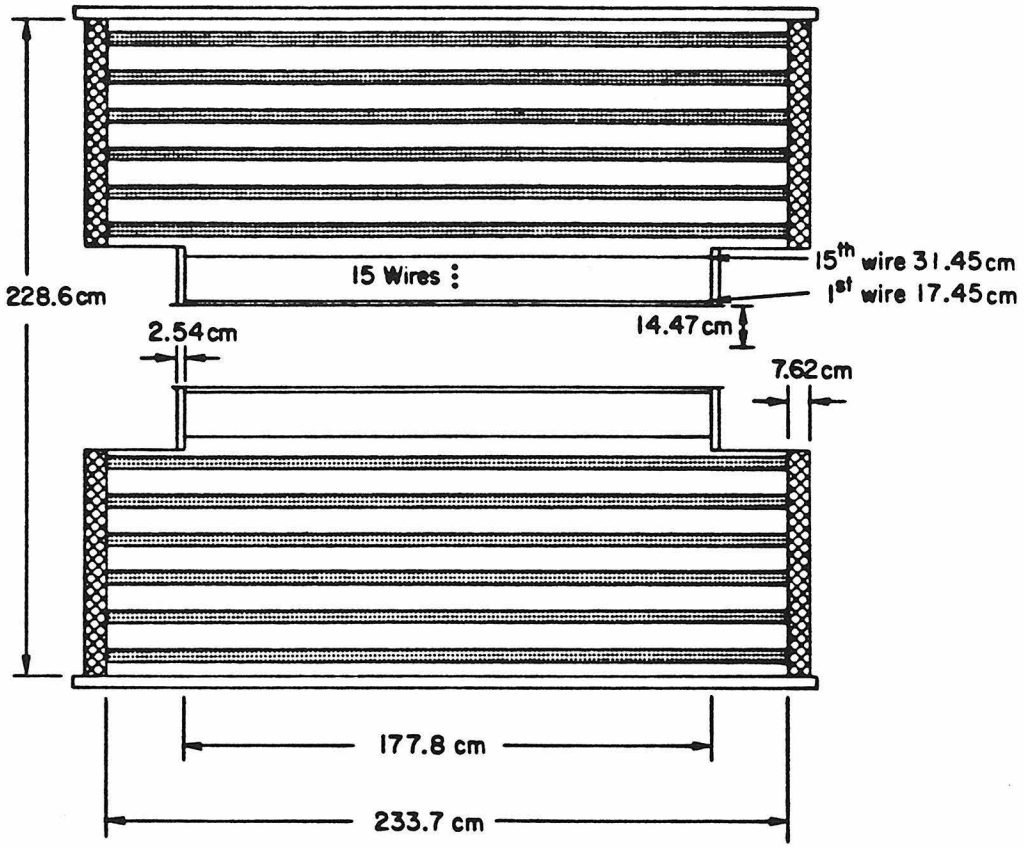

Figure 4.3.1: Main drift chamber, side view

from -3.2 to -4.2 kV. The guard wires are held at ground potential.

The pulses from Layer 2 are extremely small, only about 200 μV. After an initial period of data taking, it was found to be necessary to add preamplifiers to compensate for high frequency pickup on the cables leading from the drift chamber. These are mounted directly on the face of the chamber and provide a gain of about 20.

A further problem with Layer 2 required consideration. The high density of the wires results in considerable capacitive coupling among the sense wires. A pulse on one sense wire often induces a pulse of the opposite polarity on the adjoining sense wires. Resistors were added between all nearest and next-nearest

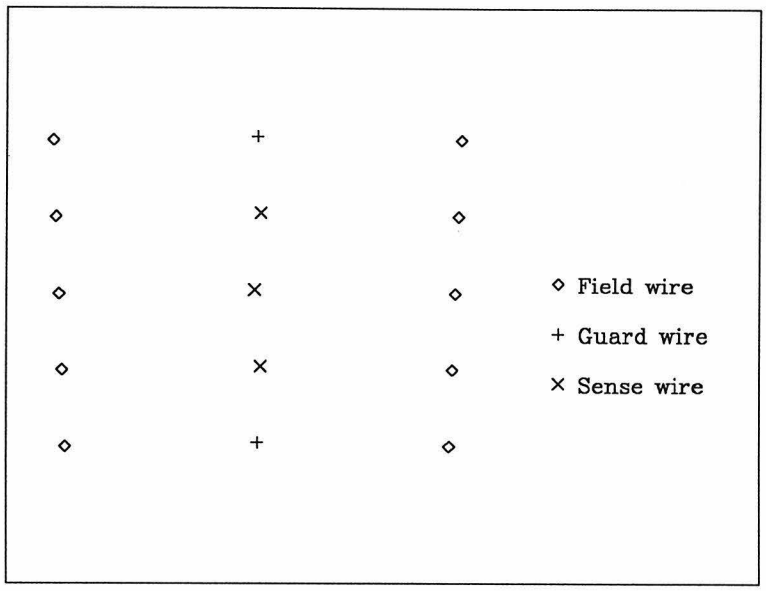

Figure 4.3.2: Main drift chamber cell, layers 3–8

neighbor sense wires to alleviate this problem.

The outer portion of the drift chamber — Layers 3-8 — consists of six concentric rings or *planes* of cells. The positions of the cells were chosen so that the cells are all of the same size throughout Layers 3-8. The number of cells in each layer is equal to sixteen times the number of that layer; there are forty-eight cells in Layer 3. The cell structure is similar to that in Layer 2 except that now there are only five field wires, and three sense wires. The sense wires are staggered by 400 μm in these *triplet* cells. The cell structure is illustrated in Fig. 4.3.2. The field wires are operated at -4.2 kV, the voltage again increasing with radius within the cells. The gain of these cells is about 2×10^5, and the spatial resolution is 250 μm.

The sense wires in Layers 2-8 are staggered to help resolve a common problem of large drift chambers, the so-called *left-right ambiguity* mentioned above. If the sense wires were aligned radially, it would be impossible to decide on the basis of the measured times alone whether a track had passed through the left or the right half of a cell. Separate fits must be performed for each combination of left-right hypotheses. The number of such combinations may be quite large and

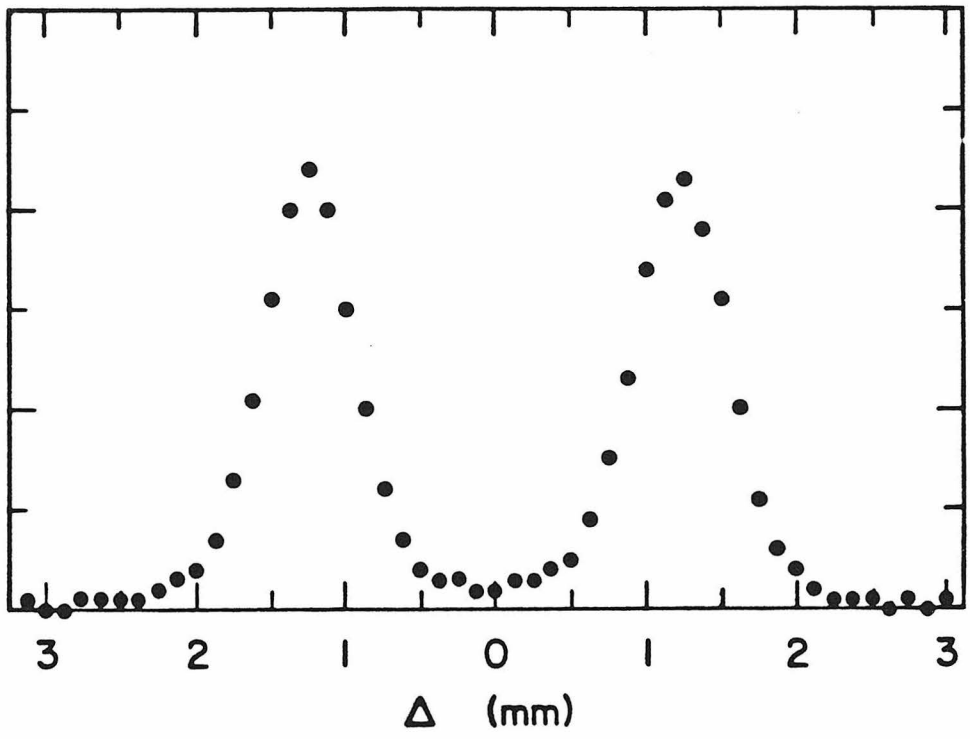

Figure 4.3.3: $\Delta \equiv 1/2(t_1 + t_3) - t_2$

this procedure may absorb an appreciable amount of computer time.

If, on the other hand, the wires are not aligned but staggered, there is a much simpler solution. For each of the triplet cells, the quantity $\Delta \equiv 1/2(t_1+t_3)-t_2$ is formed, where t_i is the time measured for the i^{th} wire. If the wires were perfectly positioned, and electric field perfectly uniform, $|\Delta|$ would equal the wire stagger and the sign of Δ would indicate whether the track passed to the right or left. It is usually possible to resolve the left-right question in this manner. Fig. 4.3.3 presents a histogram of Δ for all cells in Layer 3.

A simple non-iterative quadratic fit is performed for the left side and the right side hypotheses in Layer 2; the decision is made on the basis of the χ^2 value from the fit. An actual track is plotted in Fig. 4.3.4 as it passes through cells in Layers 2, and 3.

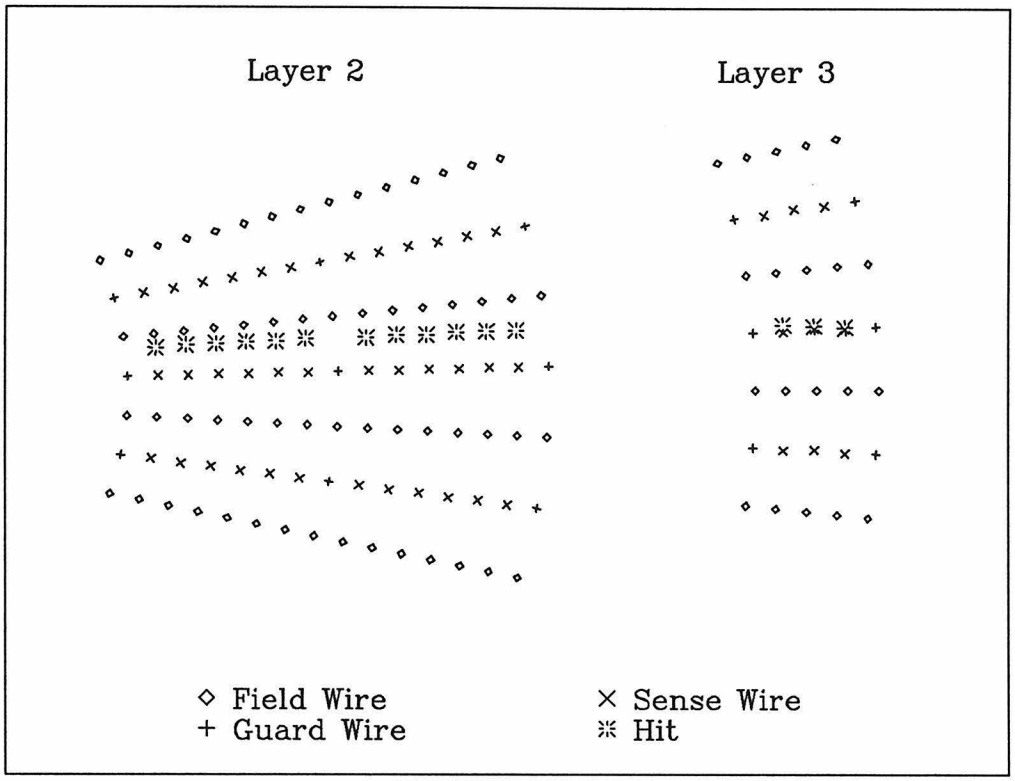

Figure 4.3.4: Track through layers 2 and 3

Two different methods are used for determining the z coordinates of drift chamber hits. Charge division is performed on the highly resistive guard wires in Layer 3, 5, and 7 and the sense wires in Layer 1. The z position is determined by comparing the amount of charge collected at each end of these wires. The relation is:

$$z = \frac{l}{2}\left(\frac{q_2 - q_1}{q_2 + q_1}\right)$$

where l is the length of the wire and q_1 and q_2 are the charges collected at the ends of the wires corresponding to a negative and positive value of z, respectively. Noise pickup and crosstalk make the charge division system rather unreliable. The resolution is at best about 5 cm. For this reason, charge division is seldom used in track fitting.

Two layers — Layers 4 and 6 — of the drift chamber have wires which are

not axial but are strung in small angle stereo, 7.7° for Layer 4 and −9.0° for Layer 6. A much better, if also more involved, procedure uses information from these layers to determine the z position. Since the wires are not axial, the z position of a hit is correlated with its position in the azimuthal angle φ. Timing information from the axial layers is used to determine the trajectory of a particle in the transverse plane. All hits in the stereo layers which are at all close to this trajectory are examined. A full helix fit is attempted for all combinations of cells with consistent timing information. A single stereo layer provides a resolution in the dip angle of about 150 mr. The wide spacing of 27 cm between the stereo layers increases this resolution to about 10 mr if information is present from both Layer 4 and 6.

A helix fit is applied to each track making use of all available information. The momentum resolution is $\sigma_p/p = 1.5\%\sqrt{1+p^2}$, the first term coming from multiple scattering. In spite of the very low mass of the drift chamber, the resolution is still dominated by multiple scattering for momenta below 1 GeV/c.

The small signal electronics of the drift chamber systems, with the exception of the preamplifiers of Layer 2, are housed in a shielded alcove near the detector. Schematic diagrams for Layer 2 and Layers 3-8 are given in Figs. 4.3.5 and 4.3.6. The electronics for Layer 1 are similar to those of Layer 2 except that the preamplifiers are mounted in the alcove and are made of discrete components.

The discriminators are based on the MVL 100 integrated circuit of LeCroy Research Systems, which contains an amplifier with a gain of 100 and a discriminator circuit with a differential output. The threshold is set by an external control voltage.

Discrete amplifiers are used for the charge division signals and for the pulse height measurements on the sense wires of Layer 2. As both timing and pulse height information is extracted from the sense wires of Layers 1 and 2, a splitter circuit is used to isolate the inputs of their discriminators and amplifiers.

The precise time at which a beam crossing occurs is obtained by an electrode

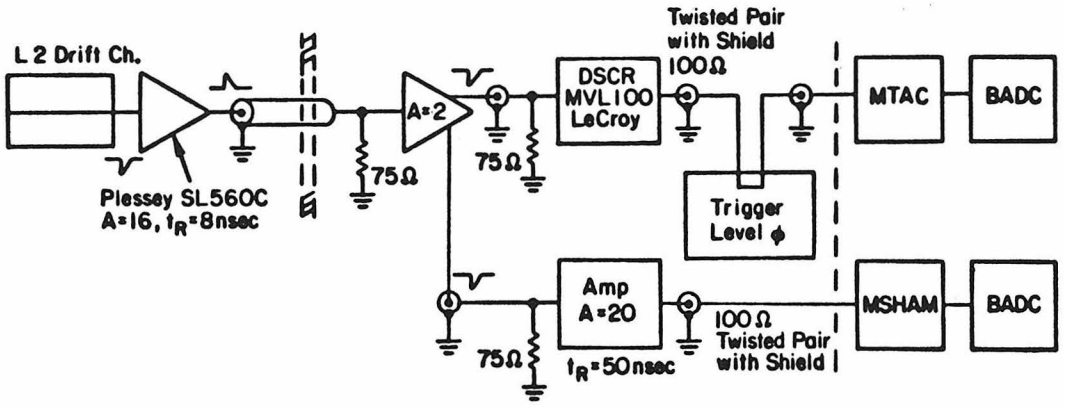

Figure 4.3.5: Electronics for Layer 2

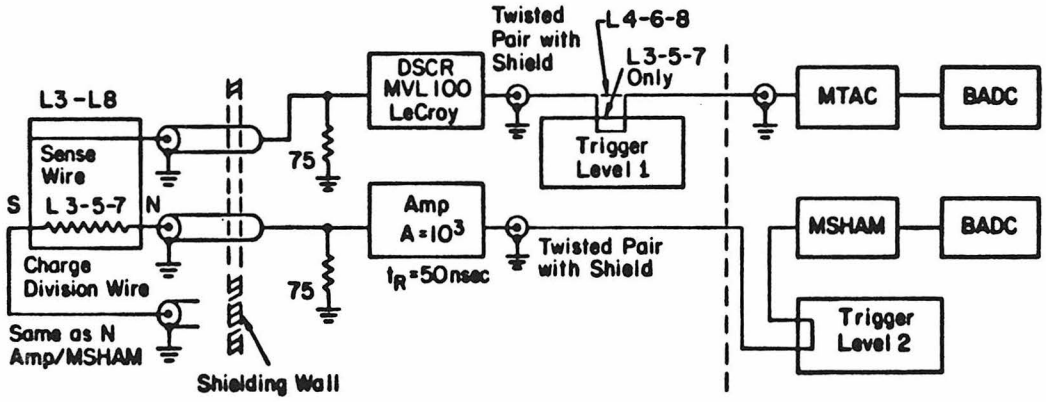

Figure 4.3.6: Electronics for Layer 3–8

inside the beam pipe. A sophisticated discriminator[55] which provides stable timing regardless of the magnitude of the input signal, is used to derive a common start signal for much of the electronics. The time variation is less than 80 psec as the beam current varies by a factor of 20. This signal initiates a voltage ramp in the multihit time-to-analog converters or MTAC's.[56] This ramp is applied to a group of storage capacitors. If a signal from one of the discriminators arrives,

the corresponding capacitor is isolated from the ramp by a FET switch. The voltage on this capacitor is then related to the time between the beam crossing and the arrival of ionization at a sense wire. In principle, an MTAC can measure up to four times for each sense wire. In practice, however, only the first is used.

The charge division and dE/dx signals are obtained by integrating the signals from the guard wires of Layers 1, 3, 5 and 7 and the sense wires of Layer 2. This is accomplished by a multihit sample-and-hold amplifier and multiplexer or MSHAM.[57] The integration gate width is 1 μsec. As before, only the first 'time bucket' is used.

The information from the MSHAM's and MTAC's are digitized by semiautonomous multichannel analog-to-digital converters or BADC's.[58] These are based on AMD 2901 bit-slice microprocessors and Datel EH12B3 ADC's. These modules perform pedestal subtractions and other simple corrections on the data before they are read out via a VAX CAMAC channel[59] into the online computer, a VAX 11/780.

4.4: Time of Flight System

An advantage of the low average momenta of particles produced at SPEAR is the possibility of the identification of these particles by their time-of-flight.[60] To this end, a series of forty-eight scintillation counters are mounted on the outer surface of the main drift chamber with steel bands. The counters are 3.2 m long and 5 cm thick. To reduce the gaps which would otherwise result, the counters are not rectangular but slightly trapezoidal in cross section. The average width of the counters is 15.6 cm. The scintillating material chosen is Nuclear Enterprises Pilot F.

Light is extracted from both ends of the scintillators with Lucite light pipes, which are tapered to 7.5 cm in order to pass through holes in the iron flux return. A second, faster taper in the shape of a cone is made at the phototube. Fig. 4.4.1

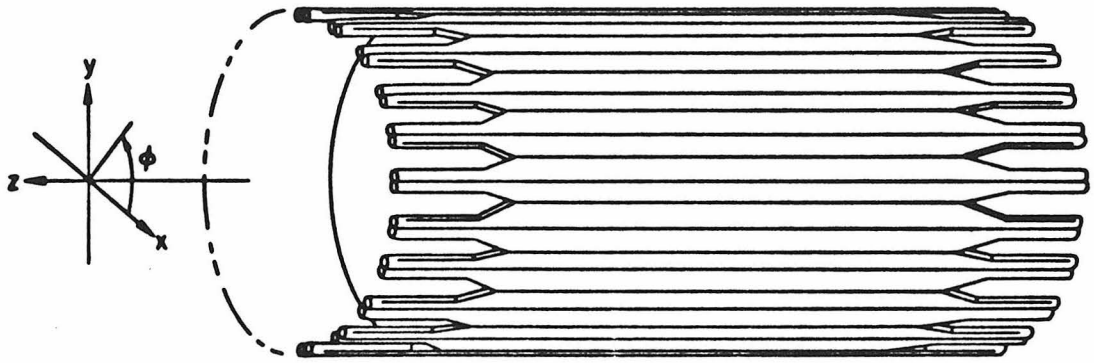

Figure 4.4.1: Orientation of scintillators and light pipes

illustrates the arrangement of scintillators and light pipes. The phototube used is the Amperex XP2020, chosen for its small transit time variations across the surface of the photocathode.

The timing resolution of the ToF system is very good. For Bhabha events, the resolution is 171 psec, whereas for hadronic events it is 189 psec. That the resolution is slightly worse for hadronic events is probably due to the possibility of inelastic interactions within the scintillators.

The ToF system's ability to separate electrons from pions may easily be predicted. The time-of-flight of a particle of mass m and momentum p is $t = l\sqrt{m^2+p^2}/p$ where l is the length of the path traversed. The difference in the times-of-flight of an electron and pion of equal momenta is then:

$$t_\pi - t_e = \frac{l}{p}\left(\sqrt{m_\pi^2+p^2} - \sqrt{m_e^2+p^2}\right)$$

For a helix of radius ρ and pitch λ, the length of a path from the interaction point to the ToF counters is:

$$l = \frac{2\rho}{\cos\lambda}\arcsin\left(\frac{R_{ToF}}{2\rho}\right)$$

The inner radius of the ToF system, R_{ToF}, is 1.14 m. Finally, the radius of the helix is:

$$\rho = \frac{p \cos \lambda}{2.998 \times 10^{-2} B}$$

The magnitude of the field strength, B, is measured in kG, the momentum in GeV/c and the radius in m. The formulae are evaluated in Figs. 4.4.2 and 4.4.3 from the $\pi - e$ and the $K - \pi$ time differences. These figures show that 2σ separation of electrons and pions is possible up to 300 MeV/c and 2σ separation of kaons and pions up to 1 GeV/c.

The performance of the ToF system meets these predictions. Fig. 4.4.4 shows values of momenta, as measured in the drift chamber, versus the corresponding velocities, as measured by the ToF system. The bands from pions, kaons, and protons are clearly visible.

For the purposes of analysis, the measured times-of-flight are converted into a weight: the probability that a given time corresponds to a particular particle mass. The weights are defined by the relation:

$$W = \exp\left(-\frac{(t_{measured} - t_{predicted})^2}{\sigma^2_{ToF}}\right)$$

The weight is calculated from the measured momentum, path length and time-of-flight for a number of particle hypotheses.

Three separate signals are provided by each phototube. A timing signal is produced by the last dynode. Such signals from each end of a scintillator are fed into opposite ends of a chronotron. This yields a trigger signal, whose time is independent of the z position of a hit within the scintillator.

The time and the pulse height of the signal from the phototube's anode are measured in a special device called a DISCO.[61] This consists of a dual threshold discriminator, a time-to-analog converter, and a sample-and-hold amplifier. The discriminator produces an output pulse when the input exceeds each of two

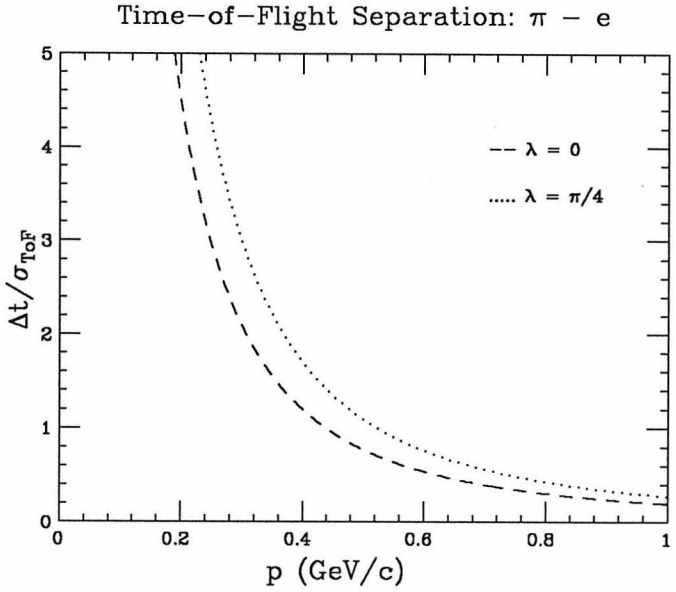

Figure 4.4.2: Predicted $\pi - e$ separation from ToF system

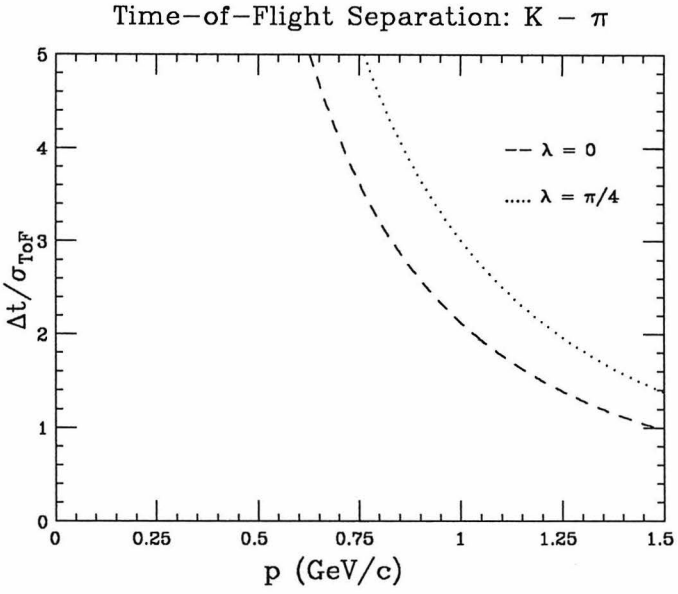

Figure 4.4.3: Predicted $K - \pi$ separation from ToF system

thresholds. It was hoped that this would reduce time slewing, but it proved to be of little use. For this reason, only the lower threshold is used. The time-to-analog converter is similar to that in the MTAC module except that the ramp *downward* is initiated by a pulse from the discriminator. The ramp is halted by a common

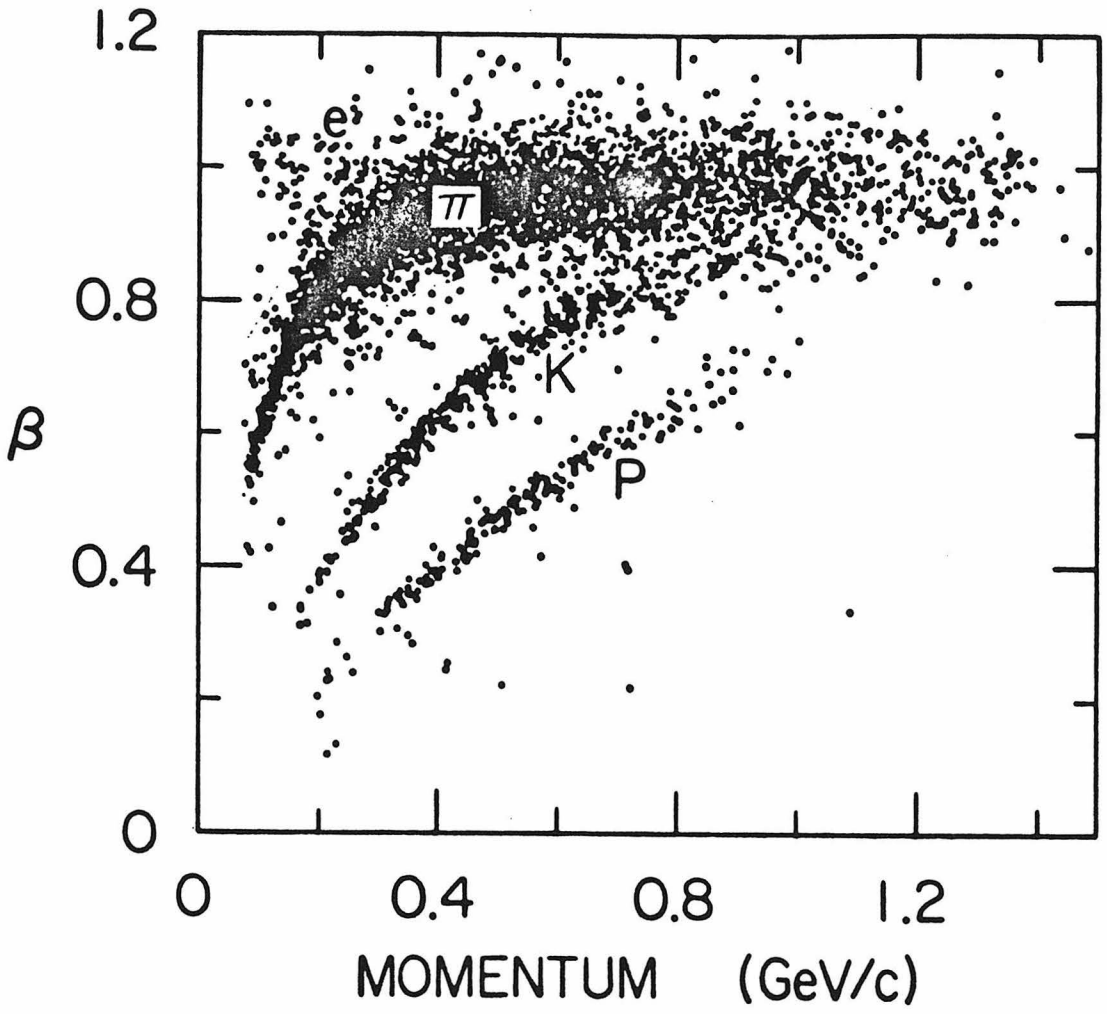

Figure 4.4.4: Momentum versus velocity

stop derived from the beam crossing signal.

The magnitude of the anode signal is related to the ionization loss in the scintillator. As explained above, the counters are 5 cm thick, which corresponds to 12% of one radiation length. Since the counters are not thin, the distribution of pulse heights should be given approximately by a Landau distribution. A histogram of ToF pulse heights for Bhabha events is given in Fig. 4.4.6, the momenta of which are plotted in Fig. 4.4.5. The solid curve in Fig. 4.4.6 is the result of a fit to the Landau function:

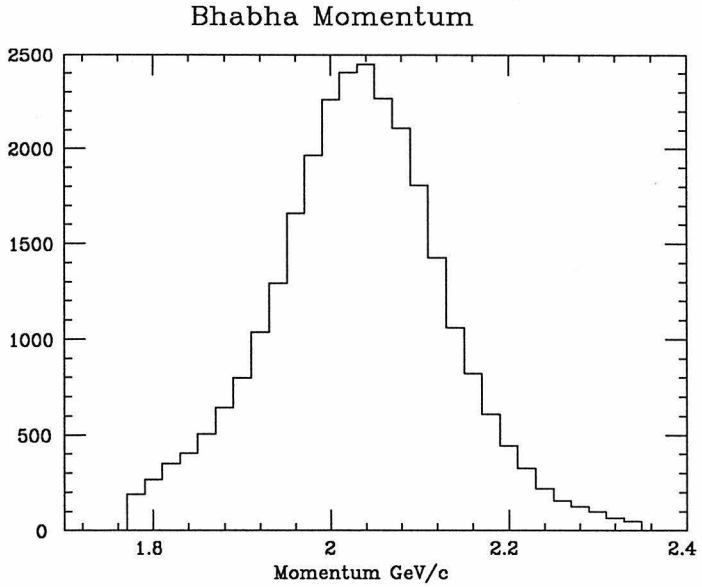

Figure 4.4.5: Momenta of Bhabha events at $\sqrt{S} = 4.14$ GeV

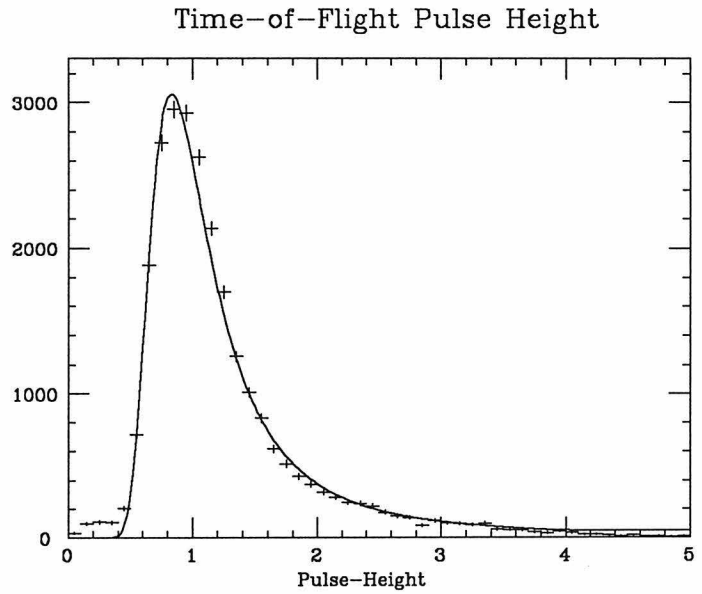

Figure 4.4.6: Pulse height from ToF counters for Bhabha events

$$\phi(\lambda) = \frac{1}{\pi} \int_0^\infty e^{-\frac{1}{2}y\pi} \cos(y\lambda + y \log y) dy$$

The parameter λ is linearly related to the pulse height.

4.5: Shower Detectors

The shower detection system has three major component parts: a barrel detector[62] and two endcap detectors.[63] The barrel shower detector is mounted within the aperture of the magnet and just outside of the ToF counters. It is assembled around an aluminum support spool 1.26 m in radius, 3.85 m long and 2.3 cm thick. The instrument consists of twenty-four layers of proportional cells — 320 axially oriented cells per layer. The cells are formed from aluminum 'I-beams'. A sense wire of 46 μm SS is drawn through the center of each cell. The layers are separated by twenty-three cylinders of radiator, this being composed of an alloy of 6% antimony and 94% lead reinforced on both sides with 0.064 cm of aluminum. The radiator is 0.28 cm thick which corresponds to one-half of one radiation length. The considerable weight of the sheets of radiator is supported by five aluminum ribs. Finally, the detector is suspended from its spool by twenty-four bolts attached to the magnet iron. A drawing of the detector is given in Fig. 4.5.1.

The two endcap detectors consist of five units each: two "D's" on either side of the beam pipe, two "keyway" detectors below and one "tombstone" detector above the beam pipe. The D's and the tombstone are mounted on a removable iron door which is part of the magnet flux return. The keyway detectors fit snugly behind and below the compensating magnets and are not easily removed. Each unit is identical in structure. Twenty-four layers of proportional cells are interspersed among twenty-four sheets of radiator. The cells are formed from rectangular aluminum tubes which are oriented vertically. The construction of the endcaps is illustrated in Fig. 4.5.2.

Charge division is used in the shower detectors to obtain the position of a shower along each wire; this is the z coordinate for the barrel and the y coordinate for the endcaps. The resolutions obtained are 0.8% of the wire length for the barrel and 1.0% for the endcaps. The resolution transverse to the wire direction

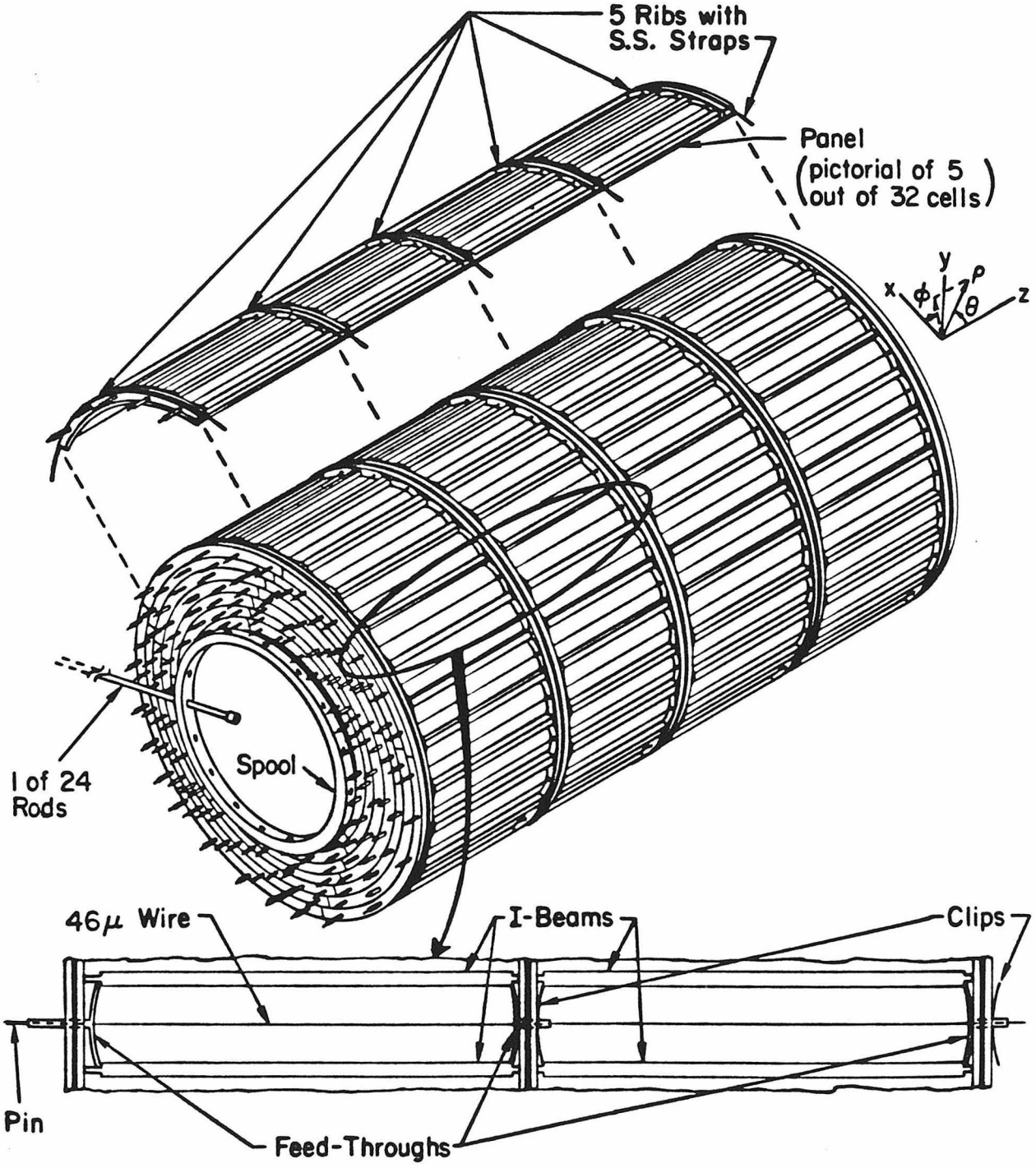

Figure 4.5.1: Barrel shower detector

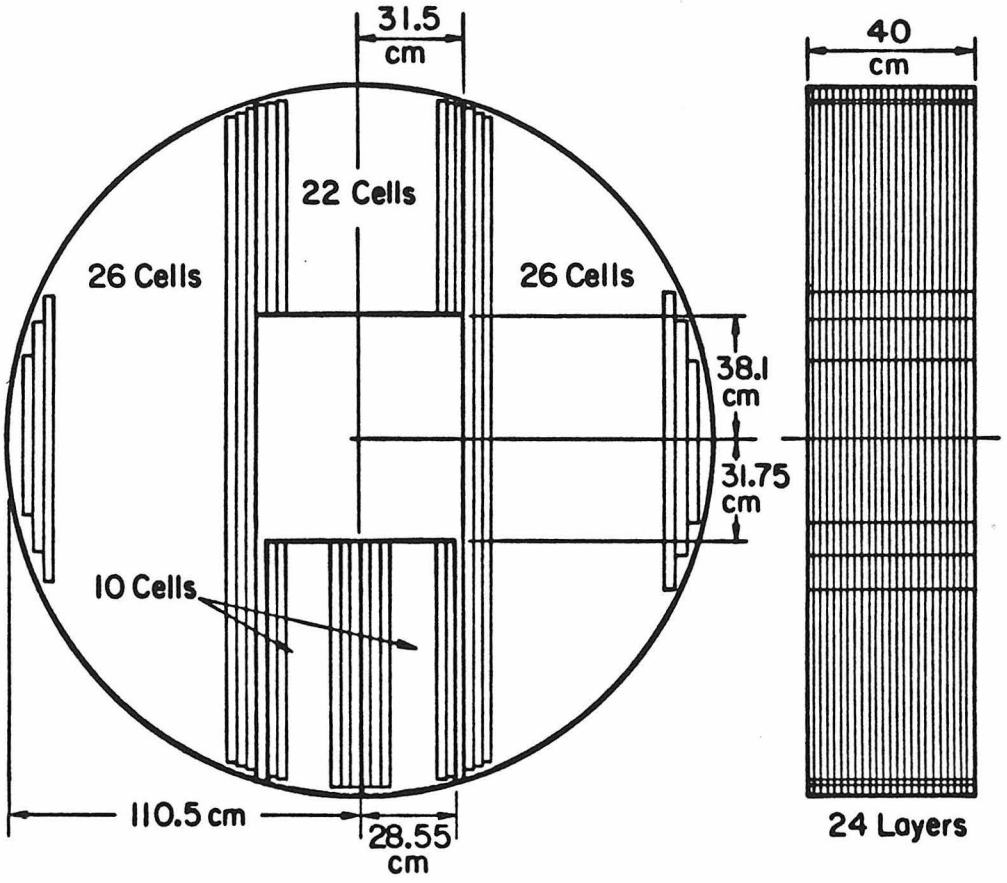

Figure 4.5.2: Endcap shower detector

is much better: $\sigma_\varphi = 7$ mr for the barrel and $\sigma_x = 7$ mm for the endcaps. The wires in the first six layers are read out separately, whereas the remaining eighteen layers are readout in groups of three.

The energy resolution of the shower detectors is modest. For the barrel, the resolution is approximately $\sigma_E/E = 17.5\%/\sqrt{E}(\text{GeV})$, while for the endcap the resolution is slightly better $\sigma_E/E = 17.0\%/\sqrt{E}(\text{GeV})$. Fig. 4.3.3 shows the value of the energy obtained in the shower counter divided by the momentum as measured in the drift chamber for Bhabha events. The effect of the support ribs is clearly seen.

The efficiency of the shower detectors for detecting low energy photons has

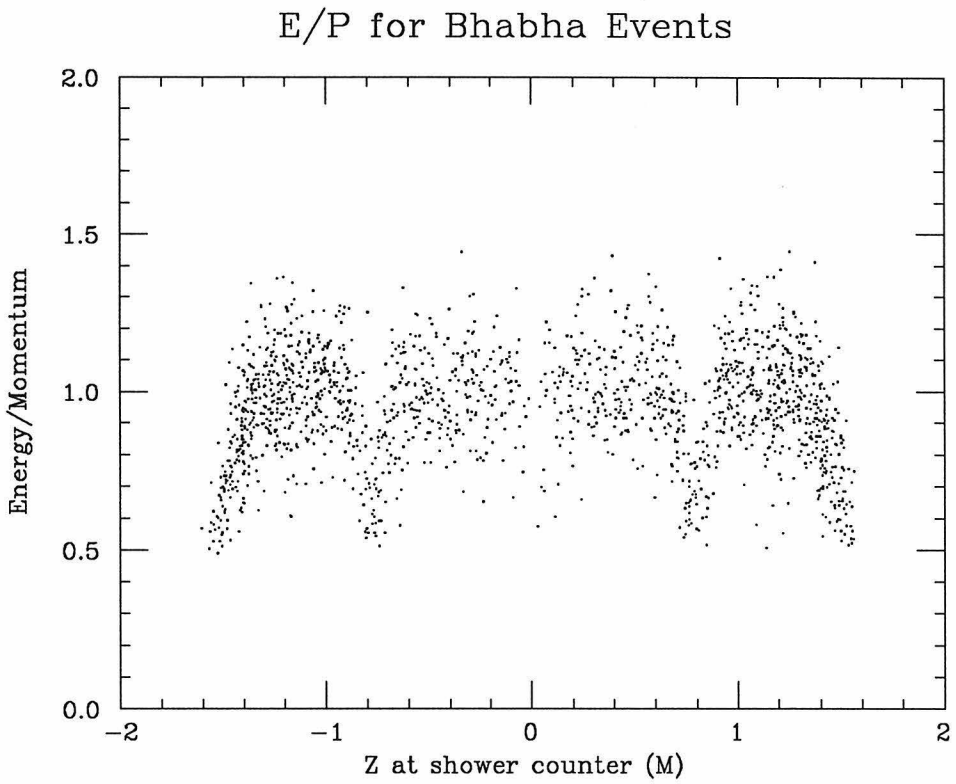

Figure 4.5.3: Energy / momentum for Bhabha events at $\sqrt{S} = 4.14$ GeV

been studied by using the large number of events available from the decay $J/\psi \rightarrow \rho^0\pi^0$. The energies of the photons from the decay of the π^0 are uniformly distributed. Any deviation from uniformity in the observed distribution indicates an inefficiency. The result of this study is given in Fig. 4.5.4. The response of the detectors is obviously quite uniform; they are completely efficient down to incident energies of 100 MeV. At 50 MeV, the efficiency falls to 75%.

4.6: Magnet

There are three magnets in the MARK III detector: the main solenoid and two compensating magnets. The main solenoid is a conventional magnet wound on an aluminum spool 2.24 cm thick of inner radius 1.715 m. The four layers of windings are composed of aluminum conductor, 5 cm by 5 cm in cross section

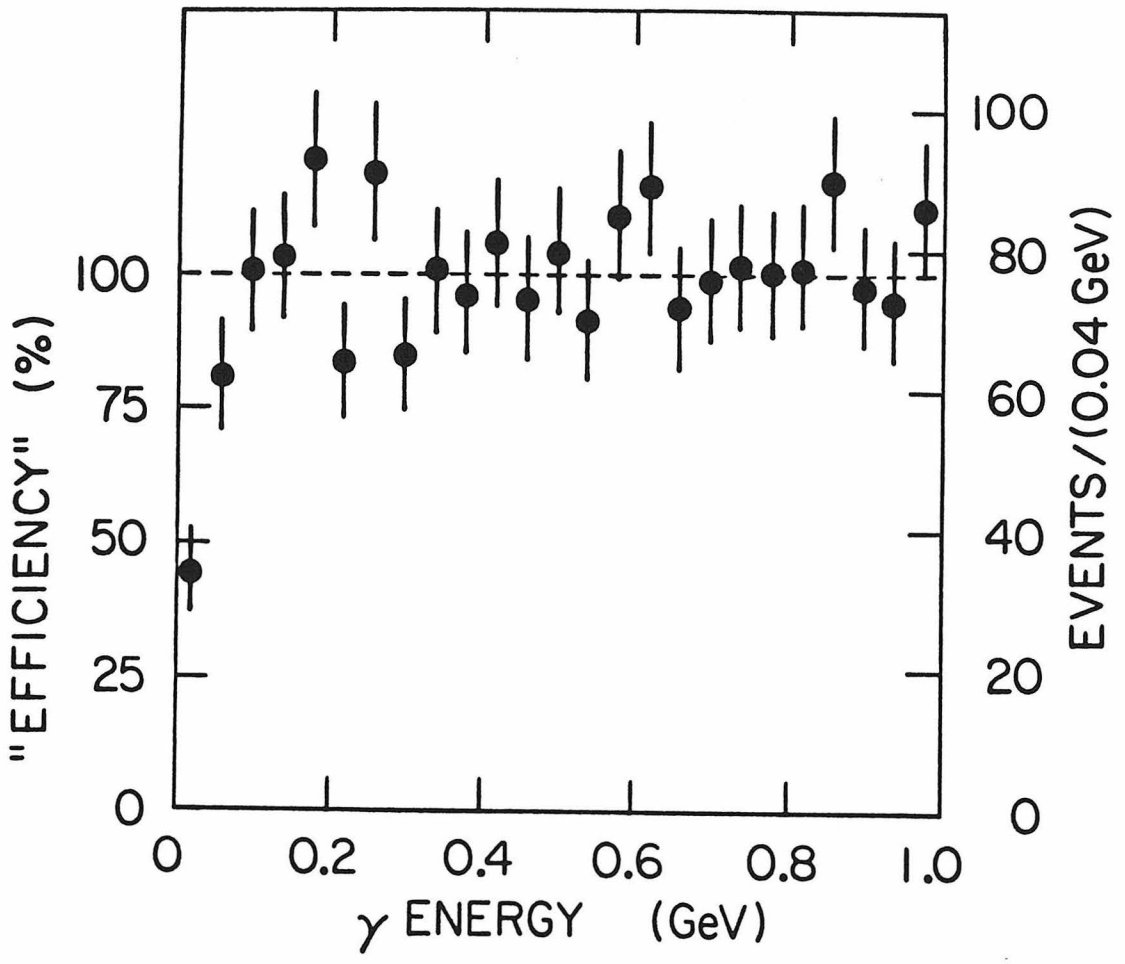

Figure 4.5.4: Shower detector efficiency

with a hole in the center 2.5 cm in diameter to accommodate the flow of cooling water. The solenoid produces a field of 0.4 T at the center of the detector and dissipates about 1 MW of heat.

An axial magnetic field placed in a storage ring has the unfortunate effect of coupling the horizontal and vertical betatron oscillations. This situation may be corrected through the use of rotated quadrupole magnets or of compensating magnets; the latter are small solenoidal magnets placed symmetrically at both ends of the larger solenoid. The strength and direction of the fields of the

compensating magnets are chosen to make the line integral of the magnetic field vanish along the direction of the beam as it passes through all three magnets. The compensating magnets surround the beam pipe and are mounted just outside Layer 2 of the main drift chamber. They have the same number of windings as the main solenoid and are operated in series with it.

Before the installation of the drift chambers and shower detectors, the magnetic field was 'mapped'. A series of measurements were made at a large number of locations within the volume of the magnet. The measuring device was a pair of orthogonal Hall effect magnetometers. These measured the strength of the field in the radial and axial directions simultaneously.

In order to reconstruct the trajectories of charged tracks, it is desirable to have an analytic function which accurately reproduces the behavior of the field.[64] The natural coordinate system of the magnetic field is the system in which it has maximal symmetry. This will be denoted everywhere by a superscript E. In this system, the field will be expanded in a series of polynomials. The coordinate system in which the field was measured will be denoted by a superscript M.

Let $\vec{x}^M$ be the position of a point p in the M system and $\vec{x}^E$ its position in the E system. These are linearly related: $\vec{x}^M = \mathcal{R}(\vec{x}^E - \vec{\Delta})$. $\mathcal{R}$ is a three dimensional rotation matrix and $\vec{\Delta}$ is the vector from the origin of E to the origin of M. Similarly, the fields are also related: $\vec{B}^M(\vec{x}^M) = \mathcal{R}\vec{B}^E(\mathcal{R}^{\mathrm{T}}\vec{x}^m + \vec{\Delta})$. The M and E systems are thus related by six parameters: three rotations and three translations.

The field in the E system is expanded in terms of nine polynomials.[65] Only the radial — ρ — and the axial — z — components are given. The azimuthal component is assumed to be identically zero in this system. The first seven polynomials describe the field of the main solenoid and the last two describe that of the two compensating magnets. The parameters λ_1 and λ_2 are the z positions of the two compensators.

$$p_{\rho 1} = 0$$

$$p_{\rho 2} = -\rho$$

$$p_{\rho 3} = -3z\rho$$

$$p_{\rho 4} = -6z^2\rho + \frac{3}{2}\rho^3$$

$$p_{\rho 5} = -10z^3\rho + \frac{15}{2}z\rho^3$$

$$p_{\rho 6} = -15z^4\rho + \frac{45}{2}z^2\rho^3 - \frac{15}{8}\rho^5$$

$$p_{\rho 7} = -21z^5\rho + \frac{105}{2}z^3\rho^3 - \frac{105}{8}z\rho^5$$

$$p_{\rho 8} = \frac{3\rho(z+\lambda_1)}{((z+\lambda_1)^2+\rho^2)^{5/2}}$$

$$p_{\rho 9} = \frac{3\rho(z-\lambda_2)}{((z-\lambda_2)^2+\rho^2)^{5/2}}$$

$$p_{z1} = 1$$

$$p_{z2} = 2z$$

$$p_{z3} = 3z^2 - \frac{3}{2}\rho^2$$

$$p_{z4} = 4z^3 - 6z\rho^2$$

$$p_{z5} = 5z^4 - 15z^2\rho^2 + \frac{15}{8}\rho^4$$

$$p_{z6} = 6z^5 - 30z^3\rho^2 + \frac{45}{4}z\rho^4 - \frac{15}{8}\rho^5$$

$$p_{z7} = 7z^6 - \frac{105}{2}z^4\rho^2 + \frac{315}{8}z^2\rho^4 - \frac{35}{16}\rho^6$$

$$p_{z8} = -\frac{\rho^2 - 2(z+\lambda_1)^2}{((z+\lambda_1)^2+\rho^2)^{5/2}}$$

$$p_{z9} = -\frac{\rho^2 - 2(z-\lambda_2)^2}{((z-\lambda_2)^2+\rho^2)^{5/2}}$$

The values of all the parameters are obtained from a least squares fit to the measured field values. The results of the fit are given in Table 4.6.I. It should be noted that the parameters relating the M and E systems are all very small

and the series of expansion coefficients A_1 and A_7 converges very quickly. The behavior of the field in the ρ, φ, and z directions is illustrated in Figs. 4.6.1 – 4.6.3.

Table 4.6.I: Magnetic Field Parameters

Parameter	Value
Rotations (radians)	
ϑ_1	-1.16×10^{-3}
ϑ_2	2.64×10^{-4}
ϑ_3	4.36×10^{-6}
Translations (millimeters)	
Δ_x	1.09
Δ_y	-1.25
Δ_z	-1.80
Compensator positions (meters)	
λ_1	1.68
λ_2	1.69
Expansion coefficients (Gauss)	
A_1	4,052
A_2	7.63
A_3	-523
A_4	-0.173
A_5	6.02
A_6	0.00129
A_7	0.0519
A_8	-57.0
A_9	-57.8

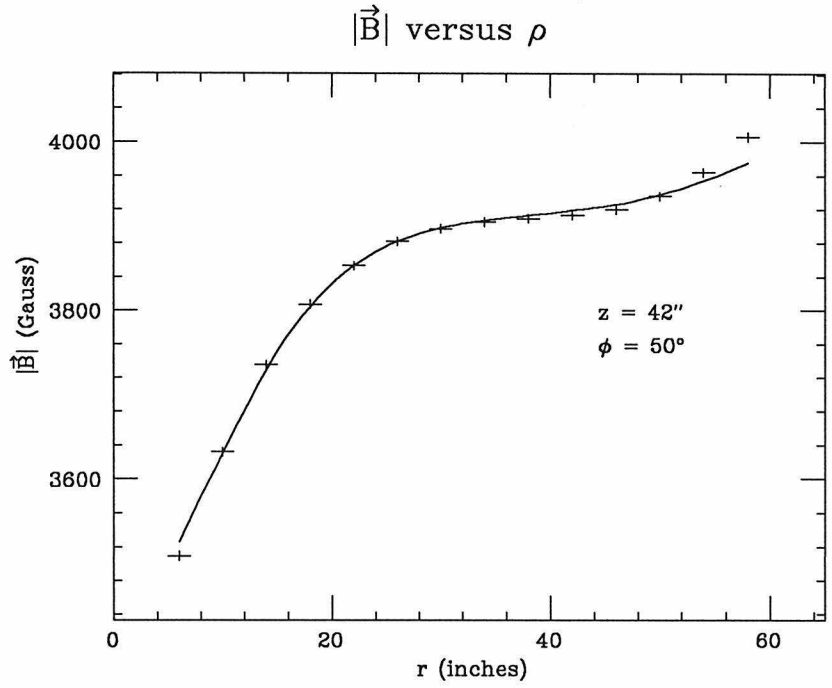

Figure 4.6.1: Magnetic field strength as a function of ρ

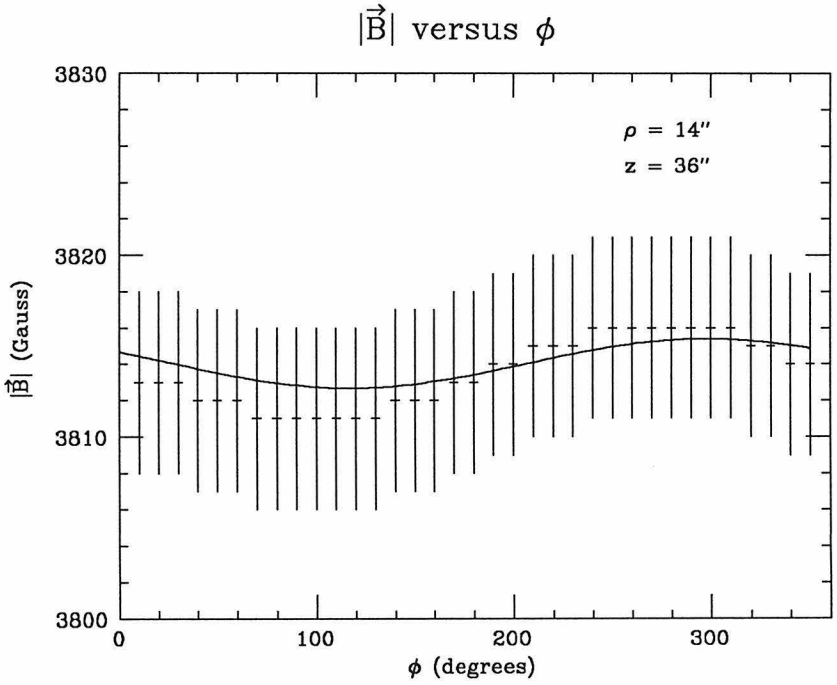

Figure 4.6.2: Magnetic field strength as a function of φ

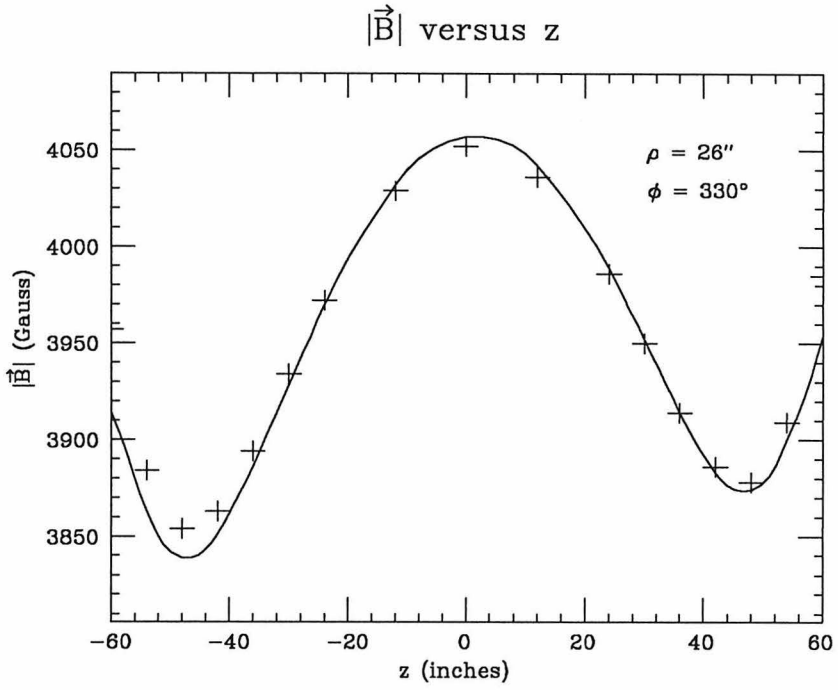

Figure 4.6.3: Magnetic field strength as a function of z

4.7: Muon System

The muon detection system consists of two banks of proportional tubes, located outside of the flux return, separated by 13 cm of steel. The proportional tubes are 2.5 cm in radius and 4.2 m long. They are arranged in an overlapping fashion in groups of eight. The azimuthal resolution of the system is 9 mm. Charge division is used to locate hits along the axis of the tubes. The resolution for this is 6 cm. A drawing of one muon tube assembly is given in Fig. 4.7.1.

The muon system is almost perfectly efficient for detecting muons with transverse momenta greater than about 700 MeV/c. Below this value, the momentum acceptance falls rapidly, dropping to zero below 600 MeV/c. The muon system is thus most useful for locating pairs of muons and for rejecting cosmic rays.

Pions and kaons which decay in flight or which manage to 'punch through' the flux return may produce a signal in the muon system. The probability for this to happen has been measured using events of the type $J/\psi \rightarrow \rho\pi$ and

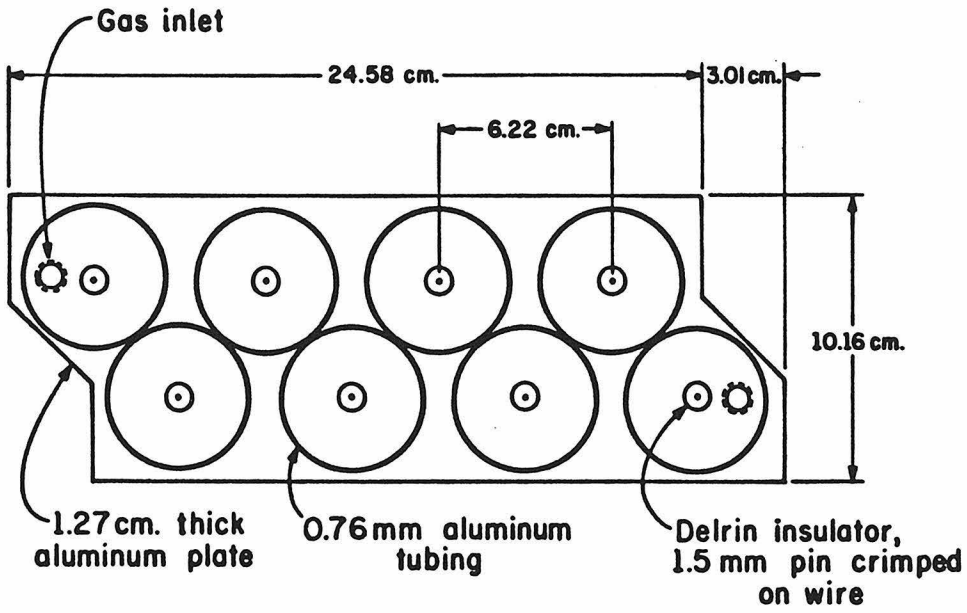

Figure 4.7.1: Muon tube assembly

$J/\psi \rightarrow K^*(892)K$. These events may be isolated easily through kinematic fitting. The probabilities are shown in Fig. 4.7.2 and 4.7.3 for pions and kaons, respectively.

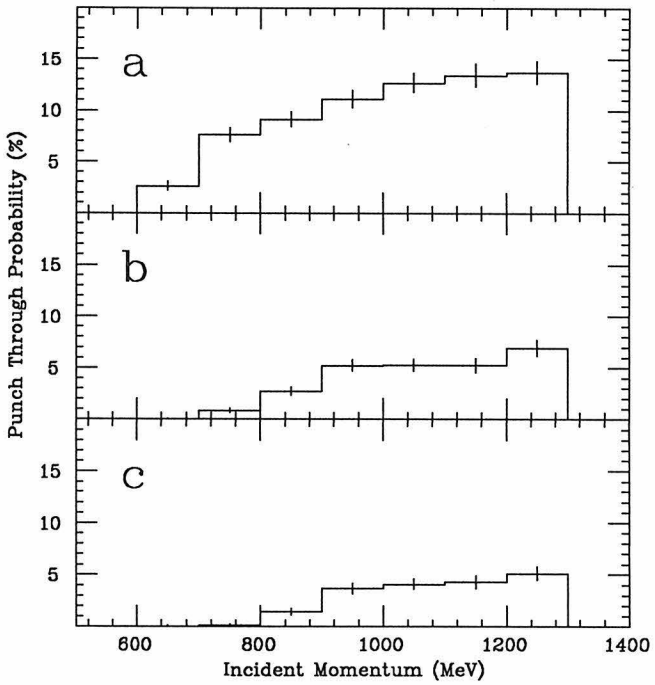

Figure 4.7.2: π punch through probability: Layer 1 (a), Layer 2(b), Layers 1&2(c)

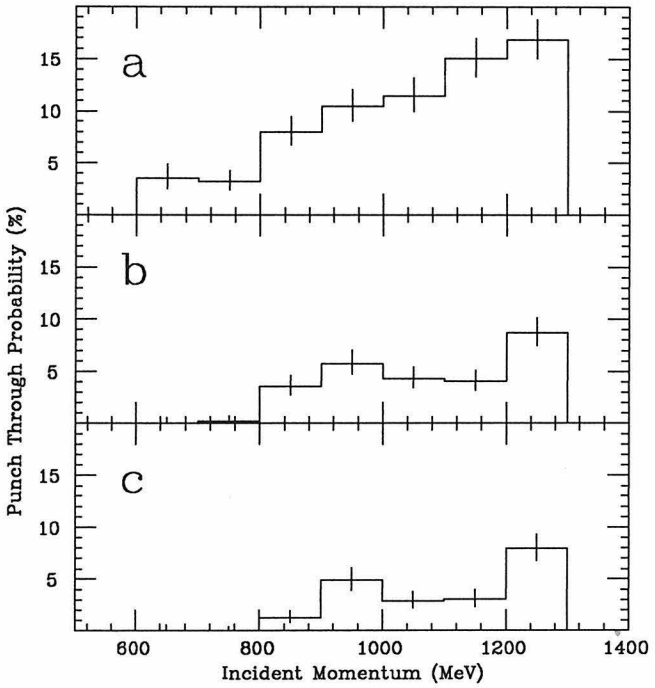

Figure 4.7.3: K punch through probability: Layer 1 (a), Layer 2(b), Layers 1&2(c)

4.8: Coverage of Systems

The various systems of the MARK III subtend different solid angles. The coverage of each system is summarized in Table 4.8.I.

Table 4.8.I: Coverage of Detector Systems

System	Coverage (% of 4π sr)
Layer 1	98%
Layer 2	93%
Layers 3-8	85%
ToF system	76%
Barrel	80%
Endcap - front	8.5%
- back	6.5%
Muon system	65%

4.9: Event Trigger

As mentioned above, the beams cross every 781 nsec at SPEAR. It takes, however, much longer — 30 msec — to digitize and record all of the information from an event, so a fast and efficient trigger is required.[66] Ordinarily, a reset signal is produced 590 nsec after each beam crossing to prepare all the electronics systems for the next beam crossing. This signal may be inhibited under two conditions by the Level 0 trigger, the lowest level of the trigger logic. The Level 0 trigger is satisfied if two Layer 1 chronotrons fire within the 100 nsec gate, or if a signal from one Layer 1 chronotron is accompanied by another from a ToF chronotron within a 27 nsec gate. The Level 0 trigger rate is about 2-3 kHz. Most such triggers are the result of collisions between beam electrons and residual gas molecules within the beam pipe.

If a Level 0 trigger occurs, the information from the main drift chamber is examined by the next level of the trigger, Level 1. This attempts to find valid tracks within Layers 1,3, and 5. A cell in Layers 3 or 5 is considered to have been hit if there signals from at least two of its three sense wires. All patterns of tracks with transverse momenta greater than 75 MeV/c are stored in programmable array logic or PAL circuits, one for each cell of Layer 5. The arrangement of PAL's is illustrated in Fig. 4.9.1. Level 1 is satisfied if two valid tracks are found or if one valid track is found with a coincident ToF hit. If a Level 1 trigger occurs, all resets are inhibited and digitization begins after which the event is processed and finally stored on tape. The Level 1 trigger rate is 3-5 Hz, providing dead time of about 10-12%.

The efficiency of the trigger was measured using events of the type $\psi' \rightarrow J/\psi\,\pi^+\pi^-$. The events were isolated by tagging on the missing mass recoiling from the $\pi^+\pi^-$ system. The information not relating to this system was examined to determine whether it would have been sufficient to cause a trigger. The momentum of the J/ψ is very low, and does not complicate this analysis. The trigger was found be 93% efficient for detecting the decay of a J/ψ.

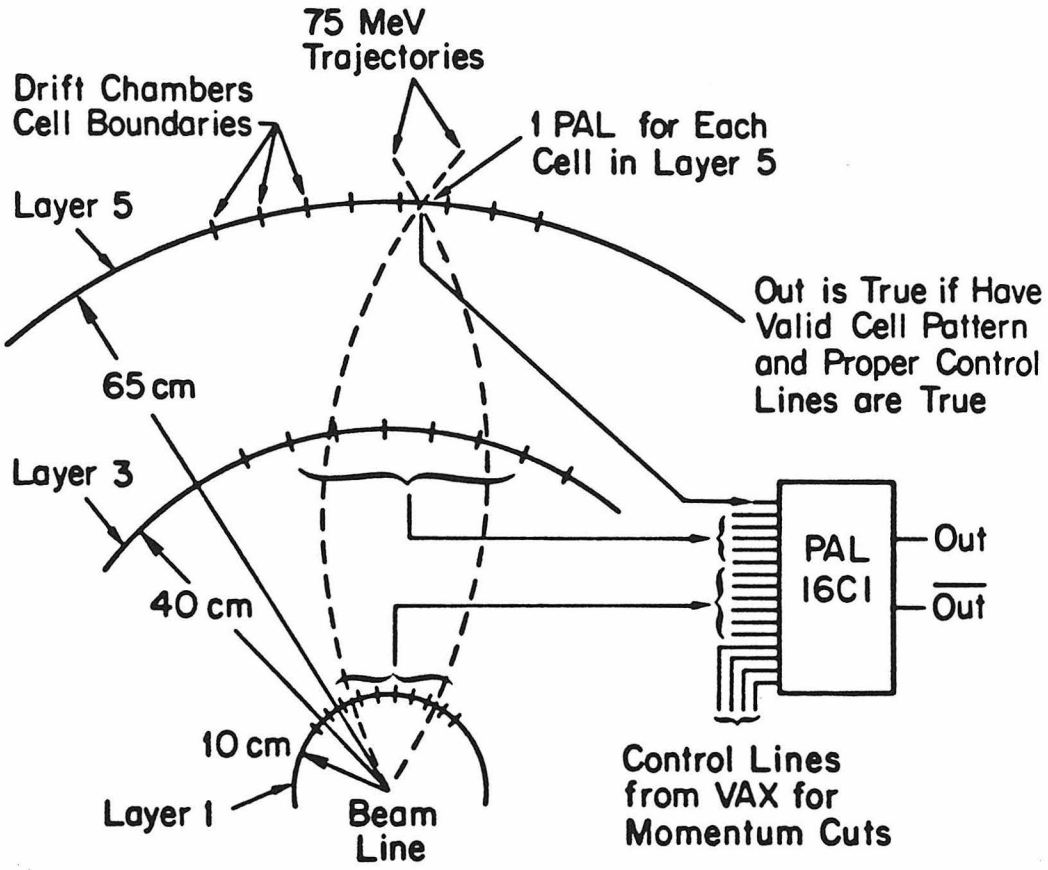

Figure 4.9.1: Arrangement of PAL circuits for trigger

Chapter 5: Data Sets

5.1: J/ψ Data Sets

The MARK III detector has been used to acquire several different data sets. The first, consisting of 0.9 million J/ψ decays, was collected in the Spring of 1982. This will be referred to as the 1982 J/ψ data set. The events in this set were used in the checkout and debugging of the detector and analysis software.

In the Spring of 1983, a further 1.8 million J/ψ decays were collected — the 1983 J/ψ data set. These data were taken after the observation of a narrow peak in the K^+K^- mass distribution for events of the type $J/\psi \rightarrow \gamma K^+K^-$ drawn from the 1982 data.[67]

Although the apparatus performed well in 1982, two improvements were made before the Spring 1983 run. As noted in the previous chapter, layer 2 of the main drift chamber is operated at a reduced gain. The noise pickup on the cables leading from layer 2 overwhelmed the very small signals. In order to remedy this problem, a preamplifier was added on the face of the chamber to each channel of layer 2. The wires in the cells of layer 2 are very close together resulting in substantial capacitive coupling among the sense wires. A signal on one wire often induced a signal of the opposite polarity on the adjacent wires. These induced signals were cancelled with the addition of a series of resistors between the sense wires. These improvements allowed the pulse heights measured in layer 2 to be used for particle identification.

5.2: ψ'' Data Sets

Following the acquisition of the 1982 J/ψ data, about 1,800 nb^{-1} were collected in the Fall of 1982 at an energy of 3.768 GeV, the peak of the ψ'' resonance. This resonance lies below $D\overline{D}^*$ threshold and decays predominantly into $D\overline{D}$

pairs, making it an ideal 'D factory'. It was possible to reconstruct D mesons from this initial sample cleanly, in several different modes.

Further data taking at the same energy in the Spring of 1983 and 1984 resulted in a total luminosity of 9,300 nb^{-1}. Altogether, these three blocks of data comprise the ψ'' data set. This includes non-resonant final states unrelated to charmonium, 21400 $D^0\overline{D}^0$ and 17000 D^+D^- pairs,[68] and 22000 $\tau^+\tau^-$ pairs.[69]

5.3: Tagged Sample

The analysis of semileptonic processes is based on a sample of *tagged* events, events in which one D could be reconstructed in an hadronic decay mode. The remainder of the event — the recoil from this reconstructed D — is then known *a priori* to have been the result of the decay of the companion $\overline{D}$. This allows identification even of semileptonic decays in which, of course, the neutrino is not detected.

Large signals were observed in eight Cabibbo favored channels:[70]

$$D^0 \to K^-\pi^+,\ K^-\pi^+\pi^+\pi^-,\ K^-\pi^+\pi^0,\ \overline{K}^0\pi^+\pi^-$$
$$D^+ \to K^-\pi^+\pi^+,\ \overline{K}^0\pi^+, \overline{K}^0\pi^+\pi^+\pi^-,\ \overline{K}^0\pi^+\pi^0$$

Here and following, D^0 implies $\overline{D}^0$ and D^+ implies D^-. All of the events in the ψ'' data set were first examined for kaons, neutral or charged. Only those events containing a kaon were considered further.

A track was classified as a charged kaon if its ToF weight was larger than its pion or proton weight, and if the measured time-of-flight differed from that predicted for a kaon by less than five standard deviations.

The procedure used to identify neutral kaons via the decay $K^0_s \to \pi^+\pi^-$ was somewhat more involved. All pairs of oppositely charged tracks were considered, provided that each track could be well-fit to a helix.[71] The position of the decay

vertex and the momenta of the tracks at this vertex were calculated as discussed in appendix 2. The mass of the candidate, as calculated at the vertex, was required to be consistent with the mass of the K_s^0. Finally, the displacement of the decay vertex from the primary vertex, the position of which was determined by performing a constrained fit to the remaining charged tracks, was required to align with the momentum of the candidate.

Appropriate combinations of particles were constructed for each of the eight modes listed above. The number of events in each mode was determined by examining a variable known as the *beam-constrained mass.* The ordinary invariant mass of a decaying particle may be calculated from the formula:

$$M = \sqrt{(\sum_j E_j)^2 - (\sum_j \vec{p}_j)^2}$$

The sums extend over all the daughter particles. The resolution in the invariant mass is about 15-20 MeV/c^2. In the decays of the ψ'', the D mesons are produced only in pairs and are thus monochromatic. The total energy of each D must equal the beam energy. The beam-constrained mass is defined by the relation:

$$M_{bc} = \sqrt{E_{beam}^2 - (\sum_j \vec{p}_j)^2}$$

The resolution for this quantity is much better than that for the invariant mass. The beam energy is known at SPEAR to within two to three MeV. Further, the momentum of each D is small, 260 and 280 MeV for the charged and neutral mesons, respectively.

Two tag modes contain neutral pions. These are identified through their decay to two photons. The momenta of pairs of photons, each with an energy of at least 150 MeV, were subjected to a fit with two constraints: the invariant mass of the pair was forced to equal the π^0 mass, and its total energy to equal the difference between the beam energy and the sum of the energies of the charged particles. The χ^2 from the fit was required to be less than six.

The beam-constrained mass distributions for the four D^0 decay modes are given in Fig. 5.3.1 and those for the D^+ in Fig. 5.3.2. The number of tags represented by each plot is determined by fitting the distribution to a function of the form:

$$F(m) = \left[a_1 + a_2\,(m - 1.8) + a_3\,(m - 1.8)^2\right] \cdot \frac{1}{2}\left(1 - \frac{2}{\pi}\arctan(\alpha(m - \beta))\right) + a_4\,\exp\left(-\frac{(m - M_D)^2}{2\sigma^2}\right)$$

The first terms parameterize the background and the Gaussian term accounts for the signal. Just above the D mass, there is no more phase space available for a decay to a pair of D mesons. The arctangent provides a sharp cutoff as observed in the data. The number of tags is calculated by integrating the background terms over the range 1.85 to 1.88 GeV/c^2 and subtracting this number from the *observed* number of events in this range. The number of tags is summarized in Tables 5.3.I and 5.3.II. The errors quoted there are the statistical errors on the number of background events.*

The decay $D^0 \to K^-\pi^+$ is virtually free of background. It may be used to illustrate a characteristic feature of decays of the ψ''. This is a vector resonance, so when it decays to a pair of pseudoscalars, these should be produced with the angular distribution $P(\cos\vartheta) = \sin^2\vartheta$ where ϑ is the polar angle. Fig. 5.3.3 is a histogram of the observed values of $\cos\vartheta$ for all detected $K^-\pi^+$ events. The solid curve in this figure is the result of a fit to the function $1 + \alpha\cos^2\vartheta$. The value of α from this fit is -0.87 ± 0.04.

* The justification for this will be given in section 7.2.

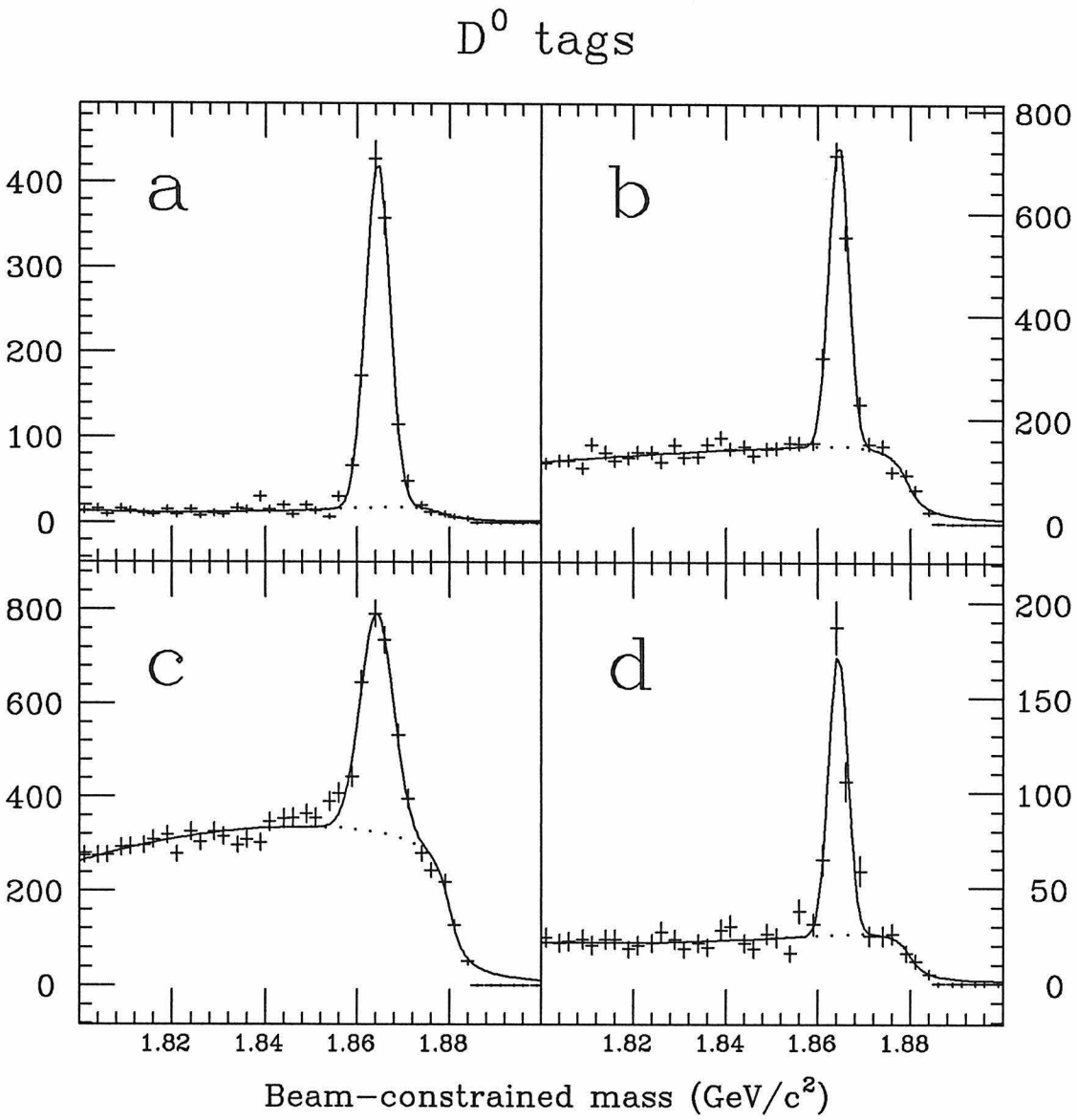

Figure 5.3.1: Beam-constrained mass of D^0 tags
$K^-\pi^+$ (a); $K^-\pi^+\pi^+\pi^-$ (b); $K^-\pi^+\pi^0$ (c); $\overline{K}^0\pi^+\pi^-$ (d)

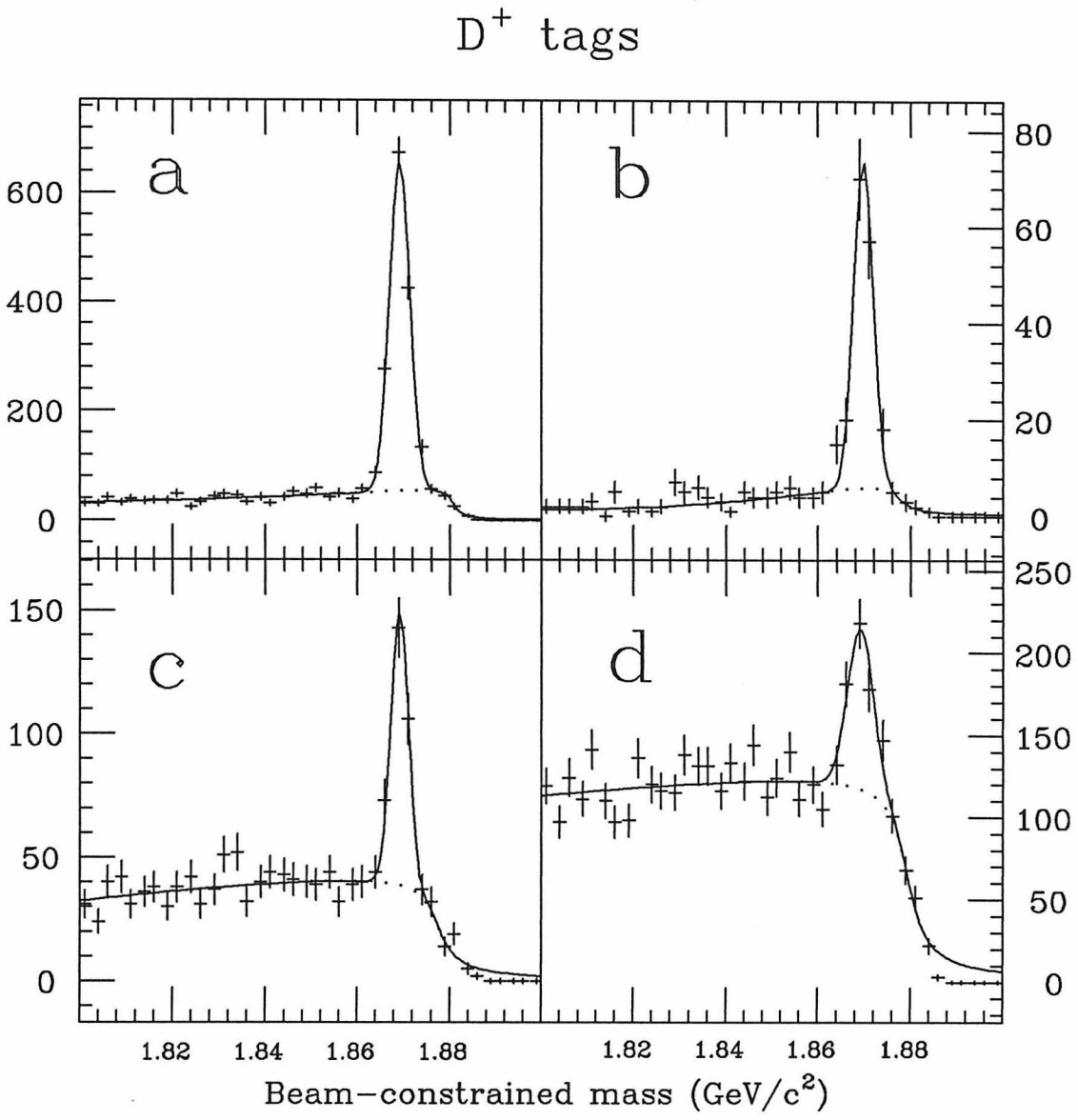

Figure 5.3.2: Beam-constrained mass of D^+ tags
$K^-\pi^+\pi^+$ (a); $\overline{K}^0\pi^+$ (b); $\overline{K}^0\pi^+\pi^+\pi^-$ (c); $\overline{K}^0\pi^+\pi^0$ (d)

Table 5.3.I: Numbers of D^0 Tags

Mode	Number of Tags
$K^-\pi^+$	1089 ± 13.8
$K^-\pi^+\pi^+\pi^-$	1254 ± 40.8
$K^-\pi^+\pi^0$	1738 ± 60.8
$\overline{K}^0\pi^+\pi^-$	325.9 ± 17.1

Table 5.3.II: Numbers of D^+ Tags

Mode	Number of Tags
$K^-\pi^+\pi^+$	1346 ± 24.6
$\overline{K}^0\pi^+$	152.8 ± 7.7
$\overline{K}^0\pi^+\pi^+\pi^-$	207.0 ± 20.9
$\overline{K}^0\pi^+\pi^0$	268.4 ± 36.8

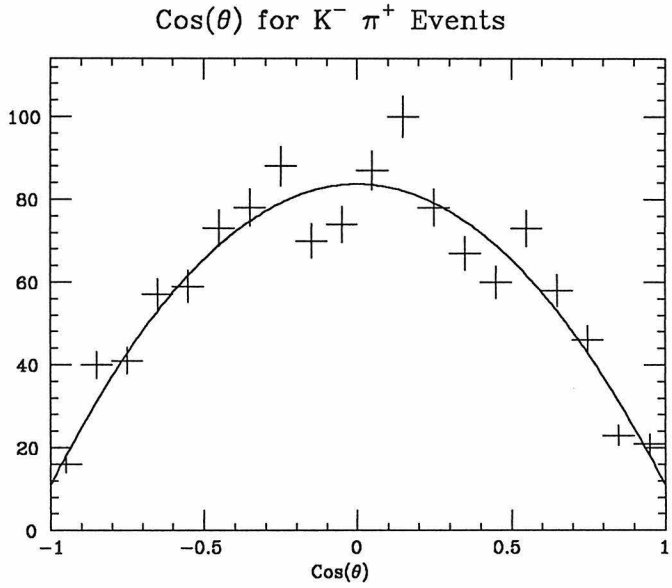

Figure 5.3.3: Angular distribution of $K^-\pi^+$ events

Chapter 6: Electron Detection

6.1: Electron Sample

The major difficulty faced in identifying electrons is separating them from hadrons. The energy resolution of the shower detectors in the MARK III is not sufficient for distinguishing unambiguously between electromagnetically interacting and minimum ionizing particles on the basis of their deposited energy. This situation is made worse by the fact that hadrons often interact inelastically within the shower detector's lead radiator.

The shower detectors are of little help for low momentum electrons which deposit about the same amount of energy as a hadron whether or not the hadron interacted. The resolution of the ToF system is quite good, nevertheless it is able to separate only very low momentum electrons from pions; the ability to separate electrons from kaons or protons extends to much higher momenta. The separation ability of the ToF system is shown in Figs. 4.4.2 and 4.4.3 as a function of momentum.

For electron identification, the ToF system is used to remove kaons and protons. The information from the ToF and shower detector system is combined to remove pions. Since the ToF counters and the barrel shower detector cover about the same fiducial region, information from the endcap shower detectors is not used.

Efficient and reliable identification of electrons requires a detailed examination of the properties of electromagnetic and hadronic showers in the shower detectors. This entails identifying a large sample of electrons and pions. These samples, of course, must be collected in ways which do not bias the study of shower development.

At electron-positron colliders, there is an excellent source of electrons, the QED Bhabha scattering process $e^+ e^- \rightarrow e^+ e^-$. The electron is nearly massless,

so radiative corrections are very important for this process. The spectrum of radiated photons is in general soft, but there is a long tail which extends up to the beam energy. A Monte Carlo calculation of this energy spectrum is shown in Fig. 6.1.1.[72] Roughly half of the photons are emitted from the initial state* and the remainder from the final state.

Photons from the initial state are seldom detected; they are emitted nearly parallel to the beam direction and so usually remain within the beam pipe. Thus, if the photon from the scattering process $e^+ e^- \rightarrow e^+ e^- \gamma$ — hereafter referred to radiative Bhabha scattering — is detected, it is most likely the result of Bremsstrahlung from one of the final state electrons. This has several fortunate consequences. The final state electron which does not radiate will have momentum approximately equal to the beam energy. The electron which does radiate will be of lower momentum; the momentum distribution peaks at high momentum but extends to very low momenta. A Monte Carlo calculation of this spectrum is shown in Fig. 6.1.2.

The electron sample was drawn from events produced by radiative Bhabha scattering. For such events, stringent cuts were placed on the photon and on the charged track of higher momentum. The charged track of lower momentum was added to the electron sample. The cuts imposed were:

1. that there must be two and only two tracks in the drift chamber with well-measured momenta and showers in the barrel shower detector.

2. that there must be at least one neutral shower in the barrel shower detector with a measured energy of at least 200 MeV.

3. that the higher momentum track should have momentum — as measured in the drift chamber — and energy — as measured in the shower detector — within two standard deviations of the beam energy.

---

* The terms initial and final state are of somewhat dubious utility as Bhabha scattering proceeds through t-channel exchange as well as s-channel annihilation. In spite of this, initial and final state radiation are the conventional terms.

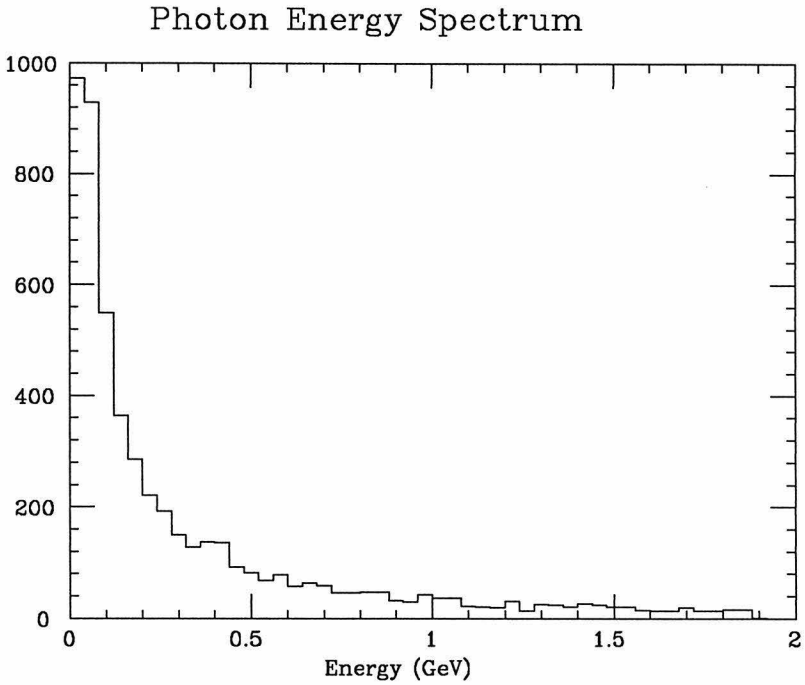

Figure 6.1.1: Monte Carlo photon energy spectrum for Bhabha events

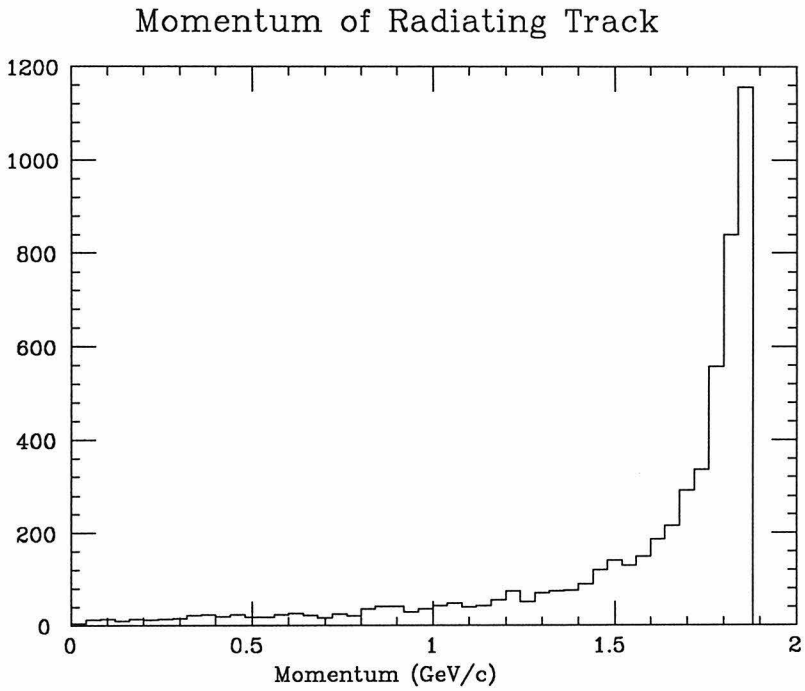

Figure 6.1.2: Monte Carlo electron momentum spectrum for Bhabha events

4. that the lower momentum track must have momentum at least 200 MeV/c below the beam energy.

5. that the direction of the neutral track should match the direction of the missing momentum. The missing momentum is defined by the relation $\vec{P}_{missing} \equiv -\vec{P}_1 - \vec{P}_2$. Here, $\vec{P}_1$ and $\vec{P}_2$ are the momenta of the charged tracks. The cuts imposed are $|\vartheta_\gamma - \vartheta_{missing}| < 0.1$ and $|\varphi_\gamma - \varphi_{missing}| < 0.006$. The angles ϑ and φ are the polar and azimuthal angles, respectively, measured in radians.

Neutral tracks were required to have a measured energy of at least 200 MeV for several reasons. The shower detector is almost completely efficient for photons of energy greater than 100 MeV. There are, however, some neutral showers which are not associated with incident photons. These are the result of 'split-offs' from the showers of charged tracks or of electronic noise. Most of these spurious neutral tracks are of low measured energy. Requiring the energy to be greater than 200 MeV removed the majority of these.

The energy requirement has another effect. The electron sample is needed to study the pattern of energy deposition by electrons in the shower detector. In the case of final state Bremsstrahlung, the photon and the radiating electron will be emitted in approximately the same direction; the larger the photon energy, the largely will be the angle between their directions. If the photon is required to deposit at least 200 MeV in the shower detector, the photon and electron showers will seldom overlap. Requiring that the radiating electron have momentum at least 200 MeV/c below the beam energy helps insure that a photon of reasonably high energy must have been emitted.

Even if the energy resolution of the shower detectors is modest, their directional resolution is excellent. Therefore, the direction of the detected photon and the direction of the missing neutral momentum should coincide closely.

A large number of events was found which passed all the cuts listed above: 3,400 and 8,500 from the 1982 and 1983 J/ψ data sets, respectively. The lower

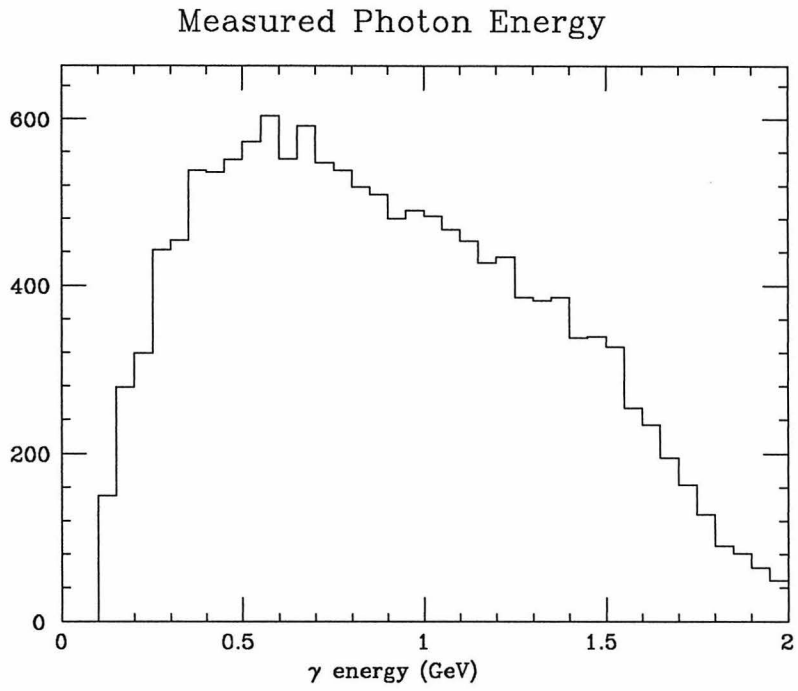

Figure 6.1.3: Energy spectrum of detected photons in radiative Bhabha events

momentum electron from each event was added to the electron sample. The photon energy spectrum for these events is shown in Fig. 6.1.3. Figures 6.1.4 and 6.1.5 illustrate the difference between the directions of the photon and the missing momentum, in ϑ and φ respectively. The momentum spectrum of the electron sample is given in Fig. 6.1.6.

6.2: Pion Sample

A sample of charged pions was drawn from two sources: the strong decay $J/\psi \to \rho\pi$ and the weak decay $K_s^0 \to \pi^+\pi^-$. The first decay has a large branching ratio — $1.22 \pm 0.12\%$ — and so is a particularly rich source. Events of this type were isolated in several steps. First, all two prong events with at least two neutral tracks were kinematically fit to the hypothesis $J/\psi \to \pi^+\pi^-\pi^0$. The sample of events so selected was already virtually free of background but a few additional cuts were imposed.

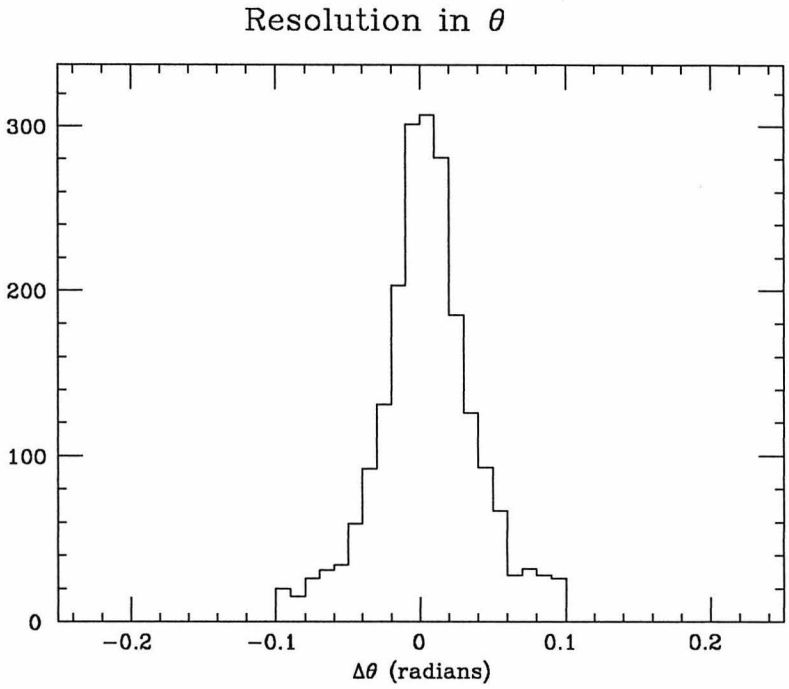

Figure 6.1.4: Difference in ϑ between direction of detected photon and missing momentum

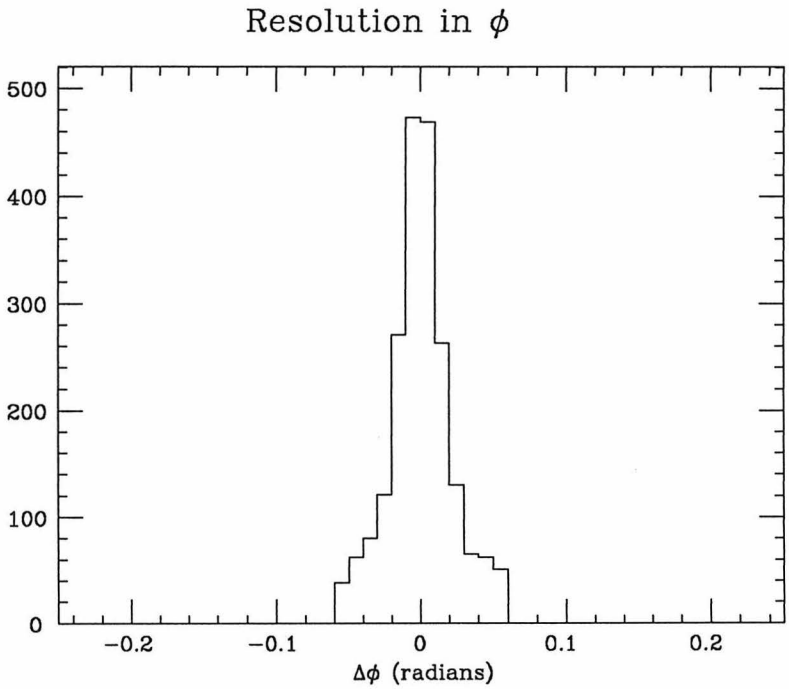

Figure 6.1.5: Difference in φ between direction of detected photon and missing momentum

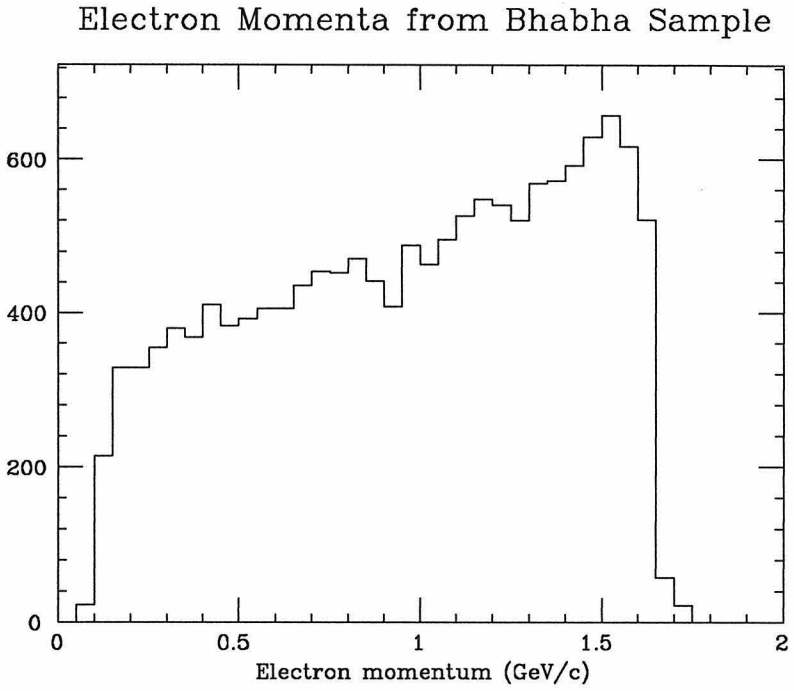

Figure 6.1.6: Momentum spectrum for electron sample

The unfit invariant mass of the π^0 was required to be in the range 75 MeV/c^2 $\leq M_{\pi^0} \leq$ 200 MeV/c^2. For events with a neutral rho, both charged pions were added to the pion sample. The charged pion recoiling from a charged rho was examined further. In order to reduce contamination from radiative Bhabha scattering, the recoiling pion was required to deposit no more than 750 MeV in the shower detector. Finally, if this track had valid ToF information — its pion weight was required to be larger than its kaon weight in order to eliminate $K^{*\pm}K^{\mp}$ events. Specifically, the requirement imposed was $W_\pi/(W_\pi + W_K) \geq 0.7$. For all $J/\psi \rightarrow \rho^{\pm}\pi^{\mp}$ events satisfying these requirements, the charged pion from the decay of the ρ was added to the pion sample. Altogether, 4,700 pions were extracted from the 1982 J/ψ data set and 10,200 from that of 1983.

The high quality of these events is illustrated in Figs. 6.2.1 to 6.2.5. The invariant mass of the neutral pion is shown in Fig. 6.2.1 while that of the ρ is given in Fig. 6.2.2. The momentum spectrum of the recoiling pion is plotted in Fig. 6.2.3 and that of the rho in Fig. 6.2.4. Finally, the momentum spectrum of

all those pions added to the pion sample is given in Fig. 6.2.5

The second source of pions was the decay $K_s^0 \rightarrow \pi^+\pi^-$. In order to isolate such events, a fitting procedure was applied to all pairs of oppositely charged tracks. The helical paths of these tracks will have zero, one, or two points of intersection — hereafter referred to as crossing points. (These crossing points may be found quite simply as described in Appendix 2) If there is no crossing point, the point of closest approach of the two helices is used; if there are two crossing points, the one closest to the primary vertex is used. The crossing point is required to be displaced from this primary vertex by at least four millimeters in the $x-y$ plane. The momenta and error matrices of each track are 'swum' to the crossing point, both tracks assumed to be pions. A fit is now performed, adjusting the 4-momenta of the tracks so that their sum aligns with the displacement of the crossing point, and requiring that this sum have the invariant mass of the K^0. The χ^2 from this fit must be less than fifty. Finally, the unfit invariant mass of the K^0 must be in range 485 MeV/c^2 $\leq M_{K^0} \leq$ 508 MeV/c^2.

For each event satisfying these requirements, both tracks were added to the pion sample. A total of 5,200 pions from K^0 decays was isolated from the 1982 J/ψ data set. A further 11,000 were isolated from the 1983 J/ψ data set. The momentum spectrum of these pions in shown in Fig. 6.2.6. The spectrum for the combined sample is plotted in Fig. 6.2.7.

6.3: Pion-electron Separation Algorithm

An algorithm was developed, on the basis of the electron and pion samples, for distinguishing between electrons and pions. The algorithm is a tree structured classifier, making use of the technique of recursive partitioning.[73] The mathematical details of this technique are summarized in appendix 1.

There are separate classification procedures or *trees* for each of seven momentum ranges. The performance of the several detection systems varies considerably

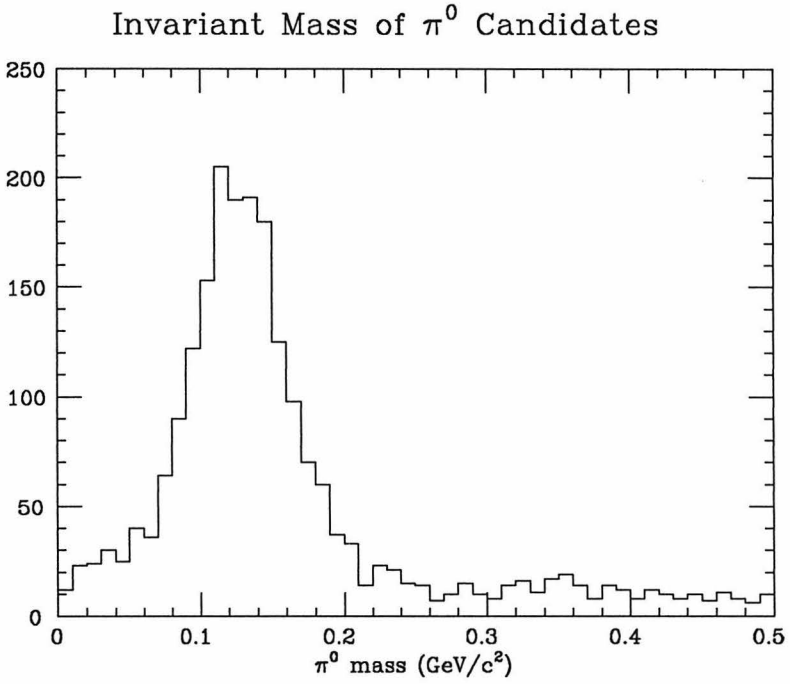

Figure 6.2.1: Invariant mass of π^0 candidates

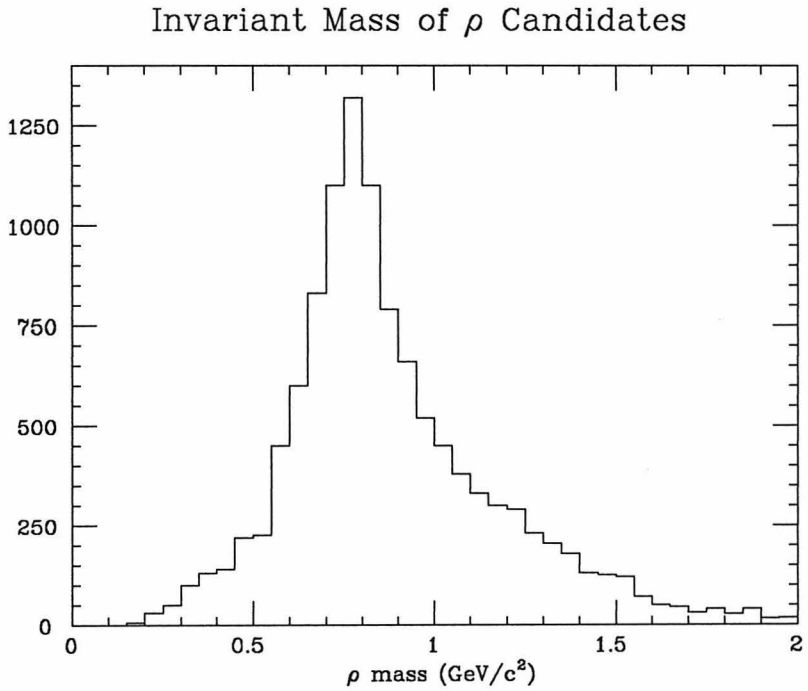

Figure 6.2.2: Invariant mass of ρ candidates

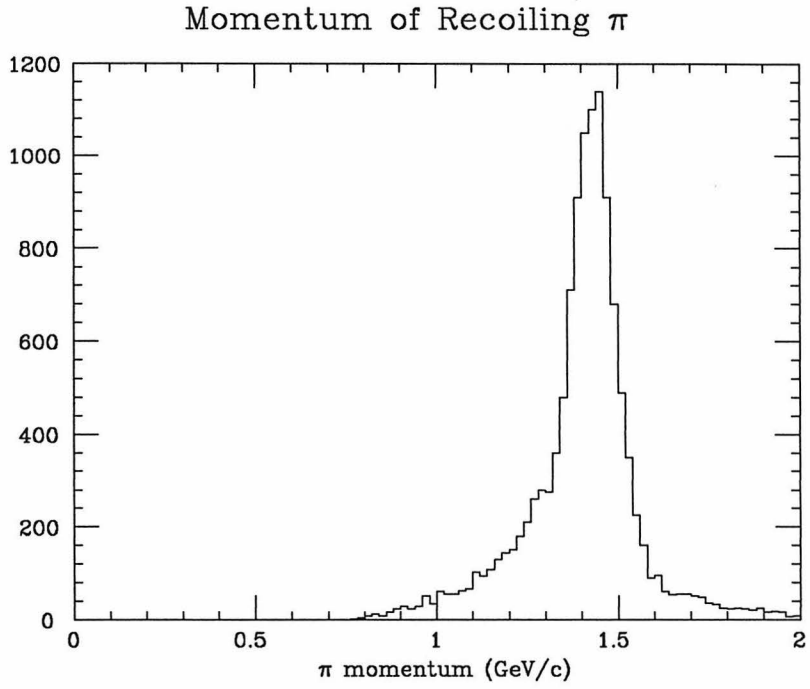

Figure 6.2.3: Momentum spectrum of π recoiling from ρ

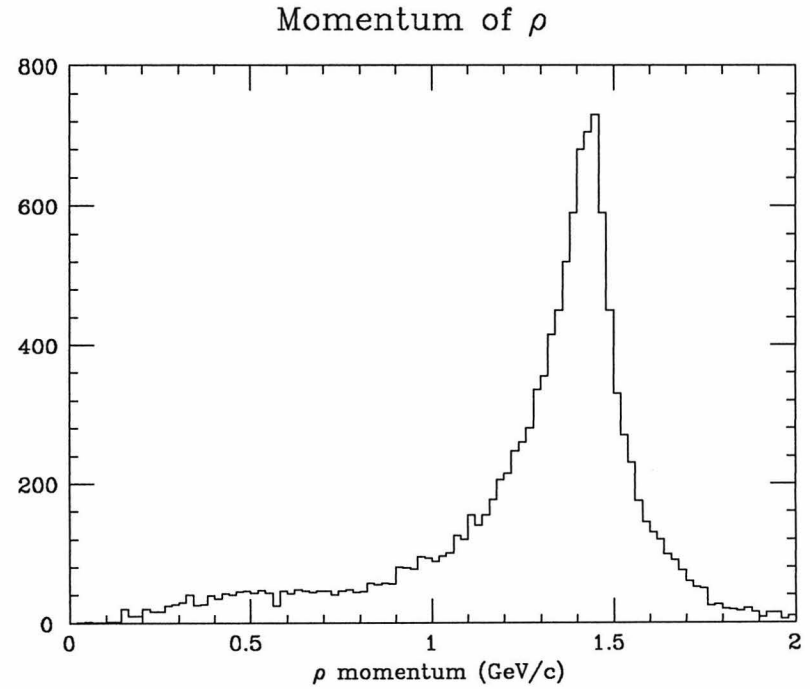

Figure 6.2.4: Momentum spectrum of ρ

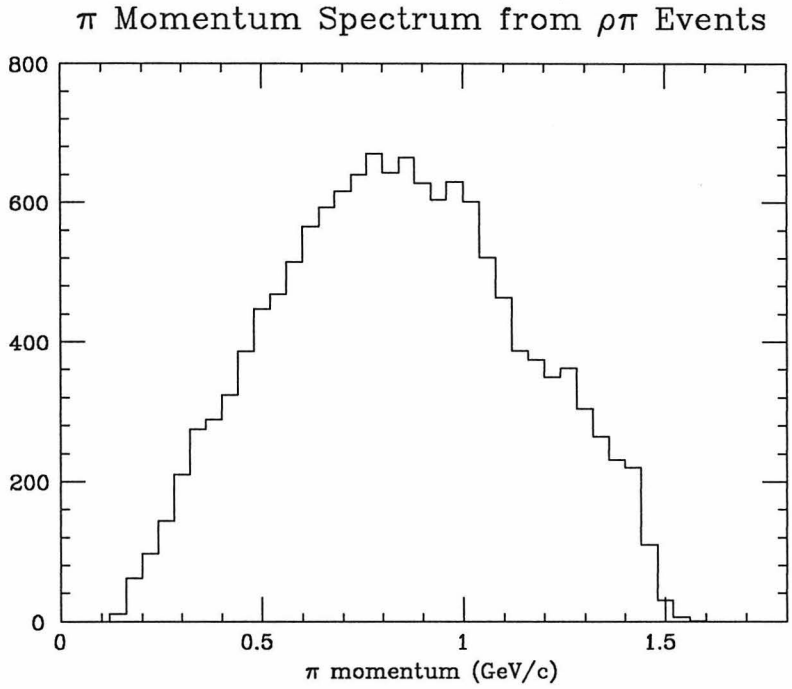

Figure 6.2.5: Momentum spectrum of π's selected from $\psi \rightarrow \rho\pi$ events

with momentum so it was necessary to find different sets of cuts in different momentum regimes. The momentum ranges are:

$$p < 300 \text{ MeV/c}$$
$$300 < p < 400 \text{ MeV/c}$$
$$400 < p < 500 \text{ MeV/c}$$
$$500 < p < 600 \text{ MeV/c}$$
$$600 < p < 800 \text{ MeV/c}$$
$$800 < p < 1000 \text{ MeV/c}$$
$$p > 1000 \text{ MeV/c}$$

Time-of-flight information is available for most but not all tracks. A separate set of trees was prepared for tracks without ToF information; for these tracks it was necessary to 'cut harder' on the information from the shower detector.

It is difficult to devise a classifier which is both highly efficient for detecting

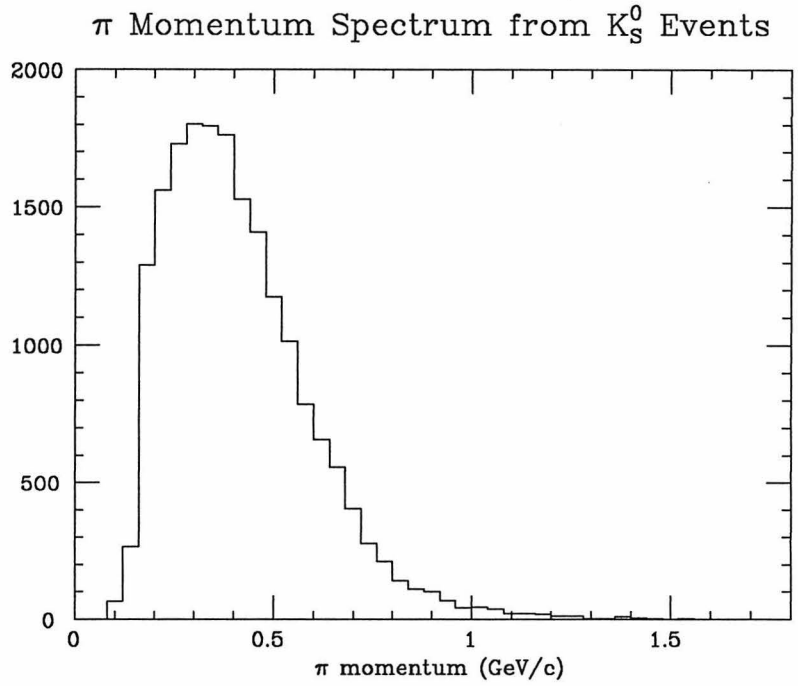

Figure 6.2.6: Momentum spectrum of π's selected from K_s^0 events

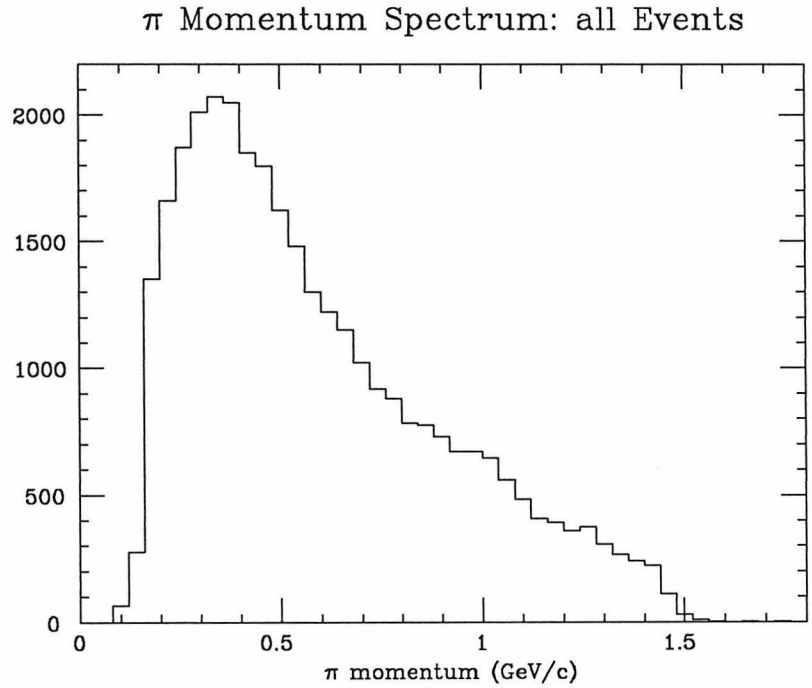

Figure 6.2.7: Momentum spectrum of all π's in pion sample

electrons and very effective in rejecting pions; there will always be a tradeoff between detection efficiency and background rejection. Separate sets of trees for the detection of electrons and pions were produced. The *electron trees* are able to detect about 80% of real electrons while rejecting about 96% of real pions. The *pion trees* do just the reverse. They accept about 80% of real pions while rejecting about 96% of real electrons. (This 'fine-tuning' was accomplished by adjusting the *cost-complexity* parameter as described in appendix 1.) In all, twenty-eight trees were produced.

A series of variables were chosen to characterize each track. An exhaustive examination of fifty-one variables was performed to determine which were most useful in distinguishing electrons from pions. The eight best were culled from this set. A description of each follows.

1. *Energy in the shower counter*: An electron will usually have a larger pulse-height in the shower detector than a non-interacting pion.

2. *Center-of-gravity of the shower*: This variable is defined by the relation $s = \sum_{i=1}^{12} X_i \cdot E_i / E_{tot}$. X_i is the position of the i^{th} layer of the shower detector from the inner surface, in radiation lengths. E_i is the energy deposited in the i^{th} layer and E_{tot} is the total energy. An electromagnetic shower will reach its maximum after between three and four radiation lengths of material,* leading to a value of s of about four. A minimum ionizing shower will deposit its energy uniformly leading to a value of s of about six. An interacting pion will often deposit its energy earlier yielding a smaller value of s.

3. *RMS azimuthal width of shower*: A minimum ionizing "shower" is typically quite narrow. If an inelastic interaction takes place, several photons will often be produced; such a shower will appear very broad. An electromagnetic shower, however, almost always appears moderately broad. This is one of the most useful variables.

---

* This is true for the momentum range 300 MeV/c $< p <$ 1500 MeV/c. The position of the *shower maximum* varies as the logarithm of the energy.

4. *Energy-layer correlation*: A longitudinal shower profile was developed for pion initiated showers. The energy-layer correlation variable measures the degree to which a given shower matches this shower profile. The profile is found by evaluating the sum

$$M_{ij} = \frac{1}{N}\sum_{i=1}^{N}(E_i - \overline{E_i})(E_j - \overline{E_j})$$

This sum extends over all pions in the sample. N is the total number of pions. The subscripts i, and j refer to the layer within the shower detector. The correlation function is

$$F = \sum_{ij}(E_i - \overline{E_i})\, M_{ij}^{-1}\, (E_j - \overline{E_j})$$

The value of F is small for pions and substantially larger for electrons.

5. *Energy divided by momentum*: This is the 'classic' variable for identifying electrons. Minimum ionizing showers yield a small value on average while electromagnetic showers yield values close to unity.

6. Energy in layers four through six:

7. Energy in layers seven through nine: Minimum ionizing showers usually have smaller values of these variables than electromagnetic showers. Dividing the shower longitudinally in this fashion has two advantages. It allows the cuts to be rescaled in the region past the electromagnetic shower maximum. It also affords two chances to trap an interacting pion, as an hadronic interaction may occur anywhere within the shower detector.

8. *Normalized ToF weight*: A normalized weight is used which is defined as $W = W_e/(W_\pi + W_e)$. This variable is 1 for a well identified electron, 0 for a well identified pion, and 1/2 if no determination may be made.

Plots of each these variables are given in Figs. 6.3.2 – 6.3.9. Momentum ranges were chosen to show the variables to best effect: $p > 0.500$ GeV/c for 6.3.2 – 6.3.8 and $p < 0.400$ GeV/c for 6.3.9.

The trees were grown using tenfold cross-validation using only the 1983 data. The performance of each tree was estimated using the 1982 data. The performance of the complete classification algorithm was finally measured using samples of electrons and pions drawn from the ψ'' data set. The same procedures were used to isolate these samples; 17,000 pions and 60,000 electrons comprise these samples. The performance of the classifier is summarized in Tables 6.3.I to 6.3.IV. The errors quoted in these tables were calculated using a method developed by F. James and M. Roos.[74]

An example of a tree is given in Fig. 6.3.1. The classification begins at the node labeled 1. The value of the appropriate variable — the total energy in the shower counter — is compared with the split value. If the measured value is less than the split, classification continues at node 2, otherwise it continues at node 4. The classification is finished when a split leads to a terminal node. The class assignment of these nodes is indicated in the figure by an e of π for an electron or pion assignment.

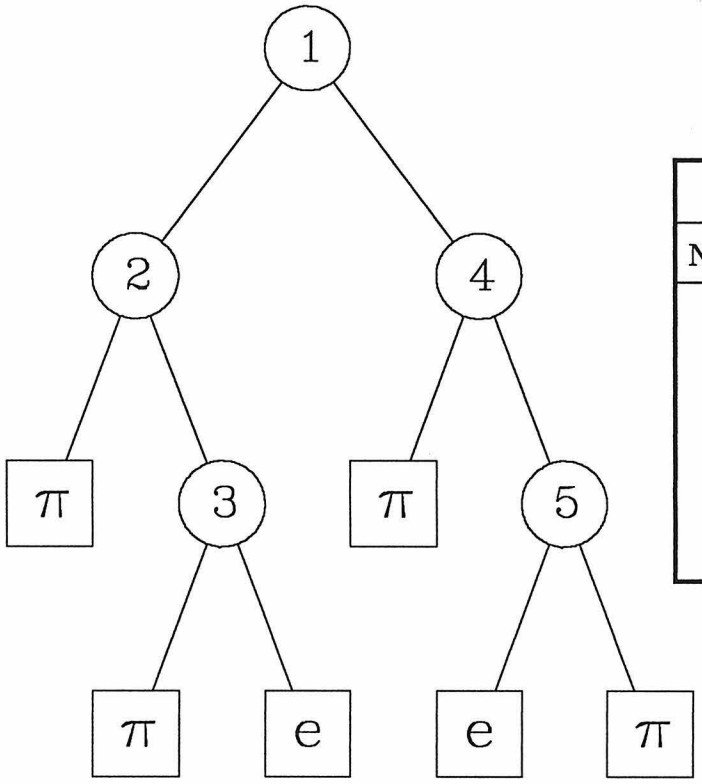

Splits		
Node	Variable	Value
1	1	0.726
2	5	0.665
3	6	0.109
4	6	0.056
5	4	189.3

Figure 6.3.1: Electron tree without ToF information — $0.8 < p < 1.0$ GeV/c
Circles indicate split nodes and boxes indicate terminal nodes

Variable No.	Definition
1	Total energy in shower detector
2	Center-of-gravity of shower
3	RMS width of shower
4	Energy layer correlation
5	Energy / momentum
6	Energy in layers 4-6 of shower detector
7	Energy in layers 7-9 of shower detector
8	Renormalized ToF weight

Table 6.3.I: Electron Tree with Good ToF Information

Momentum range	$P_{e\to e}$	$P_{\pi\to e}$
$p < 300$ MeV/c	$0.963^{+0.020}_{-0.019}$	$0.046^{+0.003}_{-0.003}$
$300 < p < 400$ MeV/c	$0.762^{+0.023}_{-0.022}$	$0.025^{+0.002}_{-0.002}$
$400 < p < 500$ MeV/c	$0.766^{+0.023}_{-0.022}$	$0.035^{+0.003}_{-0.003}$
$500 < p < 600$ MeV/c	$0.751^{+0.024}_{-0.024}$	$0.042^{+0.004}_{-0.004}$
$600 < p < 800$ MeV/c	$0.849^{+0.020}_{-0.019}$	$0.039^{+0.004}_{-0.004}$
$800 < p < 1000$ MeV/c	$0.876^{+0.022}_{-0.021}$	$0.024^{+0.009}_{-0.007}$
$p > 1000$ MeV/c	$0.905^{+0.011}_{-0.011}$	$0.077^{+0.025}_{-0.019}$

Table 6.3.II: Electron Tree without ToF Information

Momentum range	$P_{e\to e}$	$P_{\pi\to e}$
$p < 300$ MeV/c	$0.320^{+0.026}_{-0.024}$	$0.060^{+0.007}_{-0.006}$
$300 < p < 400$ MeV/c	$0.526^{+0.040}_{-0.038}$	$0.048^{+0.007}_{-0.006}$
$400 < p < 500$ MeV/c	$0.722^{+0.040}_{-0.038}$	$0.047^{+0.008}_{-0.007}$
$500 < p < 600$ MeV/c	$0.731^{+0.033}_{-0.032}$	$0.024^{+0.009}_{-0.006}$
$600 < p < 800$ MeV/c	$0.845^{+0.021}_{-0.021}$	$0.033^{+0.011}_{-0.008}$
$800 < p < 1000$ MeV/c	$0.867^{+0.019}_{-0.019}$	$0.033^{+0.024}_{-0.015}$
$p > 1000$ MeV/c	$0.881^{+0.009}_{-0.009}$	$0.024^{+0.053}_{-0.019}$

Table 6.3.III: Pion Tree with Good ToF Information

Momentum range	$P_{e\to\pi}$	$P_{\pi\to\pi}$
$p < 300$ MeV/c	$0.036^{+0.003}_{-0.003}$	$0.953^{+0.017}_{-0.016}$
$300 < p < 400$ MeV/c	$0.057^{+0.005}_{-0.005}$	$0.834^{+0.017}_{-0.017}$
$400 < p < 500$ MeV/c	$0.042^{+0.004}_{-0.004}$	$0.789^{+0.019}_{-0.018}$
$500 < p < 600$ MeV/c	$0.057^{+0.006}_{-0.005}$	$0.857^{+0.024}_{-0.024}$
$600 < p < 800$ MeV/c	$0.041^{+0.003}_{-0.003}$	$0.842^{+0.026}_{-0.025}$
$800 < p < 1000$ MeV/c	$0.045^{+0.004}_{-0.004}$	$0.877^{+0.058}_{-0.055}$
$p > 1000$ MeV/c	$0.042^{+0.002}_{-0.002}$	$0.846^{+0.091}_{-0.082}$

Table 6.3.IV: Pion Tree without ToF Information

Momentum range	$P_{e\to\pi}$	$P_{\pi\to\pi}$
$p < 300$ MeV/c	$0.437^{+0.031}_{-0.029}$	$0.836^{+0.031}_{-0.030}$
$300 < p < 400$ MeV/c	$0.290^{+0.028}_{-0.026}$	$0.882^{+0.037}_{-0.036}$
$400 < p < 500$ MeV/c	$0.203^{+0.018}_{-0.017}$	$0.938^{+0.044}_{-0.042}$
$500 < p < 600$ MeV/c	$0.068^{+0.009}_{-0.008}$	$0.858^{+0.055}_{-0.052}$
$600 < p < 800$ MeV/c	$0.065^{+0.005}_{-0.004}$	$0.880^{+0.062}_{-0.058}$
$800 < p < 1000$ MeV/c	$0.060^{+0.004}_{-0.004}$	$0.902^{+0.123}_{-0.108}$
$p > 1000$ MeV/c	$0.022^{+0.001}_{-0.001}$	$0.833^{+0.220}_{-0.174}$

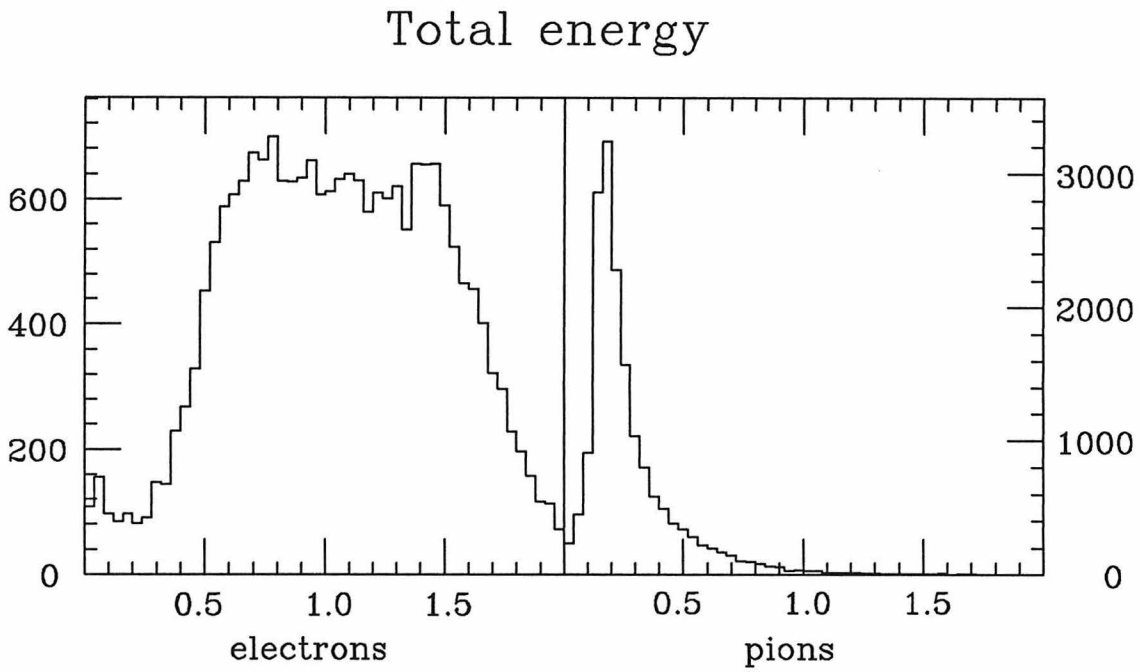

Figure 6.3.2: Total energy measured by shower detector

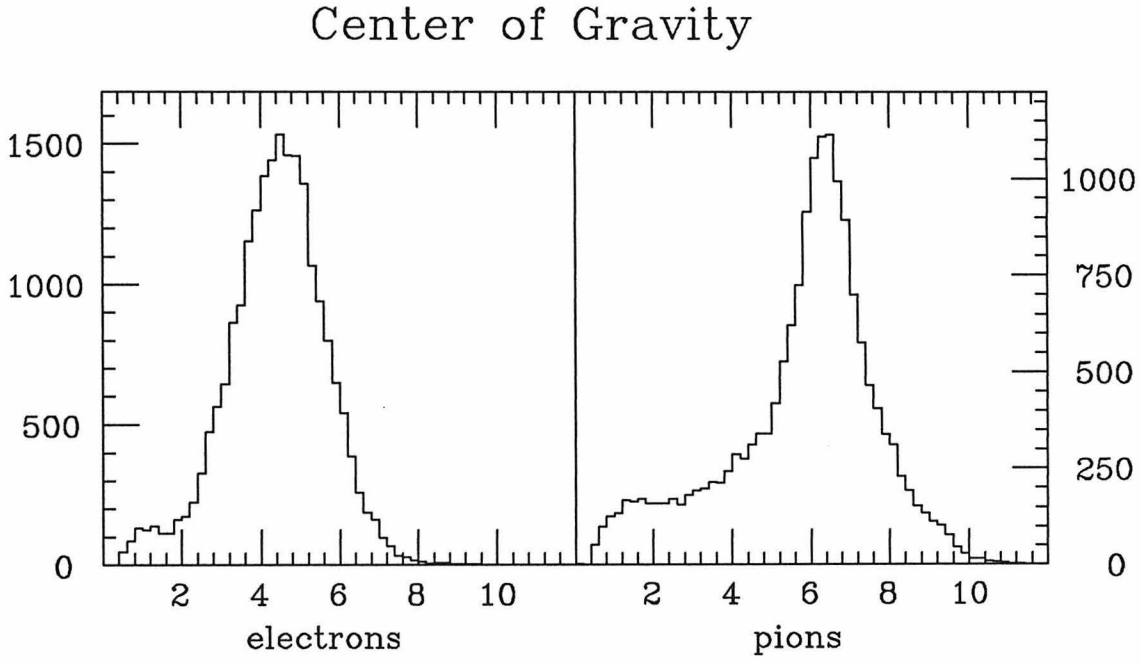

Figure 6.3.3: Center-of-gravity of shower

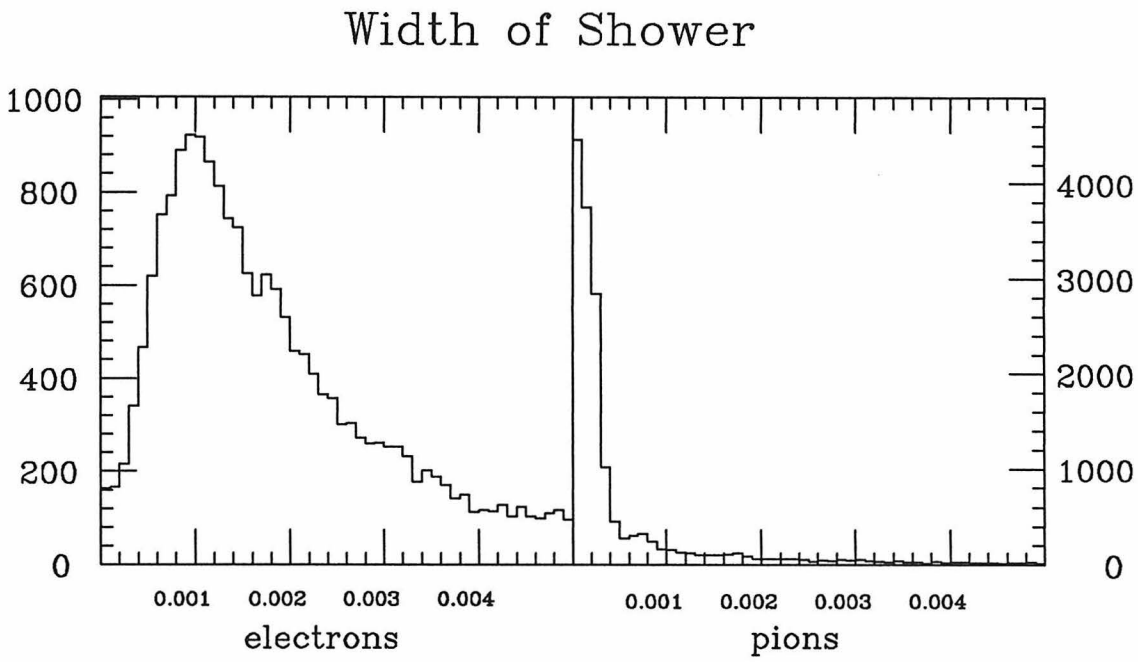

Figure 6.3.4: *RMS* azimuthal width of shower

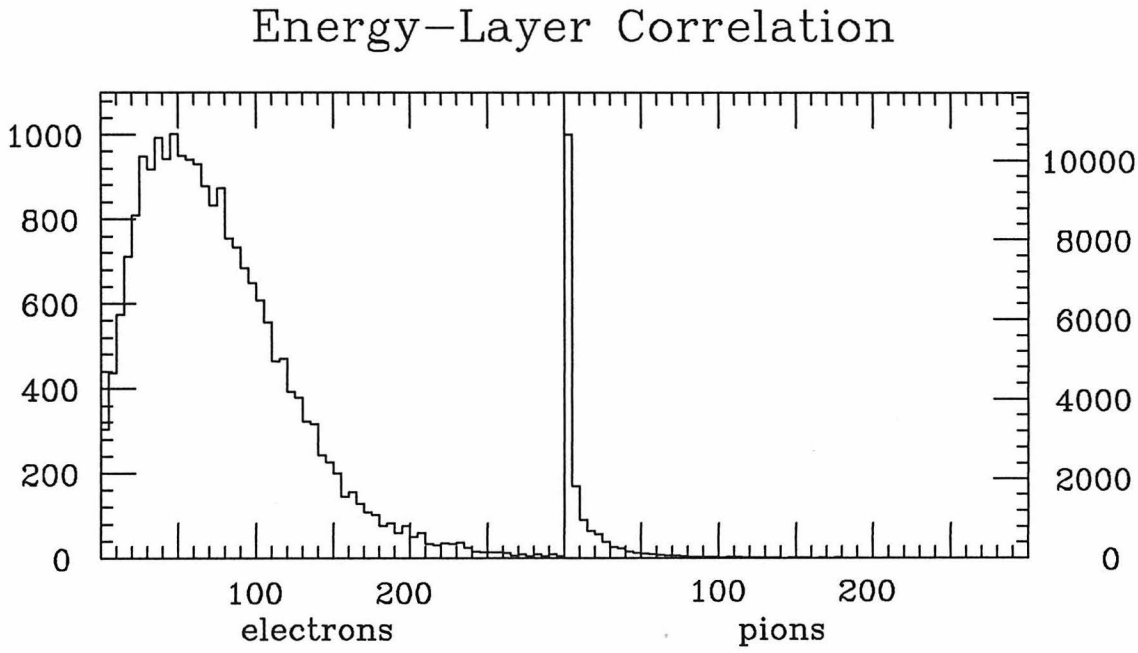

Figure 6.3.5: Energy-layer correlation

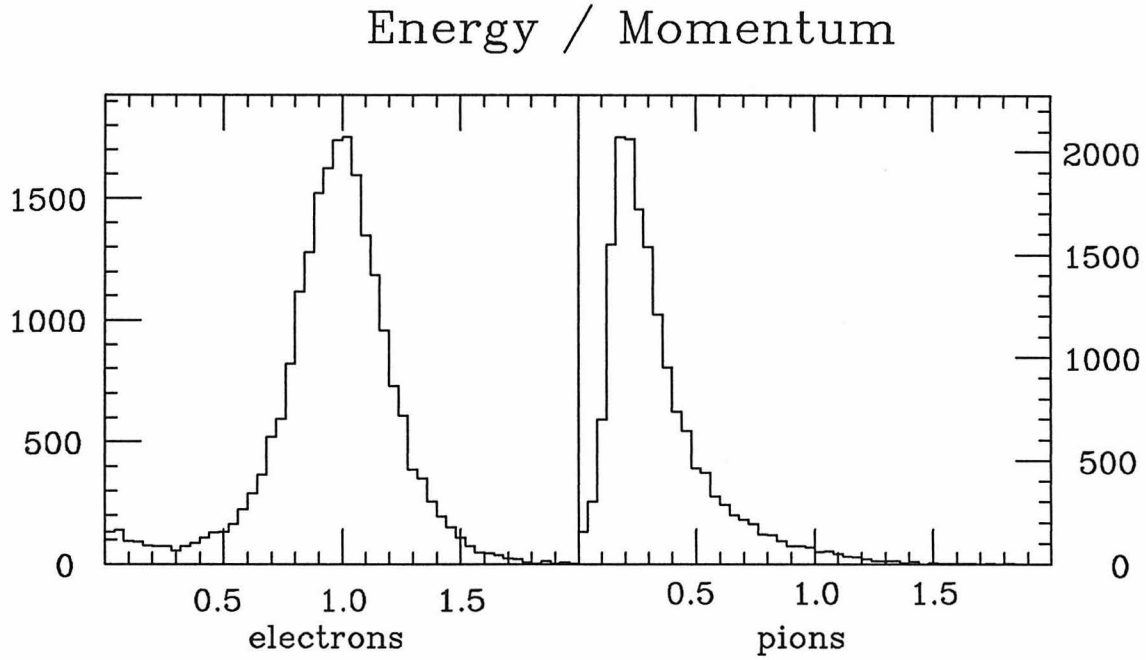

Figure 6.3.6: Energy / momentum

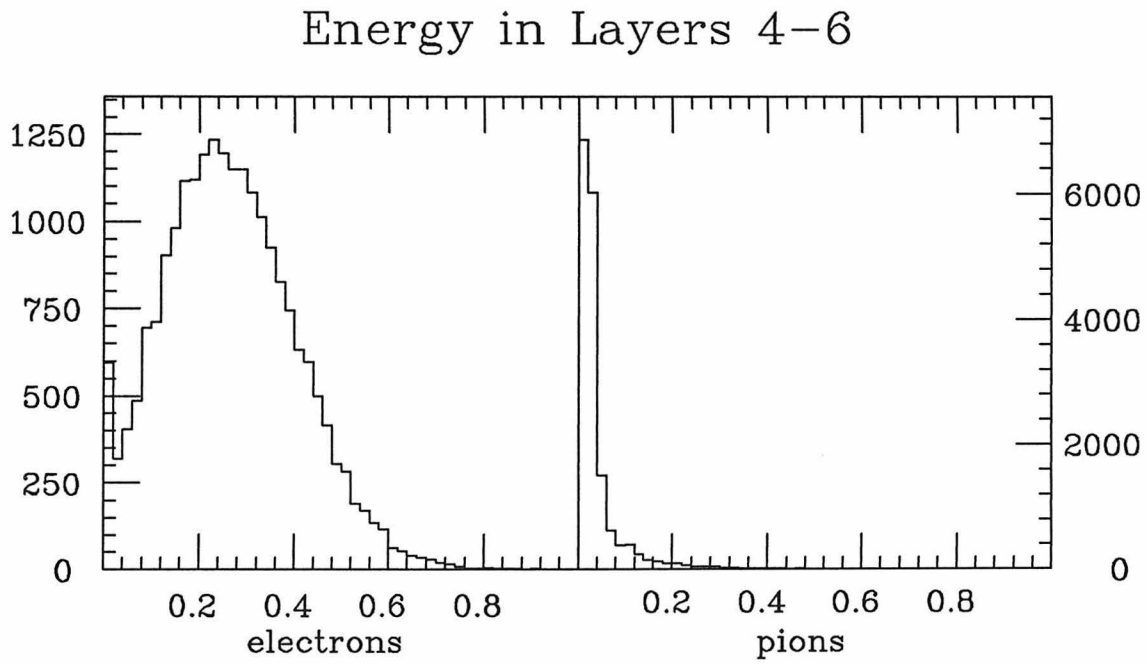

Figure 6.3.7: Energy in layers 4 – 6 of shower detector

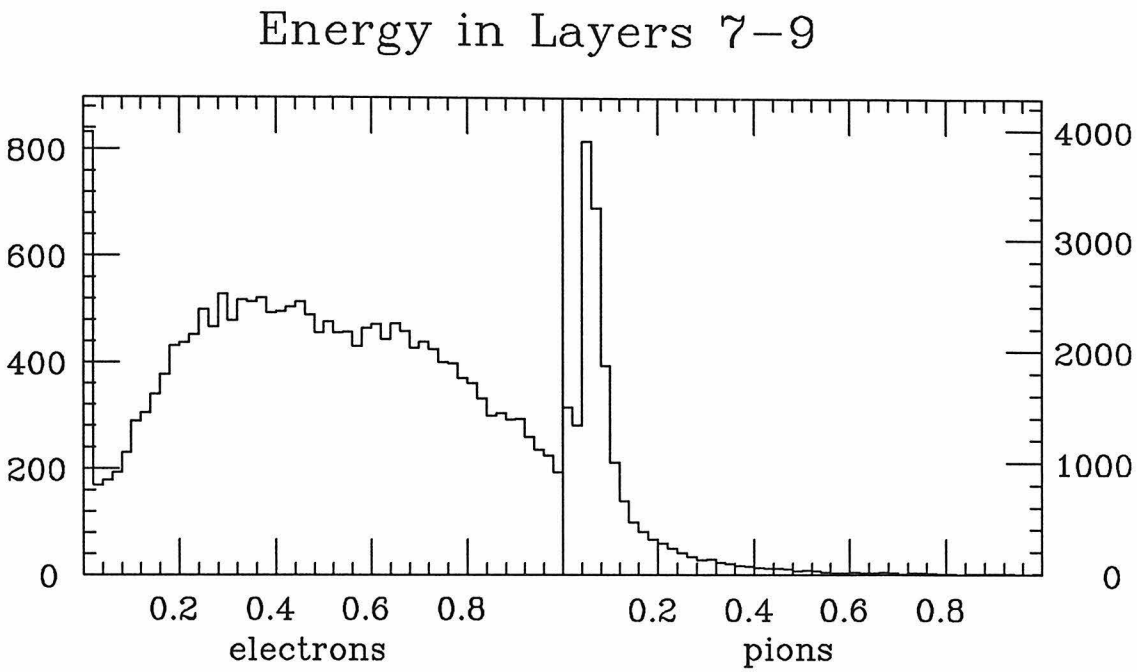

Figure 6.3.8: Energy in layers 7 – 9 of shower detector

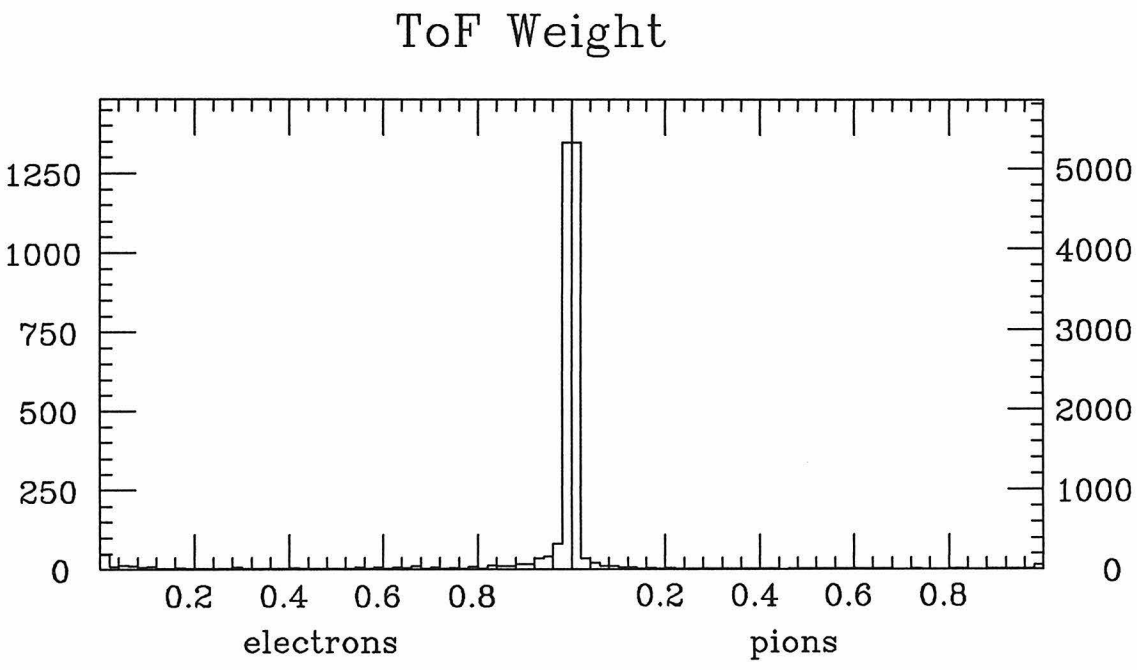

Figure 6.3.9: Normalized ToF weight

Chapter 7: Semileptonic Branching Ratios: Electron Modes

7.1: Inclusive Properties

The detailed study of charmed semileptonic decays is greatly facilitated by the associated production of charmed particles at the ψ'', where the only charmed particles produced are pairs of D mesons. There is so little phase space available that not even a pion may accompany the D pair. If one D in an event is reconstructed in an hadronic decay, the remainder of the event must consist of the decay products of the companion $\overline{D}$. Thus it is possible to isolate semileptonic decays cleanly in spite of the neutrino which, of course, is not observed.

The inclusive semileptonic branching ratios of charmed mesons are of great theoretical interest as these are related to the lifetimes of these particles.* The MARK II[75] and MARK III[76] collaborations have measured — using similar techniques — the inclusive semileptonic branching ratios of D mesons. A set of hadronic tags is first isolated, as detailed in section 5.3. The charged tracks recoiling from each tag are then examined. A track with valid ToF information is identified as a kaon if $W_K/W_{tot} \geq 0.8$. All tracks are classified as pions or electrons by the procedures of section 6.3. These procedures classify *each* track as a pion or electron. For this reason, tracks identified by the ToF system as kaons are removed from further consideration; with their relatively large ionization losses, kaons are more likely then pions to be misidentified as electrons.

The number of signal electrons is calculated through an *unfold* procedure. Let the numbers of detected electrons and pions be N_e^D and N_π^D, and let the number of signal particles be N_e^S and N_π^S. These quantities are related through

---

* This is discussed more fully in section 2.1.

the equations:

$$N_e^D = N_e^S P(e \to e) + N_\pi^S P(\pi \to e)$$
$$N_\pi^D = N_e^S P(e \to \pi) + N_\pi^S P(\pi \to \pi)$$

The factor $P(a \to b)$ is the probability that a signal particle of type a will be detected as a particle of type b. These probabilities are given in Tables 6.3.I – 6.3.IV. The number of signal electrons is obtained by inverting the above equations, with one set of equations for each of the seven momentum ranges indicated in the tables.

The number of signal electrons must be corrected for both charge-symmetric and non-charm backgrounds. One of the particles from an *hadronic* D decay may be misidentified as an electron due to the decay of a hadron, the production of a pair of electrons, or the misidentification of a hadron. These processes are all charge-symmetric, producing an equal number of electrons and positrons. Cabibbo favored semileptonic decays, being spectator decays, yield leptons whose charge is correlated with the charm of the tag; a tag of positive charm should be accompanied by an electron while a tag of negative charm should be accompanied by a positron. The number of signal events may be corrected for charge-symmetric backgrounds by analyzing the *right-sign* particles — particles with charge corresponding to the charm of the tag — and *wrong-sign* particles separately. The number of right-sign and wrong-sign electrons are unfolded separately, and the number of wrong-sign electrons subtracted from the number of right-sign electrons.

The tag samples contain not only charm decays but also hadronic decays of non-charm origin, as may be seen in Figs. 5.3.1 and 5.3.2. These non-charm events have a large range of beam-constrained masses. Thus events with masses within a control region far from the D mass may be used to correct for the effect of non-charm events under the D mass peak. The numbers of right-sign and wrong-sign particles are recorded for the control region, then unfolded and subtracted to obtain the number of control electrons. This number of electrons

from the control region is scaled appropriately and subtracted from the number of events in the D mass region.

The inclusive branching ratios are obtained by correcting the number of electrons for the detection efficiency. The inclusive branching ratios reported by the MARK II collaboration are:

$$B(D^0 \rightarrow e^+ X) = 5.5 \pm 3.7\%$$
$$B(D^+ \rightarrow e^+ X) = 16.8 \pm 6.4\%$$

The branching ratios measured by the MARK III are of higher precision:

$$B(D^0 \rightarrow e^+ X) = 7.5 \pm 1.1 \pm 0.4\%$$
$$B(D^+ \rightarrow e^+ X) = 17.0 \pm 1.9 \pm 0.7\%$$

The errors are statistical and systematic, respectively.

This inclusive analysis may be carried a step further. It is possible using the same techniques to measure the number of charged particles produced in a semileptonic decay. The tag modes considered are:

$$D^0 \rightarrow K^-\pi^+,\ K^-\pi^+\pi^+\pi^-,\ K^-\pi^+\pi^0$$
$$D^+ \rightarrow K^-\pi^+\pi^+,\ \overline{K}^0\pi^+,\ \overline{K}^0\pi^+\pi^+\pi^-,\ \overline{K}^0\pi^+\pi^0$$

For simplicity, only the states of positive charm are listed here. The decays of the $\overline{D}^0$ and D^- are, of course, considered as well. The signal region is defined as the range of tag beam-constrained masses from 1.86 to 1.87 GeV/c^2 for neutral tags and from 1.865 to 1.875 GeV/c^2 for charged tags. In both cases, the range from 1.80 to 1.84 GeV/c^2 serves as a control region.

The tagging procedure may find a number of tags in a single event. This is particularly true for those modes containing a π^0. There is no straightforward procedure for determining which of these tags is the "correct" one. For the present analysis, only the *first* tag encountered in each event is considered. The relative numbers of charged particles will be correct, but these numbers may not conveniently be converted to branching ratios.

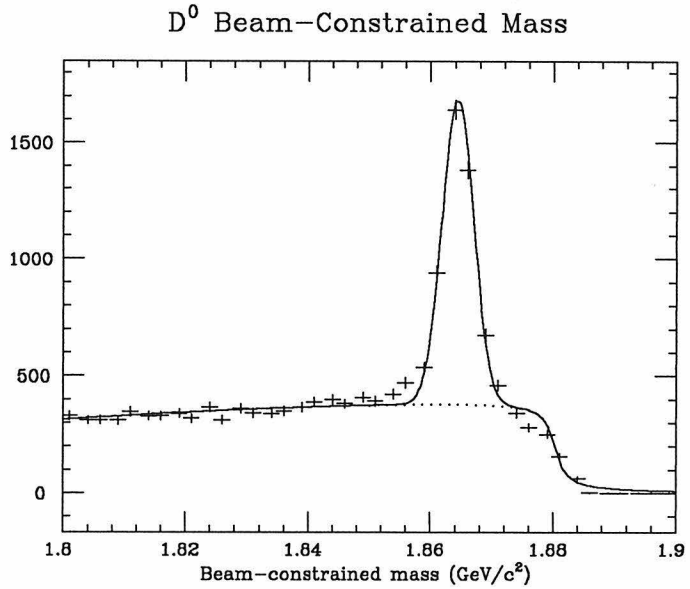

Figure 7.1.1: D^0 tag mass spectrum for multiplicity study

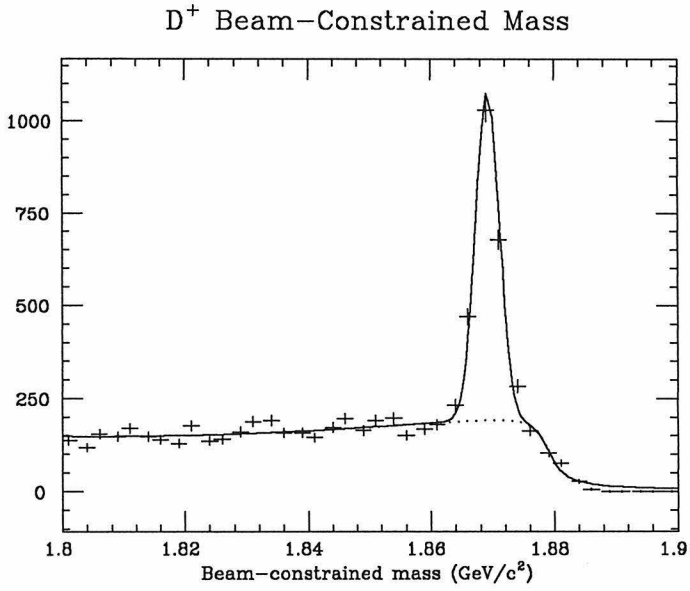

Figure 7.1.2: D^+ tag mass spectrum for multiplicity study

The numbers of signal and background events is obtained by subjecting the observed numbers of events to the fitting procedure of section 5.3. The tag spectra are given in Figs. 7.1.1 and 7.1.2 with the fitted distributions overplotted. The results of the fit are summarized in Tables 7.1.I and 7.1.II.

Table 7.1.I: D^0 tags: results of fit

Signal events (1.86 – 1.87 GeV/c^2)	3130 ± 38.9
Background events (1.86 – 1.87 GeV/c^2)	1512 ± 38.9
Background events (1.80 – 1.84 GeV/c^2)	5489 ± 74.1
scale factor = 1512/5489 = 0.276	

Table 7.1.II: D^+ tags: results of fit

Signal events (1.865 – 1.875 GeV/c^2)	1695 ± 27.7
Background events (1.865 – 1.875 GeV/c^2)	764.9 ± 27.7
Background events (1.800 – 1.840 GeV/c^2)	2444 ± 49.4
scale factor = 764.9/2444 = 0.313	

As indicated in the tables, the results from the control regions must be scaled by factors of 0.276 and 0.313 for D^0 and D^+ events, respectively.

All tracks passed to the π/e separation algorithm are required to have good z information; they must have valid information from at least one stereo layer in the drift chamber. They must also have valid ToF information. The trees for tracks without ToF information admit much larger backgrounds; compare, for example, Tables 6.3.I and 6.3.II.

The charged multiplicity of the recoil from each tag is found simply by counting the number of charged tracks not used in the tag. No further requirements are placed on these charged tracks. The number of electrons for each charged multiplicity are given in tables 7.1.III and 7.1.IV.

Table 7.1.III: Electrons from D^0 by multiplicity

Multiplicity	Signal Region		Control Region		Net
(prongs)	Right sign	Wrong sign	Right sign	Wrong sign	
1	14.1	-0.1	3.1	8.7	15.7 ± 3.9
2	137.8	23.3	40.6	30.4	111.7 ± 12.9
3	20.0	10.6	29.9	16.6	5.7 ± 5.8
4	24.2	17.3	40.5	25.3	2.6 ± 6.8
5	4.6	12.6	15.8	9.9	-9.7 ± 4.3
6	2.9	1.6	7.9	7.0	1.0 ± 2.4
7	1.0	0.8	2.9	0.9	-0.5 ± 1.4

Table 7.1.IV: Electrons from D^+ by multiplicity

Multiplicity	Signal Region		Control Region		Net
(prongs)	Right sign	Wrong sign	Right sign	Wrong sign	
1	103.3	-0.2	11.4	-0.1	99.9 ± 10.3
2	13.2	5.1	11.0	5.4	6.3 ± 4.5
3	72.0	14.7	22.5	16.6	55.5 ± 9.5
4	14.2	0.7	8.9	3.0	11.7 ± 4.0
5	8.8	4.7	3.6	3.9	4.2 ± 3.8
6	0.7	0.9	1.6	2.7	0.1 ± 1.5
7	2.2	0.0	0.9	-0.1	1.9 ± 1.5

The number of produced and detected events are related by an efficiency matrix: $N^D = \epsilon N^P$, $N^D = (N^D(\text{1prong}), \ldots, N^D(\text{7prongs}))$. For the D^0, the produced multiplicities are two, four, and six, while for the D^+, they are one, three, five, and seven. Thus the dimension of the efficiency matrix for the D^0 is 7×3 and for the D^+ is 7×4. The components of these matrices are measured

by passing Monte Carlo generated events through the same analysis programs as the data. The following decays were generated:

$$D^0 \to K^- e^+\nu_e,\ K^{*-} e^+\nu_e,\ K^- \pi^+ \pi^+ \pi^- \pi^- e^+ \nu_e$$
$$D^+ \to \overline{K}^0 e^+ \nu_e,\ \overline{K}^{*0} e^+ \nu_e,\ \overline{K}^0 \pi^+ \pi^- e^+ \nu_e,\ \overline{K}^0 \pi^+ \pi^+ \pi^- \pi^- e^+ \nu_e$$

Several of these modes may produce the same number of tracks. For example, $\overline{K}^0\pi^+\pi^-e^+\nu_e$ and $\overline{K}^0\pi^+\pi^+\pi^-\pi^-e^+\nu_e$ both have five prong components. Where there is such an overlap, the efficiencies are averaged. The efficiency matrices so obtained are:

$$\epsilon(D^0) = \begin{array}{c} \\ 1 \\ 2 \\ 3 \\ 4 \\ 5 \\ 6 \\ 7 \end{array} \begin{array}{c} \begin{array}{ccc} 2 & 4 & 6 \end{array} \\ \begin{pmatrix} 0.050 & 0.0 & 0.0 \\ 0.585 & 0.012 & 0.0 \\ 0.009 & 0.129 & 0.011 \\ 0.002 & 0.461 & 0.049 \\ 0.001 & 0.003 & 0.153 \\ 0.0 & 0.0 & 0.135 \\ 0.0 & 0.0 & 0.004 \end{pmatrix} \end{array}$$

$$\epsilon(D^+) = \begin{array}{c} \\ 1 \\ 2 \\ 3 \\ 4 \\ 5 \\ 6 \\ 7 \end{array} \begin{array}{c} \begin{array}{cccc} 1 & 3 & 5 & 7 \end{array} \\ \begin{pmatrix} 0.628 & 0.005 & 0.0 & 0.0 \\ 0.010 & 0.109 & 0.002 & 0.0 \\ 0.010 & 0.480 & 0.031 & 0.002 \\ 0.0 & 0.009 & 0.156 & 0.014 \\ 0.0 & 0.001 & 0.259 & 0.075 \\ 0.0 & 0.0 & 0.004 & 0.154 \\ 0.0 & 0.0 & 0.0 & 0.132 \end{pmatrix} \end{array}$$

The number of produced events of each multiplicity is obtained through a

least-squares fit, minimizing the χ^2 function:

$$\chi^2 = \sum_{i=1}^{7} \frac{(N_i^O - N_i^D)^2}{\sigma_i^2}$$

Here, N_i^O is the observed number of events of multiplicity i and σ_i is the standard deviation of this number. N_i^D is the number of events predicted. The results of the fit are summarized in Tables 7.1.V and 7.1.VI.

Table 7.1.V: Results of Multiplicity Fit for D^0

Multiplicity	Produced Events
2 prongs	200.3 ± 21.1
4 prongs	8.3 ± 14.5
6 prongs	-13.5 ± 15.2
χ^2/degree of freedom = 1.85	

Table 7.1.VI: Results of Multiplicity Fit for D^+

Multiplicity	Produced Events
1 prong	157.6 ± 16.4
3 prongs	90.9 ± 18.0
5 prongs	27.7 ± 12.9
7 prongs	5.4 ± 7.4
χ^2/degree of freedom = 2.18	

The results given in these tables indicate that the semileptonic decays of D^0 mesons result most often in two charged tracks with some four prong events produced as well. The semileptonic decays of D^+ mesons produce mostly one and three prong events, but there is evidence that some five prong events are produced also. The arguments of section 3.2 indicate that the mass of any resonant hadronic state produced in D semileptonic decay is likely to be bounded

by 0.9 GeV/c^2. It is thus to be expected that the following decays might yield observable signals:

$$D^0 \rightarrow K^- e^+ \nu_e,\ K^- \pi^0 e^+ \nu_e,\ \overline{K}^0 \pi^- e^+ \nu_e,\ \pi^- e^+ \nu_e,\ \rho^- e^+ \nu_e$$
$$D^+ \rightarrow \overline{K}^0 e^+ \nu_e,\ K^- \pi^+ e^+ \nu_e,\ \pi^- \pi^+ e^+ \nu_e$$

7.2: Exclusive decays

Although a great deal of information may be gleaned from inclusive measurements, of at least equal importance is the reconstruction of exclusive final states. In particular, the study of charm decays has been spurred by the abundance of exclusive measurements; many of the details discussed in chapters 2 and 3 would be of merely academic interest were it not for the results of several experiments on the exclusive hadronic decays of D and F mesons.

It was pointed out — at considerable length — in chapter 3, that the description of semileptonic decays is a much more tractable theoretical problem than that of hadronic decays. The nature of the W-lepton vertex is not disputed within the context of the Standard Model. Thus *semileptonic* decays may be used to probe the structure of the *hadronic* matrix elements. In particular, as there are no strong final state interactions between the leptons and quarks, a measurement of the semileptonic branching ratios provides information on the spin and momentum dependence of these hadronic matrix elements.

No previous experiment has had the capacity for good electron identification and good exclusive reconstruction in concert with a large enough sample of charm events to reconstruct exclusive semileptonic decays. That the MARK III detector is capable of reconstructing events in which both D's decay hadronically has been demonstrated through the direct measurement of D hadronic branching

ratios.[77] It is also possible with the MARK III to reconstruct semileptonic decays completely. In events with an hadronic tag, the four-momentum of the companion $\overline{D}$ is known *a priori*, so the missing momentum and energy — that carried by the unobserved neutrino — may be calculated unambiguously.

7.2.1: $D^0 \rightarrow K^- e^+ \nu_e$

The decay $D^0 \rightarrow K^- e^+ \nu_e$ produces the simplest final state to be isolated in the recoil spectrum. The tag sample used for isolating this decay consists of tags of the types $D^0 \rightarrow K^-\pi^+$, $K^-\pi^+\pi^+\pi^-$, and $K^-\pi^+\pi^0$. For reasons which will be explained below, *all* tags are considered; if a particular event has several tags, each is considered.

There must be two charged tracks of opposite charge recoiling from the tag. The *right-sign* track — the track with charge corresponding to the charm of the tag — is classified by the ToF system and the π/e separation algorithm. If the track has valid ToF information, it is classified as a kaon if $W_K/W_{tot} \geq 0.8$. Only tracks not classified as kaons, but identified as electrons by the π/e separator, will be considered candidate electrons. For this purpose, all of the trees of the π/e separator are used. In order to ensure the quality of the electron tracks, each must have a successful helix fit including valid z information.

The *wrong-sign* track is assumed to be a hadron. The quantity $U \equiv E_{\rm missing} - P_{\rm missing}$ is calculated for two hypotheses: that the hadron is a kaon and that it is a pion.* The missing momentum vector must 'point' to an instrumented region of the detector. The track is considered to be a kaon if the corresponding value of U is closer to zero than that for the pion hypothesis. Spectra of this variable are shown in Fig. 7.2.1 for both hypotheses for Monte Carlo events of the type

* The value of U is zero if only a single massless particle is missing. Since this variable is linear in the missing energy and momentum, its resolution depends only on the resolutions in these quantities. The resolution in the missing mass, on the other hand, also depends explicitly on the missing energy and momentum.

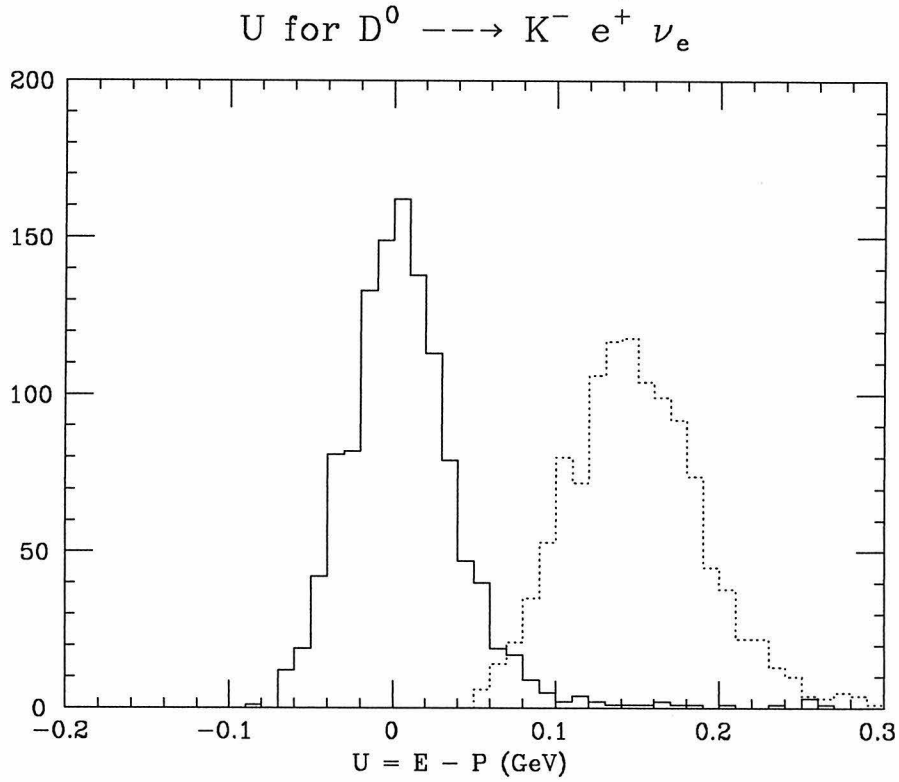

Figure 7.2.1: U for $K^-e^+\nu_e$ events from Monte Carlo
— Kaon hypothesis ··· pion hypothesis

$D^0 \to K^-e^+\nu_e$. The good separation of the two distributions is evident. If the candidate kaon track has valid ToF information, the weight must be consistent with the kaon hypothesis: specifically, $W_K/W_{tot} \geq 0.7$. Finally, the track must have a helix fit with valid z information.

Backgrounds may arise from several sources. Two-body hadronic decays such as $D^0 \to K^-\pi^+$ may be removed by placing a cut on the invariant mass of the $K\,e$ system, calculated under the assumption that the electron is really a pion. Requiring this invariant mass to be less than 1.7 GeV/c^2 removes about 60% of the two-body decays.† The position of this cut is very near the endpoint of the

† This figure is obtained by 'turning off' the π/e separator. If the candidate electrons are required to be identified by this algorithm, about 99% of the two-body decays are removed.

invariant mass spectrum for $K^-e^+\nu_e$ events, so less than 10% of the signal events are lost through imposing this cut.

The decay of the D^0 with the largest branching ratio is $D^0 \rightarrow K^-\pi^+\pi^0$. If the π^+ were misidentified as an electron this decay could be misclassified as a semileptonic decay. Such contamination may be limited by examining the neutral tracks in the recoil. A neutral track may be the result of a photon interacting in one of the shower detectors, but it may also be a 'fake photon'. These may occur for a number of reasons: chief among them are electronic noise and the 'split-offs' from hadronic and electromagnetic showers. Fake photons from electronic noise usually have low pulse heights and thus low measured energies. Split-offs are almost always near the entry point of a charged track into the shower detector. The cosine of the angle $\vartheta_{\gamma\text{charged}}$, where $\vartheta_{\gamma\text{charged}}$ is the angle between the direction of the photon and that of the nearest charged particle at the face of the shower detector, is plotted in Fig. 7.2.2 for all neutral tracks in the D tagged sample. The distribution increases substantially for values of $\cos\vartheta_{\gamma\text{charged}}$ greater than 0.96.

An *isolated photon* is defined as a neutral track with measured energy greater than 100 MeV and $\cos\vartheta_{\gamma\text{charged}} < 0.95$; the definition of an isolated photon requires also that the shower begin within the first three radiation lengths of material in the shower detector. Hadronic split-offs are not modeled in the shower simulation; it is clear, however, that a cut at $\cos\vartheta_{\gamma\text{charged}} < 0.95$ will eliminate virtually all of these split-offs. If the angular distributions of the various particles are generated with care, such a cut will not introduce serious systematic uncertainties. Neutral tracks identified as *isolated photons* are likely to be *real* photons. Hadronic backgrounds may thus be considerably diminished by discarding events with unused isolated photons. Indeed, about 50% of decays of the type $D^0 \rightarrow K^-\pi^+\pi^0$ may be eliminated by requiring that there be no isolated photons in the event.

There are two other sources of background events: the semileptonic decays

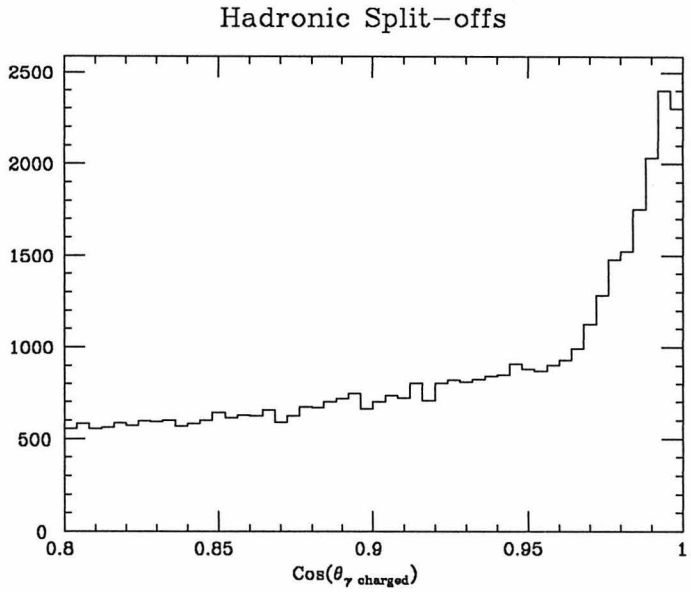

Figure 7.2.2: $\mathrm{Cos}(\vartheta_{\gamma\mathrm{charged}})$ for all events in the D tagged sample

$D^0 \to K^-\pi^0 e^+\nu_e$ and $K^0_L\,\pi^- e^+\nu_e$. In both cases, there is a great deal of missing energy. Requiring that the missing energy be less than 900 MeV removes about 40% of these events; as this is near the endpoint of the neutrino lab-frame energy spectrum for $K^- e^+\nu_e$ events, it has little effect on the detection efficiency for such events.

Forty-eight events pass the cuts detailed above. The beam-constrained masses of all the D^0 tags are compared in Fig. 7.2.3 with those of the forty-eight signal events in Fig. 7.2.4. It is clear from these two figures that the amount of non-charm contamination has been dramatically reduced. Indeed, since non-charm events populate the entire range from 1.80 – 1.88 GeV/c^2 in Fig. 7.2.3, the almost total lack of events in the range 1.80 – 1.85 GeV/c^2 in Fig. 7.2.4 makes it clear that non-charm events are not a serious source of background. Thus the only cut that need be placed on the tags themselves is a requirement that their beam-constrained masses be in the range 1.85 – 1.88 GeV/c^2. Forty-seven events remain after the imposition of this cut.

The number of backgrounds events expected is estimated by a Monte Carlo

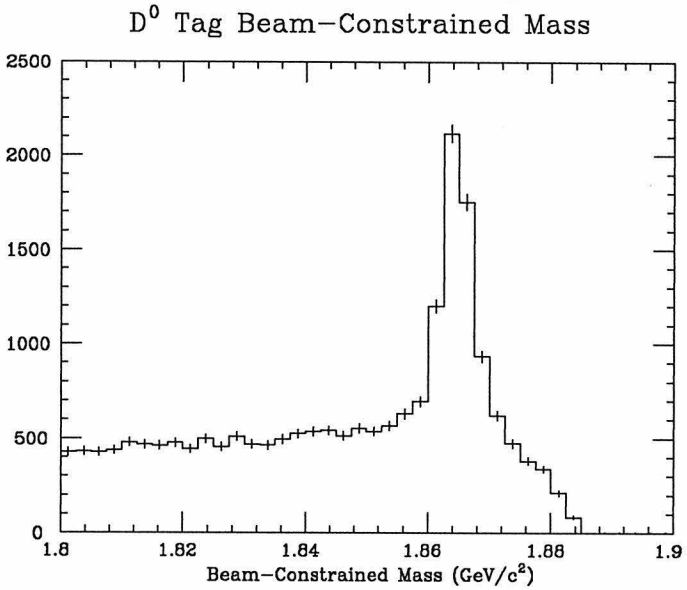

Figure 7.2.3: Tag beam-constrained mass for all D^0 tags

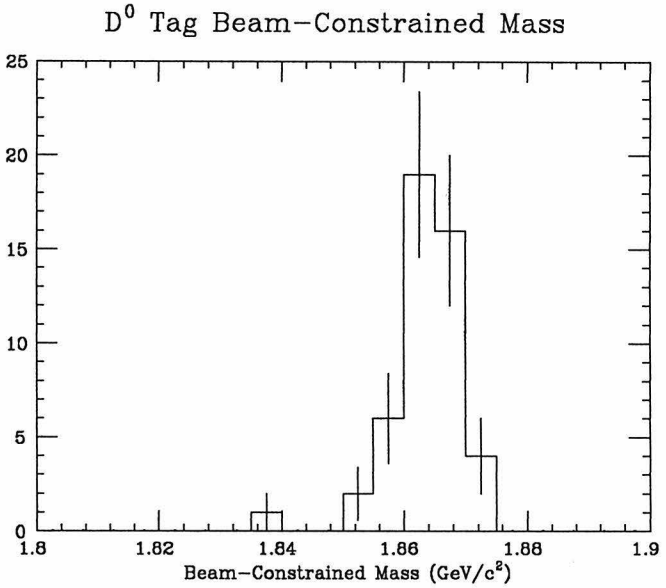

Figure 7.2.4: Tag beam-constrained mass for all signal events

simulation. The initial D and $\overline{D}$ are forced to decay to the appropriate final states. For semileptonic decays, the formulae of appendix 3 are used. For hadronic decays, the 4-momenta are generated according to phase-space.[78] Hadronic resonances produced in the D decay are allowed to decay to stable particles.

Stable particles are propagated through a model of the MARK III which simulates all of the important systems of the detector. Charged tracks are transported along a piecewise helical track. Multiple Coulomb and nuclear scattering are accounted for in all potential scattering centers before the ToF counters. The amount of material in the beam pipe, and drift chamber walls, gas and wires is tabulated — in radiation lengths for the multiple Coulomb scattering and in hydrogen equivalents* for the nuclear scattering. In the former case, the scattering angle is generated, using the momentum and the amount of material traversed, according to a Gaussian distribution. The cross-sections used in the nuclear scattering calculations are given in Tables 7.2.I – 7.2.II.[79] The scattering probabilities are:

$$P_{\text{total}} = 1 - e^{-\sigma_{\text{total}} N}$$

$$P_{\text{elastic}} = P_{\text{total}} \frac{\sigma_{\text{elastic}}}{\sigma_{\text{total}}}$$

The quantity N is the number-density of the material being traversed. If the scattering is determined to be inelastic, the particle is absorbed. If the scattering is elastic, the momentum transfer t is generated in the range:

$$-\frac{4m_p^2 p^2}{2Em + m^2 + m_p^2} \leq t \leq 0$$

Here, E,p, and m are the energy, momentum and mass of the incident particle. The probability distribution of t is given in the optical model[80] by:

$$P(t) \equiv \frac{1}{\sigma_{\text{elastic}}} \frac{d\sigma_{\text{elastic}}}{dt} = \frac{1}{\sigma_{\text{elastic}}} e^{Bt}$$

$$B = \frac{\sigma_{\text{total}}}{16\pi(1 - \sigma_{\text{total}}/\sigma_{\text{elastic}})}$$

The scattering angle is calculated from the generated value of t.

---

* The number of nuclei in one gram of material is N_0/A where N_0 is Avogadro's number and A is the atomic weight. The cross-section of a nucleus is approximately proportional to $A^{2/3}$. Thus, the *hydrogen equivalent* number-density of a material is $N = b * A^{2/3} * N_0/A$ where b is the thickness. Here, the difference in the proton and neutron cross sections is ignored.

Table 7.2.I: Total cross sections for nuclear scattering

p_{lab} (GeV/c)	Total cross section (mb)					
	π^+	π^-	K^+	K^-	p	$\overline{p}$
0.20	54.7	26.6	11.8	113.8	20.2	281.0
0.30	200.0	67.8	12.7	79.4	20.2	281.0
0.40	73.8	32.4	13.7	69.8	20.2	203.1
0.50	40.8	27.2	13.0	44.7	20.2	168.0
0.60	25.0	29.3	13.0	37.8	24.4	152.9
0.70	17.4	43.0	12.6	34.2	24.8	130.0
0.80	15.5	36.7	13.0	41.0	24.3	104.0
0.90	20.7	41.6	14.2	43.4	25.0	116.8
1.00	24.4	60.6	16.0	49.8	28.8	117.4
1.20	30.0	37.2	18.5	36.9	35.6	109.0
1.40	39.4	36.7	18.3	31.6	46.5	102.8
1.60	40.0	34.8	17.7	32.5	47.5	97.8
1.80	31.4	34.6	18.0	31.9	47.5	95.5
2.00	29.3	36.2	17.6	30.4	47.2	90.2
3.00	29.2	32.0	17.2	27.4	44.5	76.6
4.00	28.0	29.9	17.6	28.2	42.3	66.8

The ionization losses of charged particles are modeled differently in the solid materials of the detector and in the drift chamber gas. The expected energy loss in the solid materials is computed from the Landau-Sternheimer formula:[81]

$$\frac{dE}{dx} = \frac{N}{\beta^2}\left(8.991 + \log(\gamma^2) - \beta^2 - \delta\right)$$

The constant δ accounts for the Sternheimer density effect; N is a normalization constant. This formula is unreliable for materials of very low density, so for

Table 7.2.II: Elastic cross sections for nuclear scattering

p_{lab} (GeV/c)	Total cross section (mb)					
	π^+	π^-	K^+	K^-	p	$\overline{p}$
0.20	30.0	6.2	11.6	59.1	20.0	100.8
0.30	40.0	22.5	12.3	40.4	20.0	80.0
0.40	60.2	13.8	11.7	32.1	20.0	73.1
0.50	38.7	10.9	12.6	21.5	20.0	62.0
0.60	20.6	12.9	12.6	17.7	20.0	55.4
0.70	13.0	20.0	11.4	14.2	20.0	45.0
0.80	9.4	14.9	13.0	19.3	20.0	49.0
0.90	8.1	14.8	12.1	20.9	22.0	48.1
1.00	11.2	26.4	11.2	21.8	24.0	46.1
1.20	13.6	12.5	10.6	12.7	25.0	43.2
1.40	19.2	12.3	9.5	8.8	24.0	38.0
1.60	16.7	9.8	8.6	8.9	26.0	31.1
1.80	12.3	9.6	7.6	8.1	21.0	30.0
2.00	9.8	8.0	6.2	7.5	21.5	28.0
3.00	7.8	6.7	5.1	5.0	17.0	21.2
4.00	6.4	6.4	4.2	4.3	13.5	19.8

the drift chamber gas, the energy loss is generated using a function obtained by fitting to the pulse heights measured on the wires of Layer 2.

The probability of photon pair conversion is calculated for each of the various regions of the detector. In practice, given the very low mass of the detector components, significant pair production occurs only within the beam pipe and the drift chamber walls.

A time-of-flight is generated for each charged track if it hits a ToF counter.

The model produces a Gaussian distribution of times using the measured resolution of each counter.

The simulation of electromagnetic showers is based on a simple analytic model.[82] The energy deposited in each layer is generated first. Next, a series of hits on the sense wires is produced according to these generated energies; the pulse heights on each wire are 'smeared' according to a Gaussian distribution. No attempt is made to take the effect of the support ribs into account. The parameters of the model are optimized so that the Monte Carlo data reproduces the energy and angular resolutions observed in the real data.

The model used for electromagnetic showers does not produce the correct lateral or longitudinal shower development. The π/e separation algorithm depends critically on the detailed structure of the shower, so this algorithm may not be used with Monte Carlo data. Instead a 'black box' approach is adopted: it is decided on the basis of the momentum, presence or absence of ToF information, and particle type whether a track is to be classified as a pion or electron. The measured efficiencies, given in Tables 6.3.I – 6.3.IV, form the heart of the *black box*. Thus, the results obtained are statistically correct, that is the results will be correct if a large number of events is analyzed.

The energy deposited in the shower detector by hadrons and muons is generated according to the *observed* energy spectra of these particles. The hits on the wires are generated according to model describing the showers of minimum ionizing particles. The energy deposition is thus correctly modeled — even the energy deposited through inelastic interactions is taken into account — but the pattern of this energy deposition does not reflect all of the features of hadronic showers. In particular, hadronic split-offs are not modeled at all.

A number of backgrounds have been investigated. The probability, ϵ_B, that a background event may be identified as a signal event is determined from the Monte Carlo simulation; the Monte Carlo data is passed through the same analysis programs as the real data. In some cases, the probability is so small that

no events are detected. In such cases, the 63.8% confidence level upper limit — corresponding to one σ — is used. The number of background events expected is:

$$N_B = N_{\text{tags}} \cdot B_B \cdot \epsilon_B$$

Here, B_B is the branching ratio of the background process. The branching ratios for the $K^-\rho^+$ and $K^{*-}\pi^+$ final states* are derived from an analysis[83] of the resonant substructure of the decays $D^0 \to K^-\pi^+\pi^0$ and $D^0 \to \overline{K}^0\pi^+\pi^-$. The numbers of background events expected are given in Table 7.2.III. An overall uncertainty of 50% is assigned to the total number of background events.

Table 7.2.III: $D^0 \to K^- e^+ \nu_e$: Expected Backgrounds

Source	ϵ_B	B_B	N_B
$K^{*-}e^+\nu_e$	0.0076 ± 0.0014	$\sim 4\%$	1.2
$K^-\rho^+$	0.0005 ± 0.0004	$13.0 \pm 1.3 \pm 1.3\%$	0.3
$K^{*-}\pi^+$	0.0013 ± 0.0006	$8.0 \pm 1.3 \pm 1.3\%$	0.4
$K^-\pi^+\eta$	0.0003 ± 0.0003	$\leq 10\%$	0.1
$\overline{K}^{*0}\pi^0$	≤ 0.0003	$2.0 \pm 0.9 \pm 0.5\%$	0.02
$K^-\pi^+\pi^0\pi^0$	≤ 0.0003	$\sim 8\%$	0.1
		Total	2.1 ± 1.1

The efficiency for detecting the $D^0 \to K^- e^+ \nu_e$ signal is also determined by a Monte Carlo simulation. This detection efficiency is *not* independent of the tag type, as might be supposed. The more tracks there are in the tag, the more 'crowded' the event is — the more difficult it is to reconstruct all of the tracks in the recoil. Detection efficiencies are therefore calculated for each tag type. The

* See also Table 2.1.III.

decay $D^0 \to K^-\pi^+\pi^0$ is known to be dominated by the quasi two-body decay $D^0 \to K^-\rho^+$ so this final state is used to represent the $K^-\pi^+\pi^0$ tag. Little is known about the resonant substructure of the decay $D^0 \to K^-\pi^+\pi^+\pi^-$; this is generated according to phase-space. The detection efficiencies are listed in table 4.2.IV.

It is quite simple to extract a branching ratio when a large tag sample is available. If the tag and signal modes are different — as is manifestly the case for semileptonic decays — the number of signal events expected is:

$$N^S_{\text{expected}} = B \cdot N_{\text{tags}} \cdot \epsilon_S + N_{\text{background}}$$

The branching ratio is here denoted by B and the detection efficiency by ϵ_S. The uncertainty in the branching ratio obtained from this formula will be dominated by the uncertainty in the number of detected events. The uncertainty in the number of tags is *not* $\approx \sqrt{N_{\text{tags}}}$ as might be expected. The number of tags may be thought of as the number of experiments performed with the product of B and ϵ_S being the probability of success. Were there no background in the tag sample, the uncertainty in the number of tags would be zero. As there are indeed background events in the tag sample, the uncertainty in the number of tags is equal to the uncertainty in the number of background events.

In Table 7.2.IV, the branching ratio for the decay $D^0 \to K^-\, e^+\, \nu_e$ is calculated for each tag mode. The number of background events should be proportional to the number of tags, so the number of background events assigned to the i^{th} mode is:

$$N^i_{\text{background}} = N^{\text{total}}_{\text{background}} \left(\frac{N^i_{\text{tags}}}{N^{\text{total}}_{\text{tags}}} \right)$$

A weighted average is calculated from the three individual branching ratios according to the formula:

$$\overline{B} = \left[\sum_{j=1}^{3} \frac{1}{\sigma^2_{Bj}} \right]^{-1} \sum_{i=1}^{3} \frac{B_i}{\sigma^2_{Bi}}$$

As is clear from the results listed in Table 7.2.IV, the number of events detected for each tag mode is quite small. The averaging procedure employed above is correct only if the various random variables are normally distributed; it is thus of dubious applicability in the present case. It is included only to provide an 'intuitive' estimate of the branching ratio.

The branching ratio is obtained from a maximum likelihood fit. The likelihood function is:

$$\mathcal{L} = \prod_{i=1}^{3} \left(\frac{e^{-n}\, n^m}{m!} \right) \frac{1}{\sigma_i(\overline{\epsilon})\sqrt{2\pi}} \exp\left(-\frac{(\epsilon_i - \overline{\epsilon}_i)^2}{2\sigma_i^2(\overline{\epsilon})} \right) \frac{1}{\sigma_i(\overline{N})\sqrt{2\pi}} \exp\left(-\frac{(N_i - \overline{N}_i)^2}{2\sigma_i^2(\overline{N})} \right)$$

Here, m is the number of events detected against the i^{th} tag mode, n is the expected number of events, $\overline{\epsilon}_i$ the measured detection efficiency and $\overline{N}_i$ the measured number of tags. The branching ratio, the detection efficiencies and the number of tags are used as parameters in the fit. The branching ratio from the fit is given in Table 7.2.IV. The uncertainties quoted there are both the *parabolic* error — the error obtained from the covariance matrix — and the maximum likelihood error — the error given by a change of $1/2$ in $w \equiv -\log \mathcal{L}$. A plot of w is given in Fig. 7.2.5.

The errors quoted in Table 7.2.IV are purely statistical. A number of effects may contribute to the systematic error. The assumed 50% uncertainty in the number of background events is responsible for a systematic error of 3%. The electron detection efficiencies are not perfectly known; the error caused by this is estimated by folding the electron spectrum from $D^0 \rightarrow K^- e^+ \nu_e$ with the measured detection efficiencies of the π/e separator. The resulting uncertainty is about 2%. The ToF system is modeled carefully, but a systematic dependence on the ToF cuts remains, estimated to be about 5%. The *black box* approach adopted for the modeling the π/e separator guarantees that the calculated efficiencies will be correct. This method, however, relies on the ability to pair a detected track with a track generated by the Monte Carlo event generator. As electron tracks

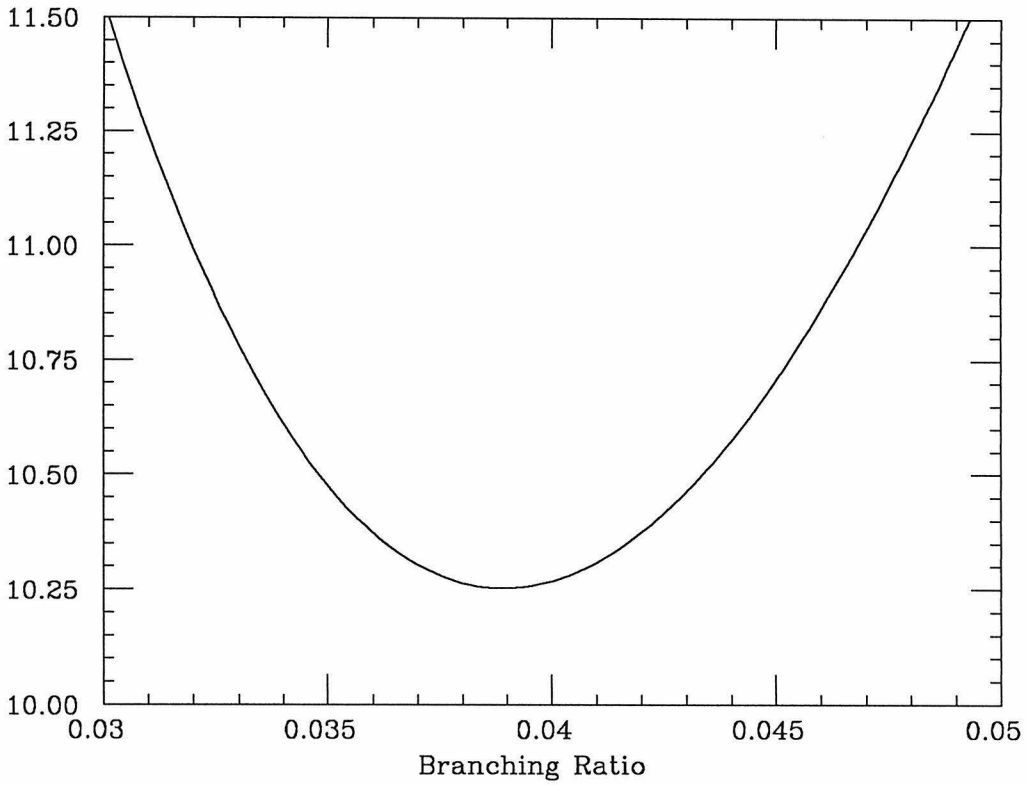

Figure 7.2.5: Plot of $w = -\log \mathcal{L}$ for $D^0 \to K^- e^+ \nu_e$

do not decay — with a resulting 'kink' — and seldom undergo a large scatter, the reconstructed and generated 4-momentum are usually quite similar. That this is not always the case introduces a small systematic error. It is difficult to quantify this error precisely, but it certainly is not larger than 5%. It might be thought that the detection efficiency could depend on the form factor chosen in the event generator. Detection efficiencies calculated using a simple pole factor, with pole mass 2.14 GeV/c^2, and a constant form factor are not, however, significantly different. If all the systematic errors are added linearly, the total systematic uncertainty is 15%.

The branching ratio for $D^0 \to K^- e^+ \nu_e$ is measured to be:

$$\boxed{\mathrm{B}(D^0 \to K^- e^+ \nu_e) = 3.9 \pm 0.6 \pm 0.6\%}$$

Table 7.2.IV: Detection Efficiencies and Branching Ratios for $D^0 \rightarrow K^- e^+ \nu_e$

Tag Mode	Events		N_{tags}	ϵ_S	B
	Signal	Background			
$K^-\pi^+$	10	0.6	1089 ± 13.8	0.289 ± 0.009	0.030 ± 0.010
$K^-\pi^+\pi^+\pi^-$	18	0.6	1254 ± 40.8	0.265 ± 0.011	0.052 ± 0.013
$K^-\pi^+\pi^0$	19	0.9	1738 ± 60.8	0.291 ± 0.013	0.036 ± 0.009
total	47	2.1	4081 ± 74.5		
Weighted Average					$3.7 \pm 0.6\%$
Fit Result with parabolic error					$3.9 \pm 0.6\%$
Fit Result with maximum likelihood error					$3.9 \pm 0.6\%$

7.2.2: $D^+ \rightarrow K^- \pi^0 e^+ \nu_e$

The analysis of this final state is very similar to that for $D^0 \rightarrow K^- e^+ \nu_e$ the primary difference being that two neutral tracks must be found which together form a π^0. The tracks must be separated from all charged tracks as explained above. No cut is placed, however, on the measured energies of the photons. There may be several combinations of photons. For example, if four photons are found, there will be six candidate π^0's. The resolution in the invariant mass of the two photon system is not sufficient for discriminating among the various combinations of photons. The angular resolution of the shower detectors is very good, but the energy resolution is simply not adequate for this task. The energies of pairs of photons are obtained from a least squares fit subject to the constraint that the mass of the two photon system equal the π^0 mass.* The value of U is calculated for each combination of photons. That combination is retained for which U is

* This involves finding the roots of a fourth order polynomial. This is accomplished by means of Newton's method with the measured energies as starting values.

nearest zero. Any isolated photons which are not part of this combination must have measured energies less than 100 MeV.

The performance of the π^0 detection procedure is illustrated in Figs. 7.2.6 – 7.2.8. A number of events of the (potentially very interesting!) type $\psi \rightarrow p\pi^0$ were generated. This state was chosen so that a single, monoenergetic π^0 would be formed recoiling against a single charged track which presumably never decays.[84] The invariant, unfit masses of the photons pairs are shown in Fig. 7.2.6. The resolutions in momentum and angle obtained from the fit are displayed in the next two figures. The fit momentum of the of π^0's is plotted in Fig. 7.2.7. It is obvious that the momentum resolution is modest. The angular resolution, however, is excellent. Fig. 7.2.8 is a plot of $\cos(\zeta)$, where ζ is defined as the angle between the generated and reconstructed directions of the π^0's.

Among the several backgrounds is one of curious origin: $D^0 \rightarrow K^- e^+ \nu_e$. This is a very small but quite interesting background. The presence of an isolated photon would preclude $D^0 \rightarrow K^- e^+ \nu_e$ decays from being detected as such. In addition, two spurious neutral tracks may seem to form a π^0; the requirement that a fit be successfully performed is *hardly* stringent. Hence, it is possible that a decay of the type $D^0 \rightarrow K^- e^+ \nu_e$ might be mistaken for $D^0 \rightarrow K^- \pi^0 e^+ \nu_e$. Such cases, fortunately, are easily removed. The value of U is calculated for both hypotheses — $D^0 \rightarrow K^- e^+ \nu_e$ and $D^0 \rightarrow K^- \pi^0 e^+ \nu_e$ — and the event retained only if U for the latter hypothesis is closer to zero.

The remaining backgrounds are all small. Three body hadronic decays such as $K^-\pi^+\pi^0$ are suppressed by a cut on the invariant mass of the $K^-\pi^0 e^+$ system calculated under the hypothesis that the electron was really a pion; the invariant mass must be less than 1.7 GeV/c^2. Other backgrounds, such as $K^-\pi^+\pi^0\pi^0$, are suppressed by eliminating events with extra isolated photons. The expected number of background events is summarized in Table 7.2.V.

The detection efficiencies and branching ratios are obtained as explained in section 7.2.1. These are given in Table 7.2.VI. In the analysis of this final state,

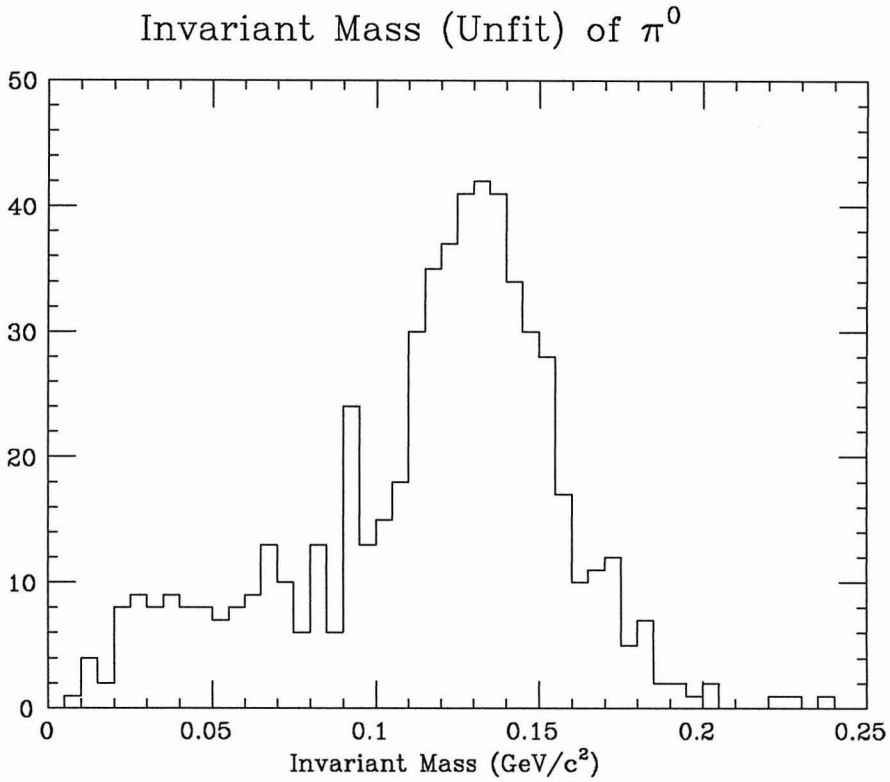

Figure 7.2.6: Invariant Mass of Photon Pairs

another potential source of systematic error has been introduced: the detection of the π^0. The requirement that the photons be well separated from all charged tracks should reduce the problem of hadronic split-offs, which are not modeled in any way in the Monte Carlo. However, the energy resolution of the shower detectors — particularly for low energy photons — makes the efficiency for detecting the π^0 somewhat difficult to calculate. This introduces an uncertainty of about 5%. The uncertainty in the number of background events yields a further error of 10%. The total systematic error is thus estimated to be 27%.

The detection efficiencies are determined from Monte Carlo events of the type $D^0 \rightarrow K^{*-} e^+ \nu_e$. The choice of the $K^- \pi^0$ mass distribution does not, however, introduce a significant systematic error. If the detection efficiencies are

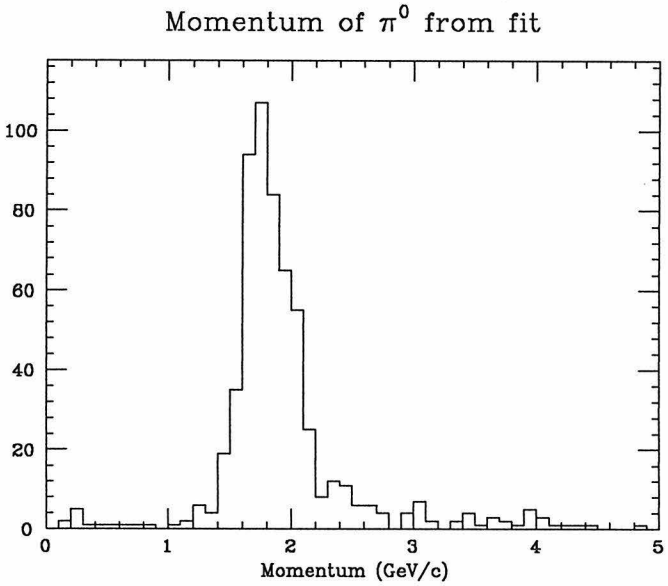

Figure 7.2.7: Reconstructed Momenta of Monoenergetic π^0's

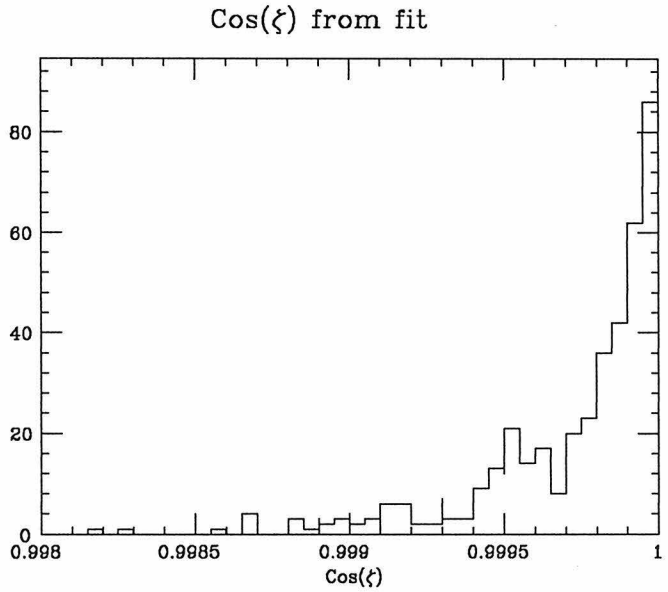

Figure 7.2.8: $\cos(\zeta)$: $\zeta \equiv$ angle between generated and reconstructed direction of π^0.

calculated using events in which the K^- and π^0 are in a non-resonant S-wave, these efficiencies change by only about one standard deviation

Table 7.2.V: $D^0 \to K^- \pi^0 e^+ \nu_e$: Expected Backgrounds

Source	ϵ_B	B_B	N_B
$K^-\rho^+$	< 0.0003	$13.0 \pm 1.3 \pm 1.3\%$	0.2
$K^{*-}\pi^+$	< 0.0003	$8.0 \pm 1.3 \pm 1.3\%$	0.1
$K^-\pi^+\pi^0\pi^0$	0.0012 ± 0.0006	$\sim 8\%$	0.4
$K^-\pi^+\eta$	0.0003 ± 0.0003	$\leq 10\%$	0.1
$\overline{K}^{*0}\pi^0$	0.0002 ± 0.0002	$2.0 \pm 0.9 \pm 0.5\%$	0.02
$\overline{K}^0\pi^+\pi^-\pi^0$	< 0.0003	$14.9 \pm 2.7 \pm 3.5\%$	0.2
$K^-e^+\nu_e$	0.0022 ± 0.0007	$3.9 \pm 0.6 \pm 0.6\%$	0.1
$\rho^-e^+\nu_e$	0.0022 ± 0.0007	$\sim 0.2\%$	0.02
		Total	1.1 ± 0.6

Table 7.2.VI: Detection Efficiencies and Branching Ratios for $D^0 \to K^- \pi^0 e^+ \nu_e$

Tag Mode	Events		N_{tags}	ϵ_S	B
	Signal	Background			
$K^-\pi^+$	2	0.3	1089 ± 13.8	0.095 ± 0.008	0.016 ± 0.013
$K^-\pi^+\pi^+\pi^-$	3	0.3	1254 ± 40.8	0.072 ± 0.010	0.030 ± 0.018
$K^-\pi^+\pi^0$	2	0.5	1738 ± 60.8	0.086 ± 0.011	0.010 ± 0.008
total	7	1.1	4081 ± 74.5		
Weighted Average					$1.4 \pm 0.6\%$
Fit Result with parabolic error					$1.7 \pm 0.8\%$
Fit Result with maximum likelihood error					$1.7^{+0.9}_{-0.7}\%$

The branching ratio for $D^0 \to K^- \pi^0 e^+ \nu_e$ is thus:

$$\boxed{B(D^0 \to K^- \pi^0 e^+ \nu_e) = 1.7^{+0.9}_{-0.7} \pm 0.5\%}$$

7.2.3: $D^0 \to \overline{K}^0 \pi^- e^+ \nu_e$

Neutral kaons are detected only through their decay $K_s^0 \to \pi^+ \pi^-$, so in the decay $D^0 \to \overline{K}^0 \pi^- e^+ \nu_e$, three charged tracks must be found in the recoil along with an electron of the correct charge; the electron is identified in the usual way. The sum of the charges of all four tracks must, of course, be zero. No isolated photons may be found in the recoil; this helps limit hadronic backgrounds.

Of the three tracks accompanying the electron, there will be two combinations of oppositely charged tracks. Either of these combinations could represent the decay products of the neutral kaon; both are examined using the vertex finding procedures presented in appendix 3. The 3-momentum of each combination is required to align with the displacement of the K_s^0 system from the primary vertex. If ξ is the angle between the momentum and vertex displacement, $|\cos(\xi)|$ must be in the range $[0.9, 1]$. If the momentum of the K_s^0 is very small, the two crossing points of its daughter tracks may *both* be very close to the primary vertex. It is then very difficult to distinguish between the two crossing points. For this reason, $\cos(\zeta)$ is allowed to be in the 'negative' range $[-1, -0.9]$.

The effect of these cuts is displayed in Figs. 7.2.9 and 7.2.10. In the first figure, the invariant mass of all candidate neutral kaons — before any particle identification cuts — is displayed. In the second figure, this same mass is shown after the cuts described above. The reduction in background is clear. The only further cut required to isolate the K_s^0 is a cut on their mass from 0.46 to 0.52 GeV/c^2. In the very unlikely event — only one of the nine signal events — that both combinations are accepted as K_s^0 candidates, a decision between them is made on the basis of the value of U, calculated using the momentum of each candidate 'swum' to the vertex. The difference in the U values is very small, so even if this procedure selects the wrong combination, it makes little difference.

The numbers of background events are estimated as before. These expected backgrounds are summarized in Table 7.2.VII. The systematic error has contribu-

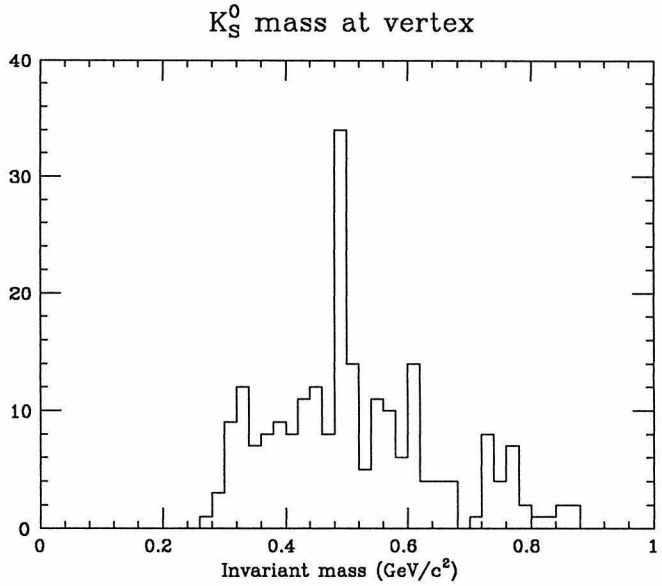

Figure 7.2.9: Invariant mass of all candidate K^0

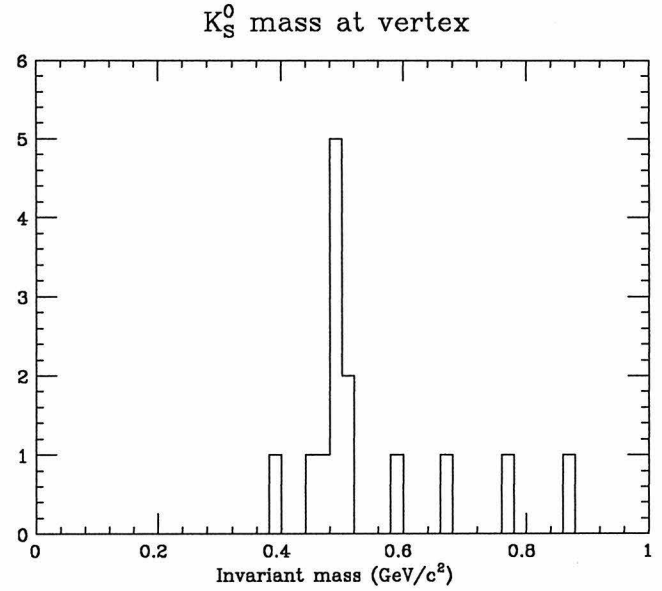

Figure 7.2.10: Invariant mass of all K^0 after all cuts

tions from a number of sources: electron detection efficiency (5%), π/e separator simulation (2%), pion detection efficiency (2%), background subtraction (5%), and $\overline{K}^0$ detection efficiency. This last effect is due primarily to a sensitivity of

Table 7.2.VII: $D^0 \to \overline{K}^0 \pi^- e^+ \nu_e$: Expected Backgrounds

Source	ϵ_B	B_B	N_B
$K^-\rho^+$	0.0002 ± 0.0002	$13.0 \pm 1.3 \pm 1.3\%$	0.1
$K^{*-}\pi^+$	0.0002 ± 0.0002	$8.0 \pm 1.3 \pm 1.3\%$	0.07
$K^-\pi^+\pi^0\pi^0$	< 0.0003	$\sim 8\%$	0.1
$K^-\pi^+\eta$	< 0.0003	$\leq 10\%$	0.1
$\overline{K}^{*0}\pi^0$	< 0.0003	$2.0 \pm 0.9 \pm 0.5\%$	0.02
$\overline{K}^0\pi^+\pi^-\pi^0$	< 0.0003	$14.9 \pm 2.7 \pm 3.5\%$	0.2
$K^-e^+\nu_e$	< 0.0007	$3.9 \pm 0.6 \pm 0.6\%$	0.1
$\rho^-e^+\nu_e$	0.0002 ± 0.0002	$\sim 0.2\%$	0.002
		Total	0.7 ± 0.4

Table 7.2.VIII: Detection Efficiencies and Branching Ratios for $D^0 \to \overline{K}^0 \pi^- e^+ \nu_e$

Tag Mode	Events		N_{tags}	ϵ_S	B
	Signal	Background			
$K^-\pi^+$	2	0.2	1089 ± 13.8	0.090 ± 0.006	0.018 ± 0.014
$K^-\pi^+\pi^+\pi^-$	5	0.2	1254 ± 40.8	0.099 ± 0.009	0.039 ± 0.018
$K^-\pi^+\pi^0$	2	0.3	1738 ± 60.8	0.086 ± 0.009	0.011 ± 0.009
total	9	0.7	4081 ± 74.5		
Weighted Average					$1.7 \pm 0.7\%$
Fit Result with parabolic error					$2.2 \pm 0.8\%$
Fit Result with maximum likelihood error					$2.2^{+0.9}_{-0.7}\%$

the detection efficiencies on the precise form of the $\cos(\varsigma)$ cut. This is estimated to cause an uncertainty of about 5%. The total systematic error is thus 19%. The detection efficiencies and individual branching ratios are listed in Table 7.2.VIII.

The branching ratio for $D^0 \to \overline{K}^0 \pi^- e^+ \nu_e$ is:

$$\boxed{B(D^0 \to \overline{K}^0 \pi^- e^+ \nu_e) = 2.2^{+0.9}_{-0.7} \pm 0.4\%}$$

7.2.4: $D^+ \to \overline{K}^0 e^+ \nu_e$ and $D^+ \to K^- \pi^+ e^+ \nu_e$

These decays both produce final states containing three charged tracks. As noted in section 7.2.1, the misidentification of a kaon as a pion — or *vice versa* — usually produces a significant change in U. Hence, it is possible to carry out a search for these two final states simultaneously.

Three charged tracks must be found, each with good z information. One of the three must be identified as electron of the appropriate charge. The track of the same charge as the electron is assumed to be a pion. The value of U is calculated under the hypotheses that the remaining track is a kaon and that it is a pion. If the value for the kaon hypothesis is closer to zero than that for the pion hypothesis, the event is analyzed further as a $D^+ \to K^- \pi^+ e^+ \nu_e$ candidate, otherwise it is analyzed as a $D^+ \to \overline{K}^0 e^+ \nu_e$ candidate.

In the latter case, the momentum of the K^0 is calculated at its vertex. The same direction and invariant mass cuts are used as in section 7.2.3. If the event is of the type $D^+ \to K^- \pi^+ e^+ \nu_e$, the ToF information of the kaon is examined. If it is valid, the kaon weight must be consistent with the kaon hypothesis as in section 7.2.1.

The numbers of background events are listed in Tables 7.2.IX and 7.2.X. The detection efficiencies and branching ratios are given in Tables 7.2.XI and 7.2.XII. The systematic error for $D^+ \to K^- \pi^+ e^+ \nu_e$ has contributions from the kaon detection efficiency (5%), pion detection efficiency (2%), electron detection efficiency (5%), π/e separator simulation (2%), and the uncertainty in the background subtraction (3%) for a total of 17%. The systematic error for $D^+ \to \overline{K}^0 e^+ \nu_e$ is determined by the $\overline{K}^0$ detection efficiency (5%), the electron

detection efficiency (5%), the π/e separator simulation (2%) and the background subtraction (5%); the sum is 17%.

The branching ratios for $D^+ \to \overline{K}^0 e^+ \nu_e$ and $D^+ \to K^- \pi^+ e^+ \nu_e$ are:

$$\boxed{\begin{array}{c} B(D^+ \to \overline{K}^0 e^+ \nu_e) = 6.3^{+2.0}_{-1.6} \pm 1.1\% \\ B(D^+ \to K^- \pi^+ e^+ \nu_e) = 3.9^{+0.9}_{-0.8} \pm 0.7\% \end{array}}$$

Table 7.2.IX: $D^+ \to \overline{K}^0 e^+ \nu_e$: Expected Backgrounds

Source	ϵ_B	B_B	N_B
$\overline{K}^{*0} e^+ \nu_e$	0.0004 ± 0.0001	$\sim 6\%$	0.05
$K^- \pi^+ \pi^+ \pi^0$	< 0.0005	$6.3^{+1.4}_{-1.3} \pm 1.2\%$	0.06
$\overline{K}^0 \rho^+$	0.003 ± 0.001	$11.2^{+2.6}_{-2.5} \pm 1.9\%$	0.8
$K^- \pi^+ \pi^+$	< 0.0004	$11.6 \pm 1.4 \pm 0.7\%$	0.09
$\overline{K}^{*0} \pi^+$	0.001 ± 0.0005	$2.7 \pm 1.8 \pm 1.6\%$	0.05
		Total	1.1 ± 0.6

Table 7.2.X: $D^+ \to K^- \pi^+ e^+ \nu_e$: Expected Backgrounds

Source	ϵ_B	B_B	N_B
$\overline{K}^0 e^+ \nu_e$	0.003 ± 0.001	$\sim 7\%$	0.4
$K^- \pi^+ \pi^+ \pi^0$	0.005 ± 0.001	$6.3^{+1.4}_{-1.3} \pm 1.2\%$	0.6
$\overline{K}^0 \rho^+$	< 0.0005	$11.2^{+2.6}_{-2.5} \pm 1.9\%$	0.1
$K^- \pi^+ \pi^+$	0.0004 ± 0.0004	$11.6 \pm 1.4 \pm 0.7\%$	0.09
$\overline{K}^{*0} \pi^+$	0.0005 ± 0.0003	$2.7 \pm 1.8 \pm 1.6\%$	0.03
		Total	1.2 ± 0.6

Table 7.2.XI: Detection Efficiencies and Branching Ratios for $D^+ \to \overline{K}^0 e^+ \nu_e$

Tag Mode	Events		N_{tags}	ϵ_S	B
	Signal	Background			
$K^-\pi^+\pi^+$	7	0.8	1346 ± 24.6	0.111 ± 0.004	0.042 ± 0.017
$\overline{K}^0\pi^+$	1	0.1	152.8 ± 7.7	0.113 ± 0.004	0.052 ± 0.055
$\overline{K}^0\pi^+\pi^+\pi^-$	2	0.1	207.0 ± 20.9	0.104 ± 0.006	0.088 ± 0.065
$\overline{K}^0\pi^+\pi^0$	5	0.1	268.4 ± 36.8	0.114 ± 0.008	0.160 ± 0.076
total	15	1.1	1974 ± 49.6		
Weighted Average					$5.0 \pm 1.5\%$
Fit Result with parabolic error					$6.3 \pm 1.8\%$
Fit Result with maximum likelihood error					$6.3^{+2.0}_{-1.6}\%$

Table 7.2.XII: Detection Efficiencies and Branching Ratios for $D^+ \to K^-\pi^+ e^+ \nu_e$

Tag Mode	Events		N_{tags}	ϵ_S	B
	Signal	Background			
$K^-\pi^+\pi^+$	16	0.8	1346 ± 24.6	0.308 ± 0.013	0.037 ± 0.010
$\overline{K}^0\pi^+$	4	0.1	152.8 ± 7.7	0.287 ± 0.012	0.089 ± 0.045
$\overline{K}^0\pi^+\pi^+\pi^-$	2	0.1	207.0 ± 20.9	0.298 ± 0.021	0.031 ± 0.023
$\overline{K}^0\pi^+\pi^0$	2	0.2	268.4 ± 36.8	0.277 ± 0.025	0.024 ± 0.019
total	24	1.2	1974.2 ± 49.6		
Weighted Average					$3.6 \pm 0.8\%$
Fit Result with parabolic error					$3.9 \pm 0.8\%$
Fit Result with maximum likelihood error					$3.9^{+0.9}_{-0.8}\%$

7.2.5: $D^0 \to \pi^- e^+ \nu_e$

In the discussion of the final state $D^0 \to K^- e^+ \nu_e$, the absolute value of U for the kaon hypothesis was required to be nearer zero than that for the pion hypothesis. Events for which $|U|$ is smaller for the latter hypothesis, but which satisfy the other requirements described in section 7.2.1, are ascribed to the decay $D^0 \to \pi^- e^+ \nu_e$. This selection is completely unbiased, so it is significant that forty-seven events are detected in the decay $D^0 \to K^- e^+ \nu_e$, while only three are detected in the decay $D^0 \to \pi^- e^+ \nu_e$.

The largest background to this decay is the decay $D^0 \to K^- e^+ \nu_e$; the discrimination based on U is good, but as is clear from Fig. 7.2.1, there is some overlap in the U spectra for the kaon and pion hypotheses. The numbers of events expected from this and other sources are enumerated in Table 7.2.XIII. The detection efficiencies are listed in Table 7.2.XIV. The systematic error is dominated by the uncertainty in the background subtraction (24%), but there are contributions as well from the electron identification (7%) and pion identification (5%) for a total of 36%.

The branching ratio for $D^0 \to \pi^- e^+ \nu_e$ is:

$$\boxed{B(D^0 \to \pi^- e^+ \nu_e) = 0.4^{+0.4}_{-0.3} \pm 0.1\%}$$

The significance of this measurement is simply stated: this is a Cabibbo-suppressed decay and it thus tests directly the elements of the weak mixing — or KM — matrix. The ratio of branching ratios for the decays $D^0 \to \pi^- e^+ \nu_e$ and $D^0 \to K^- e^+ \nu_e$ may be predicted by integrating the formulae* of appendix 3:

$$\frac{B(D^0 \to \pi^- e^+ \nu_e)}{B(D^0 \to K^- e^+ \nu_e)} = \left|\frac{U_{cd}}{U_{cs}}\right|^2 \times 1.87$$

The measured branching ratios yield a ratio $|U_{cd}/U_{cs}|^2 = 0.05 \pm 0.03 \pm 0.01$. The

* The form factor $f_+(t)$ for $D \to \pi e^+ \nu_e$ has its pole at $m^2_{D^*}$.

ratio obtained from the KM matrix elements† given in chapter 1 is 0.052 ± 0.001. Thus the observed rate of Cabibbo-suppressed semileptonic decay is consistent with the rate of neutrino induced charm production.

Table 7.2.XIII: $D^0 \to \pi^- e^+ \nu_e$: Expected Backgrounds

Source	ϵ_B	B_B	N_B
$K^-\rho^+$	< 0.0003	$13.0 \pm 1.3 \pm 1.3\%$	0.2
$K^{*-}\pi^+$	0.0003 ± 0.0003	$8.0 \pm 1.3 \pm 1.3\%$	0.1
$K^-\pi^+\pi^0\pi^0$	< 0.0003	$\sim 8\%$	0.1
$K^-\pi^+\eta$	< 0.0003	$\leq 10\%$	0.1
$\overline{K}^{*0}\pi^0$	< 0.0003	$2.0 \pm 0.9 \pm 0.5\%$	0.03
$K^-e^+\nu_e$	0.0027 ± 0.0008	$3.9 \pm 0.6 \pm 0.6\%$	0.4
		Total	0.9 ± 0.5

Table 7.2.XIV: Detection Efficiencies and Branching Ratios for $D^0 \to \pi^- e^+ \nu_e$

Tag Mode	Events		N_{tags}	ϵ_S	B
	Signal	Background			
$K^-\pi^+\pi^0$	2	0.8	1738 ± 60.8	0.229 ± 0.011	0.003 ± 0.003
$\overline{K}^0\pi^+\pi^-$	1	0.1	325.9 ± 17.1	0.280 ± 0.013	0.010 ± 0.010
total	3	0.9	2064 ± 63.2		
Weighted Average					$0.4 \pm 0.4\%$
Fit Result with parabolic error					$0.4 \pm 0.4\%$
Fit Result with maximum likelihood error					$0.4^{+0.4}_{-0.3}\%$

† These elements are taken from the 1986 edition of the *Review of Particle Properties*.

7.3: Summary of electron modes

Measurements of the branching ratios for five exclusive semileptonic decays were presented in section 7.2. As a final demonstration of the quality of the data used in these measurements, a scatterplot of U versus tag beam-constrained mass is given for each mode — the D^0 decays in Fig. 7.3.1 and the D^+ in Fig 7.3.1. In each case, there is a clear clustering of events near the D mass and a value of zero for U.

In section 7.1, it was predicted that the only Cabibbo-favored semileptonic decays yielding observable signals would be precisely those discussed in section 7.2. If these do indeed account for the bulk of D semileptonic decays, then the sum of the exclusive branching ratios should nearly equal the inclusive branching ratios. The branching ratios and their sums are collected in Table 7.3.I; the branching ratio for $D^+ \rightarrow \overline{K}^0 \pi^0 e^+ \nu_e$ is unmeasured, so in order to sum the D^+ branching ratios, it is necessary to multiply the branching ratio for $D^+ \rightarrow K^- \pi^+ e^+ \nu_e$ by the square of the Clebsch-Gordan coefficient 3/2. The sum of the exclusive branching ratios for the D^0 is in good agreement with the inclusive branching ratio. The sum for the D^+ differs from the inclusive measurement by two standard deviations.

In summary, the semileptonic decays of D mesons are dominated by final states containing either a single kaon or a kaon-pion pair. A comparison of the inclusive and exclusive branching ratios rules out any large Cabibbo-suppressed contribution; indeed, the rate observed for the decay $D^0 \rightarrow \pi^- e^+ \nu_e$ is consistent with the prediction obatined by using the value of U_{cd} measured in charm production from neutrino beams.

Table 7.3.I: D Semileptonic Branching Ratios: Electron Modes

Mode	Branching Ratio
$D^0 \to K^- e^+ \nu_e$	$3.9 \pm 0.6 \pm 0.6\%$
$D^0 \to K^- \pi^0 e^+ \nu_e$	$1.7^{+0.9}_{-0.7} \pm 0.6\%$
$D^0 \to \overline{K}^0 \pi^- e^+ \nu_e$	$2.2^{+0.9}_{-0.7} \pm 0.4\%$
$D^0 \to \pi^- e^+ \nu_e$	$0.4^{+0.4}_{-0.3} \pm 0.1\%$
$D^0 \to [K\pi]^- e^+ \nu_e$	$3.9^{+1.3}_{-1.0} \pm 0.6\%$
$D^0 \to (K^- + [K\pi]^-) e^+ \nu_e$	$7.8^{+1.4}_{-1.2} \pm 0.8\%$
$D^0 \to e^+ X$	$7.5 \pm 1.1 \pm 0.4\%$
$D^+ \to \overline{K}^0 e^+ \nu_e$	$6.3^{+2.0}_{-1.6} \pm 1.1\%$
$D^+ \to K^- \pi^+ e^+ \nu_e$	$3.9^{+0.9}_{-0.8} \pm 0.7\%$
$D^+ \to [K\pi]^0 e^+ \nu_e$	$5.9^{+1.4}_{-1.2} \pm 1.1\%$
$D^+ \to (\overline{K}^0 + [K\pi]^0) e^+ \nu_e$	$12.2^{+2.4}_{-2.0} \pm 1.6\%$
$D^+ \to e^+ X$	$17.0 \pm 1.9 \pm 0.7\%$

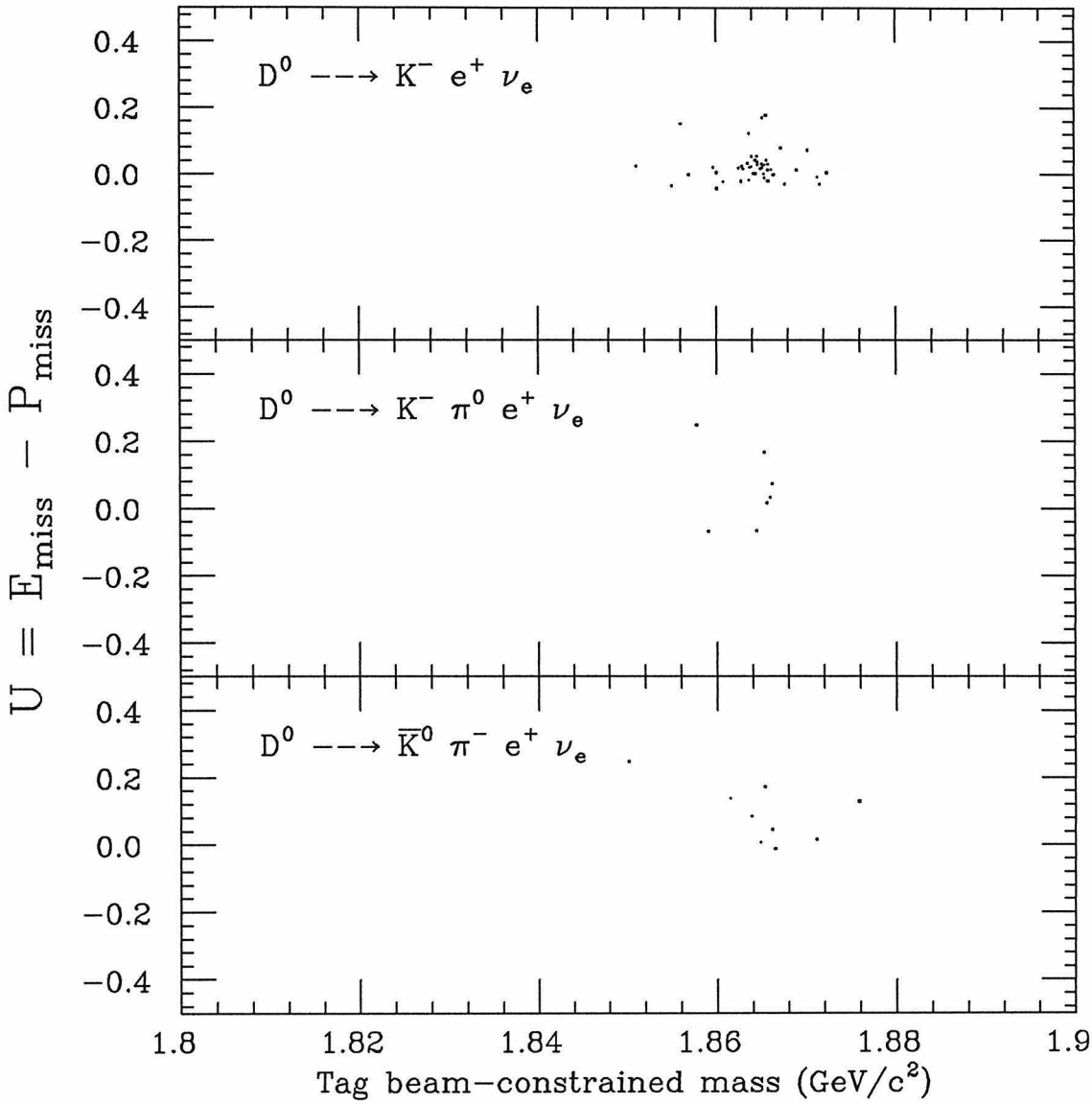

Figure 7.3.1: Tag beam-constrained mass versus U for D^0 events

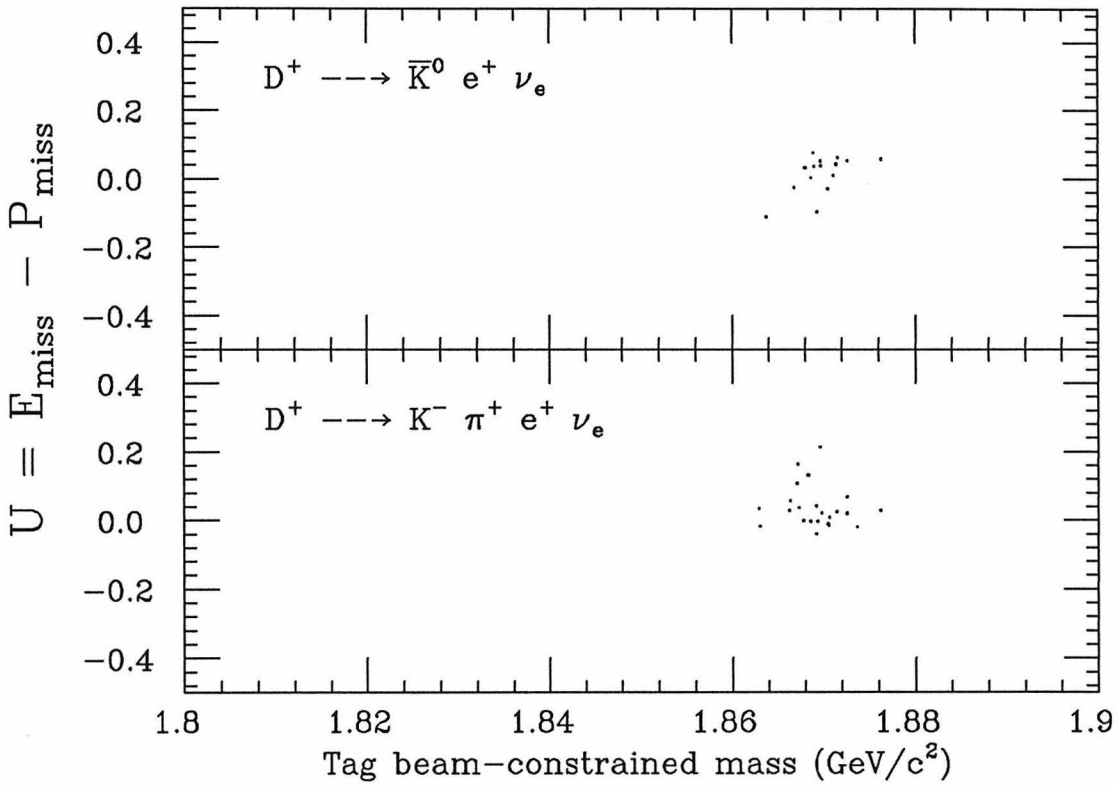

Figure 7.3.2: Tag beam-constrained mass versus U for D^+ events

Chapter 8: Semileptonic Branching Ratios: Muon Modes

8.1: Muonic decays and muon identification

The coupling of the W gauge boson to a charged lepton - neutrino pair is a *universal* coupling in the Standard Model; the W couples equally to each of the three families of leptons. The correctness of this assumption may be tested in a number of ways. For example, the rate predicted for the decay $\mu^- \rightarrow e^- \nu_\mu \overline{\nu}_e$ — including radiative corrections — is in good agreement with the measured decay rate. The ratio of the couplings of the W to the first two families may be obtained by comparing the predicted and measured values of the ratio of branching ratios $B(\tau^- \rightarrow \mu^- \nu_\tau \overline{\nu}_\mu)/B(\tau^- \rightarrow e^- \nu_\tau \overline{\nu}_e)$. This ratio is predicted[85] to be* $g(m_\mu^2/m_\tau^2)/g(m_e^2/m_\tau^2) = 0.97$. A recent measurement[86] by the MARK III is $B(\tau^- \rightarrow \mu^- \nu_\tau \overline{\nu}_\mu)/B(\tau^- \rightarrow e^- \nu_\tau \overline{\nu}_e) = 0.99 \pm 0.07 \pm 0.04$.

The universality of the W - lepton coupling may also be investigated through a comparison of the semileptonic decays of mesons. Cabibbo-favored semileptonic decays are spectator decays, so the ratio of the exclusive branching ratios for such processes is predictable. A numerical integration of the formulae given in sections A3.1 and A3.2 yields the ratio:

$$\frac{B(D^0 \rightarrow K^- \mu^+ \nu_\mu)}{B(D^0 \rightarrow K^- e^+ \nu_e)} = 0.96$$

The identification of D semileptonic decays containing muons is complicated by the angular and momentum acceptance of the MARK III's muon system; this system was not designed to aid in the analysis of semileptonic decays but rather to isolate dimuon events and to help reject cosmic rays. The muon system covers only 60% of 4π and is only efficient for muons with transverse momenta greater

* The function $g(x)$, introduced in section 2.4, is $1 - 8x + 8x^3 - x^4 - 12x^2 \log(x)$.

than 600 MeV/c. The limited momentum acceptance, in particular, is a serious problem. The transverse momentum spectra for the decays $D^0 \rightarrow K^- \mu^+ \nu_\mu$ and $D^0 \rightarrow K^{*-} \mu^+ \nu_\mu$ are shown in Figs. 8.1.1 and 8.1.2. It is clear from these figures that only about 15% of the $D^0 \rightarrow K^- \mu^+ \nu_\mu$ decays and about 3% of the $D^0 \rightarrow K^{*-} \mu^+ \nu_\mu$ decays will produce muons energetic enough to penetrate to the muon system.

It is possible to identify semileptonic decays containing muons without using the muon system. In events with an hadronic tag, the missing energy and momentum may be calculated unambiguously. Thus *kinematics* may substitute for *hardware* in the isolation of semileptonic decays. Such a procedure naturally admits somewhat larger backgrounds than the procedures of chapter 7; the number of signal events, however, is greatly increased.

8.2: $D^0 \rightarrow K^- \mu^+ \nu_\mu$

This decay — just as in the electron case — yields a particularly simple final state. The analysis is quite similar to that for the decay $D^0 \rightarrow K^- e^+ \nu_e$. The cuts on the invariant mass of the $K^- \mu^+$ system and on the missing energy are in fact identical to those described in section 7.2.1. The requirements placed on the kaon are, however, somewhat more stringent. The candidate kaon must be identified by the ToF system; the weight for the kaon hypothesis must be greater than seventy percent of the sum of the weights. This requirement is placed on the kaons as these may be reliably identified by the ToF system. With the kaon positively identified, the rejection of backgrounds through kinematic means is rendered more secure and reliable.

The hadronic decay $D^0 \rightarrow K^- \pi^+ \pi^0$ is the largest background to the decay $D^0 \rightarrow K^- \mu^+ \nu_\mu$. This situation occurs primarily because of the inability of the ToF system to distinguish between pions and muons. The ToF system is used only to remove well-identified kaons. Most of the pions which interact in

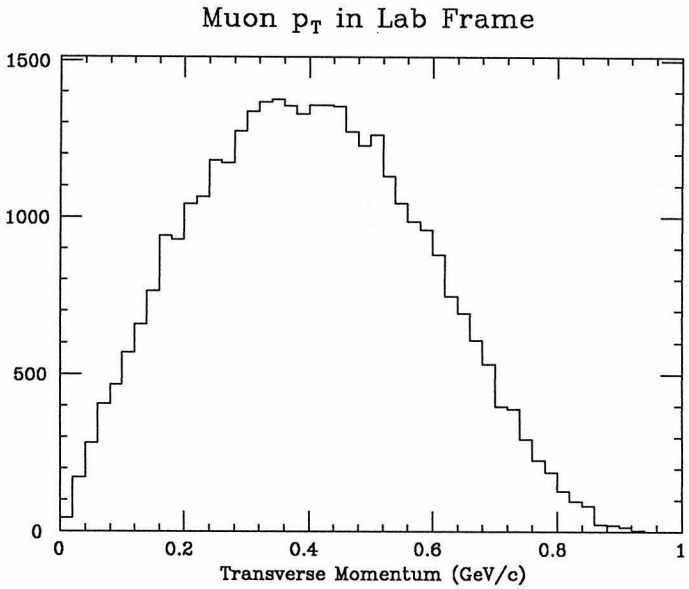

Figure 8.1.1: Muon transverse momentum spectrum for $D^0 \rightarrow K^- \mu^+ \nu_\mu$

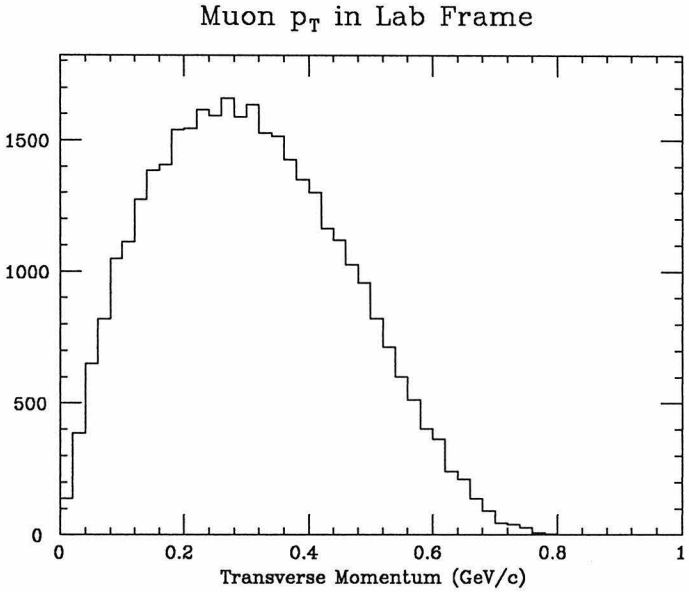

Figure 8.1.2: Muon transverse momentum spectrum for $D^0 \rightarrow K^{*-} \mu^+ \nu_\mu$

the shower detector are rejected by requiring that the energy deposited by the candidate be less than 300 MeV. The number of background events is further reduced by 'tightening' the definition of an isolated photon; in the present case, an isolated photon need only have a measured energy of 50 MeV. This energy cut

may not be lowered any further without incurring large systematic uncertainties due to fake photons.

A neutral pion escapes detection if neither of the photons from its decay are identified as isolated photons. This may happen if both of the photons enter an uninstrumented region of the detector, particularly the region from the center of the beam pipe to the innermost edge of the endcap shower detectors. This is more often the case than might expected as photons from the decay of the π^0 in the decay $D^0 \to K^- \pi^+ \pi^0$ usually have a small opening angle. In such cases, the missing *transverse* momentum — p_t — is small. The p_t spectrum for Monte Carlo events of the type $D^0 \to K^- \rho^+$, in which both photons are undetected, is shown in Fig. 8.2.1. If the missing p_t is required to be greater than 200 MeV, 60% of the remaining events are removed. A prediction of the neutrino p_t spectrum in the decay $D^0 \to K^- \mu^+ \nu_\mu$ is shown in Fig. 8.2.2. The missing p_t cut is seen to remove only about 15% of the signal events.

The expected backgrounds are enumerated in Table 8.2.I. A new type of background is encountered here; *non-charm* backgrounds must be considered for the first time. The possibility of non-charm backgrounds is taken into account by fitting the beam-constrained mass distribution of the tags for the signal events. The spectrum of this mass is shown in Fig. 8.2.3; the solid curve is the result of the fit.

The branching ratio is calculated as in chapter 7. The detection efficiencies and other relevant quantities are listed in Table 8.2.II. The systematic error is somewhat different from that for $D^0 \to K^- e^+ \nu_e$ as the dependence of the detection efficiencies on the shower detector energy must be considered. The energies deposited by muons are illustrated in Fig. 8.2.4 both for real $e^+ e^- \to \mu^+ \mu^- \gamma$ events and for Monte Carlo $D^0 \to K^- \mu^+ \nu_\mu$ events. The agreement is fairly good; the differences result in a 5% systematic error in the detection efficiencies. The energy cut for isolated photons contributes a 10% systematic uncertainty. The ToF identification of the candidate kaon causes an uncertainty

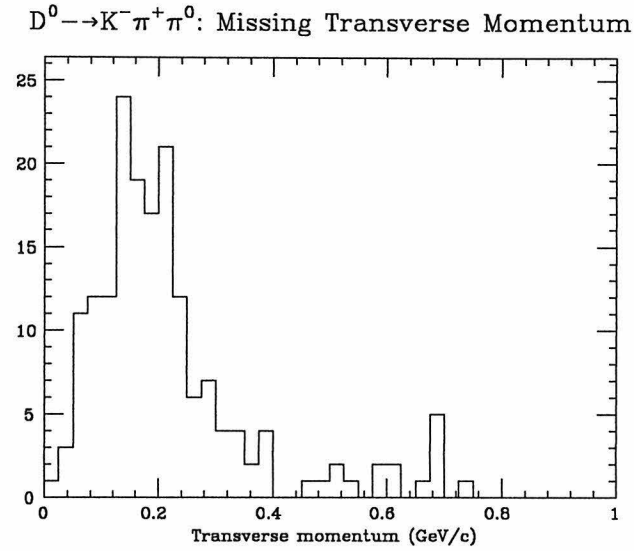

Figure 8.2.1: Missing transverse momentum spectrum for $D^0 \rightarrow K^- \pi^+ \pi^0$ events with no isolated photons

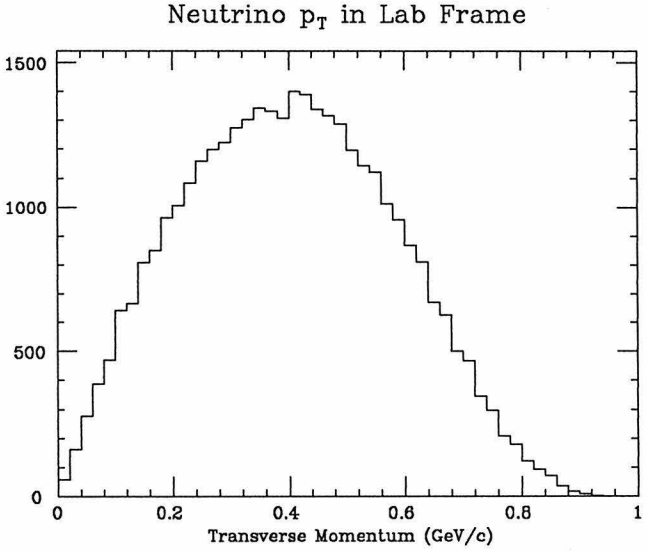

Figure 8.2.2: Neutrino transverse momentum spectrum for $D^0 \rightarrow K^- \mu^+ \nu_\mu$

of about 5%. Finally, the uncertainty in the number of background events results in a systematic error of 10%. The total systematic error is then 30%.

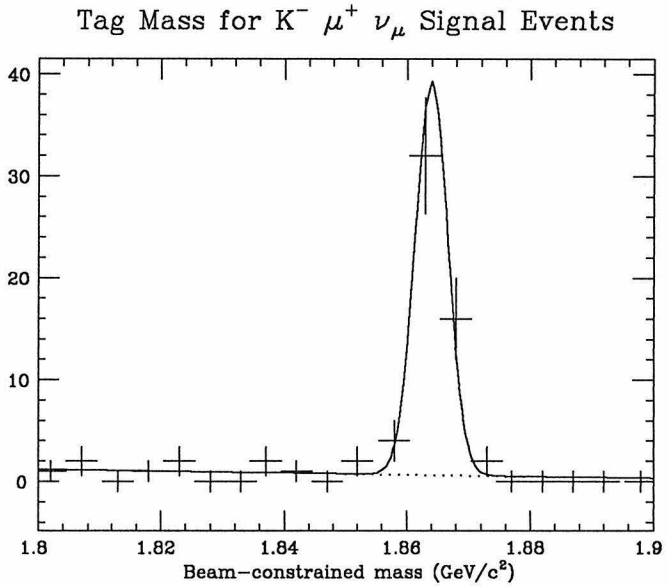

Figure 8.2.3: Tag beam-constrained mass spectrum for $D^0 \to K^- \mu^+ \nu_\mu$ events

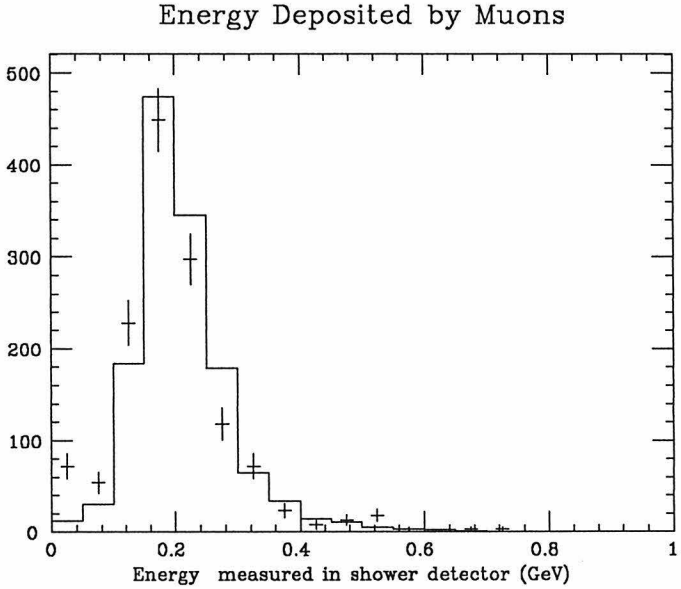

Figure 8.2.4: Energy deposited by muons:

$e^+e^- \to \mu^+\mu^-\gamma$ indicated by $\sqcap$ $\qquad$ $D^0 \to K^-\mu^+\nu_\mu$ indicated by $\dagger$

The branching ratio for $D^0 \to K^- \mu^+ \nu_\mu$ is thus:

$$\boxed{B(D^0 \to K^- \mu^+ \nu_\mu) = 4.1 \pm 0.7 \pm 1.2\%}$$

Table 8.2.I: $D^0 \to K^- \mu^+ \nu_\mu$: Expected Backgrounds

Source	ϵ_B	B_B	N_B
$K^-\rho^+$	0.0062 ± 0.0012	$13.0 \pm 1.3 \pm 1.3\%$	3.3
$K^{*-}\pi^+$	0.0043 ± 0.0010	$8.0 \pm 1.3 \pm 1.3\%$	1.4
$K^-\pi^+\pi^0\pi^0$	0.0005 ± 0.0004	$\sim 8\%$	0.2
$K^-\pi^+\eta$	0.0005 ± 0.0004	$\leq 10\%$	0.2
$\overline{K}^{*0}\pi^0$	0.0041 ± 0.0010	$2.0 \pm 0.9 \pm 0.5\%$	0.3
$\pi^+\pi^-\pi^0$	0.0003 ± 0.0003	$1.1 \pm 0.4 \pm 0.2\%$	0.01
$K^{*-}\mu^+\nu_\mu$	0.0032 ± 0.0009	$\sim 4\%$	0.5
non-charm			3.5
		Total	9.4 ± 4.7

Table 8.2.II: Detection Efficiencies and Branching Ratios for $D^0 \to K^- \mu^+ \nu_\mu$

Tag Mode	Events		N_{tags}	ϵ_S	B
	Signal	Background			
$K^-\pi^+$	14	2.5	1089 ± 13.8	0.290 ± 0.009	0.037 ± 0.011
$K^-\pi^+\pi^+\pi^-$	16	2.9	1254 ± 40.8	0.275 ± 0.012	0.038 ± 0.011
$K^-\pi^+\pi^0$	26	4.0	1738 ± 60.8	0.275 ± 0.014	0.046 ± 0.010
total	56	9.4	4081 ± 74.5		
Weighted Average					$4.1 \pm 0.6\%$
Fit Result with parabolic error					$4.1 \pm 0.7\%$
Fit Result with maximum likelihood error					$4.1 \pm 0.7\%$

8.3: $D^0 \to \overline{K}^0 \pi^- \mu^+ \nu_\mu$

Of the four-body decays discussed in section 7.2, the only corresponding muonic decay which is tractable is $D^0 \to \overline{K}^0 \pi^- \mu^+ \nu_\mu$. The decay $D^0 \to K^- \pi^0 \mu^+ \nu_\mu$ is hampered by a very large background from $D^0 \to K^- \pi^- \pi^0$. In the remaining decay, $D^+ \to K^- \pi^+ \mu^+ \nu_\mu$, it is impossible, using the techniques described in section 8.2, to distinguish the pion from the muon.

In the decay $D^0 \to \overline{K}^0 \pi^- \mu^+ \nu_\mu$, four charged tracks must be observed recoiling from the hadronic tag as the $\overline{K}^0$ is only detected through its decay to two charged pions. There are four pairs of tracks of opposite charge, any one of which may constitute the decay product of the $\overline{K}^0$. The vertex finding procedures of appendix 2 are applied to each pair of tracks; the invariant mass of each, calculated at the vertex, is plotted in Fig. 8.3.1. The number of combinations is greatly reduced by requiring that this mass lie in the range 0.46 – 0.52 GeV/c^2. Of the 239 events is this range, only eight have two combinations and none have more than two. As in section 7.2.3, a decision between them is made on the basis of U.

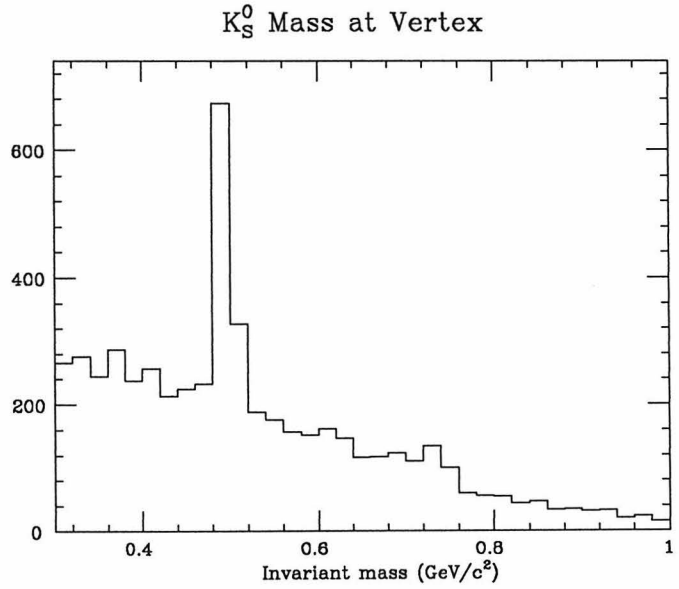

Figure 8.3.1: $D^0 \to \overline{K}^0 \pi^- \mu^+ \nu_\mu$: Invariant mass of K^0_s candidates

Once a candidate $\overline{K}^0$ is selected, the remaining 'right-sign' track is subjected to the shower detector energy cut described in section 8.2. The missing p_t must be greater than 200 MeV/c. Finally, the usual missing energy and invariant mass cuts are applied.

Another problem of combinatorics arises with this decay. As has been noted several times, the tag mass sample contains a substantial number of background events; in many cases, there is even more than one tag per event. The lack of positive identification of the muon makes it possible to exchange one or more tracks in the recoil with tracks from the tag. Thus, is a small number of cases, more than one candidate semileptonic decay may be found in an event. This problem could have appeared in the analysis of $D^0 \to K^- \mu^+ \nu_\mu$, but fortunately, the low multiplicity and strict kaon identification make the exchange of particles very unlikely. The higher multiplicity of the decay $D^0 \to \overline{K}^0 \pi^- \mu^+ \nu_\mu$, however, makes it necessary to consider such exchanges; in four of the twenty detected events, more than one candidate decay was found. There is no obvious way to distinguish among the candidates, so a procedure is adopted which is *statistically* correct; only the first candidate encountered is accepted.

The branching ratios and detection efficiencies are calculated in the usual way. The results are listed in Tables 8.3.I and 8.3.II. The systematic error has contributions from the $\overline{K}^0$ identification (5%), the background subtraction (38%), the shower detector energy cut (5%), and the isolated photon energy cut (10%) for a total of (58%).

The branching ratio for the decay $D^0 \to \overline{K}^0 \pi^- \mu^+ \nu_\mu$ is:

$$\boxed{B(D^0 \to \overline{K}^0 \pi^- \mu^+ \nu_\mu) = 2.7^{+1.1}_{-1.0} \pm 1.6\%}$$

Table 8.3.I: $D^0 \to \overline{K}^0 \pi^- \mu^+ \nu_\mu$: Expected Backgrounds

Source	ϵ_B	B_B	N_B
$K^-\rho^+$	0.0003 ± 0.0003	$13.0 \pm 1.3 \pm 1.3\%$	0.2
$K^{*-}\pi^+$	0.0003 ± 0.0003	$8.0 \pm 1.3 \pm 1.3\%$	0.1
$K^-\pi^+\pi^0\pi^0$	< 0.0003	$\sim 8\%$	0.1
$K^-\pi^+\eta$	0.0010 ± 0.0005	$\leq 10\%$	0.4
$\overline{K}^{*0}\pi^0$	< 0.0004	$2.0 \pm 0.9 \pm 0.5\%$	0.03
$\overline{K}^0\pi^+\pi^-\pi^0$	0.0043 ± 0.0010	$14.9 \pm 2.7 \pm 3.5\%$	2.5
non-charm			5.2
		Total	8.5 ± 4.3

Table 8.3.II: Detection Efficiencies and Branching Ratios for $D^0 \to \overline{K}^0 \pi^- \mu^+ \nu_\mu$

Tag Mode	Events		N_{tags}	ϵ_S	B
	Signal	Background			
$K^-\pi^+$	5	2.3	1089 ± 13.8	0.098 ± 0.004	0.025 ± 0.015
$K^-\pi^+\pi^+\pi^-$	7	2.6	1254 ± 40.8	0.106 ± 0.007	0.033 ± 0.016
$K^-\pi^+\pi^0$	8	3.6	1738 ± 60.8	0.105 ± 0.007	0.024 ± 0.012
total	20	8.5	4081 ± 74.5		
Weighted Average					$2.7 \pm 0.8\%$
Fit Result with parabolic error					$2.7 \pm 1.0\%$
Fit Result with maximum likelihood error					$2.7^{+1.1}_{-1.0}\%$

8.4: $D^+ \to \overline{K}^0 \mu^+ \nu_\mu$

The isolation of decays of the type $D^+ \to \overline{K}^0 \mu^+ \nu_\mu$ is much simpler than the procedure required for $D^0 \to \overline{K}^0 \pi^- \mu^+ \nu_\mu$. Three charged tracks are observed in the recoil so there are only two combinations of oppositely charged tracks. In only one event do both combinations satisfy the usual K_s^0 identification requirements; the value of U was again used as the arbiter. The problem of more then one candidate decay being found in an event does not appear in the present case; the multiplicity is lower than in the decay $D^0 \to \overline{K}^0 \pi^- \mu^+ \nu_\mu$ and the D^+ tagged sample has less background than the D^0 sample.

The number of background events expected is summarized in Table 8.4.I. The detection efficiencies and individual branching ratios are given in Table 8.4.II. The systematic error is due to uncertainties in the K_s^0 identification (5%), the measured energy of the muon (5%), the background subtraction (15%) and the energy of isolated photons (10%); the total systematic error is then 35%.

The branching ratio for the decay $D^+ \to \overline{K}^0 \mu^+ \nu_\mu$ is:

$$\boxed{B(D^+ \to \overline{K}^0 \mu^+ \nu_\mu) = 10.2^{+2.2}_{-2.1} \pm 3.6\%}$$

Table 8.4.I: $D^+ \to \overline{K}^0 \mu^+ \nu_\mu$: Expected Backgrounds

Source	ϵ_B	B_B	N_B
$\overline{K}^0\pi^+$	0.0037 ± 0.0012	$4.1 \pm 0.6 \pm 0.3\%$	0.3
$K^-\pi^+\pi^+\pi^0$	0.0004 ± 0.0004	$6.3^{+1.4}_{-1.3} \pm 1.2\%$	0.1
$\overline{K}^0\rho^+$	0.0130 ± 0.0022	$11.2^{+2.6}_{-2.5} \pm 1.9\%$	2.9
$K^-\pi^+\pi^+$	0.0004 ± 0.0004	$11.6 \pm 1.4 \pm 0.7\%$	0.1
$\overline{K}^{*0}\pi^+$	0.0017 ± 0.0006	$2.7 \pm 1.8 \pm 1.6\%$	0.1
non-charm			5.4
		Total	8.9 ± 4.5

Table 8.4.II: Detection Efficiencies and Branching Ratios for $D^+ \to \overline{K}^0 \mu^+ \nu_\mu$

Tag Mode	Events		N_{tags}	ϵ_S	B
	Signal	Background			
$K^-\pi^+\pi^+$	21	6.1	1346 ± 24.6	0.137 ± 0.005	0.028 ± 0.007
$\overline{K}^0\pi^+$	4	0.7	152.8 ± 7.7	0.141 ± 0.005	0.053 ± 0.029
$\overline{K}^0\pi^+\pi^+\pi^-$	4	0.9	207.0 ± 20.9	0.138 ± 0.008	0.037 ± 0.021
$\overline{K}^0\pi^+\pi^0$	8	1.2	268.4 ± 36.8	0.152 ± 0.008	0.057 ± 0.022
total	37	8.9	1974 ± 49.6		
Weighted Average					$9.4 \pm 1.9\%$
Fit Result with parabolic error					$10.2 \pm 2.2\%$
Fit Result with maximum likelihood error					$10.2^{+2.2}_{-2.1}\%$

8.5: Summary of muon modes

With the measurement of the branching ratios for three muonic decays, a comparison may be made among the semileptonic decays containing electrons and those containing muons. The branching ratios of the comparable electron and muon modes are listed in Table 8.5.I. The D^0 decays have quite similar branching ratios. The branching ratios for the D^+ decays differ by 1.8 standard deviations.

Table 8.5.I: D Semileptonic Branching Ratios:
Muon Modes — and comparable Electron Modes

Mode	Branching Ratio
$D^0 \to K^- e^+ \nu_e$	$3.9 \pm 0.6 \pm 0.6\%$
$D^0 \to K^- \mu^+ \nu_\mu$	$4.1 \pm 0.7 \pm 1.2\%$
$D^0 \to \overline{K}^0 \pi^- e^+ \nu_e$	$2.2^{+0.9}_{-0.7} \pm 0.4\%$
$D^0 \to \overline{K}^0 \pi^- \mu^+ \nu_\mu$	$2.7^{+1.1}_{-1.0} \pm 1.6\%$
$D^+ \to \overline{K}^0 e^+ \nu_e$	$6.3^{+2.0}_{-1.6} \pm 1.1\%$
$D^+ \to \overline{K}^0 \mu^+ \nu_\mu$	$10.2^{+2.2}_{-2.1} \pm 3.6\%$

If the small phase-space effect discussed in section 8.1 is ignored, the ratio of the leptonic couplings of the W may be extracted by minimizing the likelihood function:

$$\mathcal{L} = \prod_{i=1}^{3} \exp\left(-\frac{(B_i(e) - \overline{B}_i(e))^2}{\sigma_i^2(e)}\right) \prod_{j=1}^{3} \exp\left(-\frac{(B_j(\mu) - \overline{B}_j(\mu))^2}{\sigma_j^2(\mu)}\right)$$

The electronic branching ratios are used as parameters in the fit. The muon branching ratios are related to these by the equation $B_j(\mu) = \alpha^2 B_j(e)$, where α is the ratio of couplings.

The results of the fit are summarized in Table 8.5.II. The most likely value of α is clearly consistent with unity. Even with the rather large uncertainty in this value, there is no evidence for a large deviation from electron-muon universality.

Table 8.5.II: Relative Electronic and Muonic Branching Ratios

Parameter	Value from fit
$B(D^0 \to K^- e^+ \nu_e)$	$3.9 \pm 0.9\%$
$B(D^0 \to \overline{K}^0 \pi^- e^+ \nu_e)$	$2.3 \pm 0.6\%$
$B(D^+ \to \overline{K}^0 e^+ \nu_e)$	$6.1^{+1.8}_{-1.7}\%$
$\alpha \equiv \sqrt{\Gamma(D \to \mu^+ X)/\Gamma(D \to e^+ X)}$	$1.32^{+0.24}_{-0.21}$

Chapter 9: Development and Coda: Kinematic Properties of Semileptonic Decays

9.1: Inclusive and exclusive decays

The comparison of the inclusive and exclusive branching ratios, described in section 7.3, may be improved through the inclusion of the muonic decay modes. The comparable electronic and muonic branching ratios are averaged using the weighting procedure of section 7.2.1. The results are given in Table 9.1.I. The agreement among the sums of the exclusive branching ratios and the inclusive branching ratios is quite good. In particular, the D^+ measurements are in better agreement; the slight discrepancy noted in section 7.2.3 is thus seen to be just a statistical artifact. There is no evidence for the production of any final states other than those discussed in chapters 7 and 8.

Table 9.1.I: Exclusive and Inclusive Semileptonic Branching Ratios

Mode	Branching Ratio
$D^0 \to K^- l^+ \nu_l$	$3.9 \pm 0.7\%$
$D^0 \to K^- \pi^0 l^+ \nu_l$	$1.7 \pm 1.1\%$
$D^0 \to \overline{K}^0 \pi^- l^+ \nu_l$	$2.3 \pm 0.8\%$
$D^0 \to (K^- + [K\pi]^-) l^+ \nu_l$	$7.9 \pm 1.5\%$
$D^0 \to e^+ X$	$7.5 \pm 1.1 \pm 0.4\%$
$D^+ \to \overline{K}^0 l^+ \nu_l$	$7.4 \pm 1.8\%$
$D^+ \to K^- \pi^+ l^+ \nu_l$	$3.9 \pm 1.1\%$
$D^+ \to (\overline{K}^0 + [K\pi]^0) l^+ \nu_l$	$13.3 \pm 2.5\%$
$D^+ \to e^+ X$	$17.0 \pm 1.9 \pm 0.7\%$

The inclusive lepton spectrum from semileptonic D decays, measured by the MARK III, is shown in Fig. 9.1.1. The component parts of this spectrum may

be displayed by summing the appropriate exclusive modes. The lepton spectra of the detected events are shown in Fig. 9.1.2; the histograms are predictions based on the formulae of appendix 3. The agreement between the measured and predicted spectra is good for events of the type $D^0 \rightarrow K^- l^+ \nu_l$. The measured spectrum in the case $D \rightarrow K \pi l^+ \nu_l$, however, appears 'softer' than the Monte Carlo prediction for the decay $D \rightarrow K^* l^+ \nu_l$.

9.2: $D \rightarrow K e^+ \nu_e$ versus $D \rightarrow K \pi e^+ \nu_e$

The relative amounts of the decays $D \rightarrow K e^+ \nu_e$ and $D \rightarrow K \pi e^+ \nu_e$ is obtained through a maximum-likelihood fit to the measured branching ratios. The branching ratios for $D^0 \rightarrow K^- l^+ \nu_l$ and $D^+ \rightarrow \overline{K}^0 l^+ \nu_l$ are used as parameters. The branching ratio for $D^+ \rightarrow K^- \pi^+ e^+ \nu_e$ is then:

$$B(D^+ \rightarrow K^- \pi^+ l^+ \nu_l) = \frac{2}{3} \beta \, B(D^+ \rightarrow \overline{K}^0 l^+ \nu_l)$$

Here, β is the relative amount of the K and $K\pi$ final states produced and the factor $2/3$ is the square of the Clebsch-Gordan coefficient. The most likely value of β is 0.8; the uncertainty in this value is 0.3. This uncertainty includes the systematic errors of the various branching ratios.

The ratio $R \equiv B(D \rightarrow K\pi e\nu_e)/(B(D \rightarrow K\pi e\nu_e) + B(D \rightarrow Ke\nu_e))$ is easily calculated from the value of β: $R = 0.44^{+0.08}_{-0.09}$. This is slightly smaller than the value $R = 0.55 \pm 0.12$ reported by the DELCO collaboration[87] which was obtained from a fit to the observed electron energy spectrum using predictions for the spectra from $D \rightarrow K e^+ \nu_e$ and $D \rightarrow K^* e^+ \nu_e$. This measurement is necessarily dependent on the model chosen to represent these spectra. The present direct measurement does not suffer from any inherent model dependence.

Several models predict the relative branching for $D \rightarrow K e^+ \nu_e$ and $D \rightarrow K \pi e^+ \nu_e$. Each of these requires that the K–π system be composed entirely

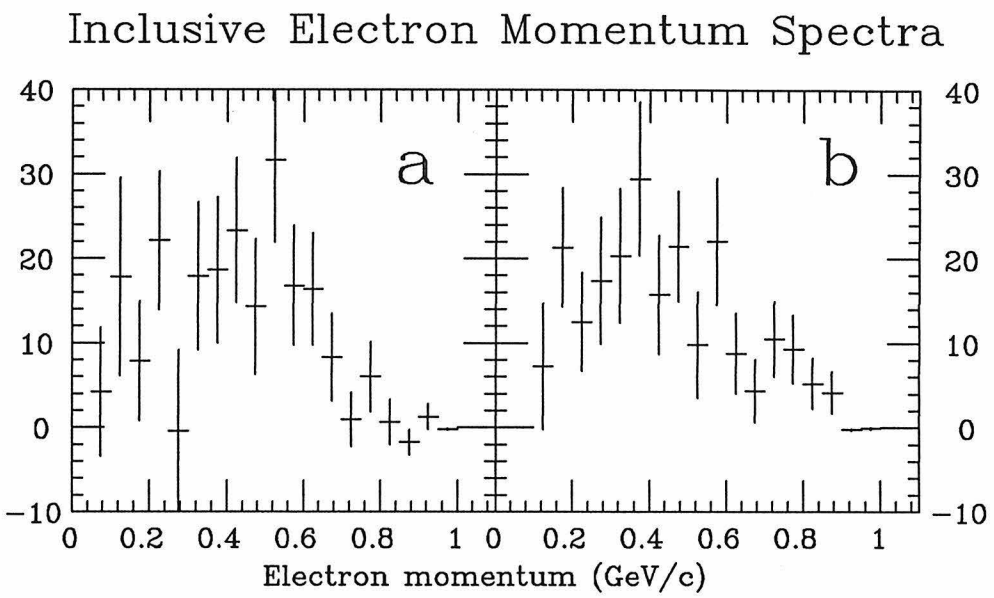

Figure 9.1.1: Inclusive electron momentum spectra
$D^0 \to e^+ X$ (a); $D^+ \to e^+ X$ (b)

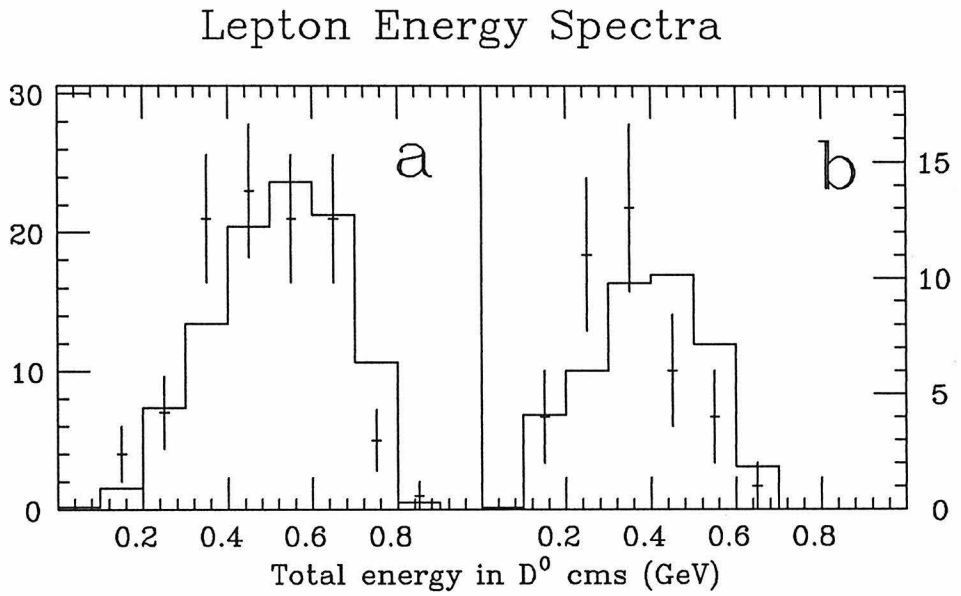

Figure 9.1.2: Exclusive lepton energy spectra in D cms:
$D \to K\, l^+ \nu_l$ (a); $D \to K\, \pi\, l^+ \nu_l$ (b)

of the $K^*(892)$ resonance. If the K–π system in such decays is *assumed* to be resonant — an assumption which will be shown in section 9.3 to be incorrect —

Table 9.2.I: Ratio of K–π Final State to Total Decay Rate

Model	Quantity	Value
Bauer, Stech, Wirbel	$K^*(K+K^*)$	0.53
Grinstein, Wise, Isgur	$K^*(K+K^*)$	0.60
Ali, Yang	$K^*(K+K^*)$	0.24 – 0.36
Suzuki	$K^*(K+K^*)$	0.73
Chao, Kramer, Palmer, Pinsky	$K^*(K+K^*)$	0.24
Observation	$[K\pi]/(K+[K\pi])$	$0.44^{+0.08}_{-0.09}$

the measured values of R may be compared with the predicted values; the values obtained from the models of Bauer, Stech, and Wirbel[88] of Grinstein, Wise and Isgur,[89] of Ali and Yang,[90] of Suzuki[91] and of Chao, Kramer, Palmer, and Pinsky[92] are summarized in Table 9.2.I. The measured value is consistent with the first three models but differs from the prediction of the fourth by 3.6 standard deviations. This is not overly surprising, as the first three models include calculations of hadronic matrix elements whereas the fourth is based on the decay of the c quark, treated as a free particle. This approach was shown in section 3.2 to be inadequate for predicting charmed mesons lifetimes. The last model uses the formalism of chiral anomalies to fix the magnitude of the vector current. This model is somewhat less restrictive in its treatment of the K–π system than the other models; unfortunately, its prediction differs from the measured value of R by 2.2 standard deviations.

9.3: Resonant structure of K–π system

Each of the models discussed in section 9.2 includes the assumption — explicitly or tacitly — that the only hadrons produced in semileptonic decays are single pseudoscalars of single vector mesons. The detected events of the type $D \to K\,\pi\,e^+\,\nu_e$ offer a direct test of this assumption.

The invariant mass of the K–π system is shown in Fig. 9.3.1 for each of the four decays $D^0 \rightarrow K^- \pi^0 e^+ \nu_e$, $D^0 \rightarrow \overline{K}^0 \pi^- e^+ \nu_e$, $D^+ \rightarrow K^- \pi^+ e^+ \nu_e$, and $D^0 \rightarrow \overline{K}^0 \pi^- \mu^+ \nu_\mu$. In each case, there is a clear peak in the mass range 0.875 – 0.925 GeV/c^2 — the range containing the $K^*(892)$ resonance — but there are also events with masses above and below this range. These events are not background. The imposition of tighter tag and particle identification cuts reduces the total number of events but not the relative number of events in the mass 'wings'.

The contribution of the $K^*(892)$ resonance to the observed mass spectrum may be estimated through the use of an unbinned maximum-likelihood fit. The model chosen includes amplitudes for both the K^* and either S-wave or P-wave 'phase-space'.* The spectra for these processes are calculated through a Monte Carlo simulation; the generated events are subjected to the same reconstruction and analysis programs as the real data. The resulting spectra are shown in Fig. 9.3.2. The spectra are smoothed by a cubic-spline algorithm.

The magnitude of the $K^*(892)$ contribution is estimated from the forty electronic events; the events from the decay $D^0 \rightarrow \overline{K}^0 \pi^- \mu^+ \nu_\mu$ contain too much background to be used. An investigation of the K–π mass acceptance indicates no serious systematic differences among the three electronic decays. Therefore, the same fitting function is used for all the events.

The data are presented in Figs. 9.3.3 and 9.3.4 along with the results of the models containing the $K^*(892)$ and S-wave or P-wave phase-space. Even though the fits were performed using unbinned maximum-likelihood techniques, for purposes of comparison, the value of χ^2 is calculated for both modes: χ^2/degree-of-freedom is 14.6/29 for the $K^* + S$-wave model and 16.8/29 for the $K^* + P$-wave model. The fit to the S-wave model is slightly better, but both fits are clearly

* The terms S-wave and P-wave phase-space will be used to denote spectra calculated as described in appendix 3; the S-wave and P-wave matrix elements are used in conjunction with non-resonant phase-space.

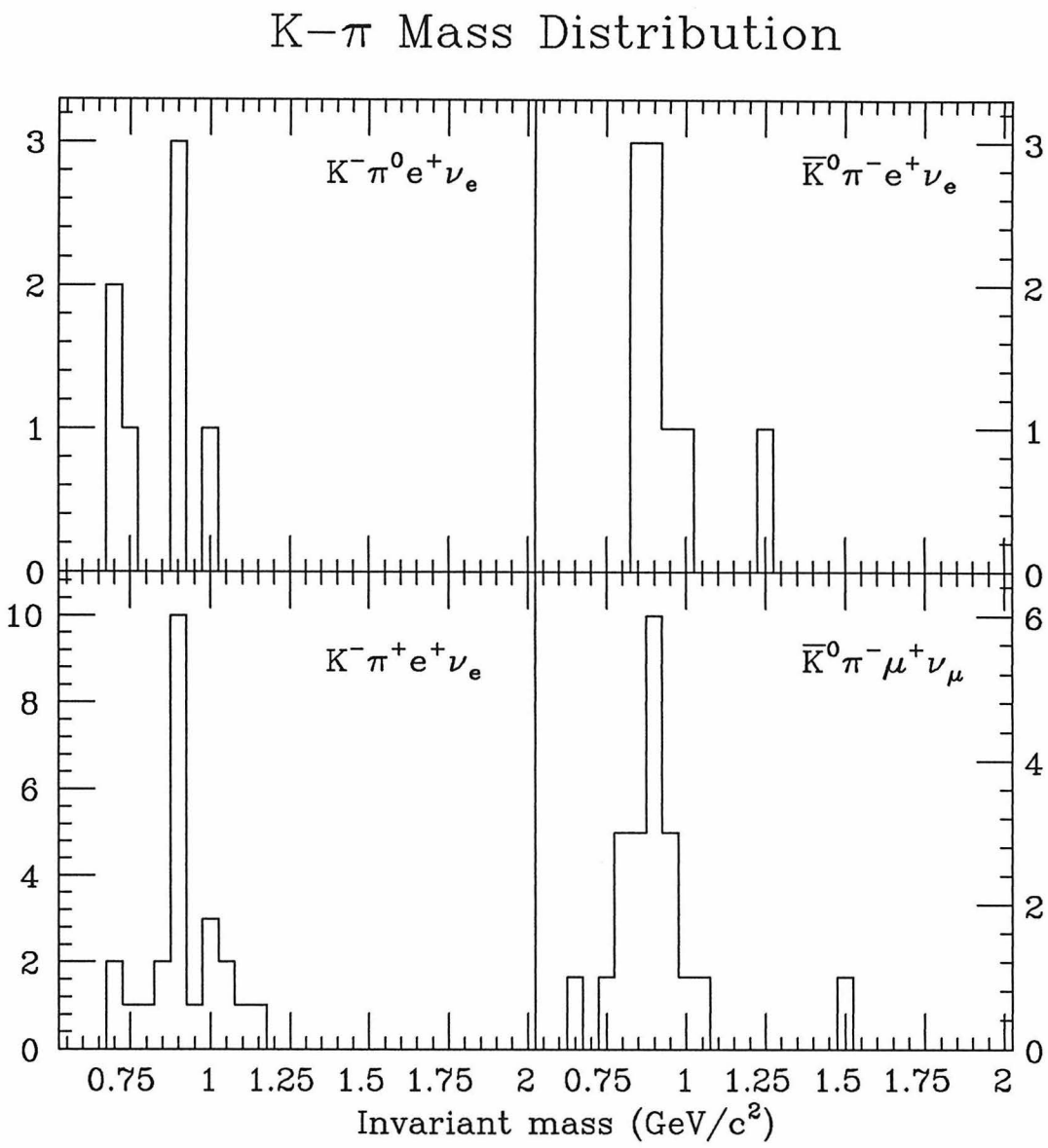

Figure 9.3.1: Invariant masses of K–π system

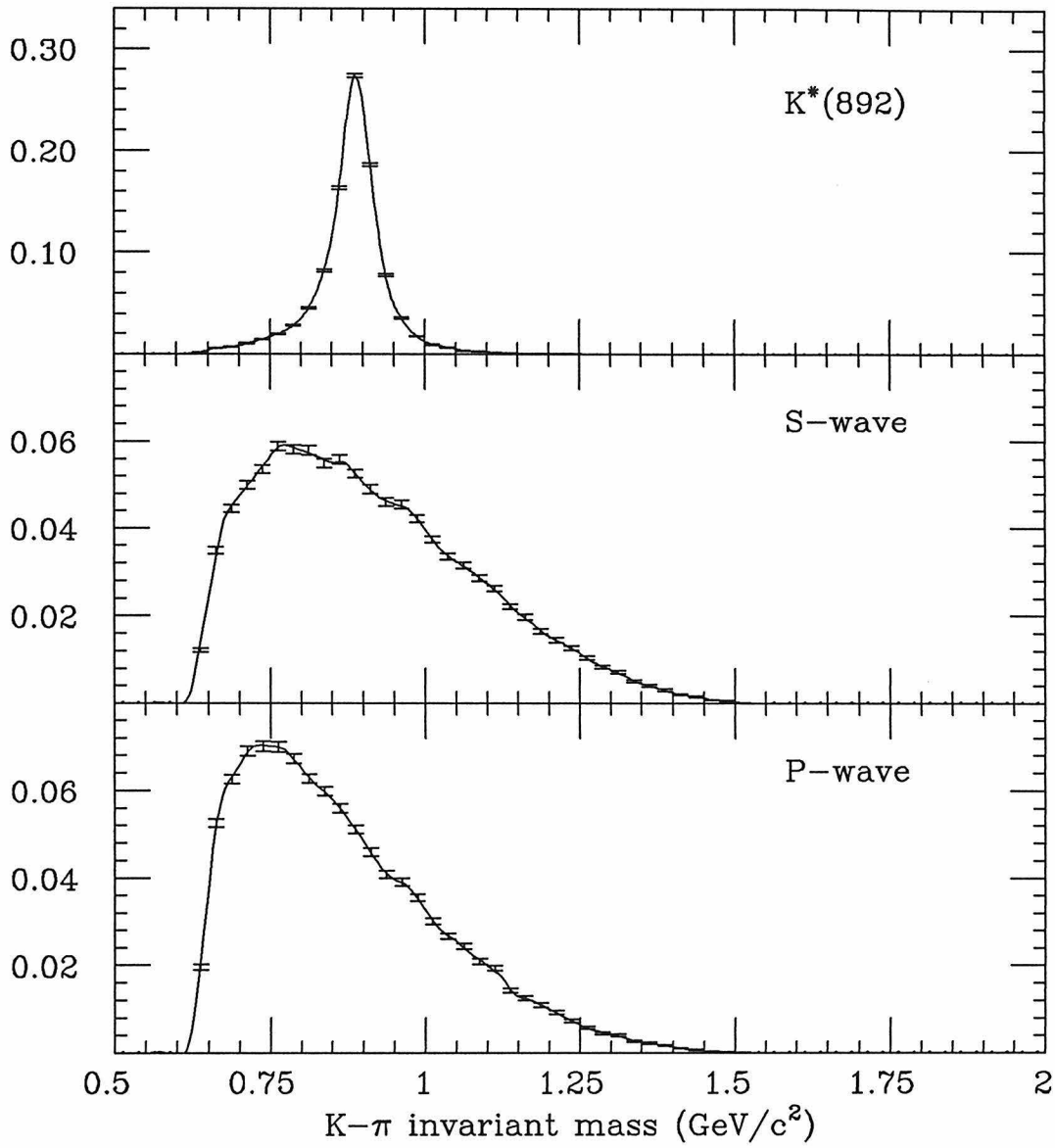

Figure 9.3.2: Predicted K–π mass distributions

acceptable from a statistical point of view. The result of the S-wave fit is:

$$\frac{B(D \to K^* e^+ \nu_e)}{B(D \to K \pi e^+ \nu_e)} = 0.55 \pm 0.13 \ (S\text{−wave})$$

The result of the P-wave fit is:

$$\frac{B(D \to K^* e^+ \nu_e)}{B(D \to K \pi e^+ \nu_e)} = 0.57 \pm 0.13 \ (P\text{−wave})$$

The contribution of the $K^*(892)$, as determined from these fits, indicates that not all of the observed events may be accounted for by the $K^*(892)$ alone. There must be a substantial non-resonant contribution as well.

It is quite difficult to assess the effect of this result on the various theoretical models. Each offers predictions for resonant hadronic states, but not for unbound, non-resonant states. Hence, they must be modified in some way to incorporate such states before they may be used reliably to calculate the rate of semileptonic decay to final states containing more than three bodies. This applies not only to D decays, but also to the decay of bottom mesons. In particular, the measurement of the of the KM matrix element U_{bu} should be carefully reexamined as this depends critically on the endpoint of the lepton momentum spectrum in semileptonic B decay; predictions of this endpoint will require revision if non-resonant final states are found to be important in B decays.

The observation of non-resonant final states in semileptonic decays is not without precedent. The decays $K^+ \to \pi^+ \pi^- e^+ \nu_e$ and $K^+ \to \pi^+ \pi^- \mu^+ \nu_\mu$ proceed at small but measurable rates. The π^+–π^- masses are of necessity below the resonance region. In the case of D decays, however, several resonances are energetically accessible, so the observation of non-resonant final states takes on much more significance.

9.4: Vector form factor

A total of 103 events are observed in the two modes $D^0 \to K^- e^+ \nu_e$ and $D^0 \to K^- \mu^+ \nu_\mu$. These modes are particularly 'clean'; of the 103, only 11.5 are expected to be from background processes. These events are thus well suited for investigation of the dynamics of the decay.

The decay $D^0 \to K^- e^+ \nu_e$ is governed by the vector form factor* $f_+(t)$; t is the square of the momentum transferred to the lepton pair, $(P_D + P_K)^2$.

---

* This is discussed at length in chapter 3.

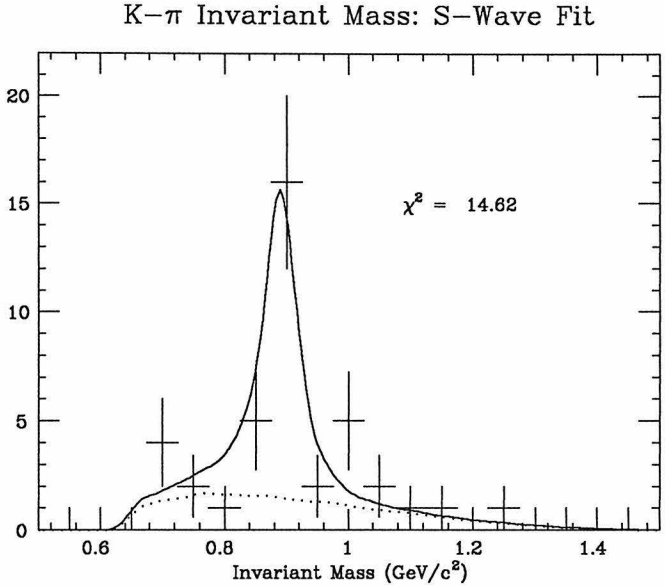

Figure 9.3.3: Invariant mass of the K–π system: fit to $K^*(892)$ + S-wave phase-space

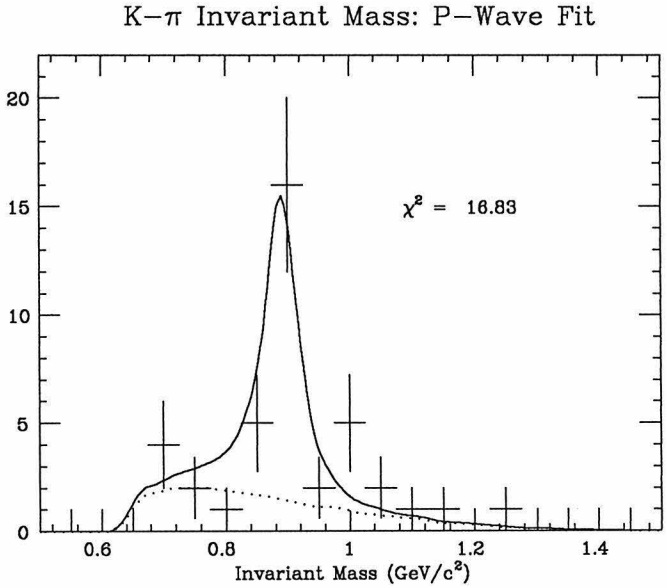

Figure 9.3.4: Invariant mass of the K–π system: fit to $K^*(892)$ + P-wave phase-space

The matrix element for the decay $D^0 \to K^- \mu^+ \nu_\mu$ contains two form factors, $f_+(t)$ and $f_-(t)$, but the effect of the second of these is very small.† The lepton energy spectra for these decays are shown in Fig. 9.3.1; the spectra are calculated according to the formulae of appendix 3. There is clearly little difference in the two spectra. The events detected in the two modes may thus safely be combined for the extraction of the vector form factor.

The Dalitz plot of the lepton and kaon energies is given in Fig. 9.4.2 for each of the two decays. The energies are found by boosting the 4-momenta to the center-of-mass of the decaying D. It is only the presence of the hadronic tag which makes this possible as the 4-momentum of the semileptonically decaying D is known *a priori*. The most obvious features of these Dalitz plots is the accumulation of events toward large kaon energies.

The kaon energy spectrum is proportional to $|f_+(t)|^2$. In the cms of the decaying D, t is equal to $m_D^2 + m_K^2 - 2m_D E_K$. Thus, the value of the form factor may be obtained from the t spectrum of the kaon. The measured t spectra are plotted in Fig. 9.4.3 for the two decay modes.

The number of events expected in the range from t to $t + dt$ is:

$$dN \propto |f_+(t)|^2 \, (x_K^2 - 4\lambda^2)^{3/2} \, \epsilon(t)$$

Here, λ is the ratio of K and D masses, x_K the energy of the kaon in dimensionless units — $x_K = 1 + \lambda^2 - t/m_D^2$ — and $\epsilon(t)$ the detection efficiency. If $|f_+(t)|$ is assumed to be a slowly varying function, the value of $|f_+(t)|$ may be estimated by:

$$f_+(t) \propto \sqrt{\frac{N}{\int_{t-\Delta/2}^{t+\Delta/2} \epsilon(t) \, (x_K^2 - 4\lambda^2)^{3/2} \, dt}}$$

where N is the number of events observed in the range $t - \Delta/2$ to $t + \Delta/2$. The

† The form factor $f_-(t)$ multiplies terms of order m_μ^2. The effect of these terms, relative to those multiplied by $f_+(t)$, is thus of order $m_\mu^2/m_D^2 = 0.003$.

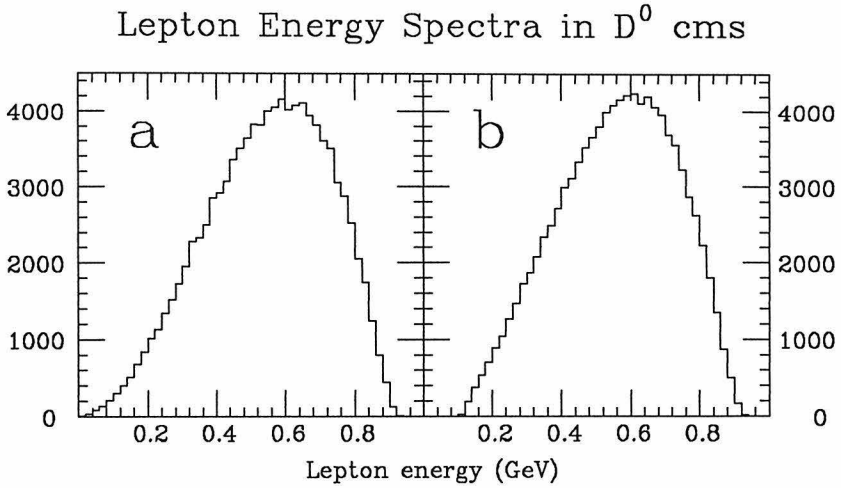

Figure 9.4.1: Energy spectra of leptons in D^0 cms:
$D^0 \to K^- e^+ \nu_e$ (a); $D^0 \to K^- \mu^+ \nu_\mu$ (b)

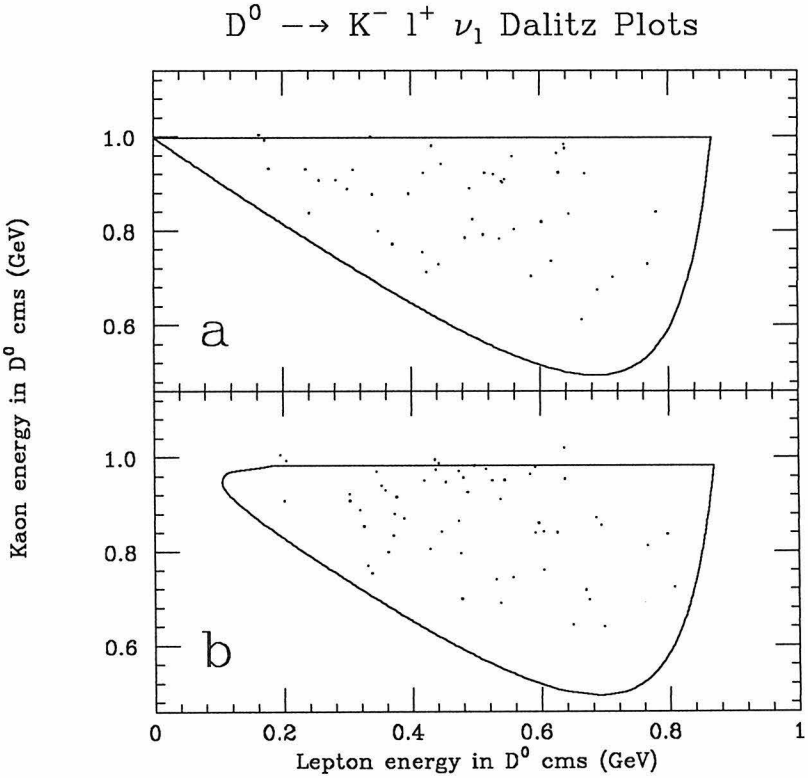

Figure 9.4.2: Dalitz plots of kaon and lepton energies:
$D^0 \to K^- e^+ \nu_e$ (a); $D^0 \to K^- \mu^+ \nu_\mu$ (b)

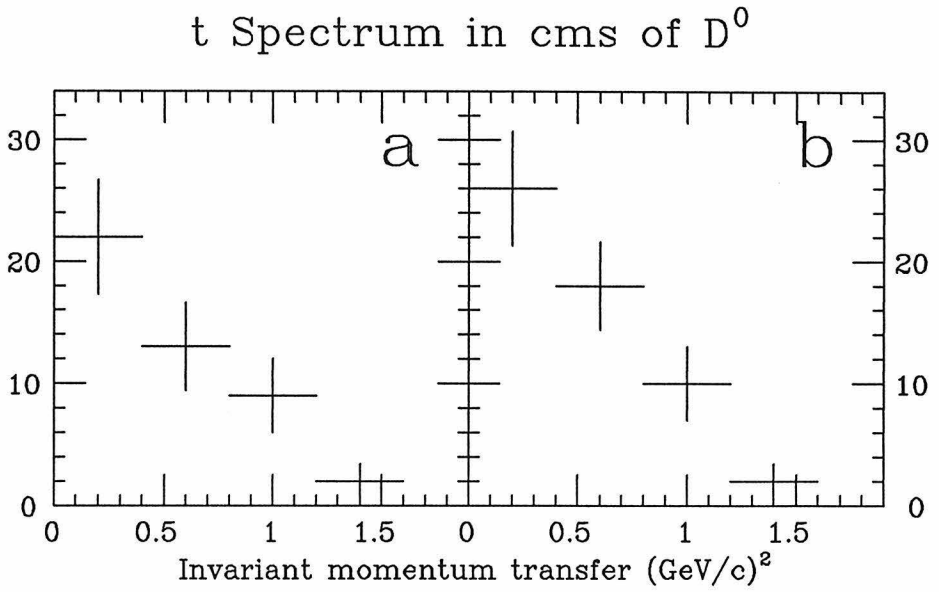

Figure 9.4.3: Kaon t spectra in D cms:
$D^0 \to K^- e^+ \nu_e$ (a); $D^0 \to K^- \mu^+ \nu_\mu$ (b)

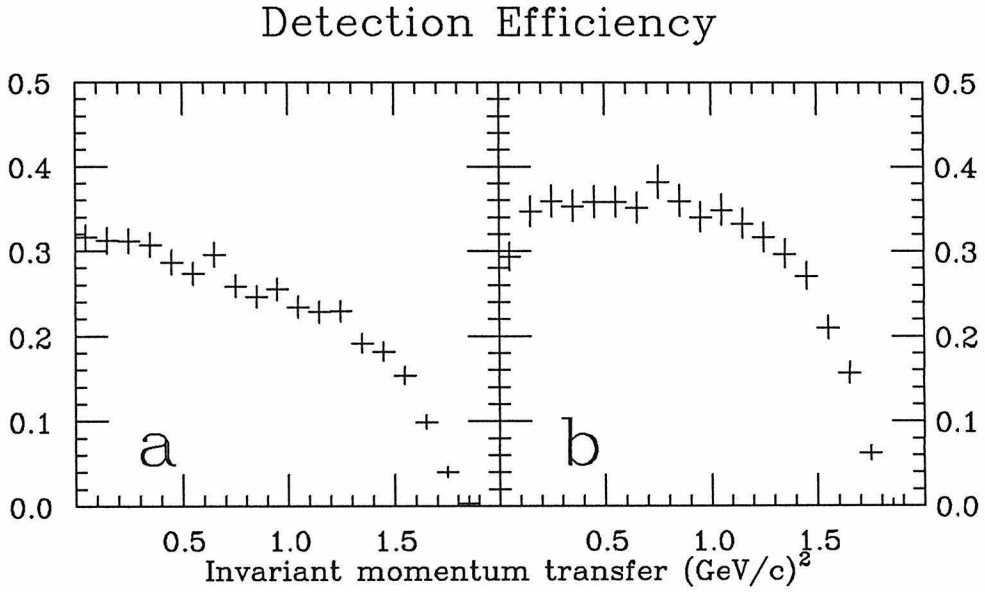

Figure 9.4.4: Detection efficiencies as functions of t:
$D^0 \to K^- e^+ \nu_e$ (a); $D^0 \to K^- \mu^+ \nu_\mu$ (b)

detection efficiencies, obtained from a Monte Carlo simulation are shown in Fig. 9.4.4.

The values of the form factor obtained by the above procedure are given in Fig. 9.4.7b. The unknown constant $f_+(0)$, discussed in section 3.3, may not, unfortunately, be determined in this manner. The values plotted are actually $f_+(t)/f_+(0)$. The calculation of the uncertainties in the values given in the figure merits some discussion. The value of the form factor in some range of t is proportional to $\sqrt{N}$, where N is the number of events detected in this range. The uncertainty in this number of events is, however, also equal to $\sqrt{N}$, at least in the limit in which Gaussian statistics apply. If the usual rules of error propagation are used, the resulting uncertainty in $g \equiv \sqrt{N}$ is quite surprising:

$$g \equiv \sqrt{N}$$
$$\delta g = \frac{\partial g}{\partial N}\,\delta N = \frac{1}{2}$$

This result, that the uncertainty in g is constant, independent of N, is surely not correct. This uncertainty may calculated numerically from the formulae:

$$\sigma_g = \sqrt{< g^2 > - < g >^2}$$
$$< g^m > = \sum_{i=0}^{\infty} i^{m/2}\,\frac{e^{-N}\,N^i}{i!}$$

The uncertainties so calculated are plotted in Fig. 9.4.5. The uncertainty approaches the value $1/2$ — the result from the simple error propagation — for large values of N.

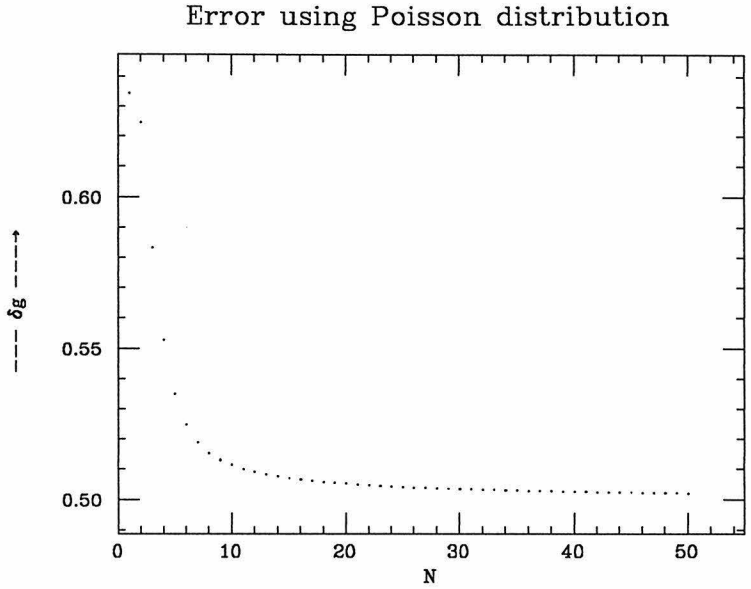

Figure 9.4.5: Uncertainty in $g \equiv \sqrt{N}$

If the vector form factor is assumed to be of the simple pole form derived in section 3.3, the pole mass may be calculated from the kaon t spectrum. The likelihood function is:

$$\mathcal{L}(M) = \prod_{i=1}^{N} \frac{(\epsilon_e(t_i) + \epsilon_\mu(t_i))\,|f_+(t)|^2\,(x_{Ki}^2 - 4\lambda^2)^{3/2}}{\int_0^{t_{\max}} (\epsilon_e(t_i) + \epsilon_\mu(t_i))\,|f_+(t)|^2\,(x_{Ki}^2 - 4\lambda^2)^{3/2}\,dt}$$

$$f_+(t) = f_+(0)\frac{m_{F^*}^2}{m_{F^*}^2 - t}$$

The maximum momentum transfer, $t_{\max}$, is $(m_D - m_K)^2$. The pole mass obtained from the fit is $m_{F^*} = 2.7^{+4.7}_{-0.7}$ GeV/c^2; the errors are evaluated at the 63.8% confidence level corresponding to one standard deviation. The likelihood function is plotted in Fig. 9.4.6; its very asymmetric shape is responsible for the fact that the positive error is so much larger than the negative error.

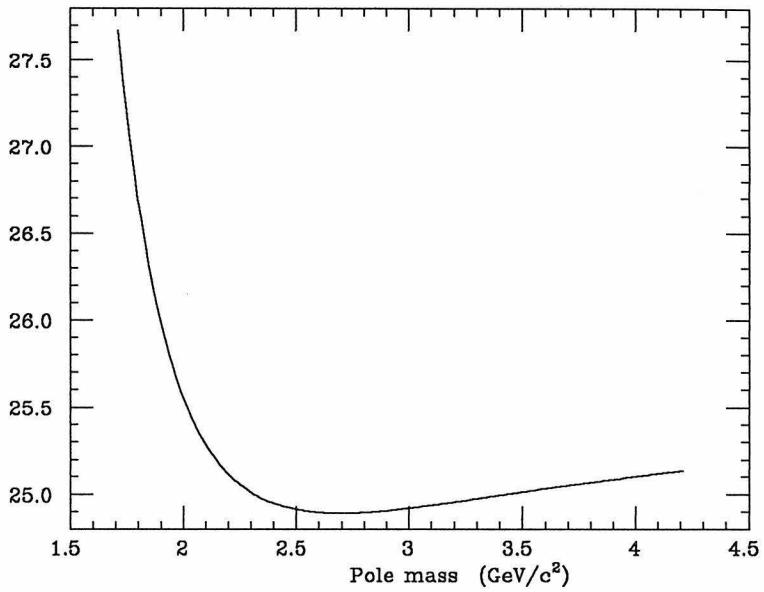

Figure 9.4.6: $w = -\log(\mathcal{L})$ for fit to pole mass

The kaon t spectrum, corrected for detection efficiency, is shown Fig. 9.4.7a; the solid curve is the predicted spectrum using the pole mass obtained from the fit. This prediction clearly provides a satisfactory description of the data. The values of $f_+(t)/f_+(0)$ obtained above are plotted in Fig. 9.4.7b. Again the result of the fit is in good agreement with the data.

The systematic uncertainty in the value of m_{F^*} due to the fitting procedure is studied by generating Monte Carlo events with various values of the pole mass, then calculating this mass from these events. The results of this investigation are shown in Fig. 9.4.8. The fitting procedure is seen to be free of any substantial systematic difficulties. Any remaining systematic uncertainty in the mass determination originates with the determination of the detection efficiencies. If the fit is applied to the electronic and muonic data separately, the results are: $m_{F^*}(e) = 2.4^{+9.0}_{-0.6}$; $m_{F^*}(\mu) = 3.1^{+10.0}_{-1.1}$. The different data sets do yield different results, however, this difference is small compared with the quite large statistical errors in the determination of m_{F^*}.

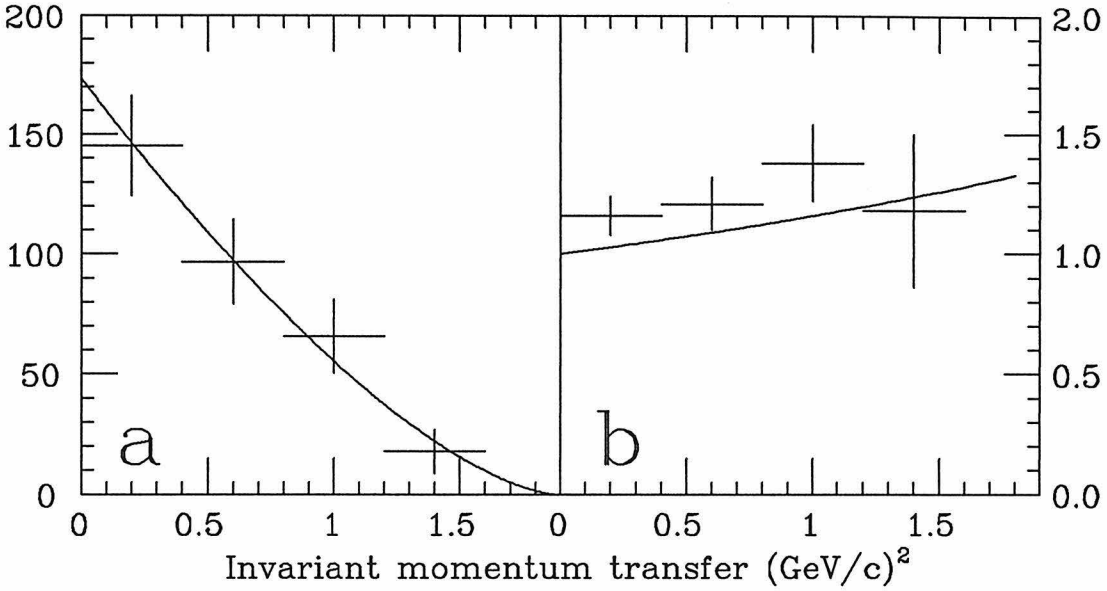

Figure 9.4.7: Kaon t spectrum corrected for detection efficiency (a); Values of vector form factor (b); Solid curves are fit result

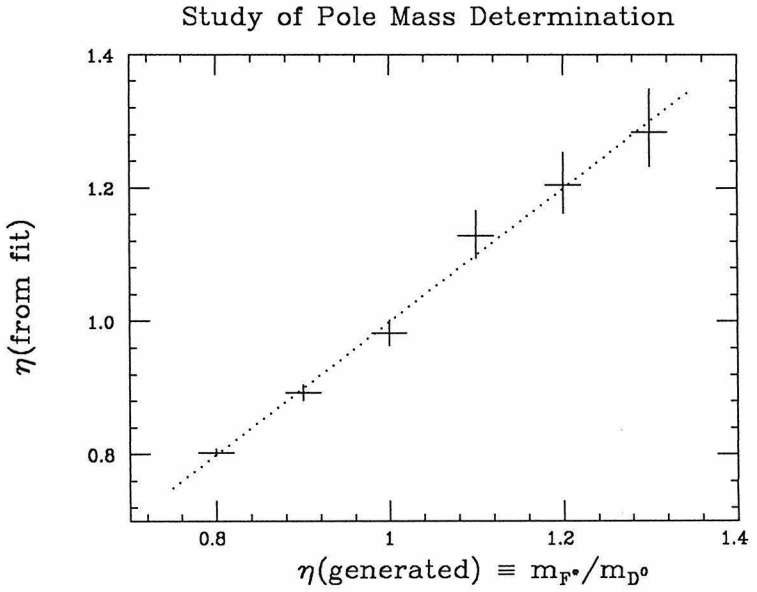

Figure 9.4.8: Comparison of generated and measured values of pole mass

9.5: Conclusions

A great deal of information on the semileptonic decays of D mesons has been discussed, all of the information concerning exclusive processes for the first time. The only previous direct measurements were of the inclusive semileptonic branching ratios.

The exclusive branching ratios obtained are absolute branching ratios. They depend neither on the magnitude of the charm production cross section nor on the integrated luminosity. These measurements are thus directly applicable to other experimental situations where the process of charm production may be completely different.

The measured values of the exclusive branching ratios demonstrate for the first time that the semileptonic decays of D mesons are dominated by the final states $K\,l^+\,\nu_l$, and $K\,\pi\,l^+\,\nu_l$. The lack of large contributions from final states such as $K\,\pi\,\pi\,e^+\,\nu_e$ confirms a basic assumption of almost all theoretical models. As there is sufficient phase-space available for such multi-body decays, the dominance of $K\,l^+\,\nu_l$, and $K\,\pi\,l^+\,\nu_l$ underscores the essential spectator character of semileptonic decays.

The semileptonic decays of kaons have been studied extensively. The dynamics of these processes are in excellent agreement with Standard Model predictions. However, the maximum momentum transfer possible in such decays is relatively small: $0 \leq t \leq (m_K - m_\pi)^2 = 0.13\ (\mathrm{GeV/c^2})^2$. In the case of D decays, this range is extended by more than an order of magnitude: $0 \leq t \leq (m_D - m_K)^2 = 1.88\ (\mathrm{GeV/c^2})^2$. Thus, the semileptonic decays of D mesons probe the Standard Model over a much larger kinematic range than do the decays of kaons. The good agreement between the measured and predicted energy spectra support the procedures used to calculate these spectra: parameterization of hadronic matrix elements through symmetry arguments, and factorization of hadronic and leptonic vertices. That the measured vector form factor is consistent with the simple

pole form lends credence to the idea of using dispersion relations to calculate form factors.

Of the heavy pseudoscalar mesons, the D is the first to be observed in semileptonic decays to four-body final states. That the hadronic part of such a final state is not completely resonant is unexpected and difficult to explain. It may have important consequences for other heavy meson systems such as the B hadron system. Little is known about these particles as only a handful have been reconstructed. If non-resonant final states are important in B decays, this will affect the relative amounts of D and D^* mesons produced in their decay which will in turn affect the calculation of the charm multiplicity from B decays. The presence of non-resonant final states might also affect the search for top — or T — mesons at the SLC and LEP. It has been proposed[93] that the limited hadronic mass range available in semileptonic decays might provide a clean signature for these T mesons. If there are non-resonant final states, these mass limits will become 'smeared out' and it is unclear how clean the signature would remain.

An important lesson to be drawn from the semileptonic decays of D mesons is the necessity of including the properties of hadrons in the calculation of semileptonic decay rates. This has proven feasible and reliable in the case of D mesons. It is even more important in the decay of the B meson; there the spectator model is of even less use due to the helicity of the neutrino. The processes $c \to s\, e^+ \nu_e$ and $D \to K\, e^+ \nu_e$ predict very similar lepton spectra. Predictions based on the processes $b \to c\, e^- \nu_e$ and $B \to D\, e^+ \nu_e$ are, however, very different. This may, in particular, affect the calculation of the endpoint of the lepton momentum spectrum so crucial to the determination of the KM matrix element U_{bc}.

Appendix 1: Recursive Partitioning

Developing Tree Structured Classification Rules

Any object may be characterized by a set of observations or measurements made on it. Further, this object may belong to one of several classes. Suppose that m measurements are performed on each object. Then there is a measurement vector, $\vec{x} = (x_1, \ldots, x_m)$, corresponding to each object. Let X be the space containing all such vectors $\vec{x}$. Suppose further that there are N classes and let C be the set $\{1, \ldots, N\}$. A *classifier*, $d(\vec{x})$, is simply a mapping from X to C.

If A_j is the set of all $\vec{x}$ in X such that $d(\vec{x}) = j$, then $A_j \cap A_i = \emptyset$ if $i \neq j$ and $X = \cup_j A_j$. Thus d *partitions* X into disjoint subsets.

A *learning set*, summarizing past experience, is necessary for devising the classifier. If there is a set of M objects, with classifications already known, the learning set which will be denoted $\mathcal{L}$ is defined as

$$\mathcal{L} = \bigcup_{i=1}^{M} (\vec{x}_i, j_i)$$
$$x_i \in X, j_i \in C$$

Each of the quantities x_i may be of one of two types:

- *ordered*: takes on values from the set of real numbers
- *categorical*: takes on values from a finite set, the elements of which have no natural order, i.e., $\{red,\ white,\ blue\}$

The usefulness of a classifier is measured by its misclassification rate, $R^*(d)$, the probability that an object drawn randomly from X will be incorrectly classified. In general, $R^*(d)$ cannot be calculated directly but several estimates may

be defined. The *resubstitution* estimate is

$$R(d) = \frac{1}{M} \sum_{(\vec{x},j)\in\mathcal{L}} \chi\big(d(\vec{x}_i) \neq j_i\big)$$
$$\chi(true) = 1$$
$$\chi(false) = 0$$

For the *test-sample* estimate, the learning set is divided into two subsets,$\mathcal{L}_1$ and $\mathcal{L}_2$. The classifier, d, is devised only from the elements of $\mathcal{L}_1$. The misclassification rate is estimated from

$$R^{ts}(d) = \frac{1}{M_2} \sum_{(\vec{x},j)\in\mathcal{L}_2} \chi\big(d(\vec{x}_i) \neq j_i\big)$$

Continuing this process, the learning set may be divided into V subsets of equal size. The classifier, d_j, is devised V times from the elements of the set $\cup_{i\neq j}\mathcal{L}_i$. Then the elements of $\mathcal{L}_j$ are used to make a test-sample estimation and finally, the *V-fold cross validation* estimate is calculated.

$$R^{cv}(d) = \frac{1}{V} \sum_{j=1}^{V} R^{ts}(d_j)$$

Tree-structured classifiers are constructed by repeatedly splitting subsets, or *nodes*, of X into two descendant subsets. The process begins with X itself. The final, or terminal, nodes form a partition of X and each one is associated with one and only one class. Several different terminal nodes may, however, be associated with the same class.

Constructing a tree classifier entails using the learning set to

- determine the splits
- identify each terminal node with a class

- decide when to declare a node terminal

Central to determining the best split for a given node is the concept of 'purity'. A node is *pure* if all of its elements are of the same class. It is maximally impure if it contains an equal number of elements of each class. This may be formalized through the use of an impurity function, ϕ, a function on the set of all N-tuples $(P_1,\ldots,P_N)$ satisfying $\sum_{i=1}^{N} P_i = 1$. It should be maximum only at the point $(1/N,\ldots,1/N)$, minimum at the N points $(1,0,\ldots,0)$, $(0,1,\ldots,0)$, $\ldots$, $(0,\ldots,0,1)$, and symmetric in all the P_j's.

The joint probability of an object being both in node t and of class j is estimated as $p(j,t) = \Pi(j) \cdot M_j(t)/M_j$ where M_j is the number of elements in $\mathcal{L}$ of class j, $M_j(t)$ the number of elements in $\mathcal{L}$ which are also in t and of class j, and $\Pi(j)$ is the *a priori* or prior probability of picking an object from X of class j. $\Pi(j)$ is often estimated as M_j/M where M is the total number of elements in $\mathcal{L}$. The probability of an object being in node t is then $P(t) = \sum_j P(j,t)$ and the conditional probability of an object in node t being of class j is $P(j|t) = P(j,t)/P(t)$. Note that $\sum_j P(j|t) = 1$. The *impurity* of a node is defined simply as

$$i(t) = \phi\big(P(1|t),\ldots,P(N|t)\big)$$

Splits are chosen which maximize the decrease in impurity. Suppose a split, s, is chosen which partitions a node t into two new nodes, t_L and t_R, with proportions $p_{_L}$ and $p_{_R}$ of the elements of t going into t_L and t_R, respectively. The decrease in impurity afforded by this split is then

$$\Delta i(s,t) = i(t) - i(t_L)p_{_L} - i(t_R)p_{_R}$$

or noting that $p_{_L} = p(t_L)/p(t)$ and $p_{_R} = p(t_R)/p(t)$

$$\Delta i(s,t) = \big(i(t)p(t) - i(t_L)p(t_L) - i(t_R)p(t_R)\big) \cdot \frac{1}{p(t)}$$

It is important to note that selecting a split to maximize $\Delta i(s,t)$ is equivalent

to selecting a split to minimize the impurity of the whole tree. If a tree has a nodes, T, the subset $\tilde{T}$ of which are terminal, the impurity of the tree is

$$I(t) = \sum_{t \in \tilde{T}} i(t)p(t)$$

Suppose some terminal node, $\tilde{t}$, in $\tilde{T}$ is partitioned according to a split $\tilde{s}$. The new tree, T', has impurity

$$I(T') = \sum_{t \neq \tilde{t}} i(t)p(t) + i(t_L)p(t_L) + i(t_R)p(t_R)$$

The resulting decrease in impurity is then

$$\begin{aligned} I(T) - I(T') &= i(\tilde{t})p(\tilde{t}) - i(t_L)p(t_L) - i(t_R)p(t_R) \\ &= \Delta i(\tilde{s}, \tilde{t}) \cdot p(\tilde{t}) \end{aligned}$$

Since $p(\tilde{t})$ is always greater than 0, a split selected to maximize $\Delta i(s,t)$ is guaranteed to minimize the impurity of the entire tree.

One last requirement needs to imposed upon the impurity function. It is necessary to insure that, all other things being equal, that split is selected which results in the purest daughter nodes. Consider the two-class problem indicated in Fig. A1.1. The same number of objects, 20, are misclassified in both cases. Case **b** is clearly preferable, however, as the right daughter node is completely pure and no further splitting is required. The split resulting in case **b** will be chosen if the impurity function decreases faster than linearly as $P(j|t) \rightarrow 1$.

The criteria for determining a split may now be summarized. First, an impurity function must be chosen with the following properties:

- ϕ is a symmetric function of N variables.
- ϕ is maximum at the point $(1/N, \ldots, 1/N)$
- ϕ is minimum at the N points $(1,0,\ldots,0)$, $(0,1,\ldots,0)$,..., $(0,\ldots,0,1)$.

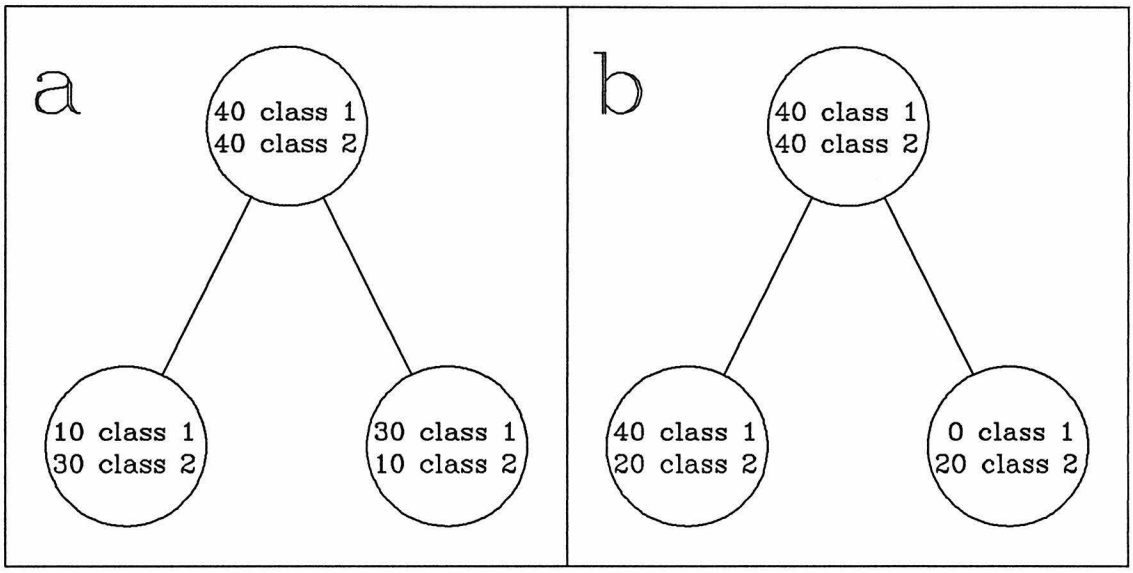

Figure A.1.1: Splits of two different purities:
Split in (b) is preferable to split in (a)
Numbers inside the circles are the class populations.

- $\frac{\partial^2 \phi}{\partial x_j^2} < 0$ for $0 \leq x_j \leq 1$. Second a split is chosen which maximizes $\Delta i(s,t)$

An *identification rule* $j(t)$ assigns to the node t a class from the set C. An obvious choice is $j(t) = \max_i P(i|t)$. It may be the case, however, that it will be more 'costly' to misclassify some classes than to misclassify others. It is possible to introduce this cost via the *cost matrix*, the elements of which are:

$$C(i|j) \geq 0 \qquad i \neq j$$
$$C(i|j) = 0 \qquad i = j$$

The cost of identifying a terminal node as class i is now $\sum_{j=1}^{N} C(i|j)P(j|t)$. The optimal identification rule, the one which minimizes this cost, is $j(t) = \min_i \sum_{j=1}^{N} C(i|j)P(j|t)$.

Impurity functions may also take this variable cost into account. One such

function is the Gini Diversity Index.

$$\phi(P(1|t),\ldots,P(N|T) = \sum_{i,j} C(i|j)P(i|t)P(j|t)$$

The third and final requirement for constructing a tree classifier is a method for determining when a node should be declared terminal. There is no known general procedure for determining whether a node should be split, but there is a simple alternative. A very large tree is produced from the learning set and then parts of this tree which are of little use are removed in a process called *pruning.*

The pruning procedure is quite simple. Denote by T_t the *branch* of T originating at the node t, that is the set consisting of t and all its descendants. An example is shown in Fig. A1.2. As noted above, the cost of a node t is

$$r(t) = \min_i \sum_j C(i|j)P(j|t)$$

The cost of a branch is then

$$R(T_t) = \sum_{t\in\tilde{T}_t} r(t)p(t)$$

where $\tilde{T}_t$ is the set of all terminal nodes in T_t.

The measure of the usefulness of a branch T_t is its cost complexity which is defined as

$$R_\alpha(T_t) = R(T_t) + \alpha|\tilde{T}_t|$$

Here and following $|S|$ denotes the cardinality of the set S. The parameter α is a penalty paid for having too many nodes. As long as $R_\alpha(T_t) < R_\alpha(t)$, T_t is preferable to just t alone, but as α increases so does the cost per terminal node. At some of value of α, it will be preferable to prune T_t, keeping only t.

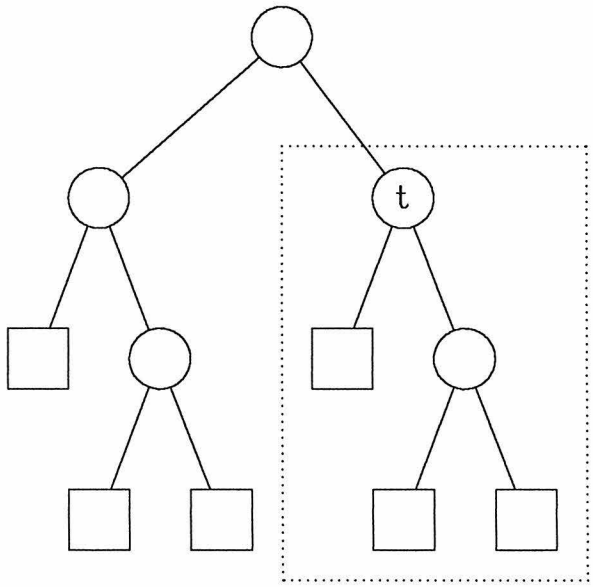

Figure A1.2: Example of a branch: dotted lines enclose T_t

The value of α at which this occurs is easily calculated. If $R_\alpha(T_t) = R_\alpha(t)$ then $R(T_t) + \alpha|\tilde{T}_t| = R(t) + \alpha$, or

$$\alpha = \frac{R(t) - R(T_t)}{|\tilde{T}_t| - 1}$$

Defining $A(t) = (R(t) - R(T_t))/(|\tilde{T}_t| - 1)$, the *weakest link* in the tree is that node for which $A(t)$ is a minimum, for as α increases this node is the first node with $R_\alpha(t) = R_\alpha(T_t)$.

The complete procedure for producing a tree-structured classifier consists in:

1. growing an overly large tree from the learning set, with at most a few elements of this set in each terminal node.
2. pruning this large tree by removing successively each weakest-link. If two or more nodes yield the same value of $A(t)$, all of them are pruned at the same time.
3. evaluating the true misclassification cost of each of the resulting subtrees, either by cross-validation or by the use of an independent test set.

The best subtree is the one with the lowest misclassification cost. This tree is used as the tree-structured classifier.

Appendix 2: Identification of K_s^0

In the plane transverse to the beam direction, the trajectory of a particle is circular. Two such trajectories intersect in this transverse plane in zero, one or two *crossing points.* (The case in which the circular paths coincide exactly will be excluded from consideration.)

The radii of the circles, as well as the position of their centers, must be calculated first in terms of the charges and momenta of the particles, their positions of closest approach to the primary vertex, and the magnitude of the magnetic field. The radii, ρ_1 ρ_2, are given by the formula $\rho = p_{xy}/(0.03 \cdot B)$, where p_{xy} is the transverse momentum and B the magnitude of the magnetic field. If $\vec{M}_i$ is the position of closest approach of the i^{th} particle, and q_i and φ_i are its charge and azimuthal position, the center of the circular path is located at:

$$C_x = M_x + q\rho \sin\varphi$$

$$C_y = M_y - q\rho \cos\varphi$$

The various angles are illustrated in Fig. A2.1.

The paths will not intersect if the circles are disjoint or if one is contained wholly within the other. Even if there is no crossing of the trajectories, these could still correspond to the decay of a K_s^0. Multiple Coulomb scattering and measurement errors will limit the accuracy to which the helices may be reconstructed. The circular projections must come within a 'grazing distance' of each other of 9 mm to be considered further.

If one circle is contained within the other, the vertex is taken to be the point halfway between the two points on the circles closest to each other, as illustrated if Fig. A2.2. The position of the vertex is:

$$\vec{V} = \vec{C}_1 + \frac{1}{2}(\Delta + \rho_1 + \rho_2)\hat{r}$$

Δ is the distance between the centers $|\vec{C}_2 - \vec{C}_1|$ and $\hat{r}$ the unit vector connecting

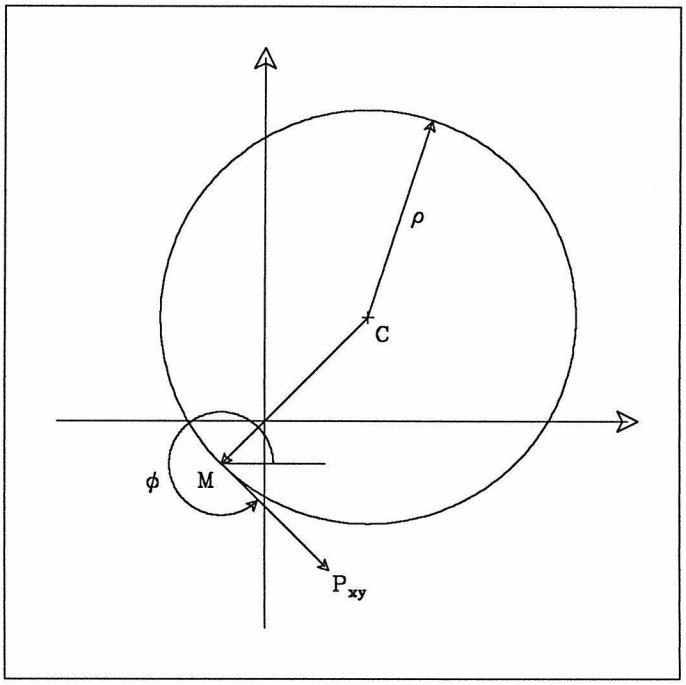

Figure A2.1: Center of helix

them $(\vec{C}_2 - \vec{C}_1)/\Delta$. The points on the circles closest to this vertex are:

$$\vec{N}_1 = C_1 + \rho_1 \hat{r} \qquad\qquad \vec{N}_2 = C_2 - \rho_2 \hat{r}$$

When the two circles are disjoint, a similar calculation yields the position of the vertex. This situation is shown in Fig. A2.3. In this case:

$$\vec{V} = \vec{C}_1 + \frac{1}{2}(\Delta + \rho_1 - \rho_2)\hat{r}$$

The points nearest the vertex are as given above. If the circles intersect in only a single point, the two formulae above yield the same vertex position:

$$\vec{V} = \vec{C}_1 + \rho_1 \hat{r}$$

This final case to be considered is that in which the circles intersect in two points. This is, unfortunately, more complicated than the previous cases. A

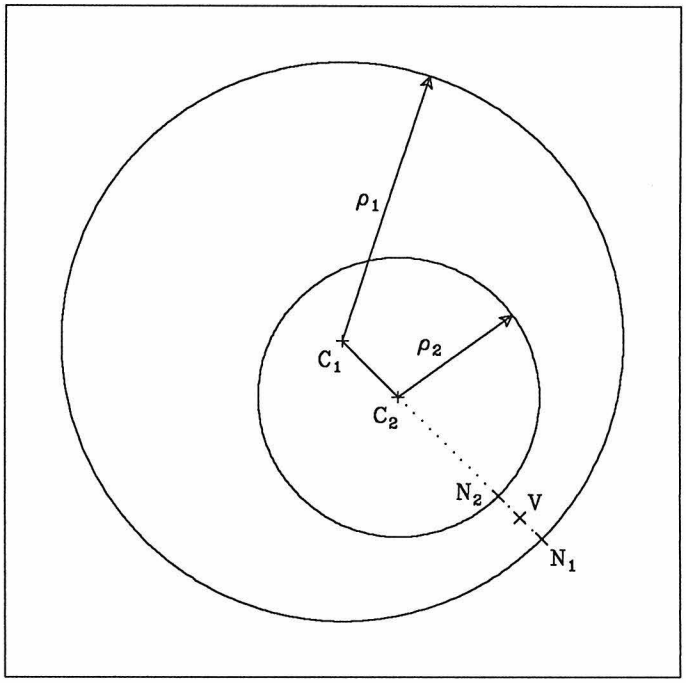

Figure A2.2: One circle within the other

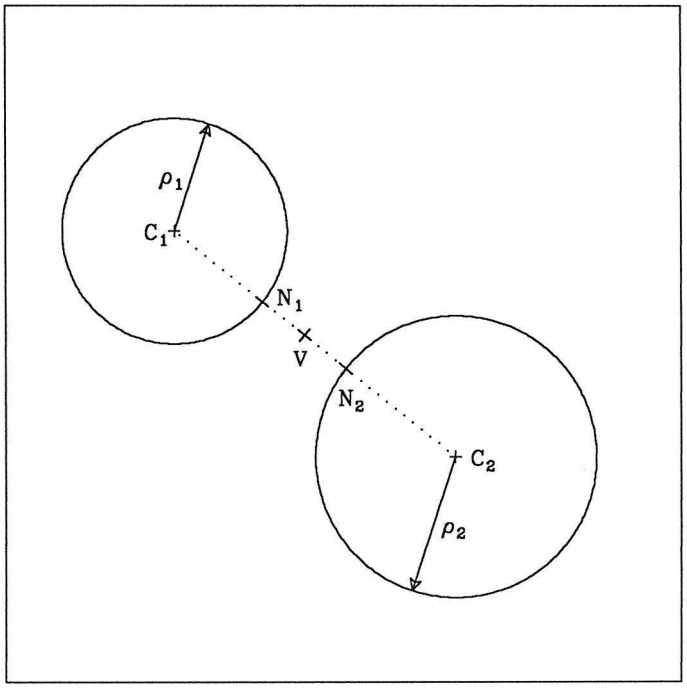

Figure A2.3: Two circles disjoint

diagram defining the various angles involved is given in Fig. A2.4. It is easily seen that $\sigma^2+\lambda_1^2 = \rho_1^2$ and $\sigma^2+\lambda_2^2 = \rho_2^2$. Also, it should be noted that $\Delta = \lambda_1+\lambda_2$. Now:

$$\rho_1^2 - \rho_2^2 + \Delta^2 = 2\lambda_1^2 + 2\lambda_1\lambda_2 = 2\lambda_1\Delta$$

Since ρ_1 and λ_1 are related — $\rho_1 \cos\zeta = \lambda_1$ — it is simple to solve for $\cos\zeta$.

$$\cos\zeta = \frac{\rho_1^2 - \rho_2^2 + \Delta^2}{2\rho_1\Delta}$$

The positions of the two crossing points may now be calculated:

$$\begin{aligned} V_{1x} &= C_{1x} + \rho_1 \cos(\xi + \zeta) \\ V_{1y} &= C_{1y} + \rho_1 \sin(\xi + \zeta) \\ V_{2x} &= C_{2x} + \rho_1 \cos(\xi - \zeta) \\ V_{2y} &= C_{2y} + \rho_1 \sin(\xi - \zeta) \end{aligned}$$

The vertex closest to the primary vertex is kept.

It is now necessary to calculate for all cases the z position of the vertex. For a helix, there is a simple relation between the angle swept out in $x-y$ plane, η, and the distance travelled in the z direction:

$$\cot\lambda = -\rho q \frac{d\eta}{dz}$$

The angle λ is the dip angle of the helix and q is the particle charge. The angle η is the sum of the two angles α and β as indicated in Fig. A2.5. The first of these, α, is the azimuthal position of the vertex in a coordinate system centered at $\vec{C_1}$.

$$\tan\alpha = \frac{V_y - C_{1y}}{V_x - C_{1x}}$$

The angle β is related to the azimuthal direction φ_1 of particle number one at it position of closest approach to the primary vertex: $\beta = -q_1 \cdot \pi/2 - \varphi_1$. The

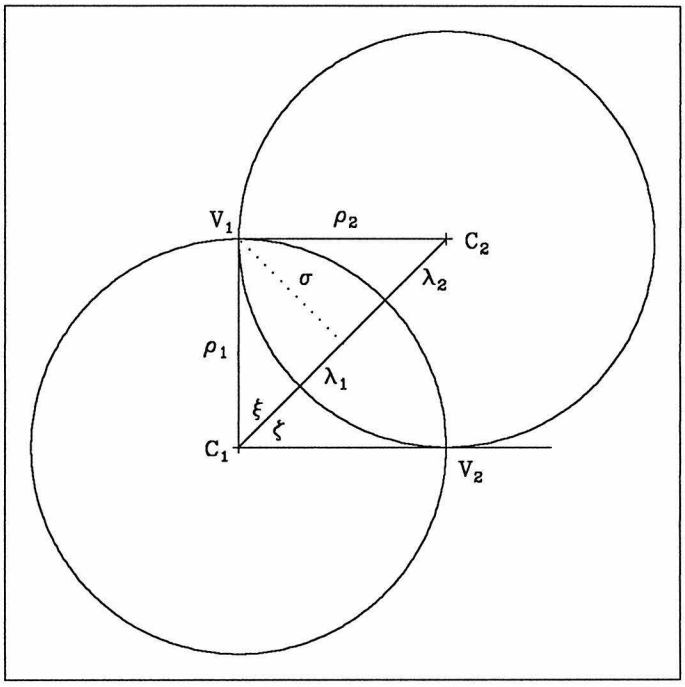

Figure A2.4: Two crossing points

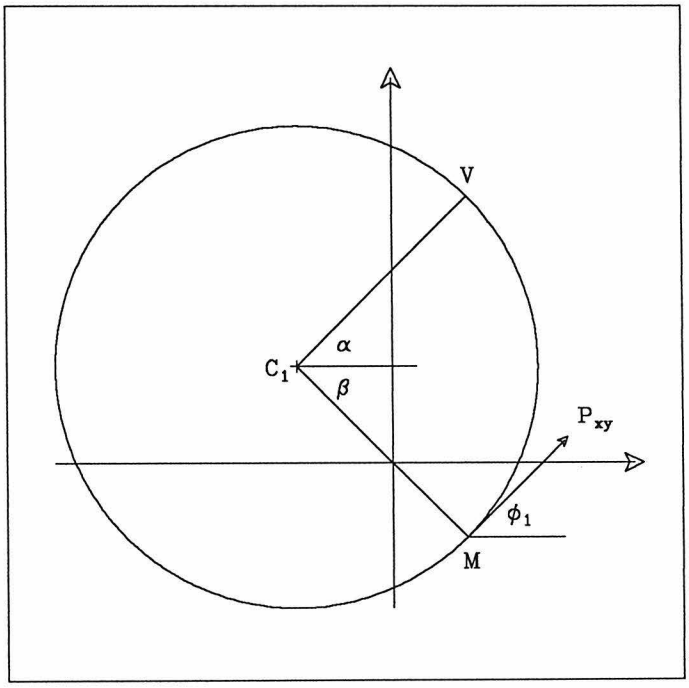

Figure A2.5: Turning angle

angle η is now given by:

$$\sin\eta = -q_1 \sin(\alpha + \varphi_1)$$

The distance travelled in the z direction is finally:

$$\Delta z = -\rho_1 q_1 \arcsin(-q_1 \, sin(\alpha + \varphi_1))$$

The resolution in the dip angle is significantly worse than the resolution in the transverse plane. For this reason, the z distance is calculated separately for both tracks. The z position of the vertex is obtained by averaging these distances.

The momenta of the two tracks must now be transformed — 'swum' — to the vertex. This accomplished most easily by calculating the swum momenta in terms of the total transverse momentum, p_{xy}: $p_x = qp_{xy} \sin\alpha$, $p_y = -qp_{xy} \cos\alpha$. The z component is unchanged.

Appendix 3: Spectra in Semileptonic Decays

A3.1: $D \to P\, e^+\, \nu_e$

The simplest semileptonic decays are those in which a pseudoscalar meson decays into another pseudoscalar, an electron and an electron-neutrino. An example of such a decay is $D \to K\, e^+\, \nu_e$. When a D meson decays semileptonically, the amplitude may be written as:

$$M = \frac{G_F}{\sqrt{2}} J^{\mu}_{hadronic}\, J_{\mu,\, leptonic}$$
$$J_{\mu,\, leptonic} = \overline{u}(\nu_l)\gamma_\mu(1-\gamma_5)v(l^+)$$

As was discussed in chapter 3, if the D decays into a kaon (or pion) and a lepton pair, the hadronic current may be parameterized in terms of two form factors:

$$J_{\mu,\, hadronic} = \sqrt{2}\cos\vartheta_C\,(f_+(t)(P_D+P_K)_\mu + f_-(t)(P_D-P_K)_\mu)$$

If the charged lepton is an electron, the second form factor $f_-(t)$ may be ignored. This is easily demonstrated by considering the contraction of $(P_D - P_K)_\mu$ with $J_{\mu,\, leptonic}$.

$$(P_D-P_K)_\mu\,\overline{u}(\nu_e)\gamma^\mu(1-\gamma_5)v(e^+) = (P_e+P_\nu)_\mu\,\overline{u}(\nu_e)\gamma^\mu(1-\gamma_5)v(e^+)$$
$$= \overline{u}(\nu_e)\not{P}_\nu(1-\gamma_5)v(e^+) + \overline{u}(\nu_e)(1+\gamma_5)\not{P}_e v(e^+)$$

The Dirac equation may be used to simplify this further since:

$$\overline{u}(\nu_e)\not{P}_\nu = m_\nu\overline{u}(\nu_e) = 0$$
$$\not{P}_e v(e^+) = -m_e v(e^+)$$

$$(P_D-P_K)_\mu\overline{u}(\nu_e)\gamma^\mu(1-\gamma_5)v(e^+) = -m_e\overline{u}(\nu_e)(1+\gamma_5)v(e^+)$$

If it is assumed that f_- is at most of the same magnitude* as f_+, this term has a negligible effect on the decay rate due to the smallness of m_e.

---

* In the PCAC limit, $f_-(t)$ should actually be much smaller in magnitude than $f_+(t)$.

The invariant amplitude is now given by:

$$M = G_F \cos\vartheta_C \, f_+(t)(P_D + P_K)_\mu \, \bar{u}(\nu_e)\gamma^\mu(1-\gamma_5)v(e^+)$$

It is necessary to square this and sum over the lepton spins.†

$$\sum |M|^2 = 8G_F^2 \cos^2\vartheta_C \, |f_+(t)|^2 (2P_e\cdot(P_D+P_K)\, P_\nu\cdot(P_D+P_K) - P_e\cdot P_\nu (P_D+P_K)^2)$$

The remaining calculations are best carried out in the rest-frame of the decaying D. It is convenient to introduce the dimensionless quantities $x_i \equiv 2E_i/m_D$ and $\lambda = m_K/m_D$. Note that if all three final state particles were massless, the range of each of the x_i's would be from 0 to 1. In terms of these, the inner products are:

$$P_D \cdot P_K = \frac{1}{2}m_D^2 x_K \qquad P_K \cdot P_e = \frac{1}{2}m_D^2(1 - x_\nu - \lambda^2)$$

$$P_D \cdot P_e = \frac{1}{2}m_D^2 x_e \qquad P_K \cdot P_\nu = \frac{1}{2}m_D^2(1 - x_e - \lambda^2)$$

$$P_D \cdot P_\nu = \frac{1}{2}m_D^2 x_\nu \qquad P_e \cdot P_\nu = \frac{1}{2}m_D^2(1 - x_K + \lambda^2)$$

The matrix element is now:

$$\sum |M|^2 = 4m_D^4 G_F^2 \cos^2\vartheta_C \, |f_+(t)|^2 (2x_e x_\nu - x_e^2 - x_\nu^2 - 4\lambda^2 + x_K^2)$$

---

† The normalization chosen for the spinors is:

$$\bar{u}u = 2m \qquad \bar{v}v = -2m$$

With this choice:

$$\sum_s u_\alpha(P,s)\bar{u}_\beta(P,s) = (\not{P} + m)_{\alpha\beta}$$

$$\sum_s v_\alpha(P,s)\bar{v}_\beta(P,s) = (\not{P} - m)_{\alpha\beta}$$

The decay rate is then given by:

$$\Gamma = \frac{1}{2m_D(2\pi)^5}\int \sum |M|^2\,\delta^4(P_D - P_K - P_e - P_\nu)\frac{d^3p_K}{2E_K}\frac{d^3p_e}{2E_e}\frac{d^3p_\nu}{2E_\nu}$$

In the rest frame of the D, $t = m_D^2(1+\lambda^2 - x_K)$, so seven of the integrals may be performed trivially, yielding the expression:

$$\Gamma = \frac{G_F^2\cos^2\vartheta_C m_D^5}{16\pi^3}\int |f_+(t)|^2(2x_e - 2x_Kx_e - x_e^2 + x_K - 1 - \lambda^2)dx_Kdx_e$$

The joint distribution of x_e and x_K is then:

$$W(x_e, x_K) = |f_+(t)|^2\,(2x_e - 2x_Kx_e - x_e^2 + x_K - 1 - \lambda^2)$$

In order to obtain the distribution of x_K, it is necessary to carry out the integration over x_e.* The result is remarkably simple:

$$W(x_K) = |f_+(t)|^2\,(x_K^2 - 4\lambda^2)^{3/2}$$

If the form factor $f_+(t)$ is taken to be constant, the electron energy spectrum

---

* The limits of integration depend on the value of x_K. The relation $(P_K + P_\nu)^2 = (P_D - P_e)^2$ is given in terms of the dimensionless quantities by:

$$1 - x_e = \lambda^2 + \frac{1}{2}x_\nu(x_K - (x_K^2 - 4\lambda^2)^{1/2}\cos\vartheta_{K\nu})$$

Solving for x_e, and making use of the identity $x_K + x_e + x_\nu = 2$:

$$x_e = 2 - x_K + \frac{2(1-\lambda^2 - x_K)}{x_K - 2 - (x_K^2 - 4\lambda^2)^{1/2}\cos\vartheta_{K\nu}}$$

The limits are given by the constraint $|\cos\vartheta_{K\nu}| \leq 1$. The upper and lower limits, x_e^u and x_e^l, are then:

$$x_e^u = 2 - x_K + \frac{2(1+\lambda^2 - x_K)}{x_K - 2 - (x_K^2 - 4\lambda^2)^{1/2}}$$

$$x_e^l = 2 - x_K + \frac{2(1+\lambda^2 - x_K)}{x_K - 2 + (x_K^2 - 4\lambda^2)^{1/2}}$$

and the distribution of $\cos\vartheta_{Ke}$ may be obtained in closed form:

$$W(x_e) = \frac{x_e^2(1-\lambda^2-x_e)^2}{1-x_e}$$

$$W(y) = \left[\frac{1}{y^5}(6+6y(1-\lambda^2)+y^2(1-\lambda^2)^2)\log(1+y(1-\lambda^2)) - \frac{3(1-\lambda^2)}{y^4}(2+y(1-\lambda^2))\right](1+y)$$

$$y = \frac{1}{2}(\cos\vartheta_{Ke}-1)$$

For the calculation of detection efficiencies, it necessary to generate a large number of events in which the kinematic variables display the correct spectra. Suppose that these distributions are determined by an integral of the form:

$$I = \int_a^b dx \int_c^d dy\, f(x,y)$$

The integration may be performed numerically by the Monte Carlo method. The variables x and y are picked at random — with a uniform distribution — in the appropriate ranges. If *many* such pairs are chosen, the value of the integral is approximately:

$$I \approx \frac{1}{N}\sum_{i=1}^{N} f(x_i,y_i)$$

The random variables x and y drawn from these N events will not, of course, have the correct spectra as the values of x and y were chosen uniformly. The *correct* distributions are:

$$P(x) = \frac{1}{I}\frac{dI}{dx} = \frac{1}{I}\int_c^d dy\, f(x,y)$$

$$P(y) = \frac{1}{I}\frac{dI}{dy} = \frac{1}{I}\int_a^b dx\, f(x,y)$$

The joint probability is:

$$P(x,y) = \frac{1}{I} f(x,y)$$

Finally, the conditional probability of y given a value of x is:

$$P(y|x) = \frac{P(x,y)}{P(x)} = \frac{f(x,y)}{\int_c^d dy\, f(x,y)}$$

The random variables x and y may be forced easily to have the correct spectra. Consider the case of a single variable $z \in [a,b]$ with the probability distribution $P(z)$. Suppose it is necessary to pick values of z randomly such that these values will reflect $P(z)$. A simple way to do this is to pick values *uniformly* in the range $[a,b]$. The variable $q_i = P(z_i)/P_{max}$, where P_{max} is the maximum value of P, is then a random variable in the range [0,1]. This value q_i is compared with another *uniformly* distributed random variable r also in the range [0,1]. The value of z_i is retained only if $r_i \leq q_i$, otherwise it is discarded and a new value generated. The probability that a value of z in the range $[\tilde{z}, \tilde{z} + dz]$ will be retained is then equal to $P(\tilde{z})dz$. Thus the set of values $\{z_i\}$ are correctly distributed. This procedure is called the *weighted-rejection* method.

This method may be generalized to any number of variables. In the present case, there are two variables x and y. If both are generated uniformly, the joint probability $f(x,y)$ divided by its maximum must be compared with a uniformly distributed random number as before. Those events retained will display the correct spectra.

For each event (x_i, y_i), $f(x_i, y_i)$ is the *weight.** The value of the integral is just the mean value of these weights. These may exhibit very large fluctuations so the value of the integral estimated from them may converge only very slowly. Often a change of variables may substantially limit these fluctuations and

---

$\star$ If the integration is over a volume of phase-space, this weight is denoted the *phase-space weight.*

thus dramatically improve the convergence. The procedure for such a change of variables is best illustrated in one dimension.

$$I = \int_a^b f(x)\,dx$$

Suppose the values of x are not to be picked uniformly but rather according to a distribution $g(x)$. Define the cumulative distribution to be $G(x) = \int_a^x g(y)\,dy$. Consider now the ratio:

$$r = \frac{G(x) - G(a)}{G(b) - G(a)}$$

Clearly, r is a random variable in the range [0,1]. Further, dr is given by:

$$dr = \frac{g(x)\,dx}{G(b) - G(a)}$$

Thus if x is distributed according to $g(x)$, r is *uniformly* distributed. The ratio above may be inverted formally to yield:

$$x = G^{-1}[G(a) + r(G(b) - G(a))]$$

The integral is now:

$$\begin{aligned} I &= \int (G(b) - G(a)) \frac{f(x(r))}{g(x(r))}\,dr \\ &\approx \frac{1}{N} \sum_{i=1}^{N} (G(b) - G(a)) \frac{f(x(r_i))}{g(x(r_i))} \end{aligned}$$

If the function g is nearly the same as f, the Monte Carlo estimate of the integral will converge very quickly.

Returning now to the case of two variables, suppose x is distributed according to:

$$g(x) = \frac{1}{I} \int_c^d f(x,y)\, dy$$

and that y is distributed according to:

$$P(y|x) = \frac{1}{I} \frac{f(x,y)}{g(x)}$$

The cumulative distributions are:

$$G(x) = \int_a^x g(x)\, dx \qquad\qquad H(y) = \int_c^y \frac{f(x,y)}{I\, g(x)}\, dy$$

Finally, define the two ratios:

$$r_1 = \frac{G(x) - G(a)}{G(b) - G(a)} = G(x)$$
$$r_2 = \frac{H(y) - H(c)}{H(d) - H(c)} = H(y)$$

The differential quantities are given by:

$$dr_1 = g(x)\, dx$$
$$dr_2 = \frac{f(x,y)}{I\, g(x)}\, dy$$

The integration is now reduced to the trivial result:

$$I = \int f(x,y)\, dxdy = \int \frac{I}{f(x,y)} f(x,y)\, dr_1 dr_2$$

Thus the weight for each event is unity.

The procedure outlined above is used to construct the 4-momenta in the Monte Carlo simulation of $D \to P\, e\, \nu_e$.

1. x_K is picked in the range $[2\lambda, 1+\lambda^2]$ according to $W(x_K)$.
2. x_e is picked in the range $[x_e^l, x_e^u]$ according to $W(x_e|x_k)$ using the value of x_K picked in step 1.
3. The polar angles, φ_e and φ_K, are picked uniformly in the range $[0, 2\pi]$; $\cos\vartheta_{K\nu}$ is picked uniformly in the range [-1,+1].
4. Finally, the angle between the 3-momenta of the kaon and electron is evaluated:

$$\cos\vartheta_{Ke} = \frac{2(1+\lambda^2 - x_K - x_e + 2x_e x_K)}{x_e(x_K^2 - 4\lambda^2)^{1/2}}$$

The various spectra are illustrated in Figs. A3.1.1 – A3.1.4. The form factor was taken to be of the simple pole form:

$$f_+(t) = f_+(0)\frac{m_{F^*}^2}{m_{F^*}^2 - t} \qquad\qquad m_{F^*} = 2.14 \text{ GeV/c}^2$$

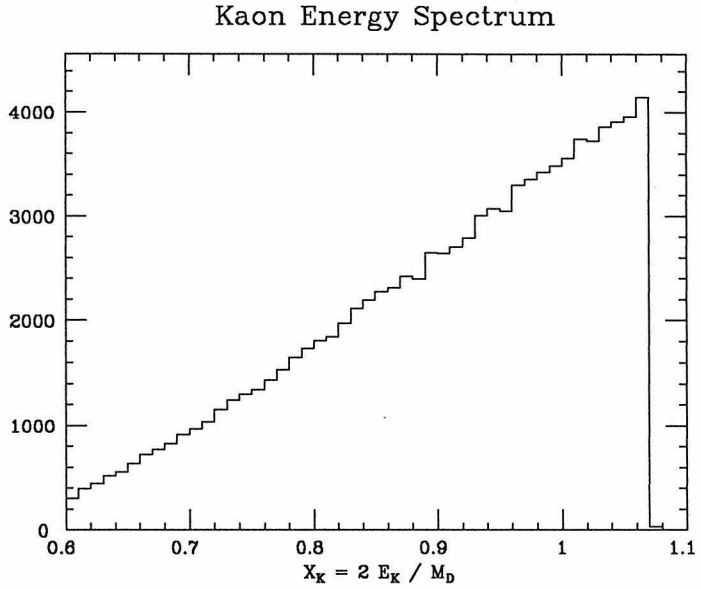

Figure A3.1.1: Energy spectrum of K^- in D^0 rest frame for $D^0 \rightarrow K^- e^+ \nu_e$

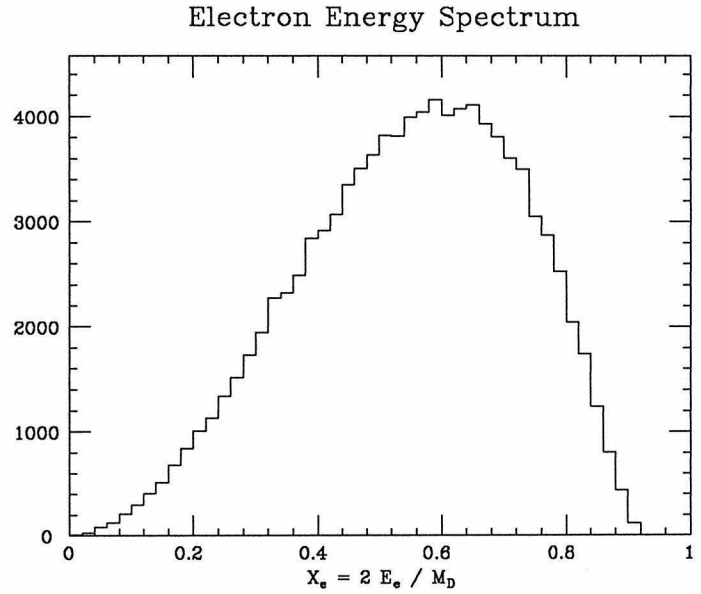

Figure A3.1.2: Energy spectrum of e^+ in D^0 rest frame for $D^0 \rightarrow K^- e^+ \nu_e$

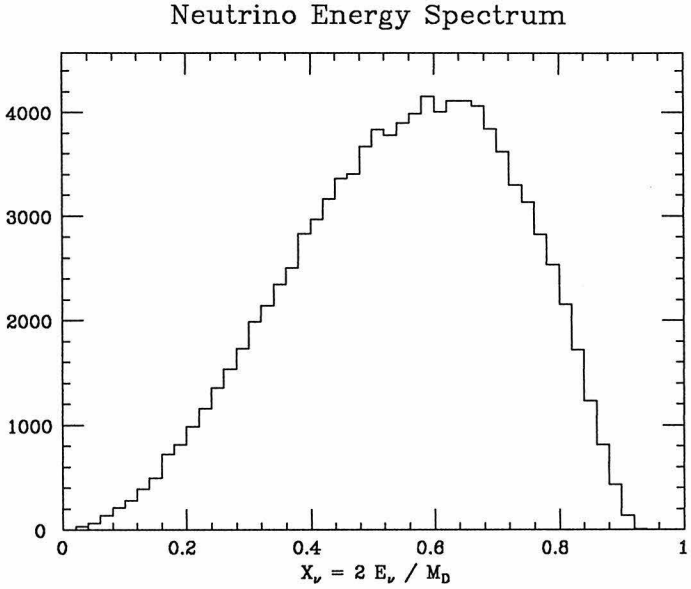

Figure A3.1.3: Energy spectrum of ν_e in D^0 rest frame for $D^0 \to K^- e^+ \nu_e$

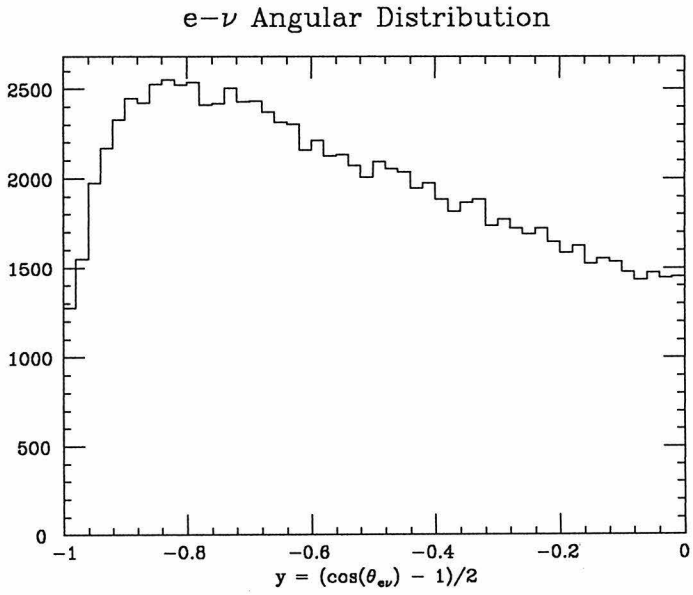

Figure A3.1.4: Distribution of $y \equiv \frac{1}{2}(\cos\vartheta_{e\nu_e} - 1)$ in D^0 rest frame for $D^0 \to K^- e^+ \nu_e$

A3.2: $D \to P\,\mu^+\,\nu_\mu$

When a D meson decays into a pseudoscalar meson, a muon, and a muon-neutrino, the form factor $f_-(t)$ may no longer be ignored. The two form factors must be relatively real to insure the T invariance of the amplitude. Ignoring the overall phase, the matrix element is given by:

$$\begin{aligned}\sum |M|^2 = 8G_F^2 \cos^2\vartheta_C \\ [f_+^2(t)(2P_\mu\cdot(P_D+P_K)P_\nu\cdot(P_D+P_K) - P_\mu\cdot P_\nu(P_D+P_K)^2) \\ +2m_\mu^2 f_+(t)f_-(t)P_\nu\cdot(P_D+P_K) + m_\mu^2 f_-^2(t)P_\mu\cdot P_\nu]\end{aligned}$$

The spectra may be calculated as before in terms of dimensionless quantities. One additional ratio is necessary: $\epsilon \equiv m_\mu/m_D$.

$$\begin{aligned}W(x_\mu,x_K) =& f_+^2(t)(8x_\mu - 4x_K x_\mu + 4x_K - 4x_\mu^2 - 4 \\ & -4\lambda^2 - 3\epsilon^2 + 3\epsilon^2 x_K + 4\epsilon^2 x_\mu + \lambda^2\epsilon^2 - \epsilon^4) \\ & +2f_+(t)f_-(t)\epsilon^2(3 - \lambda^2 + \epsilon^2 - x_K - 2x_\mu) + f_-^2(t)\epsilon^2(1+\lambda^2-\epsilon^2-x_K)\end{aligned}$$

$$\begin{aligned}W(x_K) = \Bigg[& f_+^2(t)\left(\frac{2}{3}(x_K^2-4\lambda^2) + \epsilon^2(1+\lambda^2-x_K)\right. \\ & \left. -\frac{2\epsilon^4(1-\lambda^2)^2}{(1+\lambda^2-x_K)^2} + \frac{\epsilon^6}{(1+\lambda^2-x_K)^3}\left(1+\frac{1}{3}x_K^2 - \frac{10}{3}\lambda^2+\lambda^4\right)\right) \\ & +2f_+(t)f_-(t)\epsilon^2(1-\lambda^2)\left(1-\frac{\epsilon^2}{1+\lambda^2-x_K}\right)^2 \\ & +f_-^2(t)\epsilon^2(1+\lambda^2-x_K)\left(1-\frac{\epsilon^2}{1+\lambda^2-x_K}\right)^2\Bigg](x_K^2-4\lambda^2)^{1/2}\end{aligned}$$

The range of x_K is now $[2\lambda, 1+\lambda^2-\epsilon^2]$. For a given value of x_K, the range of x_μ is:

$$2 - x_K + \frac{2(1+\lambda^2-\epsilon^2-x_K)}{x_K - 2 + (x_K^2-4\lambda^2)^{1/2}} \le x_\mu \le 2 - x_K + \frac{2(1+\lambda^2-\epsilon^2-x_K)}{x_K - 2 - (x_K^2-4\lambda^2)^{1/2}}$$

These and other spectra, evaluated in the rest frame of the decaying D are

shown in Figs. A3.2.1 – A3.2.4. The form factor $f_-(t)$ is assumed to have the form:

$$f_-(t) = f_+(0)\left(\frac{m_D^2 - m_K^2}{t}\right)\left(\frac{m_{F_0}^2}{m_{F_0}^2 - t} - \frac{m_{F^*}^2}{m_{F^*}^2 - t}\right)$$

$$m_{F_0} = 2.20 \text{ GeV/c}^2$$

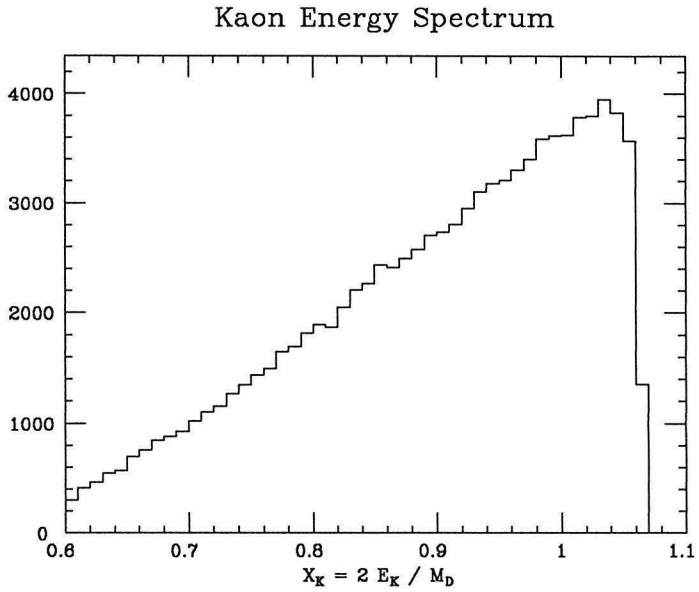

Figure A3.2.1: Energy spectrum of K^- in D^0 rest frame for $D^0 \to K^- \mu^+ \nu_\mu$

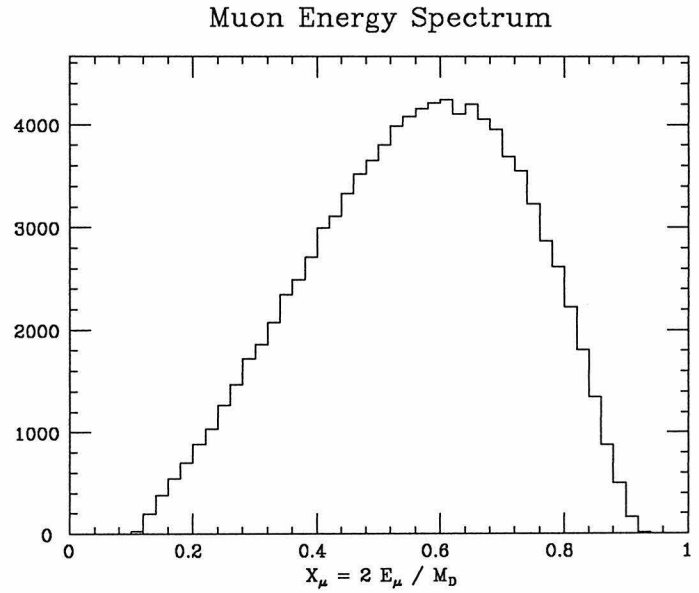

Figure A3.2.2: Energy spectrum of μ^+ in D^0 rest frame for $D^0 \to K^- \mu^+ \nu_\mu$

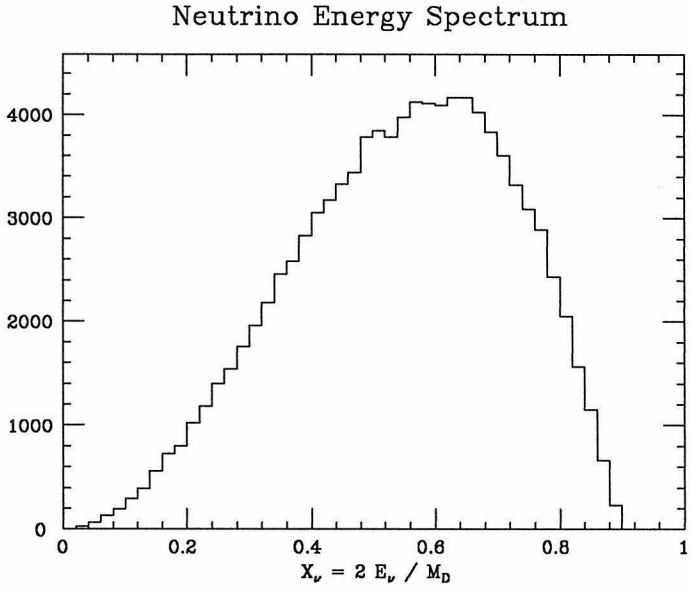

Figure A3.2.3: Energy spectrum of ν_μ in D^0 rest frame for $D^0 \to K^- \mu^+ \nu_\mu$

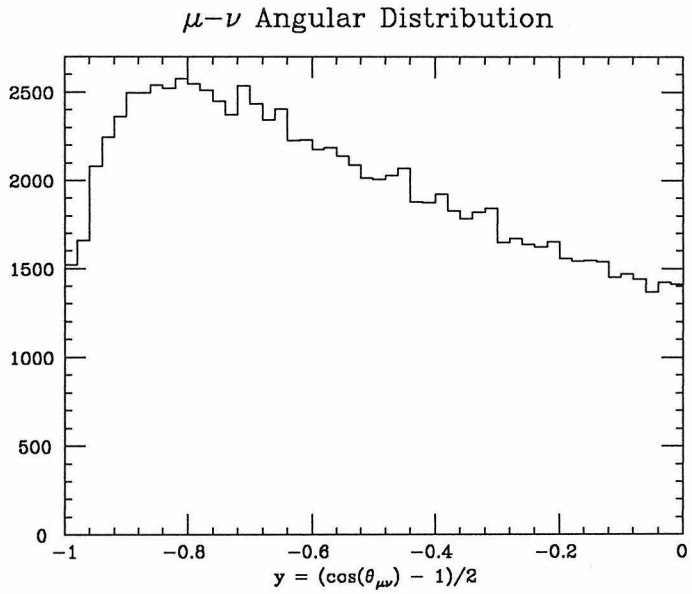

Figure A3.2.4: Distribution of $y \equiv \frac{1}{2}(\cos\vartheta_{\mu\nu_\mu} - 1)$ in D^0 rest frame for $D^0 \to K^- \mu^+ \nu_\mu$

A3.3: $D \to V\, e^+\, \nu_e$

When a D meson decays to a vector meson, an electron and an electron-neutrino, the situation is more complicated. The hadronic current is:

$$J_{\mu,\,hadronic} = \sqrt{2}\cos\vartheta_C[ig(t)\epsilon_{\mu\nu\rho\sigma}\epsilon^{*\nu}(P_D+P_V)^\rho(P_D+P_V)^\sigma \\ - f(t)\epsilon^*_\mu - a_+(t)(\epsilon^*\cdot P_D)(P_D+P_V)_\mu - a_-(t)(\epsilon^*\cdot P_D)(P_D-P_V)_\mu]$$

Just as $f_-(t)$ could be ignored in the pseudoscalar case, $a_-(t)$ may be ignored here.

It is necessary to sum the matrix element over the spins of the leptons and over the polarizations of the vector particle. The latter is accomplished through the use of the identity:

$$\sum_\lambda \epsilon^*_\mu(\lambda)\,\epsilon_\nu(\lambda) = -g_{\mu\nu} + \frac{P_{V\mu}P_{V\nu}}{M_V^2}$$

The matrix element is given by:

$$\sum|M|^2 = 8G_F^2\cos^2\vartheta_C \\ \Bigg[8g^2(t)((P_V\cdot P_e)(P_D\cdot P_V)(P_D\cdot P_\nu) + (P_V\cdot P_\nu)(P_D\cdot P_V)(P_D\cdot P_e) \\ - m_D^2(P_V\cdot P_e)(P_V\cdot P_\nu) - m_V^2(P_D\cdot P_e)(P_D\cdot P_e)) \\ - 8g(t)f(t)((P_V\cdot P_e)(P_D\cdot P_\nu) - (P_V\cdot P_\nu)(P_D\cdot P_e)) \\ + 4f(t)a_+(t)\Bigg(\frac{2(P_D\cdot P_V)(P_V\cdot P_e)(P_V\cdot P_\nu)}{m_V^2} \\ - (P_D\cdot P_e)(P_V\cdot P_e) - (P_D\cdot P_\nu)(P_V\cdot P_e)\Bigg) \\ + f^2(t)\Bigg(\frac{2(P_V\cdot P_e)(P_V\cdot P_\nu)}{m_V^2} + (P_e\cdot P_\nu)\Bigg) \\ + 4a_+^2(t)\Bigg(\frac{2(P_D\cdot P_V)^2(P_V\cdot P_e)(P_V\cdot P_\nu)}{m_V^2} - 2m_D^2(P_V\cdot P_e)(P_V\cdot P_\nu) \\ + m_D^2m_V^2(P_e\cdot P_\nu) - (P_D\cdot P_V)^2(P_e\cdot P_\nu)\Bigg)\Bigg]$$

The spectra are given by:

$$W(x_e, x_V) = 4m_D^2 g(t)^2 A - 2g(t)f(t)B + 2f(t)a_+(t)C + \frac{f^2(t)}{m_D^2}D + 4m_D^2 a_+^2(t)E$$

$$\begin{aligned}
A &= \frac{1}{4}(6x_V x_e - 4x_V - 4x_e + 3x_V^2 + 2x_e^2 - x_V^3 - 2x_V x_e^2 \\
&\quad - 2x_V^2 x_e + 2 - 2\lambda^4 - 2\lambda^2 x_V x_e + \lambda^2 x_V^2) \\
B &= 2(3x_V + 2x_e - 2x_V x_e - x_V^2 - 2 - 2\lambda^2 + \lambda^2 x_V + 2\lambda^2 x_e) \\
C &= \frac{1}{2\lambda^2}(-4x_V - 4x_e + 4x_V x_e + 2x_V^2 + 2x_e^2 \\
&\quad - x_V^2 x_e - x_V x_e^2 + 2 + 2\lambda^2 - \lambda^2 x_V^2 + \lambda^4 x_V) \\
D &= \frac{1}{2\lambda^2}(x_V + 2x_e - x_V x_e - x_e^2 - 1 + \lambda^2 - 2\lambda^2 x_V + 2\lambda^4) \\
E &= \frac{1}{8\lambda^2}(x_V^3 - x_V^2 + 2x_V^2 x_e - x_V^3 x_e - x_V^2 x_e^2 + 4\lambda^2 \\
&\quad + 4\lambda^4 - 4\lambda^2 x_V - 8\lambda^2 x_e + 4\lambda^2 x_V x_e + 3\lambda^2 x_V^2)
\end{aligned}$$

$$\begin{aligned}
W(x_V) = [&4m_D^2 g^2(t)(\frac{1}{3}x_V^2 - \frac{1}{3}x_V^3 - \frac{1}{3}\lambda^2 - \frac{2}{3}\lambda^2 x_V + \lambda^2 x_V^2 - \lambda^4) \\
&+ \frac{2f(t)a_+(t)}{\lambda^2}(\frac{1}{6}x_V^3 + \frac{2}{3}x_V^2 - x_V + \frac{4}{3}\lambda^2 - \frac{2}{3}\lambda^2 x_V - \lambda^2 x_V^2 + \lambda^4 x_V) \\
&+ \frac{f^2(t)}{m_D^2\lambda^2}(\frac{1}{6}x_V^2 + \frac{4}{3}\lambda^2 - 2\lambda^2 x_V + 2\lambda^4) \\
&+ \frac{m_D^2 a_+^2(t)^2}{\lambda^2}(\frac{1}{6}x_V^4 - 4\lambda^2 + 4\lambda^2 x_V + \frac{4}{3}\lambda^2 x_V^2 + 4\lambda^4)](x_V^2 - 4\lambda^2)^{1/2}
\end{aligned}$$

The inclusion of the vector particle introduces a further complication into the event generation; the phase-space weight is no longer simply unity. It is straightforward to calculate this weight with the observation that a decay determined by multiparticle phase-space factors into a series of quasi two-body decays. This may be demonstrated with the case of a pseudoscalar decaying into three pseudoscalars, say $D \to K\pi\pi$. If the matrix element for this process is ignored, the

decay rate is:

$$\Gamma = \frac{1}{2m_D(2\pi)^5}\int \delta^4(P_D - P_K - P_{\pi_1} - P_{\pi_2})\frac{d^3p_K}{2E_K}\frac{d^3p_{\pi_1}}{2E_{\pi_1}}\frac{d^3p_{\pi_2}}{2E_{\pi_2}}$$

This integral may be written in a more convenient form through the use of three identities:

$$\delta^4(P_D - P_K - P_{\pi_1} - P_{\pi_2}) = \int \delta^4(P_D - P_K - P)\delta^4(P - P_{\pi_1} - P_{\pi_2})\, d^4p$$

$$\int \delta(P^2 - M^2)\, dM^2 = 1$$

$$\int \delta(P^2 - M^2)\, d^4p = \int \frac{d^3p}{2E}$$

The decay rate may now be cast into the form of two quasi two-body decays:

$$\Gamma = \frac{1}{2m_D(2\pi)^5}\int \delta^4(P_D - P_K - P)\,\frac{d^3p_K}{2E_K}\frac{d^3p}{2E}\,dM^2$$
$$\delta^4(P - P_{\pi_1} - P_{\pi_2})\,\frac{d^3p_{\pi_1}}{2E_{\pi_1}}\frac{d^3p_{\pi_2}}{2E_{\pi_2}}$$

Here, M is the invariant mass of the $\pi_1 - \pi_2$ system.

Returning now to the semileptonic decay $D \rightarrow V\, e^+\, \nu_e$, assume that the vector particle is the $K^*(892)$ resonance. The matrix element for this decay must contain the weak matrix element given above and also a Breit-Wigner function for the mass of the K^*. The decay rate for the decay chain $D \rightarrow K^*\, e^+\, \nu_e$, $K^* \rightarrow K\pi$ is given by the expression:

$$\Gamma = \frac{1}{2m_D(2\pi)^8}\int \sum |M|^2 \left[\frac{1}{1 + (4/\Gamma_r^2)(M - M_r)^2}\right]$$
$$\delta^4(P_D - P_K - P_\pi - P_e - P_\nu)\frac{d^3p_K}{2E_K}\frac{d^3p_\pi}{2E_\pi}\frac{d^3p_e}{2E_e}\frac{d^3p_\nu}{2E_\nu}$$

M is the invariant mass of the $K - \pi$ system. M_r and Γ_r are the resonant mass and width of the K^*. The integration may be simplified by applying the factoring

rule derived above:

$$\Gamma = \int \left[\frac{1}{1 + (4/\Gamma_r^2)(M - M_r)^2} \right] \delta^4(P_{K^*} - P_K - P_\pi) \frac{d^3p_K}{2E_K} \frac{d^3p_\pi}{2E_\pi} dM^2$$
$$\left\{ \frac{\sum |M|^2}{2m_D(2\pi)^8} \delta^4(P_D - P_{K^*} - P_e - P_\nu) \frac{d^3p_{K^*}}{2E_{K^*}} \frac{d^3p_e}{2E_e} \frac{d^3p_\nu}{2E_\nu} \right\}$$

The integration of the terms within curly braces — {} — has already been accomplished with the results described above. Six of the remaining integrations are trivial:

$$I = \int \left[\frac{1}{1 + (4/\Gamma_r^2)(M - M_r)^2} \right] \delta^4(P_{K^*} - P_K - P_\pi) \frac{d^3p_K}{2E_K} \frac{d^3p_\pi}{2E_\pi} dM^2$$
$$= \int \left[\frac{1}{1 + (4/\Gamma_r^2)(M - M_r)^2} \right] \delta((P_{K^*} - P_K)^2 - M_\pi^2) \frac{d^3p_K}{2E_K} dM^2$$
$$= \int \left[\frac{1}{1 + (4/\Gamma_r^2)(M - M_r)^2} \right] 4\pi \frac{q_K(M^2)}{4M} dM^2$$

The function $q_K(M^2)$ gives the momentum of the K in the center-of-mass of the K^*. Its definition is:

$$q_K(M^2) = \frac{(M^4 + m_K^4 + m_\pi^4 - 2M^2m_K^2 - 2M^2m_\pi^2 - 2m_K^2m_\pi^2)^{1/2}}{2M}$$

One further simplification is in order: $dM^2 = 2M\,dM$. Now the integration is reduced to:

$$I = 2\pi \int \left[\frac{1}{1 + (4/\Gamma_r^2)(M - M_r)^2} \right] q_K(M^2) dM$$

As is clear from the discussion in section A3.1, this integral will converge much faster if M is chosen according to a Breit-Wigner distribution. This seemingly difficult task turns out to be surprisingly simple. If the random variable r is uniformly distributed in the interval [0,1], then the values of M obtained from the

following formula will display a Breit-Wigner distribution; the range of allowed masses is $[M_{min}, M_{max}]$.

$$M = M_r + \frac{\Gamma_r}{2}\tan\Bigg[\arctan\left(\frac{2}{\Gamma_r}(M_{min} - M_r)\right) + r\left(\arctan\left(\frac{2}{\Gamma_r}(M_{max} - M_r)\right) - \arctan\left(\frac{2}{\Gamma_r}(M_{min} - M_r)\right)\right)\Bigg]$$

$$dM = \left(1 + (4/\Gamma_r^2)(M - M_r)^2\right) \cdot \frac{\Gamma_r}{2}\left(\arctan\left(\frac{2}{\Gamma_r}(M_{max} - M_r)\right) - \arctan\left(\frac{2}{\Gamma_r}(M_{min} - M_r)\right)\right) dr$$

If the energies x_{K^*} and x_e are generated according to the above distributions, and the mass M according to a Breit-Wigner distribution, the phase-space weight for each generated event is:

$$W_{ps} = \pi q_K(M^2)\Gamma_r\left(\arctan\left(\frac{2}{\Gamma_r}(M_{max} - M_r)\right) - \arctan\left(\frac{2}{\Gamma_r}(M_{min} - M_r)\right)\right)$$

Figures A3.3.1 – A3.3.5 illustrate the spectra for the decay $D^0 \rightarrow K^{*-}\, e^+\, \nu_e$, $K^{*-} \rightarrow K^-\, \pi^0$. The form factors in these calculations are:

$$g(t) = g(0)\frac{m_{F^*}^2}{m_{F^*}^2 - t}$$

$$f(t) = f(0)\frac{m_{F_A}^2}{m_{F_A}^2 - t}$$

$$a_+(t) = a_+(0)\frac{m_{F_A}^2}{m_{F_A}^2 - t}$$

$$m_{F_A} = 2.25 \text{ GeV/c}^2$$

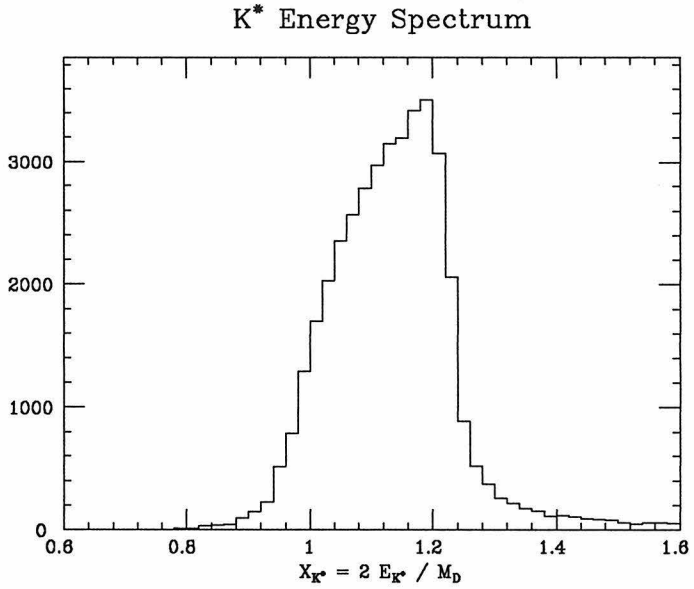

Figure A3.3.1: Energy spectrum of K^{*-} in D^0 rest frame for $D^0 \rightarrow K^{*-}\, e^+\, \nu_e$

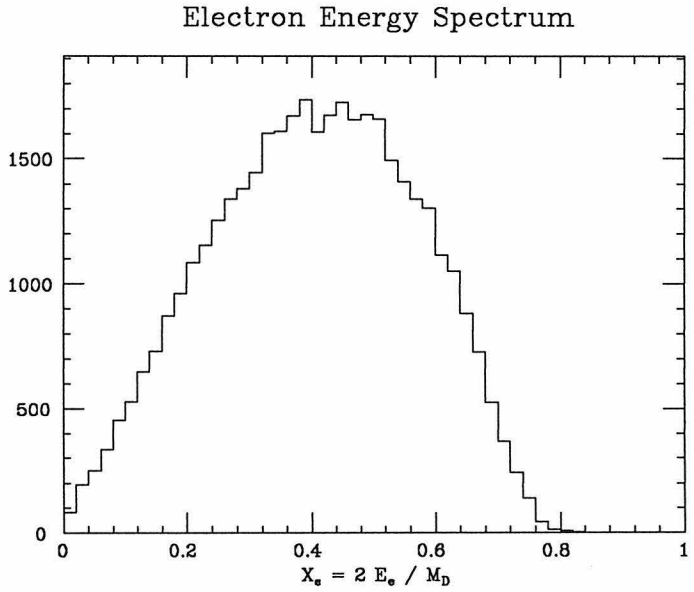

Figure A3.3.2: Energy spectrum of e^+ in D^0 rest frame for $D^0 \rightarrow K^{*-}\, e^+\, \nu_e$

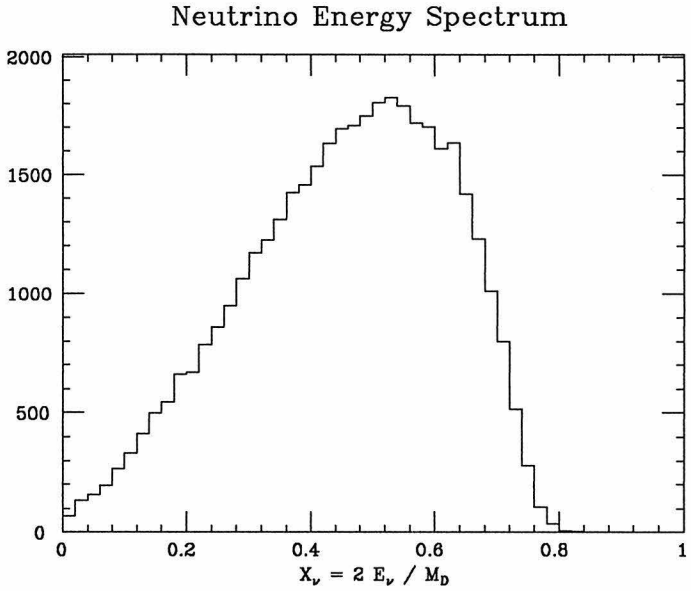

Figure A3.3.3: Energy spectrum of ν_e in D^0 rest frame for $D^0 \to K^{*-}\, e^+\, \nu_e$

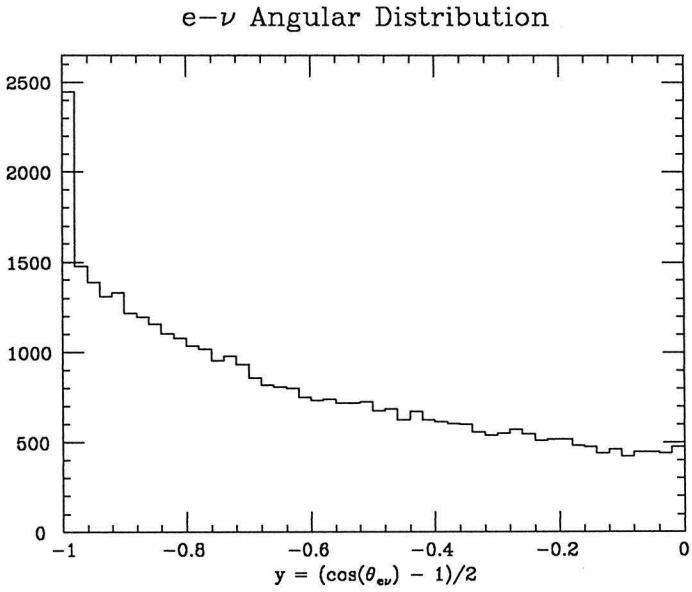

Figure A3.3.4: Distribution of $y \equiv \frac{1}{2}(\cos\vartheta_{e\nu_e} - 1)$ in D^0 rest frame for $D^0 \to K^{*-}\, e^+\, \nu_e$

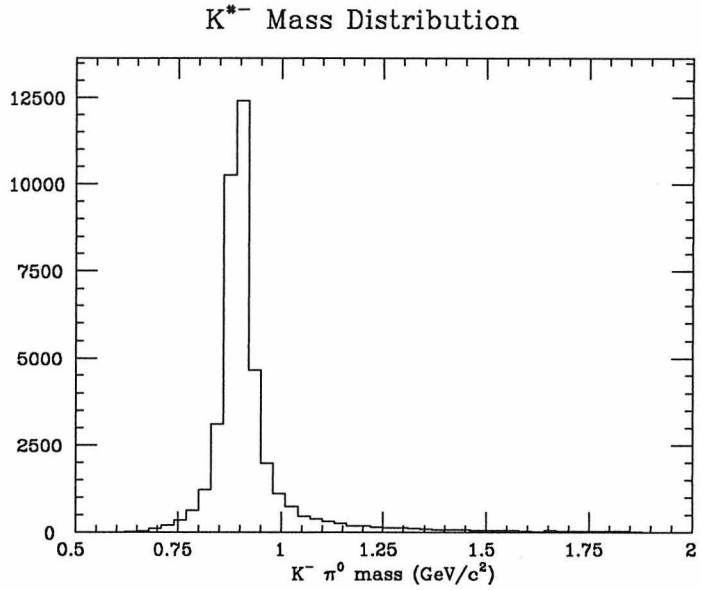

Figure A3.3.5: K^{*-} mass spectrum for $D^0 \to K^{*-} e^+ \nu_e$

A3.4: $D \to V \mu^+ \nu_\mu$

For decays of this type, the form factor $a_-(t)$ should, in principle, not be ignored. The resulting formulae, however, become quite complicated. By ignoring this form factor, the relative error introduced is of order $m_\mu^2/m_D^2 = 0.003$. This ratio is small enough that serious problems will not occur if $a_-(t)$ is ignored. thus all of the Monte Carlo simulations of $D \to V \mu^+ \nu_\mu$ are performed by using the formulae of section A3.3, replacing m_e everywhere by m_μ.

A3.5: $D \to PP e^+ \nu_e$

If the two pseudoscalar mesons are produced in a relative S or P wave, the formulae of sections A3.1 and A3.3 may be applied. In both cases, the mass of the $P_1 - P_2$ system is generated uniformly in the range $[m_{P_1} + m_{P_2}, m_D - m_e]$. the resulting phase-space weight is $2\pi q_{P_1}$; q_{P_1} is the momentum of P_1 in the center-of-mass of the $P_1 - P_2$ system.

The S-wave and P-wave mass distributions are given in Figs. A3.5.1 and A3.5.2 for the decay $D^+ \to K^- \pi^+ e^+ \nu_e$.

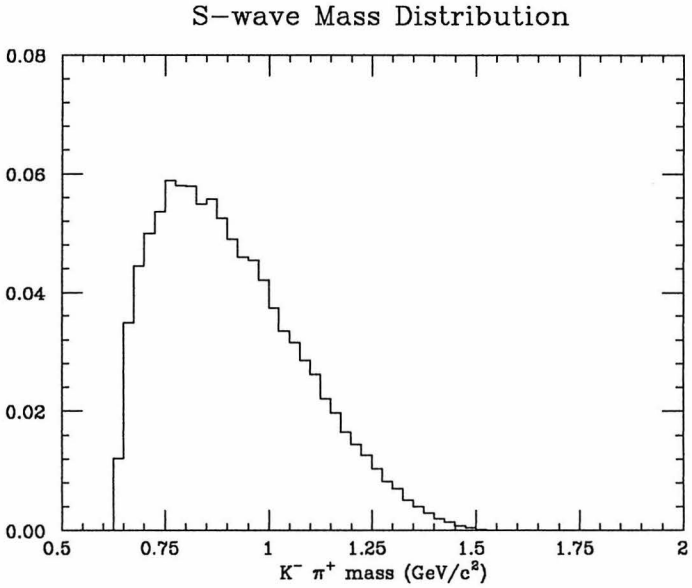

Figure A3.5.1: S-wave mass distribution for $D^0 \to K^- \pi^+ e^+ \nu_e$

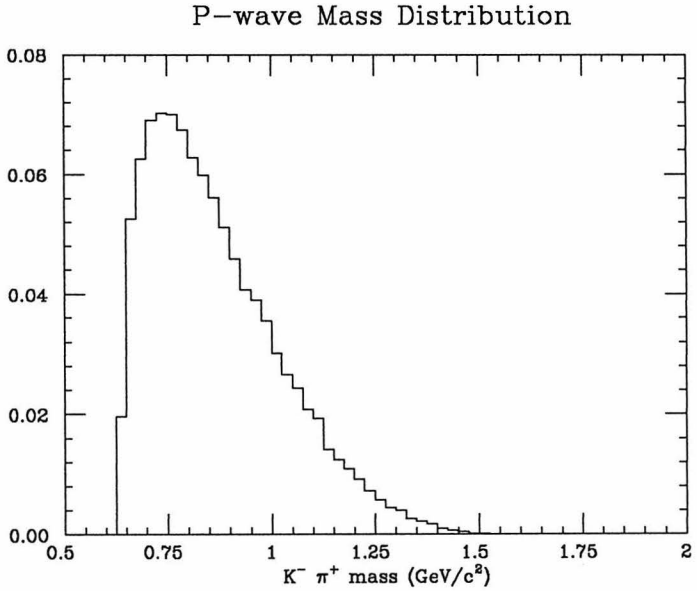

Figure A3.5.2: P-wave mass distribution for $D^0 \to K^- \pi^+ e^+ \nu_e$

References

1. The best measurement of $g-2$ for the electron is given in:
   R. S. Van Dyck, Jr., P. B. Schwinger, and H. G. Dehmelt, *Phys. Rev. Lett.* **38**, 310 (1977).
   A measurement of $g-2$ for the muon is reported in:
   J. Bailey *et al.*, *Phys. Lett.* **55B**, 420 (1975). A theoretical calculation based on the evaluation of fifty Feynman diagrams is given in:
   P. Cvitanovič, and T. Kinoshita, *Phys. Rev.* **D10**, 4007 (1974).
2. M. Gell-Mann, *Phys. Rev.* **92**, 833 (1953).
3. T. Nakano, and K. Nishijima, *Prog. Theor. Phys.* **10**, 581 (1953).
4. W. Heisenberg, *Z. Phys.* **77**, 1 (1932).
5. S. Sakata, *Prog. Theor. Phys.* **16**, 686 (1956).
6. A. Pevsner *et al.*, *Phys. Rev. Lett.* **7**, 421 (1961).
7. M. Gell-Mann, *California Institute of Technology Synchrotron Laboratory Report* **CTSL-20**.
8. Y. Ne'eman, *Nucl. Phys.* **26**, 222 (1961).
9. M. Gell-Mann, *Phys. Rev.* **125**, 1067 (1962)
   S. Okubo, *Prog. Theor. Phys.* **27**, 949 (1962).
10. M. Gell-Mann, and Y. Ne'eman, *The Eightfold Way*, W. A. Benjamin, New York (1964)
    R. E. Behrends, J. Dreitlein, C. Fronsdal, and W. Lee, *Rev. Mod. Phys.* **34**, 1 (1962).
11. V. E. Barnes *et al.*, *Phys. Rev. Lett.* **12**, 204 (1964).
12. N. Cabibbo, *Phys. Rev. Lett.* **10**, 531 (1963).
13. M. Gell-Mann, *Phys. Lett.* **8**, 214 (1964).
14. G. Zweig, (unpublished CERN report).

15. J. Joyce, *Finnegans Wake*, Penguin Books, New York (1976).

16. S. L. Glashow, *Nucl. Phys.* **22**, 579 (1961).

17. F. J. Hasert *et al.*, *Phys. Lett.* **46B**, 138 (1973).

18. G. 't Hooft, *Nucl. Phys.* **B35**, 167 (1971).

19. S. L. Glashow, J. Illiopoulos, and L. Maiani, *Phys. Rev.* **D2**, 1285 (1970).

20. M. K. Gaillard, B. W. Lee, and R. E. Shrock, *Phys. Rev.* **D13**, 2674(1976).

21. M. K. Gaillard, and B. W. Lee, *Phys. Rev* **D10**, 897 (1974).

22. J. J. Aubert *et al.*, *Phys. Rev. Lett.* **33**, 1404 (1974).

23. J.-E. Augustin *et al.*, *Phys. Rev. Lett.* **33**, 1406 (1974).

24. C. Bacci *et al.*, *Phys. Rev. Lett.* **33**, 1408 (1974).

25. The properties of charmonium are discussed in:
E. Eichten, K. Gottfried, T. Kinoshita, K. D. Lane, and T.-M Yan, *Phys. Rev.* **D17**, 3090 (1978).

26. J. E. Gaiser *et al.*, *Phys. Rev* **D34**, 711 (1986).

27. Recent results from the MARK III collaboration are summarized in:
R. M. Baltrusaitis *et al.*, *Phys. Rev.* **D33**, 629 (1986).

28. C. Edwards *et al.*, *Phys. Rev. Lett.* **48**, 70 (1982).

29. E. Eichten, K. Gottfried, T. Kinoshita, K. D. Lane, and T.-M Yan, *Phys. Rev.* **D21**, 203 (1980).

30. M. L. Perl *et al.*, *Phys. Rev. Lett.* **35** 1489 (1975).

31. Y.-S. Tsai, *Phys. Rev.* **D4**, 2821 (1971)
F. J. Gilman, and S. H. Rhie, *Phys. Rev.* **D31**, 1066 (1985).

32. These were first seen observed in hadronic interactions:
S. W. Herb *et al.*, *Phys. Rev. Lett.* **39**, 252 (1977)
W. R. Innes *et al.*, *Phys. Rev. Lett.* **39**, 1240 (1977)
The individual resonances were subsequently resolved in e^+e^- interactions:.

33. M. Kobayashi, and T. Maskawa, *Prog. Theor. Phys.* **49**, 652 (1973).

34. M. Aguilar-Benitez *et al.*, *Reviews of Particle Properties*, *Phys. Lett.* **170B** (1986).

35. L. Wolfenstein, *Phys. Rev. Lett.* **51**, 1945 (1984).

36. G. Goldhaber *et al.*, *Phys. Rev. Lett.* **37**, 255 (1976)
I. Peruzzi *et al.*, *Phys. Rev. Lett.* **37** 569 (1976).

37. A. Pais, and S. B. Treiman, *Phys. Rev.* **D15**, 2529 (1977).

38. R. M. Baltrusaitis *et al.*, *Phys. Rev. Lett.* **54**, 1976 (1985).

39. V. Lüth, *Proceedings of International Symposium on Production and Decay of Heavy Flavours*, Heidelberg(1986).

40. All $SU(n)$ formulae are drawn from:
R. Slansky, *Phys. Rept.* **79** (1981).

41. C. Quigg, *Z. Phys.* **C4**, 55 (1980).

42. R. Rückl, *Habilitationsschrift*, Universität München, 1984 (unpublished).

43. H. Albrecht *et al.*, *Phys. Lett.* **158B**, 525 (1985)
C. Bebek *et al.*, *Phys. Rev. Lett.* **56**, 1893 (1986)
R. M. Baltrusaitis *et al.*, *Phys. Rev. Lett.*, **56**, 2136 (1986).

44. R. Rückl, *op. cit.*.

45. J. F. Donoghue, *Phys. Rev.* **D33**, 1516 (1986).

46. A. J. Buras, J.-M. Gérard, R. Rückl, *Nucl. Phys.* **B268**, 16(1986).

47. N. Cabibbo, and L. Maiani, *Phys. Lett.* **79B**, 109 (1978).

48. M. Suzuki, *Phys. Rev.* **D31**, 662 (1985).

49. B. Grinstein, M. B. Wise, and N. Isgur, *DOE Research and Development Report* **CALT-68-1311** (1985).

50. J. M. Gaillard, M. K. Gaillard, F. Vannucci, *Weak Interactions*, Institute National de Physique Nucléaire et de Physique des Particules, Paris(1977).

51. J. W. Moffat, *Phys. Rev.* **D12**, 288 (1975).

52. M. Wirbel, B. Stech, and M. Bauer, *Z. Phys.* **C29**, 637 (1985).

53. S. Neddermeyer *et al.*, *Rev. Sci. Inst.* **18**, 488 (1947).

54. J. Roehrig *et al.*, *Nucl. Instr. Meth.* **226**, 319 (1984).

55. J. Fox and J.-L. Pellegrin, *PEP-NOTE-329*, 1981.

56. H. K. Kang, *IEEE Trans. Nucl. Sci.* **NS-28**, 590 (1980).

57. D. Bernstein, *IEEE Trans. Nucl. Sci.* **NS-28**, 359 (1981).

58. M. Breidenbach *et al.*, *IEEE Trans. Nucl. Sci.* **NS-25**, 706 (1978).

59. D. Nelson *et al.*, *IEEE Trans. Nucl. Sci.* **NS-28**, 336 (1981).

60. J. S. Brown *et al.*, *Nucl. Instr. Meth.* **221**, 503 (1984).

61. J. .E. Grund, *IEEE Trans. Nucl. Sci.* **NS-27**, 559 (1980).

62. K. Bunnell *et al.*, *Nucl. Instr. Meth.* **219**, 479 (1984).

63. R. Fabrizio *et al.*, *Nucl. Instr. Meth.* **227**, 220 (1984).

64. G. Gieraltowski, Argonne National Laboratory, HRS Collaboration Memorandum (unpublished).

65. These polynomials were developed by the Mark I collaboration.

66. J. Thaler *et al.*, *IEEE Trans. Nucl. Sci.* **NS-30**, 236 (1980).

67. R. M. Baltrusaitis *et. al.*, *Phys. Rev. Lett.* **56**, 107 (1986).

68. The number of $D\overline{D}$ pairs was obtained by a 'double-tag' procedure which is independent of the charm production cross-sections. This procedure is described in:
R. M. Baltrusaitis *et al.*, *Phys. Rev. Lett.* **56**, 2140 (1986)
G. T. Blaylock, *Ph.D. Thesis*, University of Illinois, 1986 (unpublished).

69. The $\tau^+\tau^-$ cross-section was calculated to $O(\alpha^3)$ by applying the formulae contained in:

F. A. Berends, R. Kleiss, S. Jadach, Z. Was, *Acta Phys. Polon.* **B14**, 413 (1983).

70. The tagging procedure is described in more detail in:
J. Hauser, Ph.D. Thesis, California Institute of Technology, *CALT-68-1275*(1985).

71. J. Becker *et al.*, *Nucl. Instr. Meth.* **A235**, 502 (1985).

72. All such spectra are based on the calculations given in:
F. A. Berends, R. Kleiss, *Nucl. Phys.* **B228**, 537 (1983)

73. J. H. Friedman, Recursive Partitioning (unpublished)

74. F. James, M. Roos, CERN-DD/80/1

75. R. H. Schindler *et al.*, *Phys. Rev.* **D24**, 78 (1981)
R. H. Schindler, Ph.D Thesis, Stanford University, *SLAC-REPORT-0219*, 1979.

76. R. M. Baltrusaitis *et al.*, *Phys. Rev. Lett.* **54**, 1976 (1985)
J. Hauser, Ph.D. Thesis, California Institute of Technology, *CALT-68-1275*, 1985

77. R. M. Baltrusaitis *et al.*, *Phys. Rev. Lett.* **56**, 2140 (1986).

78. J. H. Friedman, *Jou. Comp. Phys.* **7**, 201(1971).

79. The data are taken from compilations of the CERN High-Energy Reaction Analysis Group. The π^+ and π^- data are extracted from the review:
V. Flaminio, W. G. Moorhead, D. R. O. Morrison, and N. Rivoire, *CERN-HERA 83-01* (1983)
The K^+ and K^- data are from:
V. Flaminio, W. G. Moorhead, D. R. O. Morrison, and N. Rivoire, *CERN-HERA 83-02* (1983)
Finally, the p and $\overline{p}$ data are taken from:
E. Bracci, J. P. Droulez, V. Flaminio, J. .D. Hansen, and D. R. O. Morrison, *CERN-HERA 73-1* (1973).

80. See for example:
M. L. Perl, *High Energy Hadron Physics*, John Wiley & Sons, New York (1974).

81. R. M. Sternheimer and R. F. Peierls, *Phys. Rev.* **B11**, 3681 (1971).

82. B. B. Rossi, High-Energy Particles, Prentice-Hall, New York, 1952.

83. J. Hauser, op. cit.

84. E. Fiorini, *Proceedings of the 1983 International Symposium on Lepton and Photon Interactions at High Energies*, Cornell University, Ithaca (1985).

85. Y.-S. Tsai, *Phys. Rev.* **D4**, 2821(1971)
F. J. Gilman, S. H. Rhie, *Phys. Rev.* **D31**, 1066(1985).

86. R. M. Baltrusaitis *et al.*, *Phys. Rev. Lett.* **55**, 1842(1985).

87. W. Bacino *et al.*, *Phys. Rev. Lett.* **43**, 1073(1979)

88. M. Wirbel, B. Stech, and M. Bauer, *op. cit.*

89. B. Grinstein, M. B. Wise, and N. Isgur, *op. cit.*

90. A. Ali, T. C. Yang, *Phys. Lett.* **65B**, 275 (1976).

91. M. Suzuki, *Phys. Lett.* **155B**, 112(1985).

92. S.-C. Chao, G. Kramer, W. F. Palmer, and S. S. Pinsky, *Phys. Rev.* **D30**, 1916(1984).

93. M. Suzuki, *Phys. Rev.***D31**, 662(1985).